Computational aeroacoustics and turbulence modelling of low speed flows using subgrid scale stabilised finite element methods.

Oriol Guasch i Fortuny

Universitat Politècnica de Catalunya

Supervised by: Ramon Codina

Per la meva estimada, alegre i optimista Núria
i pels petits i entremaliats Mar i Biel.

Agraïments (Acknowledgments)

És molta la gent a qui haig d'agrair haver pogut dur a terme aquesta tesi. En primer lloc a la meva estimada Núria, que amb la seva empenta i entusiasme naturals sempre m'ha ajudat a superar els moments difícils, en que semblava que res sortia bé. La divertida Mar i el Biel trapella són el millor fruit d'aquests darrers anys i s'han dedicat a donar-me energia en forma de somriures, rialles i ocurrències i, per què no dir-ho, a treure-me-la després en forma de nits sense dormir. Els tres, d'una manera o d'una altra, han esdevingut part indissociable d'aquest treball i els ho agreixo de tot cor.

Per altra banda, se'm fa impossible elaborar una llista de tots els familiars i amics que m'han donat suport. Bé sigui a través d'una senzilla conversa, una passejada, o compartint dues de les meves grans passions com el mar i la muntanya, entre tots m'han proporcionat un entorn favorable que m'ha facilitat molt les coses. Em sento realment afortunat pels familiars i amics de què gaudeixo. La meva germana Clara i el seu marit Pól mereixen una menció especial: han estat, són i espero que seguiran essent els meus consultors particulars d'anglès, i m'han resolt una infinitat de dubtes lingüístics.

Aquells que s'han vist involucrats directament en la realització de la tesi i sense els quals aquesta no hagués vist la llum, mereixen també sens dubte el meu agraïment explícit. En aquest sentit dues persones han resultat cabdals: en Ramon Codina i en Francesc X. Magrans.

En Ramon ha estat el meu director de tesi. Després d'uns inicis difícils, amb més d'una negativa, quan vaig proposar el projecte a en Ramon de seguida s'hi va mostrar molt interessat i va fer tot el possible per tirar-lo endavant. Tenir en Ramon de director ha estat un veritable privilegi. Deixant de banda la seva desbordant capacitat científica i la seva habilitat per transmetre de forma comprensible els conceptes matemàtics més abstrusos, la seva porta sempre ha estat oberta i ha tingut una paciència infinita a l'hora de resoldre'm tot tipus de dubtes. Parlar amb en Ramon de qualsevol tema, no només de matemàtiques, és sempre un plaer. Per altra banda, també vull agrair als meus companys de doctorat la seva col.laboració. En particular, a Javier Principe, programador incansable que ha estat sempre disposat a ajudar-me sense queixa en les meves lluites peculiars contra els ordinadors. A més, les fructíferes converses que he mantingut amb ell, i amb en Guillaume Houzeaux, en Herbert Coppola, en Santiago Badia i en Daniel Pérez, m'han resultat molt útils per comprendre un munt de conceptes científics.

L'altra persona gràcies a la qual he pogut fer aquesta tesi és en Francesc X. Magrans. En Francesc és el director d'ICR, Enginyeria pel Control del Soroll, empresa on vaig entrar a treballar al cap de pocs anys d'haver acabat la carrera, i amb la qual he estat vinculat des d'aleshores. L'ambient de treball que en Francesc ha aconseguit crear a ICR és força original i divertit, i sobretot molt estimulant des d'un punt de vista científic. Quan li vaig comentar la idea que em rondava pel cap, de fer una tesi doctoral, en Francesc de seguida s'hi va mostrar favorable i em va ajudar a organitzar, trobar i fins i tot proporcionar el recolzament econòmic que tota aventura com aquesta requereix. El seu suport en tots els sentits ha estat incondicional al llarg d'aquests anys i espero poder seguir aprenent i treballant al seu costat força més temps. També vull estendre el meu agraïment a en

Jordi Jové i en Pere V. Rodríguez d'ICR per la seva ajuda i comprensió durant aquesta aventura.

Contents

Chapter 1

Introduction and objectives

Aeroacoustics has emerged from the fields of acoustics and fluid mechanics and is concerned with sound generated by unsteady and/or turbulent flows and also by their interaction with solid boundaries. This type of sound is commonly known as *aerodynamic sound*. In contrast to classical acoustics, forces and motions inside the flow are the sources of sound rather than the externally applied ones. On the other hand, *Computational Aeroacoustics* (CAA) is a relatively new computational field that aims at simulating and predicting aerodynamically generated noise. CAA has become nowadays an active research field due to its applications in the aeronautic, railway, automotive and underwater industries.

The first purpose and main result of this thesis consists in developing a strategy, to be implemented in a finite element code, that results in useful low speed CAA predictions. In order to do so, *Lighthill's acoustic analogy* is central to this work. Lighthill showed how the compressible Navier-Stokes equations could be reordered in the form of an inhomogeneous acoustic wave equation with a source term built from the double divergence of what is now known as Lighthill's tensor. This tensor involves combinations of the flow variables and their derivatives (velocity, pressure and density) and under certain hypothesis it acquires a simple, treatable expression. The idea is then to obtain this source term either by means of experiment, analytical development or computation and to solve its corresponding wave equation. The standard procedure involves finding a formal integral solution to the wave equation using an appropriate Green's function and hence to obtain the radiated acoustic field in this way. However, a different approach will be followed in this thesis.

The herein proposed methodology to make CAA predictions of viscous low speed flows can be conceptually divided in three steps. In the first step, a *Computational Fluid Dynamics* (CFD) simulation is to be performed in order to find the acoustic source term. For low speed flows, an incompressible CFD simulation can be carried out. In the case of dealing with turbulent flows, it is customary to make use of *Large Eddy Simulation* (LES) models, which involve filtering the Navier-Stokes equations with a low-pass filter at the continuum level. This is traditionally done via a convolution operation that yields a scale separation into resolvable large scales and non-resolvable small scales. The influence of the small scales onto the large ones is modelled and then, the resulting LES equation

for the large scales is discretised and solved. Although widely used, this procedure poses several mathematical difficulties concerning, for instance, the influence and interaction of errors arising from the physical LES modelling with errors arising from the numerical discretisation scheme.

Recently, a somehow alternative approach to simulate turbulent flows has been under development. The idea has its roots on the stabilisation methods used to prevent the numerical instabilities arising in the finite element solution of partial derivative equations. One of such stabilisation approaches, the *Subgrid Scale* (SGS) stabilised finite element method, is precisely based on a scale separation between those scales that can be captured by the computational mesh and those being not resolvable by the mesh. The influence of the small non-resolved scales onto the large scales has to be modelled and the various ways into how this is done give place to different SGS methods. An important point is that in SGS the scale separation is performed by projection onto the appropriate finite element spaces rather than at the continuum level. When applied to the Navier-Stokes equations, the SGS strategy sets up the problem of simulation of turbulent flows as a pure numerical problem rather than a question of physical LES modelling followed by numerical discretisation. In this sense, it provides a more natural and straightforward approach and avoids some of the drawbacks of classical LES modelling. The second main outcome of this thesis precisely aims at giving support to this idea i.e., that no physical LES modelling is needed for the simulation of turbulent flows, if an appropriate discretisation scheme is used. Using results from statistical fluid mechanics applied to SGS finite element methods, it will be heuristically argued that the main feature a LES model should fulfil can be recovered from the additional stabilisation terms in the equations.

The second step of the proposed methodology for CAA involves obtaining the acoustic source term, namely the double divergence of Lighthill's stress tensor. Instead of following the standard integral formulation, a different approach will be used. The source term in the time domain will be obtained from the CFD computation. Then, it will be Fourier transformed to the frequency domain and used to build an inhomogeneous Helmholtz equation to be solved again using a SGS finite element method. If some acoustic time domain information was necessary, it would be possible to anti-transform the obtained results to get it. However this will rarely be the case in practical situations as for most industrial applications the acoustic pressure spectrum is the desired final result. On the other hand, several possibilities can be considered for obtaining the source term depending on the weak form selected to solve the inhomogeneous Helmholtz equation. Our choice has been to directly compute Lighthill's stress tensor double divergence. As we are considering the low speed case, the incompressibility constraint makes possible to compute Lighthill's stress tensor double divergence even when linear interpolating functions are used. This procedure has the main advantage that it offers a direct visualisation of the aeroacoustic source terms, which can be of great help for engineering design processes.

The third step consists in computing the acoustic field by solving the inhomogeneous Helmholtz equation. It is a well-known fact that for large wavenumbers, the weak form associated to this problem is non positive definite giving rise to what is known as the pollution error. A dispersion analysis of the interior stencil associated to the

discrete problem shows that the pollution error can be attributable to the fact that waves propagate with a discrete wavenumber instead of the continuous one. The difference between the discrete and continuous wavenumbers increases for large wavenumbers and a phase error appears in the approximated wave.

A similar behaviour is observed for the convected counterpart of the Helmholtz equation, namely the *convected Helmholtz equation*, which is of importance in several areas of aeroacoustics such as aerodynamic sound generated by aircraft engine fans and compressors. As a third main contribution of this thesis, we will address the problem of developing a SGS stabilised finite element method for the convected Helmholtz equation in two dimensions. The method will be formally equivalent to the *Galerkin Least-Squares* (GLS) method and its key point will consist in finding an appropriate stabilisation parameter by means of a dispersion analysis. We will see that the proposed method clearly improves the results of the Galerkin approach to the problem and that our stabilisation parameter will reduce to well-known results for the Helmholtz equation in the case of no convection.

The thesis is organized as follows. Chapter 2 is wholly devoted to physical aeroacoustics. It starts by presenting a reminder on several issues of classical acoustics for readers not familiar with it. The main equations, approximations and concepts such as the multipolar character of the acoustic field are reviewed. After that, we move to aeroacoustics and the central concept of acoustic analogy is defined. Lighthill's acoustic analogy and its generalization to include the presence of solid boundaries are shown, as well as the usual integral approach used to solve them.

Chapter 3 begins with the presentation of the proposed three-step methodology to solve low speed CAA problems. Then, the methodology is implemented. The SGS stabilised finite element method used to solve the incompressible Navier-Stokes equations in the first step of the proposed CAA approach is explained in full detail. The method has the particularity of performing a time tracking of the subscales and it maintains all terms arising from the scale decomposition in the material derivative of the velocity field. An overview of the SGS approach to solve the inhomogeneous Helmholtz equation in the third step of the CAA method is also carried out. The chapter finishes with two numerical examples consisting on the computation of the aerodynamic noise generated by flow past a single and tandem cylinders at different Reynolds numbers (*aeolian tones* problem).

Chapter 4 begins with a review of the mathematical theory of existence and uniqueness of the Navier-Stokes equations. We then present some aspects of turbulent flows with emphasis on the Kolmogorov theory, as well as on some introductory results of statistical fluid mechanics. We continue with an explanation of the standard approach to LES and recent attempts towards a mathematical definition of it. These are based on the concept of *suitable approximations* to the Navier-Stokes equations. Next, the dichotomy between the SGS and LES approaches for the simulation of turbulent flows is established. The core of the chapter is then dedicated to show, by means of heuristic reasoning, that a purely numerical approach should suffice to simulate turbulent flows. That is, if an appropriate SGS scheme is used, performing a physical LES approach turns to be redundant. The chapter ends presenting two numerical examples that seem to give further support to this

idea. The case of two-dimensional decaying isotropic turbulence and the three-dimensional case of a turbulent flow impinging on a plate are considered.

In chapter 5 we concentrate on the third step of the method i.e., on the computation of the acoustic field. First, a general framework relating the wave and convected wave equations as well as their time Fourier transform counterparts (Helmholtz and convected Helmholtz equations) is setted up. The latter equations are shown to correspond to particular cases of *Convection-Diffusion-Reaction* (CDR) systems. Next, the numerical problems arising in the Galerkin finite element solution of the Helmholtz and convected Helmholtz equations are analysed in view of well-posedness and convergence theorems. A numerical study of the pollution error and pattern of convergence of one and two-dimensional propagating waves is also carried out. The kernel of the chapter consists in the proposal of a SGS stabilised finite element method for the convected Helmholtz equation that reduces to already well-known approaches in the case of no convection. The performance of the method is tested by means of some examples including the case of aeolian tones already described in Chapter 3.

In chapter 6 the possibilities to apply the CAA strategy to industrial cases is analysed. The case of flow past a high-speed train is considered. Flow separation at the leading car as well as pressure fluctuations beneath the turbulent boundary layer become a source of both, mechanical vibrations that will result in interior noise and aerodynamic noise sources radiating outwards. Due to computational limitations, the obtained results from the simulations are of no immediate application in the industrial frequency range of interest. However, the simulations clearly show how one could proceed to acquire the desired information using supercomputer devices (tests are being currently performed) and show much better performance than those achieved with commercial codes for the same meshes.

Conclusions and future lines of research are finally drawn in Chapter 7. On the other hand, we would like to note that all chapters are intended to be quite self-contained. This is specially the case of chapters 4 and 5. Some information in the thesis may then be somehow repeated in benefit of this consideration as well as for the sake of clarity. We also note that no state of the art chapter has been included. Detailed bibliography on each subject is provided in the introductory sections at the beginning of each chapter, as well as throughout them.

Chapter 2

Aeroacoustics

In this introductory chapter we will review some aeroacoustics theory. Given that aeroacoustics is a scientific branch lying somewhere in the middle between fluid mechanics and acoustics, we will start by reminding some key concepts on acoustics. The basic equations as well as the Green function approach, the Kirchoff-Helmholtz formulation or the multipolar character of the acoustic field will be briefly introduced. Then, we will move to aeroacoustics by introducing the notion of acoustic analogy. Special attention will be paid to Lighthill's acoustic analogy, which is central to this work. Other analogies accounting for the effects of boundaries in the aerodynamic noise generation process will be also considered, as well as the standard integral approaches to solve them.

2.1 Introduction

Let us start with a brief historical note of the physical problem at hand, namely the calculation of aerodynamically generated sound. As mentioned in the introductory Chapter 1, the term *aerodynamic noise or sound* was coined to designate noise generated by unsteady and/or turbulent flows and by their interaction with boundaries. Whereas *classical* acoustics concentrates on the mechanisms of noise generation and wave propagation within a fluid, when an external force is applied to it (e.g. the vibration of a plate, a loudspeaker, etc.), aeroacoustics focuses on noise generated by the flow internal forces and motions (e.g. a rotating eddy, a jet plane, a fan blade, etc.).

Although at the end of the XIX century and start of the XX century some initial research was made on aeroacoustics, specially concerning the problem of Aeolian tones (sound generated by flow impinging on a cylinder, see e.g., [116,260,279] (c.f. [249])) it was not until Lighthill's celebrated papers on the generation of aerodynamic sound [206, 207], that aeroacoustics became a research field on its own. Lighthill work was initially motivated by the need of beginning to build jet airplanes for commercial use. The noise generated by military airplanes at that time was extreme and there was an urgent necessity to build low-noise jet aircrafts to be used in inhabited areas. Lighthill's discovery of the concept of acoustic analogy and one of its first results, the eight-power law for the generated acoustic power, allowed to combine large gains in aircraft's propulsive power

with a great reduction in the amount of radiated noise. This was achieved by means of wide jets of high bypass ratio and a low exit velocity (see e.g., [209]). Lighthill's work placed again acoustics into the field of fluid mechanics [52] and was the start of what has been termed the first golden age of aeroacoustics [124].

The original Lighthill's acoustic analogy established an analogy between the compressible Navier-Stokes equations and the sound radiated by a distribution of quadrupole sources in a stationary fluid for the case of unbounded flows. The presence of boundaries was soon taken into account in the work of Curle, [56], for the case of non-moving rigid boundaries and generalised in the well-known Ffowcs-Williams - Hawkings equation [71, 72] (see also [99]). On the other hand, the powerfulness of the acoustic analogy relied on how the so-named Lighthill's tensor could be approximated; the various approximations taking into account fewer or more interaction effects between the hydrodynamic source field and the acoustic one. Some well-known analogies are those of Lilley [210], Phillips [248], Ribner [261] and Legendre [199], c.f. [209].

More related to the work developed in this thesis are the approximations carried out for low Mach number flows, which emphasize the role of vorticity as a source of sound. Crow [55] showed by the method of Matched Asymptotic Expansions that the incompressible Reynolds tensor approximation to Lighthill's tensor (see below), with the hydrodynamic velocity field given by the Biot-Savart law (see e.g., [10]), was indeed a first order approximation acceptable for low Mach numbers. More recently, Ristorcelli [263] performed a two-time perturbation analysis of the problem and proposed a compressibility correction to the Reynold's tensor only involving the solenoidal velocity flow and pressure (see also the interesting related work in [271]).

On the other hand, the integral solution to Lighthill's equation with the double divergence of the incompressible Reynolds tensor as a source term was rearranged by Howe so as to demonstrate the dependence of the sound field on vorticity [134]. This has the advantage that it is only necessary to integrate in those regions with non-vanishing vorticity to obtain the far field acoustic pressure. In this way, Howe recovered the results of Powell [256,257] on the generation of vortex sound. He also considered the case of sound generation in the presence of an irrotational mean flow and proposed the time derivative of the velocity potential as the appropriate acoustic variable, instead of the density or pressure fluctuations [134, 135]. For the case of a rotational mean flow he proposed the stagnation enthalpy as the appropriate acoustic variable [134]. However and as expected, at the far field both quantities, the total enthalpy and the time derivative of the velocity potential resembled the acoustic pressure fluctuations. Under certain conditions, the Powell-Howe analogy can be modified in a more convenient way for computations (see Møhring analogy [230] and also [258]). It is worthwhile to point out that the development of acoustic analogies in order to face specific problems concerning the interactions of hydrodynamic and sound fields is still a subject of current research (see e.g., [100]).

Since Lighthill's work and for several decades, aeroacoustics has been mainly developed in the field of aeronautics. Aeronautics largely motivated the first intense advances in the field and it has been doing it so, up to nowadays. A large amount of flow phenomena involving the generation of aerodynamic noise can be found in aeronautic

industry. Aeroacoustics of rotating devices such as propeller and propfans, rotors or turbomachinery are of importance not only because of the high level of the generated noise but also because of fatigue problems associated to it. Aerodynamic noise generated by jets, shear flows and flow coherent motion is crucial in aviation as well as combustion noise and the problem of sonic booms. A very complete and up to date treatise concerning these topics can be found in the books [147, 148] (see also [189] for related subjects). The literature on each of these topics is vast and out of the scope of this introduction so detailed bibliography on them will be not given here. Only an exception will be made concerning trailing edge noise (i.e., noise generated by flow passing by the trailing edge of a wing). This problem has received much attention, both from an analytical point of view (see [136, 138, 141, 142, 144]) as well as from a computational point of view (see e.g., [115, 219, 244, 292]). This is so because of the problem's simple geometry, which is suitable for analytical approaches as well as for using very fine computational meshes. Large eddy simulations are frequently used to perform a first Computational Fluid Dynamic simulation, which is used as a source term for an acoustic analogy. In this sense see also [270, 294].

Nowadays, aeroacoustic problems have extended to many other industrial sectors. One of them is railways, where the appearance of high-speed trains operating at speeds much higher than conventional trains, has resulted sometimes in the predominance of aeroacoustic sources when compared to traditional ones, such as rolling noise. This subject will be addressed in more detail in Chapter 6 and references will be given therein. Aeroacoustic issues have also become of importance in the automotive sector. The success in reducing mechanical noise sources has made aerodynamic noise relevant. Typical problems are noise generated by rear-view mirrors or by the ventilation system. The reduction of aerodynamic noise is also imperative in a large variety of industrial devices such as fans, plotters, heat exchangers, ventilation systems, etc. It is also a subject of investigation in underwater acoustics because noise generated by submarine propellers can be used to detect them. Again, a large amount of literature exist on each of these subjects and it is not our purpose to review it here. Some information can be found in some general books on aeroacoustics. In this sense and for an easy introduction, [14, 193] prove useful. For a much deepest insight [19, 101, 145, 146] should be consulted, as well as [54].

This chapter is organized as follows. In section 2.2 we review some fundamental concepts on classical acoustics. In section 2.3 we introduce Lighthill's acoustic analogy that accounts for aerodynamic noise radiation from viscous low speed flows. Further analogies, such as the Ffowcs-Williams equation that allows to account for the presence of boundaries while still making use of the free space Green function formalism are introduced in section 2.4. The standard formal integral solution to these acoustic analogies is also presented. Finally, conclusions are given in section 2.5.

2.2 Reminder on physical acoustics

2.2.1 Introduction

Sound can be defined as a vibration or mechanical perturbation propagating in an elastic media such as a gas, a liquid or a solid. For every particular situation, the characteristics of this vibration are given by the solution of the corresponding *wave equation* to be presented in the next sections.

The above definition is rather general and includes the cases of ultrasonic, sonic and infrasonic vibrations. In this work we will concentrate on perturbations that can be perceived by human hearing and that are generically termed as *noise*.

Human hearing is sensible to pressure variations, p', with respect to a reference pressure, $p_0 = 2 \times 10^{-5}$ Pa [1], between a certain frequency range. These pressure variations are known as *acoustic pressure*. Actually, human hearing is not directly proportional to acoustic pressure but it responds logarithmically to the changes in acoustic intensity (proportional to $|p'|^2$). Consequently, doubling the intensity of a sound will only result in a slight increase of our perception, while to duplicate this perception it would be necessary to intensify the acoustic energy a hundred times. For this reason, and because human hearing is able to perceive pressure fluctuations comprising several orders of magnitude, a decibel scale is usually employed to measure sound. The *sound pressure level* is defined as

$$L_p = SPL = 20 \log \left(\frac{|p'|}{p_0} \right). \tag{2.1}$$

We note that a pressure fluctuation having the atmospheric pressure magnitude, $p' = p_0 = 10^5$ Pa, would result in an extremely high value of $SPL\,(p_0) \approx 194$ dB. A very loud sound of 120 dB corresponds to an acoustic pressure of $p' = 2 \times 10^{-5} 10^{120/20} = 20$ Pa so that

$$\frac{p'}{p_0} = 2 \times 10^{-4} \ll 1. \tag{2.2}$$

On the other hand, human beings are able to distinguish sound frequencies ranging from about 20 Hz to 20 000 Hz. Hearing response is not equal for all frequencies: it is rather insensitive at low frequencies while it is specially receptive between 1 000 Hz and 4 000 Hz. In order to emulate the human hearing response when making a noise measurement, the measured physical acoustic pressure has to be filtered. For a sound of moderate intensity the so-called *filter A* is used. For noises of very loud intensity, hearing becomes less sensitive at low frequencies and other filters reproduce better its response (filters C and D).

The concepts and definitions on classical acoustics to be presented in the subsequent sections can be found in many books on acoustics and mechanics, see e.g., [14, 73, 101, 146, 233]. We would like to remark that only a brief overview will be given here and that it will

[1] p_0 corresponds to the threshold value where human hearing starts to perceive sound at the frequency of 1000 Hz.

suffer from a serious bias given that special emphasis will be placed in those areas that are important for aeroacoustics. Reference [146] will be closely followed in some cases.

2.2.2 Equations of a compressible fluid

Using the Eulerian description of a fluid (in 3D), its state at time t and position $\boldsymbol{x} = (x_1, x_2, x_3)$ can be described by the velocity vector field $\boldsymbol{u}(\boldsymbol{x}, t)$ and by specifying any thermodynamic variables. The motion of the fluid is then governed by five scalar equations, which can be derived from the conservations laws for mass, momentum and energy.

On the other hand, and in what concerns notation, through all this thesis we will denote by ∂_t the partial time derivative $\partial/\partial t$, by ∂^2_{tt} the partial time derivative of order two $\partial^2/\partial t^2$, by ∂_i the spatial partial derivative $\partial/\partial x_i$, $i = 1 \div d$, and by ∂^2_{ij} the spatial partial derivatives up to order two $\partial^2/\partial x_i \partial x_j$, $i, j = 1 \div d$. d denotes the space dimension and we will take $d = 1, 2, 3$ in the exposition. D_t will denote the *material* derivative, $D_t = \partial_t + \boldsymbol{u} \cdot \nabla$ and, as usual, we will also identify $x_1 \equiv x$, $x_2 \equiv y$ and $x_3 \equiv z$. The classical summation convention will be adopted for repeated indices.

The continuity equation

The law of mass conservation states that the rate of increase of fluid mass inside a fixed volume Ω should equal the net influx due to convection across the boundary $\partial\Omega$, plus the contribution of any mass source distribution inside Ω. This is expressed by the *continuity equation*

$$\partial\rho + \nabla \cdot (\rho \boldsymbol{u}) = Q \tag{2.3}$$

where $\rho(\boldsymbol{x}, t)$ stands for the fluid density and $Q(\boldsymbol{x}, t)$ for the mass source distribution. Equation (2.3) can also be written as

$$\frac{1}{\rho} D_t \rho + \nabla \cdot \boldsymbol{u} = q \tag{2.4}$$

where $q = Q/\rho$ corresponds to a volume source distribution.

It comes straightforwardly from the above equations that, in the case of an incompressible flow ($\rho = \text{const}$) with no sources ($Q = q = 0$), the continuity equation reduces to the *incompressibility constraint* $\nabla \cdot \boldsymbol{u} = 0$.

The momentum equation

Newton's second law on momentum conservation leads to the *momentum equation*, also known as the *Navier-Stokes equation*. This equation relates the rate of change of momentum of a fluid particle to the *surface forces* (pressure plus viscous or frictional forces) and *body forces* experienced by the fluid. The momentum equation reads

$$\rho D_t \boldsymbol{u} - \nabla \cdot \boldsymbol{\sigma} = \boldsymbol{f} \tag{2.5}$$

where $\boldsymbol{f}$ is the body force per unit volume and $\boldsymbol{\sigma}$ is the *Cauchy stress tensor* that for a *Newtonian fluid* becomes

$$\boldsymbol{\sigma} = -p\boldsymbol{I} + \mu\left[\nabla\boldsymbol{u} + \nabla\boldsymbol{u}^{\top} - \frac{2}{3}\left(\nabla\cdot\boldsymbol{u}\right)\boldsymbol{I}\right]. \tag{2.6}$$

In (2.6), p is the pressure, μ the dynamic coefficient of viscosity and $\boldsymbol{I}$ the identity. For an incompressible flow $\nabla\cdot\boldsymbol{u} = 0$ and the Cauchy stress tensor can be written as

$$\boldsymbol{\sigma} = -p\boldsymbol{I} + 2\mu\boldsymbol{S}, \tag{2.7}$$

with $\boldsymbol{S}$ standing for the *rate-of-strain tensor*

$$\boldsymbol{S} := \frac{1}{2}\left(\nabla\boldsymbol{u} + \nabla\boldsymbol{u}^{\top}\right). \tag{2.8}$$

One can also define the *momentum flux tensor*

$$\boldsymbol{\Phi} := \rho\left(\boldsymbol{u}\otimes\boldsymbol{u}\right) - \boldsymbol{\sigma} \tag{2.9}$$

and, using (2.3) with $Q = 0$, rewrite the momentum equation in the *Reynolds form*

$$\partial_t\left(\rho\boldsymbol{u}\right) + \nabla\cdot\boldsymbol{\Phi} = \boldsymbol{f}. \tag{2.10}$$

The energy equation

In this work we will limit to the case of *homentropic* flows i.e., the specific entropy of the fluid, s, will be assumed uniform and constant throughout the fluid. The energy equation then reduces to the condition

$$\partial_t s = 0, \tag{2.11}$$

(i.e., $s =$ constant) with the pressure, p, the density, ρ, and the entropy, s, being related by an equation of the type

$$p = p\left(\rho, s\right), \quad s \text{ constant}. \tag{2.12}$$

We remind that for an ideal gas $p = \text{const}\rho^{\gamma}$, with γ being the specific heat ratio $\gamma = C_p/C_V$, and that for an incompressible flow $\rho =$ const (C_p and C_V respectively stand for the specific heats at constant pressure and volume).

2.2.3 Inhomogeneous wave equation and Helmholtz equation

We have explained in the introduction that one usually talks about noise when the pressure perturbations satisfy a certain wave equation. It will be shown now how to obtain the latter.

From (2.2), we observe that even for very intense noise, the pressure fluctuations are very small relative to the atmospheric pressure, p_0. We can then linearise the continuity and momentum equations (2.4) and (2.5) relative to the mean pressure and density values

p_0 and ρ_0. Denoting the pressure and density fluctuations by $p' := p - p_0$, $\rho' := \rho - \rho_0$, and assuming propagation in an inviscid stationary fluid, provided that $p'/p_0 \ll 1$, $\rho'/\rho_0 \ll 1$, we obtain the linearised versions of (2.4), (2.5):

$$\frac{1}{\rho_0}\partial_t \rho' + \nabla \cdot \boldsymbol{u} = q, \tag{2.13}$$

$$\rho_0 \partial_t \boldsymbol{u} + \nabla p' = \boldsymbol{f}. \tag{2.14}$$

Taking the time derivative of (2.13) and subtracting the divergence of (2.14) yields

$$\partial_{tt}^2 \rho' - \nabla^2 p' = \rho_0 \partial_t q - \nabla \cdot \boldsymbol{f}. \tag{2.15}$$

We can now make use of the homentropic equation (2.12) to relate p' and ρ'. For the undisturbed state we will have $p_0 = p(\rho_0, s)$, whereas for the perturbed state it will follow

$$p_0 + p' = p(\rho_0 + \rho', s) \approx p(\rho_0, s) + \partial_\rho p(\rho, s)\,|_{0,s=\mathrm{ct}} \rho'. \tag{2.16}$$

The derivative in (2.16) is evaluated at (p_0, ρ_0) and has the dimensions of a squared velocity. In fact, its square root defines the *speed of sound*

$$c_0 = \sqrt{\partial_\rho p\,|_{0,s=\mathrm{ct}}}\,. \tag{2.17}$$

It is implicit in the approximations yielding to (2.17) that wave propagation under these conditions is an adiabatic phenomena. From (2.17) and (2.16) it follows that $p' = \rho' c_0^2$, which inserted into (2.15) gives

$$\left(\frac{1}{c_0^2}\partial_{tt}^2 - \nabla^2\right) p' = \rho_0 \partial_t q - \nabla \cdot \boldsymbol{f}. \tag{2.18}$$

Equation (2.18) is an *inhomogeneous wave equation* for the pressure fluctuations p' (acoustic pressure). Observe that neither a steady volume source distribution $q(\boldsymbol{x})$ nor a spatially constant force $\boldsymbol{f}(t)$ produce any sound.

The notation in (2.18) is often simplified by using the d'Alambertian operator, which is defined as $\Box^2 := [(1/c_0^2)\,\partial_{tt}^2 - \nabla^2]$. It then follows that (2.18) can be rewritten as

$$\Box^2 p' = \rho_0 \partial_t q - \nabla \cdot \boldsymbol{f}. \tag{2.19}$$

It should be noted that the density fluctuations ρ' also satisfy a wave equation. Moreover, in the case of $\boldsymbol{f} = \boldsymbol{0}$, (2.14) implies the existence of a velocity potential φ, such that $\boldsymbol{u} = \nabla\varphi$, and both φ and $\boldsymbol{u}$ do also satisfy a wave equation.

If we now assume a time harmonic behaviour of angular frequency ω for the acoustic pressure, as well as for the source terms in (2.18), and take into account that ∂_t is replaced by $-i\omega$, we obtain the inhomogeneous *time-reduced* or Helmholtz equation

$$\left(-\nabla^2 - k_0^2\right)\hat{p}' = -i\omega\rho_0\hat{q} - \nabla \cdot \hat{f}, \tag{2.20}$$

which is the analogous to (2.18) in the frequency domain, i.e., its Fourier transform. The hat in (2.20) is used to denote explicit frequency dependence, e.g., $\hat{p}' = \hat{p}'(\boldsymbol{x}, \omega)$, and k_0 stands for the *wavenumber* $k_0 = \omega/c_0$.

The operators $[(1/c_0^2)\,\partial_{tt}^2 - \nabla^2]$ and $-[\nabla^2 + k_0^2]$ are respectively known as the *wave equation* and *Helmholtz operators*. Obviously, they are both linear operators.

2.2.4 Green functions and the Kirchoff-Helmholtz formulation

Free space Green function

In order to solve acoustic problems we should be able to find solutions to the wave equation (2.18), or to the Helmholtz equation (2.20), in any finite or infinite physical domain $\Omega \subseteq \mathbb{R}^d$, with prescribed boundary conditions on $\partial\Omega$, and for a general source distribution $s(\boldsymbol{x}, t)$ or $\hat{s}(\boldsymbol{x}, \omega)$ (s will be used from now on to denote a generic acoustic source term, do not confuse it with entropy). The use of Green functions prove very useful to do so given that the wave and Helmholtz operators are linear.

The time-domain free-space Green function $G_0(\boldsymbol{x}, \boldsymbol{y}, t-\tau)$ in $\mathbb{R}^3$ is the sound field generated by an impulsive point source located at $\boldsymbol{x} = \boldsymbol{y}$ at time $t = \tau$. Hence, it is the causal solution to the differential problem of finding p' in $\mathbb{R}^3$ such that

$$\left(\frac{1}{c_0^2}\partial_{tt}^2 - \nabla^2\right) G_0 = \delta(\boldsymbol{x} - \boldsymbol{y})\,\delta(t-\tau) \qquad t \geq \tau \tag{2.21}$$

$$G_0 = 0 \qquad t < \tau. \tag{2.22}$$

The solution is given by (see e.g., [101, 146, 233])

$$G_0(\boldsymbol{x}, \boldsymbol{y}, t-\tau) = \frac{1}{4\pi\,|\boldsymbol{x}-\boldsymbol{y}|}\delta\left(t - \tau - \frac{|\boldsymbol{x}-\boldsymbol{y}|}{c_0}\right), \tag{2.23}$$

which is nothing but an impulsive and spherically symmetric wave expanding outwards of the source located at $\boldsymbol{y}$, having spherical symmetry and whose amplitude decreases inversely with the distance to $\boldsymbol{y}$, $|\boldsymbol{x}-\boldsymbol{y}|$.

The Fourier transform of (2.23) is the free-space Green function in the frequency domain and corresponds to solving the Helmholtz equation (2.20) with a point source. It is given by

$$\hat{G}_0(\boldsymbol{x}, \boldsymbol{y}, \omega) = \frac{\mathrm{e}^{ik_0|\boldsymbol{x}-\boldsymbol{y}|}}{4\pi\,|\boldsymbol{x}-\boldsymbol{y}|}. \tag{2.24}$$

Usefulness of the free space Green function

Suppose now that we are faced with the problem of solving (2.18) in an unbounded domain for a general source distribution $s(\boldsymbol{x}, t)$, i.e.,

$$\left(\frac{1}{c_0^2}\partial_{tt}^2 - \nabla^2\right) p' = s(\boldsymbol{x}, t). \tag{2.25}$$

We can think of $s(\boldsymbol{x}, t)$ as being built from a distribution of impulse point sources as the one in the r.h.s of (2.21), given that we can expand it as

$$s(\boldsymbol{x}, t) = \int_{\mathbb{R}^3}\int_{-\infty}^{+\infty} s(\boldsymbol{y}, \tau)\,\delta(\boldsymbol{x}-\boldsymbol{y})\,\delta(t-\tau)\,d\boldsymbol{y}d\tau. \tag{2.26}$$

Taking into account (2.21)-(2.23), each constituent $s(\boldsymbol{y},\tau)\,\delta(\boldsymbol{x}-\boldsymbol{y})\,\delta(t-\tau)\,d\boldsymbol{y}d\tau$ will generate an acoustic field (outward propagating wave) $s(\boldsymbol{y},\tau)\,G_0(\boldsymbol{x},\boldsymbol{y},t-\tau)\,d\boldsymbol{y}d\tau$. The superposition principle allows the summation of the contributions of all constituents to obtain the acoustic field generated by $s(\boldsymbol{x},t)$:

$$\begin{aligned} p'(\boldsymbol{x},t) &= \int_{\mathbb{R}^3}\int_{-\infty}^{+\infty} s(\boldsymbol{y},\tau)\,G_0(\boldsymbol{x},\boldsymbol{y},t-\tau)\,d\boldsymbol{y}d\tau \\ &= \frac{1}{4\pi}\int_{\mathbb{R}^3}\frac{s(\boldsymbol{y},t-|\boldsymbol{x}-\boldsymbol{y}|/c_0)}{|\boldsymbol{x}-\boldsymbol{y}|}d\boldsymbol{y} \\ &= \frac{1}{4\pi}\int_{\mathbb{R}^3}\frac{[s]}{|\boldsymbol{x}-\boldsymbol{y}|}d\boldsymbol{y}, \end{aligned} \tag{2.27}$$

where we have made use of (2.23) in the second line of (2.27). The delimiters [ ] in the last line of (2.27) are standard notation to denote evaluation of s at times $t-|\boldsymbol{x}-\boldsymbol{y}|/c_0$. The value $t-|\boldsymbol{x}-\boldsymbol{y}|/c_0$ is usually termed the *retarded time*. Hence, equation (2.27) represents the acoustic pressure at position $\boldsymbol{x}$ and time t, as a superposition of the acoustic fields generated by sound sources located at $\boldsymbol{y}$ at the corresponding retarded times. Integral equations such as (2.27) are called *retarded potentials* in acoustics.

Similarly, in the frequency domain we will have for the Fourier transform of the source distribution, $\hat{s}(\boldsymbol{x},\omega)$,

$$\begin{aligned} \hat{p}'(\boldsymbol{x},\omega) &= \int_{\mathbb{R}^3}\hat{s}(\boldsymbol{y},\omega)\,\hat{G}_0(\boldsymbol{x},\boldsymbol{y},\omega)\,d\boldsymbol{y} \\ &= \int_{\mathbb{R}^3}\frac{\mathrm{e}^{ik_0|\boldsymbol{x}-\boldsymbol{y}|}}{|\boldsymbol{x}-\boldsymbol{y}|}\hat{s}(\boldsymbol{y},\omega)\,d\boldsymbol{y}, \end{aligned} \tag{2.28}$$

where now, use has been made of (2.24).

Hence, we observe that once the free-space Green function is known it is quite straightforward to obtain the pressure field generated by any source distribution in an unbounded domain (at least formally).

The Kirchoff-Helmholtz equation

When surfaces are present and/or the wave equation is to be solved in a bounded domain, the above approach has to be modified to take into account the influence of boundaries. For a domain $\Omega\subseteq\mathbb{R}^3$ with boundary $\partial\Omega\equiv\Gamma=\Sigma\cup S$ such that $\Sigma\cap S=\varnothing$ (Σ stands for the domain exterior boundary while S stands for the surface of any interior body, see Fig. 2.1) let us first address the following Helmholtz problem:

$$\begin{aligned} &\left(-\nabla^2-k_0^2\right)\hat{p}'=\hat{s}(\boldsymbol{x},\omega)\ \text{ in }\Omega \\ &+\text{ boundary conditions on }\Gamma. \end{aligned} \tag{2.29}$$

To find a solution to (2.29) we consider the *reciprocal* or *adjoint* problem

$$\begin{aligned} &\left(-\nabla_{\boldsymbol{y}}^2-k_0^2\right)\hat{G}(\boldsymbol{x},\boldsymbol{y},\omega)=\delta(\boldsymbol{x}-\boldsymbol{y})\ \text{ in }\Omega \\ &+\text{ boundary conditions on }\Gamma, \end{aligned} \tag{2.30}$$

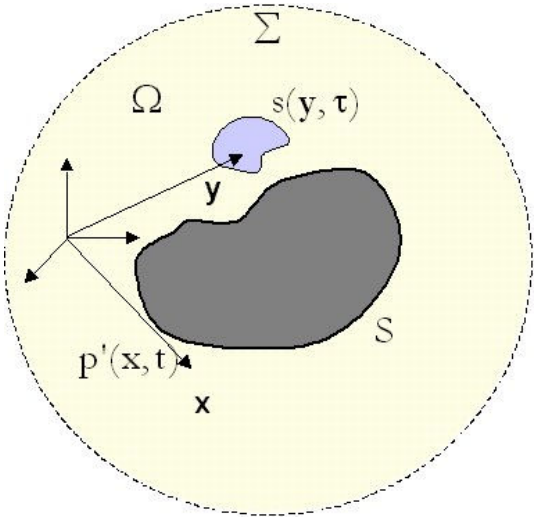

Figure 2.1: Geometry for the Kirchoff-Helmholtz formulation.

where the subscript $\boldsymbol{y}$ in the nabla operator denotes differentiation with respect to the components of $\boldsymbol{y}$. $\hat{G}$ is a Green function and satisfies the *reciprocal theorem* i.e., $\hat{G}(\boldsymbol{x}, \boldsymbol{y}, \omega) = \hat{G}(\boldsymbol{y}, \boldsymbol{x}, \omega)$.

We can now find a formal solution $\hat{p}'(\boldsymbol{x}, \omega)$ to (2.29) following the next steps (see e.g., [145]): first replace $\boldsymbol{x}$ by $\boldsymbol{y}$ in (2.29) and multiply it by $\hat{G}(\boldsymbol{x}, \boldsymbol{y}, \omega)$. Then subtract the resulting equation from the product of (2.30) and $\hat{p}'(\boldsymbol{x}, \omega)$. Finally, integrate the result with respect to $\boldsymbol{y}$ over the whole domain and apply Green's second identity (or the divergence theorem) to obtain

$$\begin{aligned}\hat{p}'(\boldsymbol{x}, \omega) = &- \int_{\Omega} \hat{s}(\boldsymbol{y}, \omega)\, \hat{G}(\boldsymbol{x}, \boldsymbol{y}, \omega)\, d\Omega \\ &- \int_{\Gamma} \left[\hat{p}'(\boldsymbol{y}, \omega)\, \nabla_{\boldsymbol{y}} \hat{G}(\boldsymbol{x}, \boldsymbol{y}, \omega) - \nabla_{\boldsymbol{y}} \hat{p}'(\boldsymbol{y}, \omega)\, \hat{G}(\boldsymbol{x}, \boldsymbol{y}, \omega)\right] \cdot \boldsymbol{n}\, d\Gamma, \end{aligned} \tag{2.31}$$

where the unit normal $\boldsymbol{n}$ on Γ is directed towards the fluid. If $\boldsymbol{x} \in \Gamma$ then the acoustic pressure in the l.h.s of (2.31) has to be divided by 2. On the other hand, Ω in (2.31) can be of infinite radius i.e., $\Omega = \mathbb{R}^3$. In this case the Sommerfeld radiation condition (see Chapter 5) ensures that there is no contribution from the infinite surface Σ to the acoustic pressure, so that Γ in the surface integral of (2.31) has to be replaced by S. If in addition $S = \varnothing$, we recover (2.27). The expression (2.31) is known as the *Kirchoff-Helmholtz equation.*

Equation (2.31) is valid for any Green function solving (2.30) and in particular it allows the use of the simple free-space Green function, $\hat{G}_0$. The surface integral can be evaluated if $\hat{p}'$ and $\nabla \hat{p}'$ are known on Γ. However, it should be noted that these quantities cannot be prescribed independently.

One could also consider avoiding the necessity to perform the surface integrals in (2.31) by choosing modified Green functions that satisfy appropriate vanishing conditions

on the surface. The problem is that finding these Green functions is only possible for solid bodies having very simple geometries (spheres, cylinders, half-planes, etc.). An exception that it is worthwhile to mention is the case of acoustically *compact* bodies. That is, when the characteristic length of the body, say L, is small compared to the wavelength λ of the sound generated by the source distribution $\hat{s}$, it is possible to compute approximate Green functions with appropriate boundary behaviour for a large variety of geometry shapes. These Green functions are termed *compact Green functions*, see e.g., [145, 146].

In the special case of $\hat{G} = \hat{G}_0$ we obtain, using (2.24), the frequency domain Kirchoff-Helmholtz equation

$$\begin{aligned}\hat{p}'(\boldsymbol{x},\omega) = &-\frac{1}{4\pi}\int_\Omega \frac{\mathrm{e}^{ik_0|\boldsymbol{x}-\boldsymbol{y}|}}{|\boldsymbol{x}-\boldsymbol{y}|}\hat{s}(\boldsymbol{x},\boldsymbol{y},\omega)\; d\Omega \\ &- \frac{1}{4\pi}\int_\Gamma \hat{p}'(\boldsymbol{y},\omega)\,\partial_{\boldsymbol{n}}\frac{\mathrm{e}^{ik_0|\boldsymbol{x}-\boldsymbol{y}|}}{|\boldsymbol{x}-\boldsymbol{y}|}\,d\Gamma + \frac{i\omega\rho_0}{4\pi}\int_\Gamma \hat{u}_{\boldsymbol{n}}\frac{\mathrm{e}^{ik_0|\boldsymbol{x}-\boldsymbol{y}|}}{|\boldsymbol{x}-\boldsymbol{y}|}\,d\Gamma,\end{aligned} \tag{2.32}$$

where $\partial_{\boldsymbol{n}}$ stands for the derivative in the normal direction to the surface and $\hat{u}_{\boldsymbol{n}}$ is the velocity component normal to the surface. Use has been made of the Fourier transform of (2.14) (with $\boldsymbol{f} = \boldsymbol{0}$) in (2.32).

The time domain version of the Kirchoff-Helmholtz equation can be found by Fourier transforming (2.31) making use of the convolution theorem. This yields

$$\begin{aligned}p'(\boldsymbol{x},t) = &\int_{-\infty}^{+\infty}\int_\Omega s(\boldsymbol{y},\tau)\,G(\boldsymbol{x},\boldsymbol{y},t-\tau)\,d\Omega d\tau \\ &+\int_{-\infty}^{+\infty}\int_\Gamma \left[p'(\boldsymbol{y},\tau)\,\nabla_{\boldsymbol{y}}G(\boldsymbol{x},\boldsymbol{y},t-\tau) - \nabla_{\boldsymbol{y}}p'(\boldsymbol{y},\tau)\,G(\boldsymbol{x},\boldsymbol{y},t-\tau)\right]\cdot\boldsymbol{n}\,d\Gamma d\tau.\end{aligned} \tag{2.33}$$

In the special case of $G = G_0$ (with G_0 given by (2.23)), equation (2.33) becomes

$$p'(\boldsymbol{x},t) = \frac{1}{4\pi}\int_\Omega \frac{[s]}{|\boldsymbol{x}-\boldsymbol{y}|}\,d\Omega + \frac{\rho_0}{4\pi}\partial_t\int_\Gamma \frac{[u_{\boldsymbol{n}}]}{|\boldsymbol{x}-\boldsymbol{y}|}d\Gamma - \frac{1}{4\pi}\partial_i\int_{\partial\Omega}\frac{[p']}{|\boldsymbol{x}-\boldsymbol{y}|}n_i\,d\Gamma. \tag{2.34}$$

The last two terms in (2.34) represent distributions of monopoles and dipoles sources on the surface (see section 2.2.6, below).

2.2.5 Acoustic far field approximations

The Fraunhofer approximation

In many acoustic applications we will be mainly interested in knowing the acoustic field far away from the sources that generate it. Some useful expressions can be derived in these circumstances.

For simplicity, let us place the origin of coordinates inside the source region (see Fig. 2.2). When $|\boldsymbol{x}| \to \infty$ and for $\boldsymbol{y}$ in the source region, it follows (using Taylor

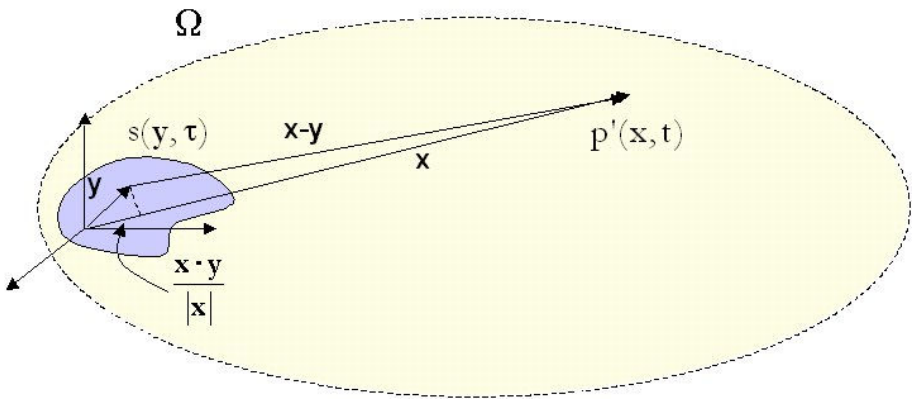

Figure 2.2: Far field approximations.

developments) that

$$|\boldsymbol{x}-\boldsymbol{y}| = \left(|\boldsymbol{x}|^2 + |\boldsymbol{y}|^2 - 2\boldsymbol{x}\cdot\boldsymbol{y}\right)^{1/2} = |\boldsymbol{x}|\left[1 - \frac{2\boldsymbol{x}\cdot\boldsymbol{y}}{|\boldsymbol{x}|^2} + \frac{|\boldsymbol{y}|^2}{|\boldsymbol{x}|^2}\right]^{1/2}$$
$$\approx |\boldsymbol{x}|\left[1 - \frac{\boldsymbol{x}\cdot\boldsymbol{y}}{|\boldsymbol{x}|^2} + \mathcal{O}\left(\frac{|\boldsymbol{y}|^2}{|\boldsymbol{x}|^2}\right)\right] \tag{2.35}$$

so that

$$|\boldsymbol{x}-\boldsymbol{y}| \approx |\boldsymbol{x}| - \frac{\boldsymbol{x}\cdot\boldsymbol{y}}{|\boldsymbol{x}|}, \quad \frac{|\boldsymbol{y}|}{|\boldsymbol{x}|} \ll 1. \tag{2.36}$$

Moreover, and using (2.36),

$$\frac{1}{|\boldsymbol{x}-\boldsymbol{y}|} \approx \frac{1}{|\boldsymbol{x}| - \frac{\boldsymbol{x}\cdot\boldsymbol{y}}{|\boldsymbol{x}|}} \approx \frac{1}{|\boldsymbol{x}|}\left(1 + \frac{\boldsymbol{x}\cdot\boldsymbol{y}}{|\boldsymbol{x}|^2}\right). \tag{2.37}$$

Consequently,

$$\frac{1}{|\boldsymbol{x}-\boldsymbol{y}|} \approx \frac{1}{|\boldsymbol{x}|} + \frac{\boldsymbol{x}\cdot\boldsymbol{y}}{|\boldsymbol{x}|^3}, \quad \frac{|\boldsymbol{y}|}{|\boldsymbol{x}|} \ll 1. \tag{2.38}$$

Let us consider now the retarded potential in (2.27). From the above results we can approximate its value at the far-field as

$$p'(\boldsymbol{x},t) = \frac{1}{4\pi}\int_{\mathbb{R}^3} \frac{s\left(\boldsymbol{y}, t - |\boldsymbol{x}-\boldsymbol{y}|/c_0\right)}{|\boldsymbol{x}-\boldsymbol{y}|} d\boldsymbol{y}$$
$$\approx \frac{1}{4\pi|\boldsymbol{x}|}\int_{\mathbb{R}^3} s\left(\boldsymbol{y}, t - \frac{|\boldsymbol{x}|}{c_0} + \frac{\boldsymbol{x}\cdot\boldsymbol{y}}{c_0|\boldsymbol{x}|}\right) d\boldsymbol{y}, \tag{2.39}$$

where we note that we have only retained $1/|\boldsymbol{x}|$ from (2.38) to approximate the term controlling the amplitude value in (2.39), while we have kept the whole of (2.36) for the retarded time of the source distribution s. This is done to retain possible phase differences between the waves generated at the various locations, $\boldsymbol{y}$, of the source distribution.

The far-field approximation (2.39) is called the *Fraunhofer* approximation.

Interchanging spatial and time derivatives

Another far-field approximation that is very frequently used in acoustics and aeroacoustics is a rule for interchanging spatial and time derivatives. It is not difficult to show that, for $|\boldsymbol{x}| \to \infty$ we can replace (see e.g., [146])

$$\partial_i \leftrightarrow -\frac{1}{c_0}\frac{x_i}{|\boldsymbol{x}|}\partial_t. \tag{2.40}$$

2.2.6 Monopoles, Dipoles and Quadrupoles

Some types of sources are of importance in acoustics theory and deserve special attention. This is the case of monopolar, dipolar and quadrupolar sources.

A *monopole point source* is a volume source, see (2.4), of the type $q(t)\,\delta(\boldsymbol{x})$, which results in an acoustic source $s(\boldsymbol{x},t) = \rho_0 \partial_t q(t)\,\delta(\boldsymbol{x})$, see (2.18). From (2.39) it is apparent that, in free space, a point monopole will generate an acoustic field

$$p'(\boldsymbol{x},t) = \frac{\rho_0}{4\pi\,|\boldsymbol{x}|}\partial_t q\left(t - \frac{|\boldsymbol{x}|}{c_0}\right). \tag{2.41}$$

A *dipole point source* corresponds to an acoustic source of the type $s(\boldsymbol{x},t) = \nabla \cdot [\boldsymbol{f}(t)\,\delta(\boldsymbol{x})]$. Making use of (2.25)-(2.27) it is not difficult to show that the acoustic pressure generated by the point dipole is given by

$$p'(\boldsymbol{x},t) = \nabla \cdot \left(\frac{\boldsymbol{f}\left(t - \frac{|\boldsymbol{x}|}{c_0}\right)}{4\pi\,|\boldsymbol{x}|}\right). \tag{2.42}$$

The acoustic field generated by a dipole is equivalent to the one generated by two monopoles of equal magnitude but opposite sign strengths placed a very short distance apart.

A *quadrupolar point source* involves a double divergence instead of a single one like in the dipole case. The source term is given by $s(\boldsymbol{x},t) = (\nabla \otimes \nabla) : [\boldsymbol{T}(t)\,\delta(\boldsymbol{x})]$ and the generated acoustic field is

$$p'(\boldsymbol{x},t) = (\nabla \otimes \nabla) : \left(\frac{\boldsymbol{T}\left(t - \frac{|\boldsymbol{x}|}{c_0}\right)}{4\pi\,|\boldsymbol{x}|}\right). \tag{2.43}$$

$\otimes$ stands for the tensor product and : for a double contraction. The quadrupolar acoustic field can also be recovered using combinations of two dipoles placed a short distance apart. In the case of the two dipoles lying in the same axis we will talk of a *longitudinal* quadrupole, while if the two dipoles are parallel one to the other and antiphase, we will have a *lateral* quadrupole. In Fig. 2.3 we have plotted the squared pressure acoustic fields generated by monopoles, dipoles and quadrupoles and we show an schematic draw of them.

Finally, we note that a source of the type $s(\boldsymbol{x},t) = \rho_0 \partial_t q(\boldsymbol{x},t)$ represents a *distributed monopole*. A source $s(\boldsymbol{x},t) = \nabla \cdot \boldsymbol{f}(\boldsymbol{x},t)$ corresponds to a *distributed dipole* and $s(\boldsymbol{x},t) = (\nabla \otimes \nabla) : \boldsymbol{T}(\boldsymbol{x},t)$ is a *distributed quadrupole*.

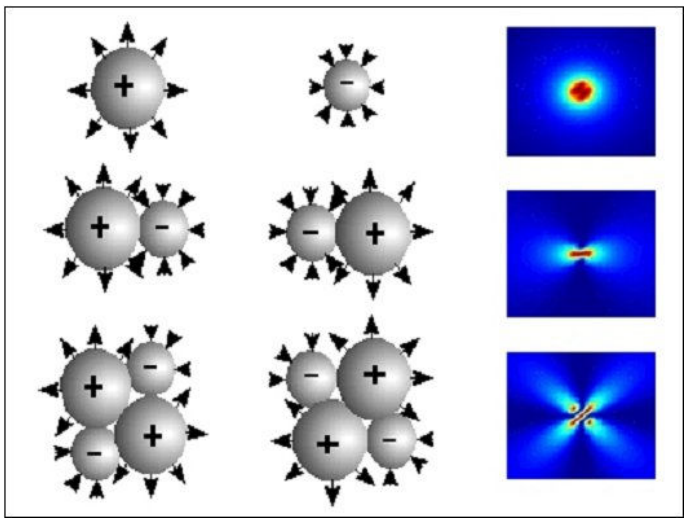

Figure 2.3: Characteristic acoustic sources: monopole, dipole and lateral quadrupole.

According to the latter, the last term in (2.34) corresponds to a distributed surface dipole. Using the Fraunhofer approximation (2.39) and the spatial-time derivatives interchanging rule (2.40), we can approximate the far-field pressure generated by such a dipole as

$$\begin{aligned} p'(\boldsymbol{x},t) &= \frac{1}{4\pi}\partial_i \int_{\mathbb{R}^3} \frac{f_i\left(\boldsymbol{y}, t-|\boldsymbol{x}-\boldsymbol{y}|/c_0\right)}{|\boldsymbol{x}-\boldsymbol{y}|} d\boldsymbol{y} \\ &\approx \frac{1}{4\pi}\partial_i \left[\frac{1}{|\boldsymbol{x}|}\int_{\mathbb{R}^3} f_i\left(\boldsymbol{y}, t-\frac{|\boldsymbol{x}|}{c_0}+\frac{\boldsymbol{x}\cdot\boldsymbol{y}}{c_0|\boldsymbol{x}|}\right) d\boldsymbol{y}\right] \\ &\approx \frac{1}{4\pi|\boldsymbol{x}|}\partial_i \left[\int_{\mathbb{R}^3} f_i\left(\boldsymbol{y}, t-\frac{|\boldsymbol{x}|}{c_0}+\frac{\boldsymbol{x}\cdot\boldsymbol{y}}{c_0|\boldsymbol{x}|}\right) d\boldsymbol{y}\right] \\ &\approx -\frac{x_i}{4\pi|\boldsymbol{x}|^2}\partial_t \left[\int_{\mathbb{R}^3} f_i\left(\boldsymbol{y}, t-\frac{|\boldsymbol{x}|}{c_0}+\frac{\boldsymbol{x}\cdot\boldsymbol{y}}{c_0|\boldsymbol{x}|}\right) d\boldsymbol{y}\right], \end{aligned} \tag{2.44}$$

where f_i in (2.44) would correspond to $p'n_i$ in the special case of (2.34).

2.2.7 The multipole expansion

We will finish this reminder on physical acoustics presenting a well-known and useful result: the multipole expansion of a source distribution (see e.g., [145, 233, 249] for a proof).

The acoustic far field of a source distribution, $s(\boldsymbol{x},t)$, of characteristic size, L, is the same as that generated by the infinite series of point multipoles

$$\sum_{|\alpha|=0}^{\infty} S^{\alpha}(t)\, D^{\alpha}\left[\delta(\boldsymbol{x})\right] \tag{2.45}$$

with $\alpha := (\alpha_1, \ldots, \alpha_n)$ standing for a multi-index in $\mathbb{R}^n$ (we will mostly use $n = 2, 3$) such that $|\alpha| = \alpha_1 + \ldots + \alpha_n$ and $D^\alpha := \partial^{|\alpha|}/\partial x_1^{\alpha_1} \ldots \partial x_n^{\alpha_n}$. S^α is given by

$$S^\alpha(t) = \frac{(-1)^{|\alpha|}}{|\alpha|!} \int_{\mathbb{R}^3} y_1^{\alpha_1} \ldots y_n^{\alpha_n} s(\boldsymbol{y}, t)\, d\boldsymbol{y}. \tag{2.46}$$

It can be shown that that far-field acoustic pressure, $p'(\boldsymbol{x}, t)$, is then given by [145]

$$p'(\boldsymbol{x}, t) \approx \sum_{|\alpha|=0}^{\infty} D^\alpha \left[\frac{S^\alpha(t - |\boldsymbol{x}|/c_0)}{4\pi |\boldsymbol{x}|} \right], \quad |\boldsymbol{x}| \to \infty. \tag{2.47}$$

For $k_0 L \ll 1$, the acoustic pressure can be just approximated by the the first term in the series (monopole). If this term vanishes for symmetry reasons, then the dipole term would dominate, its amplitude being reduced by a factor $\sim (k_0 L)$ with respect to the monopole one. If the dipole also vanishes, the quadrupole term dominates with an amplitude reduction of $\sim (k_0 L)^2$ when compared with the monopole and so on.

The expansion (2.47) is at the basis of *active noise control* techniques [238] because it allows to approximate any source field by a set of easier multipole sources. Hence, it accounts for the possibility to generate a "cancelling" sound with more or less simple devices.

2.3 Lighthill's acoustic analogy

2.3.1 The concept of acoustic analogy

Central to aeroacoustics is the concept of *acoustic analogy*. An attempt to define what it is understood by the term *acoustic analogy* was provided in [53]:

Definition 2.1 *The term acoustic analogy refers to the recasting of the exact equations of fluid motion in the form of an inhomogeneous wave equation appropriate to the fact that in the far field (and ignoring here nonlinear waveform distortion) pressure fluctuations propagate through still fluid at the ambient flow speed c_0. Thus*

$$\left(\frac{1}{c_0^2} \partial_{tt}^2 - \nabla^2 \right) h(\boldsymbol{x}, t) = s(\boldsymbol{x}, t), \tag{2.48}$$

for some h equivalent to p' at the far-field. The r.h.s of (2.48) acts as a source term for h and may include all propagation mechanisms such as scattering by turbulent eddies and temperature inhomogeneities, refraction in the mean velocity and temperature fields, fluid shielding of each eddy by the local (moving) fluid environment, nonlinear self-distortion of propagating sound waves, etc.

Several acoustic analogies have been cited in the introduction of this Chapter. In what follows, we will concentrate on Lighthill's acoustic analogy derived in the pioneering work [206, 207]. It will be shown how to obtain this analogy as well as its approximation in the case of low Mach numbers, which will be used throughout this thesis.

2.3.2 Lighthill's acoustic analogy for low Mach number flows

As stated in definition 2.1, an acoustic analogy is based on a reordering of the equations for fluid motion so as to obtain an inhomogeneous wave equation. Lighthill was the first to reformulate the compressible continuity and momentum equations of a fluid in order to do so. The source terms of the resulting inhomogeneous wave equation are expected to be only important within the vortical (turbulent) region of the flow and, in a first approximation, the generated sound is expected to have a negligible back-reaction on it (see e.g., [101, 145, 146, 206, 208]). This is an acceptable hypothesis if the compressibility of the source flow can be disregarded, i.e., in the case of low Mach numbers. We will see that the powerfulness of Lighthill's approach, at least for the cases we will be interested in, precisely relies on whether incompressibility can be assumed or not.

To derive Lighthill's equation we start from the continuity and momentum equations (in Reynolds form) for a compressible flow with neither mass sources nor body forces acting on it. Equations (2.3) and (2.10) then become

$$\partial_t \rho + \nabla \cdot (\rho \boldsymbol{u}) = 0 \tag{2.49}$$

$$\partial_t (\rho \boldsymbol{u}) + \nabla \cdot \boldsymbol{\Phi} = 0. \tag{2.50}$$

Next, we proceed analogously to what have been done to obtain (2.15), which was the first step to achieve a wave equation. Hence, we take the time derivative of (2.49) and subtract from it the divergence of (2.50). This yields

$$\partial_{tt}^2 \rho - \nabla \cdot (\nabla \cdot \boldsymbol{\Phi}) = (\nabla \otimes \nabla) : \boldsymbol{\Phi}. \tag{2.51}$$

Given that only the divergence of the momentum flux tensor, $\boldsymbol{\Phi} = \rho (\boldsymbol{u} \otimes \boldsymbol{u}) - \boldsymbol{\sigma}$ introduced in (2.9), appears in the equations of fluid motion, we can redefine the Cauchy stress tensor, $\boldsymbol{\sigma}$, for convenience so as to include a constant pressure p_0:

$$\boldsymbol{\sigma} \equiv -(p - p_0)\boldsymbol{I} + \mu \left[\nabla \boldsymbol{u} + \nabla \boldsymbol{u}^\top - \frac{2}{3} (\nabla \cdot \boldsymbol{u}) \boldsymbol{I} \right]. \tag{2.52}$$

On the other hand, we note that in the case of an ideal, linear acoustic medium, the momentum flux tensor adopts an easy expression as momentum transfer can only be produced by pressure. In this case the momentum flux tensor becomes

$$\boldsymbol{\Phi}_0 = (p - p_0)\boldsymbol{I} = c_0^2 (\rho - \rho_0)\boldsymbol{I}, \tag{2.53}$$

where we have used the fact that $p' = \rho' c_0^2$ in the last equality (remind that by definition $p' := p - p_0,\ \rho' = \rho - \rho_0$).

Taking into account that we can replace $\partial_{tt}^2 \rho$ by $\partial_{tt}^2 (\rho - \rho_0)$ in (2.51), we can take the double divergence of (2.53), $(\nabla \otimes \nabla) : \boldsymbol{\Phi}_0 = c_0^2 \nabla^2 (\rho - \rho_0)$, and subtracting it at both sides of (2.51) arrive at

$$\left(\partial_{tt}^2 - c_0^2 \nabla^2\right)(\rho - \rho_0) = (\nabla \otimes \nabla) : \boldsymbol{T} \tag{2.54}$$

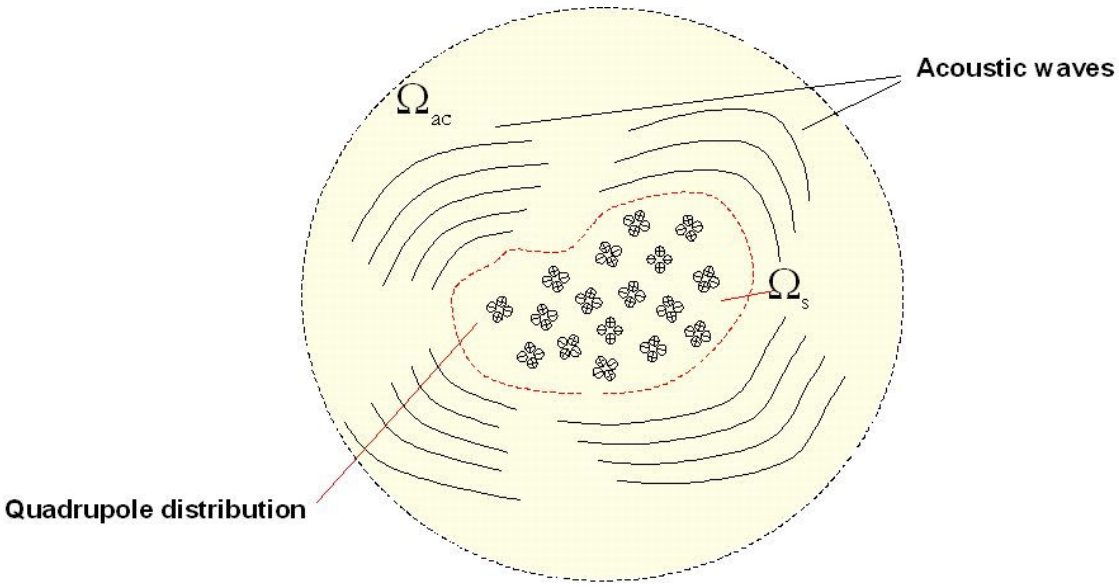

Figure 2.4: Equivalence of Lighthill's acoustic analogy.

where

$$\boldsymbol{T} := \boldsymbol{\Phi} - \boldsymbol{\Phi}_0 = \rho\,(\boldsymbol{u} \otimes \boldsymbol{u}) + \left[(p - p_0) - c_0^2\,(\rho - \rho_0)\right] \boldsymbol{I} - \boldsymbol{\sigma}. \tag{2.55}$$

Equation (2.54) is the celebrated Lighthill equation and the tensor $\boldsymbol{T}$ is known as Lighthill's stress tensor. Note that in order to derive (2.54) no approximation has been performed. Hence, Lighthill's equation has to be viewed as an alternative formulation of the compressible fluid motion equations. Note also that (2.54) corresponds to an inhomogeneous wave equation whose source term involves a double divergence, which corresponds to a distributed quadrupolar source term (see section 2.2.6). Consequently, Lighthill's recasting of the fluid motion equations turns to be analogous to the problem of obtaining the sound radiation of a distribution of quadrupole sources located in a source region Ω_S, into a stationary, ideal fluid occupying a domain Ω_{ac} (see Fig. 2.4 and e.g., [54,101,145,206]). This is the reason why (2.54) is referred to as an acoustic analogy. The strength of the quadrupole sources in (2.54) is given by $\boldsymbol{T}$. In fact, (2.54) was the first acoustic analogy to be derived and as no approximation has been performed to obtain it, it is said to be an *exact* acoustic analogy. Since the appearance of (2.54) much work has been carried out based on the acoustic analogy approaches as already explained in the introduction.

As no approximations have been made to derive (2.54) it is obvious that this equation retains all the complexity of the original compressible fluid motion equations. Therefore, (2.54) must account not only for the aerodynamic sound generation but also for several effects such as the convection by the flow, the refraction due to sound speed variations, the self-modulation due to acoustic non-linearity or the attenuation due thermal and viscous effects (see e.g. [145]). The Lighthill tensor, $\boldsymbol{T}$, is responsible for all these outcomes. The first term of the tensor in (2.55) is the non-linear Reynolds stress tensor $\rho\,(\boldsymbol{u} \otimes \boldsymbol{u})$, which

is expected to be mainly important in the vortical region of the flow. The second term of the tensor is the excess of momentum transfer by the pressure over that in an ideal, linear fluid of density ρ_0 and sound speed c_0. The mean density variations and the wave amplitude nonlinearities are responsible for it. Finally, the viscous stress tensor $\boldsymbol{\sigma}$ plays a sound attenuation role. The practical utility of the Lighthill acoustic analogy precisely relies on neglecting some of the effects described above by simplifying the expression for the Lighthill tensor. As these effects mainly depend on the compressibility of the flow, we will assume it to be incompressible (i.e., $\nabla \cdot \boldsymbol{u} = 0$), which is an acceptable hypothesis in the case of low Mach numbers ($M^2 \ll 1$, M being the Mach number $M = U/c_0$ with U a characteristic flow velocity). Taking into account that we will be mainly interested in high Reynolds number flows, typical of aeronautical and railway engineering applications, the viscous stress in (2.54) will be neglected. Moreover, the mean density and sound speed will be taken as uniform so that the second term in (2.54) becomes zero. The Lighthill equation under these assumptions becomes

$$\left(\partial_{tt}^2 - c_0^2 \nabla^2\right)(\rho - \rho_0) = \rho_0 \left(\nabla \otimes \nabla\right) : (\boldsymbol{u} \otimes \boldsymbol{u}), \tag{2.56}$$

where we remind that $\boldsymbol{u}$ now accounts for a solenoidal velocity field.

However, the validity of the above equation (2.56) is by no means obvious. Crow [55] investigated Lighthill's equation (2.54) in terms of a perturbation series in the fluctuating Mach number $M_t = |\boldsymbol{u}|/c_0$. Using the pressure fluctuations instead of the density ones, it follows that,

$$\left(M_t^2 \partial_{tt}^2 - \nabla^2\right)(p - p_0) = \rho_0 \left(\nabla \otimes \nabla\right) : (\boldsymbol{u} \otimes \boldsymbol{u}) + M_t^2 \left(\nabla \otimes \nabla\right) : \boldsymbol{T}^1 + \ldots \tag{2.57}$$

with $\boldsymbol{T}^1$ representing contributions to the source term from interactions between incompressible and acoustic modes of the flow. Consequently, it seems quite inconsistent to use the approximation (2.56) because this would correspond to neglect the $\mathcal{O}\left(M_t^2\right)$ terms in the r.h.s of (2.57), while retaining them in the l.h.s. Despite this apparent drawback, Crow [55] showed using the method of Matched Asymptotic Expansions that (2.56) is in fact valid for compact flows with small Mach number. This validity seems to be due to the fact that $\partial_{tt}^2 p'$ is negligible in those flow regions where $\left(\nabla \otimes \nabla\right) : \boldsymbol{T}^1$ is not and vice versa. As a consequence, keeping the acoustic pressure double derivative in the l.hs. of (2.57) and ignoring the $\boldsymbol{T}^1$ contribution in the r.h.s results in an acceptable slight error because the acoustic field becomes accurate to order Mach number. Not so long ago, Ristorcelli [263] has proposed a closure model to resolve the above inconsistency for weakly compressible flows that only makes use of the solenoidal velocity and pressure fields.

Now, accepting (2.56) as valid for our purposes and if the Reynolds stress tensor (source term) in (2.56) can be known somehow, equation (2.56) gives a useful representation of the aerodynamically generated sound. However, rather than being interested in solving (2.56) we will be mainly interested in its Fourier transform. In this way we can directly obtain the density fluctuation (and hence the pressure fluctuation) spectrum, which is the desired information in most engineering problems. The Fourier

transform of (2.56) gives place to an inhomogeneous Helmholtz equation. This will allow us to take benefit from several numerical techniques developed for it as well as for the more general convection-diffusion-reaction equation, the former being a particular case of it.

Taking into account that $p' = c_0^2 \rho'$, the counterpart of (2.56) in the frequency domain becomes the inhomogeneous Helmholtz equation

$$\left(-\nabla^2 - k_0^2\right) \hat{p}' = \rho_0 \left(\widehat{\boldsymbol{u} \otimes \boldsymbol{u}}\right). \tag{2.58}$$

The centerline of this thesis will be to solve the physical problem expressed by means of equation (2.58) in a given computational domain Ω and with prescribed boundary conditions on $\partial\Omega$. This first involves finding the source term (Reynolds stress) and then solving the inhomogeneous Helmholtz equation (2.58).

2.3.3 Formal integral solution

The free-space solution to equation (2.56) has been traditionally worked out by means of the integral formulation presented in section 2.2.4. That is, the acoustic pressure at the far field can be obtained by convolving the source term (Lighthill's tensor double divergence) with the free-space acoustic Green function as in (2.27) (see e.g., [54, 101, 233, 249]). This yields ([54, 145, 146, 206]) for a point at the far field, $|\boldsymbol{x}| \to \infty$,

$$\begin{aligned} p'(\boldsymbol{x}, t) &= \frac{1}{4\pi} \int_{\mathbb{R}^3} \frac{1}{|\boldsymbol{x} - \boldsymbol{y}|} \rho_0 \partial_{y_i} \partial_{y_j} u_i u_j \left(\boldsymbol{y}, t - |\boldsymbol{x} - \boldsymbol{y}| / c_0\right) d\boldsymbol{y} \\ &\approx \frac{1}{4\pi} \partial_i \partial_j \int_{\mathbb{R}^3} \frac{1}{|\boldsymbol{x} - \boldsymbol{y}|} \rho_0 u_i u_j \left(\boldsymbol{y}, t - |\boldsymbol{x} - \boldsymbol{y}| / c_0\right) d\boldsymbol{y} \\ &\approx \frac{\rho_0 x_i x_j}{4\pi c_0^2 |\boldsymbol{x}|} \partial_{tt}^2 \int_{\mathbb{R}^3} u_i u_j \left(\boldsymbol{y}, t - \frac{|\boldsymbol{x}|}{c_0} + \frac{\boldsymbol{x} \cdot \boldsymbol{y}}{c_0 |\boldsymbol{x}|}\right) d\boldsymbol{y}, \end{aligned} \tag{2.59}$$

where we have made use of the Fraunhofer approximation (2.39) and the interchanging of spatial and time derivatives (2.40) in the last line.

Equation (2.59) gives the acoustic pressure at a point $\boldsymbol{x}$ and time t once the Reynolds stress is known (either by means of experiment, analytical development or CFD computation). As already mentioned, this tensor is only expected to have a non-zero value in the vortical (turbulent) region of the flow so that the integral in (2.59) becomes finite. A dimensional analysis of the various terms appearing in (2.59) leads to the well-known Lighthill's eight power law, which states that the generated total acoustic power depends on U^8 (see [206]). It can also be shown that the ratio between the generated acoustic power and the energy supplied to the flow in order to maintain turbulence is proportional to M^5. This verifies the fact that the aerodynamically generated sound is a small side-effect of the whole flow motion.

2.4 The presence of boundaries

2.4.1 The Ffowcs Williams-Hawkings equation

So far, we have placed the problem of aerodynamic sound generation and propagation in free space, i.e., $\mathbb{R}^3$. However, in most practical cases the presence of boundaries plays a crucial role. Think, for instance, in the case of noise generated by fan or helicopter blades or in the case of noise generated by turbulence in shear layers separating an exhausting high speed jet from the quiescent medium. In order to address these types of problems, it could be possible to follow the procedure of the last section using an appropriate Green function for the geometry at hand, instead of the one for free space (see also the discussion on the Kirchoff-Helmholtz equation in section 2.2.4). However, and as mentioned in section 2.2.4, this is not usually an easy task, specially in the case of complex geometries. An alternative approach was proposed by Ffowcs-Williams and Hawkings [72] (see also [71]), which consists in reformulating the source terms in (2.54) to account for the presence of boundaries. This allows to keep making use of the free space Green function when an integral formulation of the problem is carried out.

The Ffowcs Williams-Hawkings procedure starts by introducing a closed control surface S in the flow. A function $f(\boldsymbol{x}, t)$ is defined such that

$$\begin{aligned} f(\boldsymbol{x}, t) &= 0 && \forall \boldsymbol{x} \in S \\ f(\boldsymbol{x}, t) &> 0 && \forall \boldsymbol{x} \text{ in the flow} \\ f(\boldsymbol{x}, t) &< 0 && \forall \boldsymbol{x} \text{ inside } S. \end{aligned} \tag{2.60}$$

If S moves with speed $\boldsymbol{v}$, the following relation fulfils

$$\partial_t f + \boldsymbol{v} \cdot \nabla f = 0. \tag{2.61}$$

The Heaviside function $H(f)$ is then defined having a unit value everywhere in the flow and a zero value inside S. Multiplying the continuity and momentum equations (2.49)-(2.50) by $H(f)$ and following an analogous procedure to the one used to derive Lighthill's equation (2.56), we arrive at the differential form of the *Ffowcs Williams-Hawkings equation*

$$\Box^2 \left[H(f)\, c_0^2 (\rho - \rho_0) \right] = (\nabla \otimes \nabla) : [\boldsymbol{T} H(f)] + \nabla \cdot [\boldsymbol{s}\, \delta(f)] + \partial_t [q\, \delta(f)], \tag{2.62}$$

where $\boldsymbol{T}$ is the Lighthill tensor (2.55), δ is the Dirac delta at $f = 0$ and

$$\boldsymbol{s} = -\rho \boldsymbol{u} \otimes (\boldsymbol{u} - \boldsymbol{v}) - (p - p_o)\, \boldsymbol{I} + \boldsymbol{\sigma} \tag{2.63}$$

$$q = \rho_o \boldsymbol{v} + \rho (\boldsymbol{u} - \boldsymbol{v}). \tag{2.64}$$

Note that if no surfaces were present, $H(f) = 1$ and $\delta(f) = 0$ so that Lighthill's equation (2.54) is recovered. Hence the difference between (2.54) and (2.62) is the appearance of two new source terms, which according to section 2.2.6 represent distributions of dipoles and monopoles placed at S.

2.4.2 Formal integral solution

By convolving (2.62) with the free field acoustic Green function (2.23) we obtain the integral Ffowcs Williams-Hawkings equation that accounts for the effects of boundaries in the flow

$$\begin{aligned} H\left(f\right)c_0^2\left(\rho-\rho_0\right) \approx & \frac{1}{4\pi}\partial_i\partial_j\int_{\Omega(\tau)}\frac{\left[T_{ij}\right]}{\left|\boldsymbol{x}-\boldsymbol{y}\right|}\,d\Omega \\ & -\frac{1}{4\pi}\partial_i\int_{S(\tau)}\frac{\left[\rho u_i\left(u_j-v_j\right)+\left(p-p_0\right)\delta_{ij}-\sigma_{ij}\right]}{\left|\boldsymbol{x}-\boldsymbol{y}\right|}n_j\,dS \\ & -\frac{1}{4\pi}\partial_t\int_{S(\tau)}\frac{\left[\rho\left(u_i-v_i\right)+\rho_0 v_i\right]}{\left|\boldsymbol{x}-\boldsymbol{y}\right|}n_i dS. \end{aligned} \tag{2.65}$$

The surface integrals in (2.65) are over the retarded time surface defined by $f\left(\boldsymbol{y},\tau\right)=0$ with the surface normal directed into the region where $f>0$. (2.65) is a generalization of the Kirchoff-Helmholtz equation (2.34) and also consists of distributed surface dipoles and monopoles (second and third lines) plus a quadrupole contribution due to the velocity Reynolds stress tensor. We remind that the delimiters [ ] indicate evaluation at retarded times.

A particular interesting case of the Ffowcs Williams-Hawkings equation is that of the control surface being stationary. In this case $\boldsymbol{v}=0$ and equation (2.65) reduces to *Curle's equation* [56]:

$$\begin{aligned} H\left(f\right)c_0^2\left(\rho-\rho_0\right) \approx & \frac{1}{4\pi}\partial_i\partial_j\int_{\Omega}\frac{\left[T_{ij}\right]}{\left|\boldsymbol{x}-\boldsymbol{y}\right|}\,d\Omega \\ & -\frac{1}{4\pi}\partial_i\int_{S}\frac{\left[\rho u_i u_j+\left(p-p_0\right)\delta_{ij}-\sigma_{ij}\right]}{\left|\boldsymbol{x}-\boldsymbol{y}\right|}n_j\,dS \\ & -\frac{1}{4\pi}\partial_t\int_{S}\frac{\left[\rho u_i\right]}{\left|\boldsymbol{x}-\boldsymbol{y}\right|}n_i dS. \end{aligned} \tag{2.66}$$

If in addition the surface S is rigid ($\boldsymbol{u}=0$ at S), (2.66) further simplifies to

$$\begin{aligned} H\left(f\right)c_0^2\left(\rho-\rho_0\right) \approx & \frac{1}{4\pi}\partial_i\partial_j\int_{\Omega}\frac{\left[T_{ij}\right]}{\left|\boldsymbol{x}-\boldsymbol{y}\right|}\,d\Omega \\ & -\frac{1}{4\pi}\partial_i\int_{S}\frac{\left[\left(p-p_0\right)\delta_{ij}-\sigma_{ij}\right]}{\left|\boldsymbol{x}-\boldsymbol{y}\right|}n_j\,dS. \end{aligned} \tag{2.67}$$

Using the above integral equations in order to compute the generated aerodynamic sound field it is not an easy task and care has to be taken, specially in what concerns the evaluation of the surface terms at the corresponding retarded times (see e.g. [8, 53, 145]). However, accurate codes have been developed for some industrial applications, which show good performance. Further details on this and further possibilities to perform computations of aerodynamically generated noise will be given in next chapter.

On the other hand, it is worthwhile to mention that the integral formulations presented above can be also developed in the frequency domain (see e.g., [8, 51, 53, 54, 72]).

2.5 Conclusions

After reviewing some fundamental concepts on physical acoustics, we have introduced Lighthill's acoustic analogy, which is central to aeroacoustics theory. For low Mach numbers, the source term of this analogy can be approximated by the double divergence of the Reynolds tensor for the incompressible velocity field. If one assumes the latter as known data, a formal integral solution to the aerodynamic noise problem can be found by convolving the source term with the acoustic free-space Green function. If boundaries are present, Lighthill's acoustic analogy can be reformulated so as to include their effect. This leads to the also celebrated Ffowcs-Williams/Hawkings equation, whose integral solution is widely used as a basis for computational aeroacoustics.

As an alternative to this conventional approach, a three-step methodology will be introduced in next chapter. The methodology will basically consist of a CFD calculation to obtain the incompressible velocity field, a computation of the acoustic source and its time Fourier transform, and solving the time Fourier transform of Lighthill's acoustic analogy. Stabilised finite element methods will be used to implement it. Some special issues concerning the computation of the aerodynamic and acoustic fields will be respectively addressed in Chapters 4 and 5.

Chapter 3

Computational aeroacoustics

In this chapter we will propose and implement the three-step methodology briefly described in Chapter 1 to compute aerodynamic noise generated by low speed flows. Use will be made of Subgrid Scale (SGS) stabilised finite element methods. In what concerns the first step of the method, i.e., the computational fluid dynamics simulation of incompressible flows, special emphasis will be placed on a recently developed SGS procedure that, as a novelty, accounts for the time tracking of the subscales keeping all non-linear terms in their modelling. A SGS method will be also used to compute the acoustic field generated in the third step of the method. Numerical examples of aeolian tones generated by flow past single and parallel cylinders at different Reynolds numbers will be also presented to test the good performance of the method.

3.1 Introduction

The first golden age of aeroacoustics lasted from the late 1940's until the 1970's (see section 2.1). At that time, computer science had evolved enough so as to begin to consider the idea of approaching the problem of aerodynamically generated noise using computational resources. That was the beginning of Computational Aeroacoustics (CAA). Its amazingly rapid development showing large potential, combined with the progress in new air vehicles (for both civilian transportation and military applications) and the stricter noise regulations yield the conclusion, at the beginning of the 1990's, that a second golden age of aeroacoustics was emerging [209, 293].

Up to nowadays, several CAA strategies have been developed in order to face a large variety of aerodynamic noise problems typical of aeronautics, railways or automotive sectors (among others). The physics underlying the various phenomena leading to the generation of aerodynamic noise may be quite different from case to case, depending on the compressibility of the flow, the possible interaction (feedback loops) between the aerodynamic and acoustic fields, the possible shock wave formation, the importance of non-linear propagation effects, etc.,. However it is our purpose to focus herein on the numerical computation of aerodynamic noise generated by viscous low speed flows. Computational Aeroacoustics of viscous subsonic flows has to face with several difficulties

(some of them shared with other types of flows) such as (see e.g., [53]):

- The large audibility range of human hearing that comprises from 0 dB to almost 140 dB, which corresponds to intensity changes of several orders of magnitude.
- The wide frequency range perceived by human hearing that comprises from 20 Hz to 20.000 Hz (i.e., about 10 octaves whereas sight involves just one octave). Moreover, hearing is specially sensitive in the $[1000, 4000]$ Hz range, which is 4 to 5 octaves higher than the energy containing scales.
- The high disparity between the energy of the aerodynamic field and the energy of the aeroacoustic field the former generates (see section 2.3.3). The power ratio is of order $\sim M^5$, with M being the Mach number. Hence, the acoustic field is a small by product of the flow motion and its weak values sometimes may result masked by the dispersion and diffusion errors of the numerical algorithms.

  The following example can serve to illustrate the weakness of the acoustic field [53]: The sound intensity emitted by a standard jet plane at taking off is as large as the intensity emitted by the whole population of a middle town shouting simultaneously. However, all this acoustic energy will not suffice to fry an egg!
- The large scale disparity between the sizes of the flow eddies and the wavelength of the acoustic waves they generate.
- It is of crucial importance for the numerical solution to maintain the multipolar character of the acoustic field. Substituting a quadrupolar source by a dipolar one may lead to strong errors in the evaluation of both, the directivity and the intensity of the acoustic field, unless integrations are very carefully performed (see section 2.4.2).
- Another important question (no to be addressed in this work) concerns the sound propagation at large distances $\sim$ 300 m, where non-linear phenomena such as steepening may play an important role (see e.g., [293]).

As mentioned, several numerical approaches have been developed to face the above CAA problems in the past thirty years (see e.g., [8,32,53,68,293,297]). These approaches include the Direct Numerical Simulation (DNS) (see e.g., [169, 227, 228]) the use of the Kirchoff-Helmholtz integral over a surface enclosing all sources (e.g., [69, 87, 228, 293]) the use of asymptotic matching (e.g., [271] following [55]) and some less extended alternatives such as the stochastic approach in [6] or the numerical techniques for near-field computations in [58]. Recent developments have also included the use of dispersion-relation-preserving schemes [282] and its grid-optimized version [34]. However, the most extended way to perform CAA computations for low speed flows probably involves the use of acoustic analogies. Acoustic analogies have been applied to solve some academic problems, such as those related to the generation of sound fields by interacting vortices (e.g., [173, 174]). More recently, problems such as computing the noise generated by

turbulence past the trailing edge of a wing have been also addressed [219, 244, 292]. CAA problems of industrial interest are nowadays being attempted with the use of supercomputing facilities.

Acoustic analogies in CAA are usually solved following an integral formulation. The integral form of the Ffowcs-Williams and Hawkings equation (2.65) is frequently used [8, 66, 217] neglecting the quadrupolar contribution (Reynolds stresses) and using a CFD code to determine the velocity and pressure on the problem surfaces. However, we will not follow this somehow standard approach here. As it has been explained in Chapter 1, a three-step approach will be followed involving a CFD simulation, obtaining an acoustic source term from it, and solving an inhomogeneous Helmholtz equation to compute the generated aeroacoustic field. The differential equations in the first and third step of the proposed method (Fig. 3.1) will be solved using subgrid scale (SGS) stabilised finite element methods. The use of finite elements poses no mesh restrictions when dealing with complex geometries, which makes the approach suitable for industrial problems. Moreover, this procedure avoids some of the problems found when using the standard integral approach such as evaluating the source term at appropriate retarded times. It also avoids neglecting any term (noise sources inside the flow interior domain are also considered), it accounts for the presence of boundaries in a natural way and allows a direct visualization of the acoustic source term. The finally resulting method resembles that in Refs. [243], [244] although it presents several differences concerning the acoustic source term, the stabilised weak forms used in the numerical formulation, the treatment of sound propagation under Galilean and Lorentz transformations [106] and some implementation aspects. Finally it is worthwhile to mention that recent CAA has been also carried out work in the framework of finite volumes (see e.g., the space-time and solution-element approach in [31]).

The chapter is organized as follows. In section 3.2 the proposed CAA methodology for low speed flows is presented. Next, in section 3.3 we state the initial and boundary value differential problems to be solved. The functional framework to be used in this and subsequent chapters is also introduced, as well as the variational formulation of the former differential problems. In section 3.4 the Galerkin finite element approach to solve the variational problems is presented and its drawbacks outlined. The stabilised finite element methods that avoid the typical difficulties of the Galerkin approach are formulated in section 3.5. In section 3.6 two numerical examples dealing with aerodynamic noise generated by flow past a single cylinder and by two cylinders for different Reynolds numbers are presented. Conclusions are finally drawn in section 3.7.

3.2 Proposed methodology to solve aeroacoustic problems

Once the physical problem of the generation of aerodynamic sound has been presented in the previous chapter, as well as one of the standard ways to solve it, we will next establish the proposed alternative method to do so. Our main goal will be to find a numerical

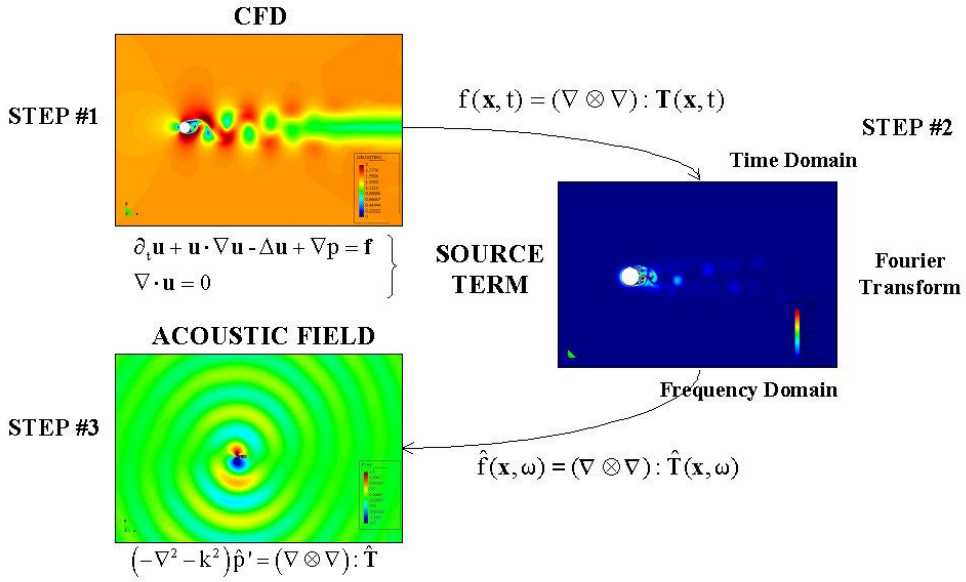

Figure 3.1: Scheme of the proposed methodology for computational aeroacoustics.

solution for the time Fourier transform of the original Lighthill acoustic analogy using the Reynolds tensor to approximate Lighthill's tensor (equation (2.58)).

The proposed methodology [105–107] is embedded in the framework of finite element methods and can be conceptually divided in three steps. In the first step a computational fluid dynamic (CFD) simulation of the incompressible Navier-Stokes equations is performed to obtain the flow velocity field. In the second step the source term in the r.h.s of (2.56) i.e., the double divergence of the Reynolds tensor, is computed and time Fourier transformed. Finally, in the third step the result is inserted in the inhomogeneous Helmholtz equation (2.58) and solved to obtain the acoustic pressure field. A scheme of the approach is shown in Fig. 3.1.

In what follows, the three steps will be exposed in some detail.

3.2.1 First step: Computational Fluid Dynamic Simulation

The CFD computation aims at obtaining the flow velocity vector, $\boldsymbol{u}$, from the solution of the time evolving incompressible Navier-Stokes equations. The mathematical problem consists in solving the latter equations in a given computational domain $\Omega \subset \mathbb{R}^d$ (where $d = 2$ or 3 is the number of space dimensions) with boundary $\partial\Omega$ and prescribed initial and boundary conditions. The boundary $\partial\Omega$ can be split into two disjoint sets $\partial\Omega = \overline{\Gamma_D \cup \Gamma_N}$ respectively accounting for those boundaries with prescribed Dirichlet and Neumann

conditions. The problem to be solved can be straightforwardly derived from the results in section 2.2.2 and reads

$$\partial_t \boldsymbol{u} - \nu \Delta \boldsymbol{u} + \boldsymbol{u} \cdot \nabla \boldsymbol{u} + \nabla p = \boldsymbol{f} \quad \text{in } \Omega,\ t > 0, \tag{3.1}$$

$$\nabla \cdot \boldsymbol{u} = 0 \quad \text{in } \Omega,\ t > 0, \tag{3.2}$$

$$\boldsymbol{u}(\boldsymbol{x}, 0) = \boldsymbol{u}_0(\boldsymbol{x}) \quad \text{in } \Omega,\ t = 0, \tag{3.3}$$

$$\boldsymbol{u}(\boldsymbol{x}, t) = \boldsymbol{u}_D(\boldsymbol{x}, t) \quad \text{on } \Gamma_D,\ t > 0, \tag{3.4}$$

$$\boldsymbol{n} \cdot \boldsymbol{\sigma}(\boldsymbol{x}, t) = \boldsymbol{t}_N(\boldsymbol{x}, t) \quad \text{on } \Gamma_N,\ t > 0, \tag{3.5}$$

with ν representing the kinematic flow viscosity, $\boldsymbol{f}$ the external force and $\boldsymbol{t}_N$ the traction on the boundary.

In the case of high Reynolds number problems we will be faced with the difficulty to simulate turbulent flows. There exist mainly three options to do so (see e.g., [255], [265]) namely the RANS (Reynolds Averaged Navier-Stokes equations) approach, the DNS (Direct Numerical Simulation) approach and the LES (Large Eddy Simulation) approach. In general, the RANS approach turns to be not appropriate for aeroacoustic simulations because it cannot properly capture time fluctuations. On the other hand, DNS computational cost scales as $\mathrm{Re}^{9/4}$, which makes it not feasible for the typical high Reynolds number problems found in aeronautics, railways or automotive applications. Hence, the right option seems to be LES that performs a spatial scale decomposition $\boldsymbol{u} = \bar{\boldsymbol{u}} + \boldsymbol{u}'$, $p = \bar{p} + p'$ for the velocity and the pressure in (3.1)-(3.5). $(\bar{\boldsymbol{u}}, \bar{p})$ stands for some *large* scales that are expected to be computationally resolvable while $(\boldsymbol{u}', p')$ stands for the *small* scales, which are not expected to be computable.

In the standard LES approach, the scale decomposition is carried out by convolving (3.1)-(3.5) with a filter function [255, 265]. As it is known, this gives place to a *closure* problem because an extra term of the type $\boldsymbol{\mathcal{R}} := \overline{\boldsymbol{u} \otimes \boldsymbol{u}} - \bar{\boldsymbol{u}} \otimes \bar{\boldsymbol{u}}$, which has to be modelled, appears in the equations. This term is known as the *residual stress* tensor. Once having a model for $\boldsymbol{\mathcal{R}}$, the resulting LES equations can be discretised and a numerical solution attempted. However, there is another possible strategy that consists in performing the scale decomposition by means of a projection onto the finite element space [157]. In this case, the large scales represent those scales that can be directly captured with the computational mesh, while the small scales represent those scales that cannot be captured by the mesh. An advantage of such a procedure is that it avoids some of the typical problems encountered in standard LES such as the merging of errors arising from the *closure* model and from the adopted numerical strategy.

This alternative approach to LES has been developed in the framework of Subgrid Scale (SGS) stabilised finite element methods [150, 153] and constitutes a reliable alternative to the standard LES simulation of turbulent flows (see e.g., [26, 44, 158, 159]). In the following sections the SGS method adopted in this work [42–44, 47] will be presented in full detail, whereas considerations on its possibilities concerning the simulation of turbulent flows will be addressed in chapter 4.

3.2.2 Second step: The source term

The second step of the method consists in obtaining the acoustic source term, i.e., $\rho_0 (\nabla \otimes \nabla) : (\boldsymbol{u} \otimes \boldsymbol{u})$, from the flow velocity vector, $\boldsymbol{u}$, computed in the first step of the method. As the source term involves a double divergence it cannot be directly computed using finite elements of class C^0, unless it is integrated by parts transferring one derivative to the test function. However, there also exists the possibility to approximate the source term with first order derivative terms thanks to the incompressibility constraint. Effectively,

$$\begin{aligned}(\nabla \otimes \nabla) : \boldsymbol{T} \approx \rho_0 (\nabla \otimes \nabla) : (\boldsymbol{u} \otimes \boldsymbol{u}) &= \rho_0 \nabla \cdot [(\nabla \otimes \boldsymbol{u}) \cdot \boldsymbol{u} + \boldsymbol{u} (\nabla \cdot \boldsymbol{u})] \\ &= \rho_0 \nabla \cdot [(\nabla \otimes \boldsymbol{u}) \cdot \boldsymbol{u}] = \rho_0 \boldsymbol{u} \cdot \nabla (\nabla \cdot \boldsymbol{u}) + \rho_0 (\nabla \otimes \boldsymbol{u}) : (\nabla \otimes \boldsymbol{u})^\top \\ &= \rho_0 (\nabla \otimes \boldsymbol{u}) : (\nabla \otimes \boldsymbol{u})^\top =: s(\boldsymbol{x}, t) \end{aligned} \tag{3.6}$$

where $\nabla \cdot \boldsymbol{u} = 0$ has been used twice and we have defined $s(\boldsymbol{x}, t)$ in the last line (the notation $\nabla \otimes \boldsymbol{u} \equiv \nabla \boldsymbol{u}$ will be used indistinctly throughout the thesis). This approximation allows the direct visualization of the source term while keeping the advantages of using C^0-class finite elements.

The second step of the method finishes by performing the time Fourier transform of $s(\boldsymbol{x}, t)$ to get $\hat{s}(\boldsymbol{x}, \omega)$. To obtain the appropriate degree of accuracy for $\hat{s}(\boldsymbol{x}, \omega)$ it would be necessary to store a large amount of instantaneous velocity fields. This requires a huge amount of computer memory resources. To avoid this problem, the following strategy has been used. The frequencies at which the source term $\hat{s}(\boldsymbol{x}, \omega)$ is wanted are chosen prior to start the CFD computation. During the evolution of the CFD computation $s(\boldsymbol{x}, t)$ is automatically computed at each time step as well as its contribution to $\hat{s}(\boldsymbol{x}, \omega)$. At the end of the simulation only $\hat{s}(\boldsymbol{x}, \omega)$ is retained hence avoiding the need to store $s(\boldsymbol{x}, t)$, except for the steps at which a visualization of the source term is desired. Moreover, if there is a prior knowledge of the frequency range at which the analysis is to be performed (this is often the case in several practical engineering problems where experimental data is available) the computations can be further reduced. Consequently, although steps one and two of the methodology have been differentiated for the sake of clarity, in practice they are carried out simultaneously.

3.2.3 Third step: Computing the acoustic field

In the third step of the method, the inhomogeneous Helmholtz equation (2.58) obtained from the time Fourier transform of (2.56) is solved using $\hat{s}(\boldsymbol{x}, \omega)$ in (3.6) as the source term. The mathematical problem to be faced is that of finding the acoustic pressure $\hat{p}'(\boldsymbol{x}, \omega) : \Omega_{ac} \to \mathbb{C}$, being $\Omega_{ac} \subset \mathbb{R}^d$, $(d = 2, 3)$ a bounded computational domain with boundary $\partial\Omega_{ac} = \Gamma_D \cup \Gamma_B$ $(\Gamma_D \cap \Gamma_B = \emptyset)$ such that

$$-\left(\nabla^2 + k_0^2\right) \hat{p}' = \hat{s} \quad \text{in } \Omega_{ac}, \tag{3.7}$$

$$\hat{p}' = \hat{p}'_D \quad \text{on } \Gamma_D, \tag{3.8}$$

$$\nabla \hat{p}' \cdot \boldsymbol{n} = M [\hat{p}'] + \hat{g} \quad \text{on } \Gamma_B. \tag{3.9}$$

In (3.7)-(3.9) $k_0 = \omega/c_0$ is the wavenumber, $\boldsymbol{n}$ stands for the normal pointing outwards the exterior boundary Γ_B, $\hat{g} : \Gamma_B \to \mathbb{C}$ represents prescribed data on Γ_B and $M[\hat{p}']$ is an integral operator defining a non-reflecting condition. If Γ_B is far enough from the source region, the non-local boundary condition specified by $M[\hat{p}']$ can be replaced by the local condition $ik_0\hat{p}'$, so that (3.9) becomes a Sommerfeld's radiation condition,

$$\nabla\hat{p}' \cdot \boldsymbol{n} = ik_0\hat{p}' + \hat{g} \quad \text{on } \Gamma_B. \tag{3.10}$$

In all forthcoming simulations we will consider large enough computational domains so that (3.10) applies. In fact $\nabla\hat{p} \cdot \boldsymbol{n} - ik_0\hat{p} \sim \mathcal{O}(R^{-1})$ being R a measure of the radius of the computational domain [163].

The third step of the method will be addressed in detail in Chapter 5 where (3.7)-(3.10) as well as their convected counterpart will be solved using stabilised finite element methods.

3.3 Variational problem statement

3.3.1 Functional framework

Prior to establish the variational or weak formulation of problems (3.1)-(3.5) and (3.7)-(3.10), we will introduce the general functional framework that will be used throughout this work. We will denote by $L^p(\Omega)$ the spaces of functions whose p power ($1 \leq p < \infty$) is integrable in Ω (with respect to the Lebesgue measure). The spaces $L^p(\Omega)$ are Banach spaces with associated norm

$$\|u\|_p := \left(\int_\Omega |u(\boldsymbol{x})|^p \, d\boldsymbol{x} \right)^{\frac{1}{p}}, \quad p < \infty. \tag{3.11}$$

The case $p = \infty$ corresponds to the space of bounded functions in Ω. The associated norm is then given by the essential supremum of all functions bounded in Ω i.e., $\|\boldsymbol{u}\|_\infty := \operatorname{ess\,sup}_\Omega |\boldsymbol{u}(x)|$. For $1 < p < \infty$, $L^p(\Omega)$ are *reflexive* spaces with *duals* $L^q(\Omega)$, being $1/p + 1/q = 1$. A case of special interest is that of $L^2(\Omega)$, which is a Hilbert space with scalar product

$$(\boldsymbol{u}, \boldsymbol{v}) := \int_\Omega \boldsymbol{u}(\boldsymbol{x})\boldsymbol{v}(\boldsymbol{x}) d\Omega \tag{3.12}$$

and induced norm $\|\boldsymbol{u}\|_{L^2(\Omega)} \equiv \|\boldsymbol{u}\| = (\boldsymbol{u}, \boldsymbol{u})^{1/2}$. Boldface will be used to designate the vector counterpart of $L^p(\Omega)$ corresponding to d-dimensional functions i.e., $\boldsymbol{L}^p(\Omega) \equiv (L^p(\Omega))^d$. From a physical point of view and in what concerns the Navier-Stokes equations (3.1)-(3.5), $\boldsymbol{L}^2(\Omega)$ can be identified with the space of velocity fields with bounded kinetic energy, given that $\|\boldsymbol{u}\|^2 = 2E(\boldsymbol{u})$, with $E(\boldsymbol{u})$ standing for the kinetic energy per unit mass.

The Sobolev spaces $W^{m,p}(\Omega)$ are space of functions in $L^p(\Omega)$ such that their derivatives up to order $m \in \mathbb{N}$ also belong to $L^p(\Omega)$. $W^{m,p}(\Omega)$ are Banach spaces with

norm denoted by $\|\cdot\|_{m,p}$. For $p = 2$, $W^{m,2}(\Omega)$ are Hilbert spaces and the notation $H^m(\Omega) \equiv W^{m,2}(\Omega)$ will be used to refer to them. Moreover, $H_0^m(\Omega)$ will stand for the subspace of functions in $H^m(\Omega)$ vanishing on $\partial\Omega$ together with their derivatives in the normal direction up to order $m-1$. We note that the case $m = 1$ is of special interest. $H^1(\Omega)$ has associated the scalar product

$$(\boldsymbol{u}, \boldsymbol{v})_{H^1} := \frac{1}{L^2}(\boldsymbol{u}, \boldsymbol{v}) + (\nabla \boldsymbol{u}, \nabla \boldsymbol{v}) \tag{3.13}$$

and the norm $\|\boldsymbol{u}\|_{H^1} = (\boldsymbol{u}, \boldsymbol{u})_{H^1}^{1/2}$. In (3.13), L represents a characteristic length (for instance, $L = \mathrm{diam}(\Omega)$) with $L = 1$ for dimensionless variables. On the other hand, $H^{-1}(\Omega)$ stands for the topological dual of $H_0^1(\Omega)$. In the case of f and g being distributions such that the product fg is integrable in the domain Ω, we will use the brackets, $\langle \cdot, \cdot \rangle_\Omega$ to denote the integral

$$\langle f, g \rangle_\Omega = \int_\Omega fg \, d\Omega \tag{3.14}$$

so that, in particular, $\langle \cdot, \cdot \rangle$ will correspond to the duality pairing between $H_0^1(\Omega)$ and $H^{-1}(\Omega)$. For $f, g \in L^2(\Omega)$, $\langle \cdot, \cdot \rangle$ will correspond to the inner product $(\cdot, \cdot)$. Again, boldface will designate the vector counterparts of all these spaces.

For $\boldsymbol{u}$ being a velocity field, we have seen that, when $\boldsymbol{v} = \boldsymbol{u}$, the first term in (3.13) corresponds to twice the kinetic energy. In what concerns the second term, it corresponds to the enstrophy root square. The enstrophy $\mathcal{E}(\boldsymbol{u})$ is an important quantity given that it determines the rate of dissipation of kinetic energy in a flow. In $\mathbb{R}^d$, $\mathcal{E}(\boldsymbol{u})$ can be represented in terms of the vorticity field, $\boldsymbol{\omega} = \nabla \times \boldsymbol{u}$, as $\mathcal{E}(\boldsymbol{u}) := \|\boldsymbol{\omega}\|_2^2$. Hence, from a physical point of view the space $\boldsymbol{H}^1(\Omega)$ can be identified with the space of velocity and vorticity fields having bounded kinetic energy and enstrophy [75].

Finally, to deal with the time evolution of the pressure and velocity fields we will need to introduce the spaces $L^p(0, T; Z(\Omega))$ that for $1 \leq p < \infty$ are defined as

$$L^p(0, T; Z(\Omega)) := \left\{ f : (0, T) \longrightarrow Z(\Omega) | \int_0^T \|f(\boldsymbol{x})\|_Z^p \, dt < \infty \right\}, \tag{3.15}$$

with $Z(\Omega)$ being any of the above introduced spatial functional spaces. $\|\cdot\|_X$ is used to designate the norm in a Banach space, X. In the case $p = \infty$ we will have

$$L^\infty(0, T; Z(\Omega)) := \left\{ f : (0, T) \longrightarrow Z(\Omega) | \operatorname{ess\,sup}_{t \in (0,T)} \|f(\boldsymbol{x})\|_Z^p < \infty \right\}. \tag{3.16}$$

Once more, a bold character will be used for the vector counterpart of all these spaces.

The functional spaces presented above represent the general functional framework were most problems in this thesis will be stated. However, additional functional spaces will be required and introduced where appropriate throughout the work.

3.3.2 Variational forms

Weak form of the Navier-Stokes equation

Once having introduced an appropriate functional framework, we are now in disposition to present the variational or weak form of the Navier-Stokes equations (3.1)-(3.5). Let us consider in what follows the case of homogeneous Dirichlet conditions (the extension to the inhomogeneous case and Neumann boundary conditions can be done in the usual manner) and use $\mathcal{V}_0^d$ and $\mathcal{Q}_0$ to designate the functional spaces

$$\mathcal{V}_0^d \equiv \boldsymbol{H}_0^1(\Omega) := \left\{ \boldsymbol{u}\left(\boldsymbol{x}\right) \in H^1\left(\Omega\right)^d \left| \boldsymbol{u} = 0 \text{ on } \Gamma_D \right. \right\} \tag{3.17}$$

$$\mathcal{Q}_0 := \left\{ q\left(\boldsymbol{x}\right) \in L^2\left(\Omega\right) \left| \int_\Omega q d\Omega = 0 \text{ if } \Gamma_N = \emptyset \right. \right\}. \tag{3.18}$$

The weak or variational form corresponding to (3.1)-(3.5) is then found as usual by multiplying these equations by test functions $\boldsymbol{v} \in \mathcal{V}_0^d$, $q \in \mathcal{Q}_0$ and integrating over the whole domain Ω. Hence, the variational problem consists e.g., in finding $[\boldsymbol{u}, p] \in \boldsymbol{L}^2\left(0, T; \mathcal{V}_0^d\right) \times \boldsymbol{L}^1\left(0, T; \mathcal{Q}_0\right)$ such that

$$\int_\Omega \boldsymbol{v} \cdot \left[\partial_t \boldsymbol{u}^n + \left(\boldsymbol{u} \cdot \nabla \boldsymbol{u}\right)\right] d\Omega + \nu \int_\Omega \nabla \boldsymbol{v} : \nabla \boldsymbol{u} d\Omega - \int_\Omega p \nabla \cdot \boldsymbol{v} d\Omega = \int_\Omega \boldsymbol{v} \cdot \boldsymbol{f} d\Omega \tag{3.19}$$

$$\int_\Omega q \nabla \cdot \boldsymbol{u} d\Omega = 0 \tag{3.20}$$

for all $[\boldsymbol{v}, q] \in \mathcal{V}_0^d \times \mathcal{Q}_0$. In order to shorten the notation in (3.19)-(3.20) and subsequent equations, we will make use of (3.12), (3.14) and define

$$l\left(\boldsymbol{v}\right) := \langle \boldsymbol{v}, \boldsymbol{f} \rangle \tag{3.21}$$

(note that the brackets in (3.21) correspond to the duality pair between $H^{1/2}\left(\Gamma_N\right)$ and $H^{-1/2}\left(\Gamma_N\right)$). The weak form (3.19)-(3.20) can then be rewritten as

$$\left(\partial_t \boldsymbol{u}, \boldsymbol{v}\right) + \langle \boldsymbol{u} \cdot \nabla \boldsymbol{u}, \boldsymbol{v} \rangle + \nu \left(\nabla \boldsymbol{u}, \nabla \boldsymbol{v}\right) - \left(p, \nabla \cdot \boldsymbol{v}\right) = l\left(\boldsymbol{v}\right) \tag{3.22}$$

$$\left(q, \nabla \cdot \boldsymbol{u}\right) = 0 \tag{3.23}$$

Weak form of the inhomogeneous Helmholtz equation

The procedure to find the continuous weak form for the inhomogeneous Helmholtz equation (3.7)-(3.9) in the third step of the proposed CAA method, is analogous to the one developed in the previous section. We consider again homogeneous Dirichlet conditions and introduce the functional space

$$\mathcal{W}_0 := \left\{ q\left(\boldsymbol{x}\right) \in H^1\left(\Omega_{ac}\right); q = 0 \text{ on } \Gamma_D \right\}. \tag{3.24}$$

We then multiply the differential equation by a test function w and integrate over the acoustic domain Ω_{ac}. Using the notation introduced in the previous sections, the weak problem can be formulated as: find $\hat{p}' \in \mathcal{W}_0$ such that

$$(\nabla \hat{p}', \nabla w) - k_0^2 (\hat{p}', w) - ik_0 \langle \hat{p}', w \rangle_{\Gamma_B} = \langle \hat{s}, w \rangle + \langle \hat{g}, w \rangle_{\Gamma_B} \tag{3.25}$$

for all $w \in \mathcal{W}_0$. Note that the acoustic pressure is a complex number so that the integrals in (3.25) involve the complex conjugate of the test function. Notice also that domain integrations in the scalar products take place now in Ω_{ac}.

3.4 Galerkin finite element approximation

3.4.1 Time discretisation and finite element triplet

Time discretisation of the Navier-Stokes equations

To find a numerical solution to the Navier-Stokes equations (3.1)-(3.5) in the first step of the proposed CAA methodology (section 2.5.1) we will have to discretise them in time and space. The time discretisation scheme that has been used in this work is the generalized trapezoidal rule. Let us consider a partition of the computational time interval $0 < t^0 < \ldots < t^N = T$ with a constant time step size $\delta t := t^{n+1} - t^n$, and let us introduce the following notation for a generic time-dependent function $\varphi(t)$,

$$\delta\varphi^n := \varphi^{n+1} - \varphi^n, \tag{3.26}$$

$$\varphi^{n+\alpha} := \alpha\varphi^{n+1} + (1-\alpha)\varphi^n \tag{3.27}$$

$$\delta_t\varphi^n := \delta\varphi^n / \delta t \tag{3.28}$$

where $\alpha \in [0,1]$ and φ^n stands for the value of φ at time t^n. According to (3.26)-(3.28), the time discrete version of the Navier-Stokes (3.1)-(3.5) for homogeneous Dirichlet conditions can be written as

$$\delta_t \boldsymbol{u}^n - \nu\Delta\boldsymbol{u}^{n+\alpha} + \mathcal{N}^n(\boldsymbol{u}) + \nabla p^{n+1} = \boldsymbol{f}^{n+\alpha} \quad \text{in } \Omega, \tag{3.29}$$

$$\nabla \cdot \boldsymbol{u}^{n+\alpha} = 0 \quad \text{in } \Omega, \tag{3.30}$$

$$\boldsymbol{u}^0 = \boldsymbol{u}_0 \quad \text{in } \Omega, \tag{3.31}$$

$$\boldsymbol{u}^{n+\alpha} = 0 \quad \text{on } \Gamma_D, \tag{3.32}$$

$$\boldsymbol{n} \cdot \boldsymbol{\sigma}^{n+\alpha} = \boldsymbol{t}_N^{n+\alpha} \quad \text{on } \Gamma_N, \tag{3.33}$$

with $\mathcal{N}^n(\boldsymbol{u})$ representing an approximation to the convective term. Depending on the value of α in (3.29)-(3.33) we will have a first or second order accurate in time scheme for the solution. The most widely used schemes are

First order schemes

- $\alpha = 0$: *Forward Euler scheme*. Conditionally stable i.e., δt has to be small enough. In this case the convection term is given explicitly, $\mathcal{N}^n(\boldsymbol{u}) = (\boldsymbol{u}^n \cdot \nabla)\boldsymbol{u}^n$.

- $\alpha = 1$: *Backward Euler scheme*. Unconditionally stable. In this case the convection term is given implicitly, $\mathcal{N}^n(\boldsymbol{u}) = (\boldsymbol{u}^{n+1} \cdot \nabla)\boldsymbol{u}^{n+1}$. A linearisation process is needed at each time step.

- It is also possible to use an explicit advection velocity even if $\alpha = 1$, namely $\mathcal{N}^n(\boldsymbol{u}) = (\boldsymbol{u}^n \cdot \nabla)\boldsymbol{u}^{n+1}$. This results in an unconditionally stable scheme.

Second order schemes

- $\alpha = 1/2$: *Crank-Nicolson scheme*. Unconditionally stable. *This will be the most used scheme in this work*. The convection term is implicit and given by $\mathcal{N}^n(\boldsymbol{u}) = \left(\boldsymbol{u}^{n+1/2} \cdot \nabla\right)\boldsymbol{u}^{n+1/2}$. A linearisation process is needed at each time step.

- $\alpha = 1/2$: *Adams-Bashforth/Crank-Nicolson scheme*. Conditionally stable i.e., δt has to be small enough. Instead of using $\alpha = 1/2$ for the convection term, this term is explicitly obtained from $\mathcal{N}^n(\boldsymbol{u}) = \frac{1}{2}\left[3(\boldsymbol{u}^n \cdot \nabla)\boldsymbol{u}^n - (\boldsymbol{u}^{n-1} \cdot \nabla)\boldsymbol{u}^{n-1}\right]$.

The above presented schemes use a one step approximation for the temporal derivative. Higher step approximations are also possible (e.g., *Gear schemes*) although we will not use them in this work.

Given that we aim at using a finite element method to solve the Navier-Stokes equations, we will be interested in the time discretisation of the weak form (3.22)-(3.23) rather than on (3.29)-(3.33). The time discrete spatial continuous weak form of the Navier-Stokes problem can then be stated as: from known $\boldsymbol{u}^n$, find $\boldsymbol{u}^{n+\alpha} \in \mathcal{V}_0^d$, $p^{n+1} \in \mathcal{Q}_0$ such that

$$(\delta_t \boldsymbol{u}^n, \boldsymbol{v}) + \left\langle \boldsymbol{u}^{n+\alpha} \cdot \nabla \boldsymbol{u}^{n+\alpha}, \boldsymbol{v} \right\rangle + \nu\left(\nabla \boldsymbol{u}^{n+\alpha}, \nabla \boldsymbol{v}\right) - \left(p^{n+1}, \nabla \cdot \boldsymbol{v}\right) = l(\boldsymbol{v}) \tag{3.34}$$

$$\left(q, \nabla \cdot \boldsymbol{u}^{n+1}\right) = 0 \tag{3.35}$$

for all $\boldsymbol{v} \in \mathcal{V}_0^d$, $q \in \mathcal{Q}_0$.

Finite element triplet

As just mentioned above, for the spatial discretisation of the Navier-Stokes equations (3.1)-(3.5) and of the Helmholtz equation (3.7)-(3.9), finite elements will be used. Just to set up some notation we remind that a finite element is a triple $(\Omega_e, \mathcal{P}_k(\Omega_e), \Sigma_e)$ consisting of (see e.g. [22, 172]):

- Ω_e: a geometrical object (subdomain of an Ω-partition).

- $\mathcal{P}_k(\Omega_e)$: a finite dimensional linear space of polynomials of degree $\leq k$ defined on Ω_e. We will generally denote by $\mathcal{V}_h$ the space $\mathcal{V}_h := \{f \in C^0(\Omega) \mid f|_{\Omega_e} \in \mathcal{P}_k(\Omega_e)\}$.

- Σ_e: set of k-unisolvent degrees of freedom, i.e., $\forall\, f_h(\boldsymbol{x}) \in \mathcal{P}_k(\Omega_e)\ \exists!\, \boldsymbol{F} = \{F^1, \ldots, F^n\} \in \Sigma_e |\ f_h(\boldsymbol{x}) = \sum_{a=1}^{n} N^a(\boldsymbol{x})\, F^a$ with $n = \dim \mathcal{P}_k(\Omega_e)$. N^a are termed the *base* or *shape* functions and F^a the *nodal* values.

3.4.2 Galerkin discrete weak forms

Galerkin finite element approximation of the Navier-Stokes equations

Let us now proceed to the spatial discretisation of (3.34)-(3.35). Given a finite element partition of Ω with n_e elements, n_u nodes for the velocity, n_p nodes for the pressure and the finite dimensional subspaces $\mathcal{V}_{h,0}^d \subset \mathcal{V}_0^d$ and $\mathcal{Q}_{h,0} \subset \mathcal{Q}_0$ to respectively approximate the velocity and the pressure, the Galerkin finite element approach to (3.34)-(3.35) can be stated as: from known $\boldsymbol{u}_h^n$, find $\boldsymbol{u}_h^{n+\alpha} \in \mathcal{V}_{h,0}^d$, $p_h^{n+1} \in \mathcal{Q}_{h,0}$ such that

$$\begin{aligned}&(\delta_t \boldsymbol{u}_h^n, \boldsymbol{v}_h) + \nu(\nabla \boldsymbol{u}_h^{n+\alpha}, \nabla \boldsymbol{v}_h) + \langle \boldsymbol{u}_h^{n+\alpha} \cdot \nabla \boldsymbol{u}_h^{n+\alpha}, \boldsymbol{v}_h \rangle \\ &- \left(p_h^{n+1}, \nabla \cdot \boldsymbol{v}_h\right) + \left(q_h, \nabla \cdot \boldsymbol{u}_h^{n+1}\right) = l(\boldsymbol{v}_h)\end{aligned} \tag{3.36}$$

for all $\boldsymbol{v}_h \in \mathcal{V}_{h,0}^d$, $q_h \in \mathcal{Q}_{h,0}$. $\boldsymbol{f}$ and $\boldsymbol{t}_N$ in $l(\boldsymbol{v}_h)$ (r.h.s of (3.36)) are assumed to be continuous in time and evaluated at the time step $n + \alpha$.

On the other hand, $\boldsymbol{u}_h$ and p_h are of the type

$$\boldsymbol{u}_h = \left(\sum_{a=1}^{n_u} N_u^a U_x^a, \sum_{a=1}^{n_u} N_u^a U_y^a, \sum_{a=1}^{n_u} N_u^a U_z^a \right) \tag{3.37}$$

$$p_h = \sum_{b=1}^{n_p} N_p^b P^b \tag{3.38}$$

with N_u^a being the velocity shape functions, $\left(U_x^a, U_y^a, U_z^a\right)$ the nodal velocity values for every coordinate, N_p^b the shape functions for the pressure and P^b the nodal pressure values. Substitution of (3.37)-(3.38) into (3.36) yields an algebraic system of equations for the nodal velocities and pressures that has to be linearised and then solved at each time step. The velocity and pressure at any point in Ω can be finally obtained by interpolation from these nodal values.

It is well known that the Galerkin formulation (3.36) suffers from several numerical problems. For instance, numerical instabilities are encountered for high Reynolds number problems i.e., when the non-linear convective term in the equation dominates the viscous one. Moreover, a compatibility condition (*inf-sup* or *LBB* condition) is required to control the pressure term. This condition does not allow to use equal order interpolations to approximate the velocity and pressure fields. This is certainly a problem because the use of equal order polynomials results in a much easier implementation of the numerical method as well as to the saving of computational time. On the other hand, further numerical instabilities are found when small time steps are used, specially at early stages of evolutionary processes. To circumvent all these difficulties that turn the Galerkin formulation (3.36) useless in practice, *stabilised* finite elements are required. In section

3.5 we will concentrate on Subgrid Scale (SGS) stabilised finite element methods, which provide a very powerful framework to address the above mentioned numerical problems.

Galerkin finite element approximation of the inhomogeneous Helmholtz equation

The discrete weak form corresponding to the Galerkin finite element approximation of (3.25) can be stated as follows: given a finite element partition of Ω_{ac} with ${n_e}'$ elements and ${n_p}'$ nodes, and the finite dimensional subspaces $\mathcal{W}_{h,0} \subset \mathcal{W}_0$, find $\hat{p}'_h \in \mathcal{W}_{h,0}$ such that

$$(\nabla \hat{p}'_h, \nabla w_h) - k^2 (\hat{p}'_h, w_h) - ik \langle \hat{p}'_h, w_h \rangle_{\Gamma_B} = \langle \hat{s}_h, w_h \rangle + \langle \hat{g}, w_h \rangle_{\Gamma_B} \tag{3.39}$$

for all $w_h \in \mathcal{W}_{h,0}$. Again,

$$\hat{p}'_h = \sum_{b=1}^{{n_p}'} N_p^b \hat{P}'^b \tag{3.40}$$

with N_p^b being the acoustic pressure shape functions and $\hat{P}'^b$ its nodal values.

The Galerkin weak form in (3.39) also presents numerical difficulties. The weak form becomes non-positive definite for large wavenumbers and it can be shown that the problem *inf-sup* constant presents an inverse dependence [163] with the wavenumber k. This leads to a loss of stability and to the appearance of the so-called *pollution* error for large values of k. A dispersion analysis shows that this error is related to the fact that discrete waves propagate with a discrete wavenumber $k_h \neq k$. The difference $k_h - k$ increases for large wavenumbers and a phase error appears in the numerically computed waves. SGS stabilised finite elements can also be used to address this problem as it will be outlined in next section and analysed in full detail in Chapter 5.

3.5 Subgrid Scale (SGS) stabilised finite element methods

3.5.1 Outline of the SGS stabilisation approach

In the past two decades, several stabilisation strategies have been developed to circumvent the numerical instabilities that arise in the Galerkin finite element solution of partial differential equations. We will concentrate here on the *Subgrid Scale* (SGS) approach (also termed *Variational Multiscale Method* (VMM) or *Residual-Based stabilisation*) originally developed by Hughes [150, 153] for the scalar convection-diffusion-reaction equation and latter extended to other equations by many authors. For the sake of clarity, the main ideas of the method will be first outlined for an abstract stationary variational problem and then explicitly presented in detail for problems (3.34)-(3.35) and (3.25) in subsequent sections.

Let us consider the abstract variational continuous problem of finding $y \in \mathcal{Y}$ such that

$$m\left(y, z\right) = n\left(z\right) \tag{3.41}$$

for all $z \in \mathcal{Z}$. m and n respectively represent (for simplicity) bilinear and linear continuous weak forms, while $\mathcal{Y}$ and $\mathcal{Z}$ are infinite dimensional spaces. The subgrid scale approach to find a numerical solution to (3.41) consists in first splitting $\mathcal{Y}$ and $\mathcal{Z}$ into $\mathcal{Y} = \mathcal{Y}_h \oplus \tilde{\mathcal{Y}}$ and $\mathcal{Z} = \mathcal{Z}_h \oplus \tilde{\mathcal{Z}}$. $\mathcal{Y}_h$ and $\mathcal{Z}_h$ stand for the finite dimensional spaces (discrete spaces) where the numerical solution belongs, while $\tilde{\mathcal{Y}}$ and $\tilde{\mathcal{Z}}$ represent infinite dimensional spaces (continuous spaces) to respectively complete $\mathcal{Y}_h$, $\mathcal{Z}_h$ in $\mathcal{Y}$ and $\mathcal{Z}$. Variables y and z can then be decomposed as $y = y_h + \tilde{y}$, $z = z_h + \tilde{z}$ and substituted in (3.41) to obtain

$$m\left(y_h, z_h\right) + m\left(\tilde{y}, z_h\right) = n\left(z_h\right) \quad \forall z_h \in \mathcal{Z}_h \tag{3.42}$$

$$m\left(y_h, \tilde{z}\right) + m\left(\tilde{y}, \tilde{z}\right) = n\left(\tilde{z}\right) \quad \forall \tilde{z} \in \tilde{\mathcal{Z}}. \tag{3.43}$$

Consequently, (3.41) has been transformed into two equations, (3.42) governing the dynamics of the resolvable "large" scales and (3.43) governing the dynamics of the "small" subgrid scales. The key idea consists in finding an approximate solution or model for the subscales equation, substitute it in the large scales equation and solve for them. In other words, the subgrid scale approach aims at simulating the influence of those small scales of the continuous problem, which cannot be captured by the numerical discretisation, onto the numerical solution. The influence of these small continuous scales is what is not taken into account in the Galerkin numerical approach to the problem.

Note that the separation between scales performed in the subgrid scale approach (3.42)-(3.43) is based on a projection onto the spaces $\mathcal{Z}_h$ and $\tilde{\mathcal{Z}}$, and that the modelling for the subscales is carried out once the problem has been already discretised.

3.5.2 A SGS stabilised finite element method for the Navier-Stokes equations

To apply the SGS stabilised finite element method to (3.34)-(3.35), we will decompose the velocity and velocity test functions as $\boldsymbol{u}^n = \boldsymbol{u}_h^n + \tilde{\boldsymbol{u}}^n$, $\boldsymbol{u}^{n+\alpha} = \boldsymbol{u}_h^{n+\alpha} + \tilde{\boldsymbol{u}}^{n+\alpha}$ and $\boldsymbol{v} = \boldsymbol{v}_h + \tilde{\boldsymbol{v}}$, which correspond to the space splitting $\mathcal{V}_0^d = \mathcal{V}_{h,0}^d \oplus \tilde{\mathcal{V}}_0^d$ and $\mathcal{V}^{d,n+\alpha} = \mathcal{V}_h^{d,n+\alpha} \oplus \tilde{\mathcal{V}}^{d,n+\alpha}$. For simplicity, it will be assumed that the velocity subscales will be zero at the element boundaries as well as on $\partial\Omega$. The former allows to understand the velocity subscales as bubble functions vanishing on interelement boundaries (see e.g., [47] and references therein). We will also decompose the pressure and pressure test function as $p^{n+1} = p_h^{n+1} + \tilde{p}^{n+1}$, $q = q_h + \tilde{q}$ corresponding to the space splitting $\mathcal{Q}_0 = \mathcal{Q}_{h,0} + \tilde{\mathcal{Q}}_0$.

Inserting the above decompositions in (3.34)-(3.35) yields a system of equations analogous to (3.42)-(3.43). The equation corresponding to the large scales (hence analogous to (3.42)) becomes, after integrating some terms by parts and neglecting terms

involving integrals over interelement boundaries [44, 47],

$$
\begin{aligned}
(\delta_t \boldsymbol{u}_h^n, \boldsymbol{v}_h) &+ \nu(\nabla \boldsymbol{u}_h^{n+\alpha}, \nabla \boldsymbol{v}_h) + \langle \boldsymbol{u}_h^{n+\alpha} \cdot \nabla \boldsymbol{u}_h^{n+\alpha}, \boldsymbol{v}_h \rangle \\
&- (p_h^{n+1}, \nabla \cdot \boldsymbol{v}_h) + (q_h, \nabla \cdot \boldsymbol{u}_h^{n+\alpha}) \\
&- \sum_{\Omega_e} \langle \tilde{\boldsymbol{u}}^{n+\alpha}, \nu \Delta \boldsymbol{v}_h + \boldsymbol{u}_h^{n+\alpha} \cdot \nabla \boldsymbol{v}_h + \nabla q_h \rangle_{\Omega_e} \\
&+ (\delta_t \tilde{\boldsymbol{u}}^n, \boldsymbol{v}_h) + \langle \tilde{\boldsymbol{u}}^{n+\alpha} \cdot \nabla \boldsymbol{u}_h^{n+\alpha}, \boldsymbol{v}_h \rangle \\
&- \langle \tilde{\boldsymbol{u}}^{n+\alpha}, \tilde{\boldsymbol{u}}^{n+\alpha} \cdot \nabla \boldsymbol{v}_h \rangle \\
&- (\tilde{p}^{n+1}, \nabla \cdot \boldsymbol{v}_h) = l(\boldsymbol{v}_h). \qquad (3.44)
\end{aligned}
$$

The first two lines of (3.44) contain the Galerkin terms previously found in (3.36). The third line corresponds to terms that are already obtained in the stabilisation of the linearised and stationary version of the Navier-Stokes equations [42, 43] (Oseen problem). It is well-known that the inclusion of these terms in the formulation allow to circumvent the convection instabilities described in section 3.3.3, and to use equal interpolations for the velocity and pressure fields. The fourth and fifth lines contain terms arising from the effects of the velocity subscales, $\tilde{\boldsymbol{u}}$, in the material derivative of the equation. The first term in the fourth line accounts for the time derivative of the subscales, while we will justify in section 3.4.3 that the second term provides global momentum conservation [47], which is not satisfied in the Galerkin finite element approach. The fifth line corresponds to a Reynolds stress for the subscales (note that $-\langle \tilde{\boldsymbol{u}}, \tilde{\boldsymbol{u}} \cdot \nabla \boldsymbol{v}_h \rangle = -\langle \tilde{\boldsymbol{u}} \otimes \tilde{\boldsymbol{u}}, \nabla \boldsymbol{v}_h \rangle$). It will be explained in section 3.4.3 that this term may be identified with the *direct* effects of the subscale turbulence onto the large scales [47]. Finally, the term in the sixth line accounts for the effects of the pressure subscales.

The key point of the formulation in (3.44) that distinguish it from the standard SGS approach (i.e., that has resulted in the appearance of the additional fourth and fifth lines in (3.44)) has been to keep all terms associated to the effects of the velocity subscales $\tilde{\boldsymbol{u}}$ in the material derivative of the exact velocity field. Effectively,

$$
\begin{aligned}
\frac{\mathrm{D}}{\mathrm{D}t}\boldsymbol{u} &= \frac{\mathrm{D}}{\mathrm{D}t}(\boldsymbol{u}_h + \tilde{\boldsymbol{u}}) \\
&= \partial_t \boldsymbol{u}_h + \partial_t \tilde{\boldsymbol{u}} + \tilde{\boldsymbol{u}} \cdot \nabla \boldsymbol{u}_h + \boldsymbol{u}_h \cdot \nabla \boldsymbol{u}_h + \tilde{\boldsymbol{u}} \cdot \nabla \tilde{\boldsymbol{u}} + \boldsymbol{u}_h \cdot \nabla \tilde{\boldsymbol{u}}. \qquad (3.45)
\end{aligned}
$$

Note that $\partial_t \boldsymbol{u}_h$ and $\boldsymbol{u}_h \cdot \nabla \boldsymbol{u}_h$ (once discretised in time) appear in the Galerkin formulation (3.36) and that the last term in (3.45) contributes to the standard SGS stabilisation in (3.44). The remaining terms $\partial_t \tilde{\boldsymbol{u}}$, $\tilde{\boldsymbol{u}} \cdot \nabla \boldsymbol{u}_h$ and $\tilde{\boldsymbol{u}} \cdot \nabla \tilde{\boldsymbol{u}}$ are the *new* terms respectively accounting for the time dependence of the velocity subscales, momentum conservation and the subscale Reynolds stresses. Given that we have written (3.45) prior to time discretisation, we note that with the above formulation time and space discretisation do commute (see [47] for details).

Our aim is to find now the solution $\boldsymbol{u}_h^{n+\alpha}$, $\tilde{\boldsymbol{u}}^{n+\alpha}$ and p_h^{n+1}, $\tilde{p}^{n+1}$ in (3.44), given $\boldsymbol{u}_h^n$, $\tilde{\boldsymbol{u}}^n$ and for all $\boldsymbol{v}_h \in \mathcal{V}_{h,0}^d$, $q_h \in \mathcal{Q}_{h,0}$. Obviously, to do so we first need a value for the subscales $\tilde{\boldsymbol{u}}^{n+\alpha}$, $\tilde{p}^{n+1}$ that has to be obtained from the solution of the small subgrid scales equation

of the problem (analogous to (3.43)). This equation can be written in differential form as [44, 47]

$$\delta_t \tilde{\boldsymbol{u}}^n + (\boldsymbol{u}_h^{n+\alpha} + \tilde{\boldsymbol{u}}^{n+\alpha}) \cdot \nabla \tilde{\boldsymbol{u}}^{n+\alpha} - \nu \Delta \tilde{\boldsymbol{u}}^{n+\alpha} + \nabla \tilde{p}^{n+1} = \boldsymbol{r}_{u,h}^{n+\alpha} \tag{3.46}$$

$$\nabla \cdot \tilde{\boldsymbol{u}}^{n+\alpha} = r_{p,h}^{n+\alpha}, \tag{3.47}$$

with $\boldsymbol{r}_{u,h}^{n+\alpha}$ and $r_{p,h}^{n+\alpha}$ representing residuals of the finite element components $\boldsymbol{u}_h$ and p_h given by

$$\boldsymbol{r}_{u,h}^{n+\alpha} = -\mathcal{P}[\delta_t \boldsymbol{u}_h^n + (\boldsymbol{u}_h^{n+\alpha} + \tilde{\boldsymbol{u}}^{n+\alpha}) \cdot \nabla \boldsymbol{u}_h^{n+\alpha} - \nu \Delta \boldsymbol{u}_h^{n+\alpha} + \nabla p_h - \boldsymbol{f}], \tag{3.48}$$

$$r_{p,h}^{n+\alpha} = -\mathcal{P}[\nabla \cdot \boldsymbol{u}_h^{n+\alpha}]. \tag{3.49}$$

Following [42, 44, 47] we will refer to the case $\mathcal{P} = \mathcal{I}$ (identity) as the *Algebraic Subgrid Scale* (ASGS) method, whereas $\mathcal{P} = \Pi_h^{\perp} = \mathcal{I} - \Pi_h$, Π_h standing for the L^2 projection onto the appropriate velocity or pressure finite element space, leads to the *Orthogonal Subscales stabilisation* (OSS) approach.

Using arguments based on a Fourier analysis for the subscales [44], the system of equations (3.46)-(3.47) can be approximated as

$$\delta_t \tilde{\boldsymbol{u}}^n + \frac{1}{\tau_1^{n+\alpha}} \tilde{\boldsymbol{u}}^{n+\alpha} = \boldsymbol{r}_{u,h}^{n+\alpha} \tag{3.50}$$

$$\frac{1}{\tau_2^{n+1}} \tilde{p}^{n+1} = r_{p,h}^{n+\alpha} + \tau_1 \delta_t r_{p,h}^n, \tag{3.51}$$

where the stabilisation parameters τ_1 and τ_2 have the expressions

$$\tau_1^{n+\alpha} = \left(c_1 \frac{\nu}{h^2} + c_2 \frac{\left| \boldsymbol{u}_h^{n+\alpha} + \tilde{\boldsymbol{u}}^{n+\alpha} \right|}{h} \right)^{-1} \tag{3.52}$$

$$\tau_2^{n+1} = \frac{h^2}{c_1 \tau_1^{n+1}} \,. \tag{3.53}$$

c_1 and c_2 in (3.52)-(3.53) are algorithmic parameters with recommended values of $c_1 = 4$ and $c_2 = 2$ for linear elements [41], while h stands for a characteristic mesh element size. From a physical point of view, the approximation (3.50)-(3.51) to problem (3.46)-(3.47) ensures that the kinetic energy of the modelled subscales resembles the kinetic energy of the exact subscales [43].

The advantages of tracking the subscales in time and the relation between the stabilisation parameter and the time step value are analysed in detail in [42, 47]. On the other hand, we note that the value for the time discretisation parameter α appearing in the equations for the subscales (3.50)-(3.51) does not have to necessarily coincide with the one used for the large scales equation (3.44). Actually, it is strongly recommended to use a first order time integration scheme for the subscales while using a higher-order scheme for the large scales. This is so because subscales will be highly discontinuous functions and a

more dissipative scheme is needed for them. Moreover, this approximation still keeps the same order of accuracy in time of the finite element solution. A formal argumentation of this point can be found in [46].

Equation (3.44) together with the subscales extracted from the solution of the approximated equations (3.50)-(3.51) with stabilisation parameters (3.52)-(3.53) constitute the methodology that will be used to solve the incompressible Navier-Stokes equations, even in the case of dealing with turbulent flows. In fact, this approach has been recently developed and presents several originalities and advantages when compared with other methods. Some of them will be commented in the next section. The reader is referred to [47] for further information on the subject.

3.5.3 Some physical properties of the formulation

In this section we will focus on the physical meaning of the two additional terms that have appeared in the formulation (3.44). It has been advanced that these terms play the role of conservation of momentum and of subscale turbulence (subscale Reynolds stresses). In order to see this and to simplify the notation, we will consider (3.44) prior to its time discretisation i.e., $\boldsymbol{u}, \tilde{\boldsymbol{u}}, p, \tilde{p}$ will be now time continuous functions and $\delta_t \varphi^n$ will be replaced by the time derivative $\partial_t \varphi$. Given that as mentioned, time and spatial discretisation commute in our formulation, this poses no problem at all.

Conservation of momentum

Let us start by analysing the effect of $\langle \tilde{\boldsymbol{u}} \cdot \nabla \boldsymbol{u}_h, \boldsymbol{v}_h \rangle$. The purpose of what follows is to present a version of the results in [161], simplified and adapted to the present setting.

Let $\mathcal{V}_h^d$ be the velocity finite element space without imposing the Dirichlet boundary conditions, that is, with degrees of freedom also associated to the boundary nodes. Let $\boldsymbol{t}$ be the stress vector (traction) on the boundary Γ and consider the following augmented problem instead of (3.44):

$$\begin{aligned}
&(\partial_t \boldsymbol{u}_h, \boldsymbol{v}_h) + \nu(\nabla \boldsymbol{u}_h, \nabla \boldsymbol{v}_h) + \langle \boldsymbol{u}_h \cdot \nabla \boldsymbol{u}_h, \boldsymbol{v}_h \rangle \\
&\quad - (p_h, \nabla \cdot \boldsymbol{v}_h) + (q_h, \nabla \cdot \boldsymbol{u}_h) - \langle \boldsymbol{v}_h, \boldsymbol{f} \rangle - \langle \boldsymbol{v}_h, \boldsymbol{t} \rangle_\Gamma \\
&\quad + (\partial_t \tilde{\boldsymbol{u}}, \boldsymbol{v}_h) + \langle \tilde{\boldsymbol{u}} \cdot \nabla \boldsymbol{u}_h, \boldsymbol{v}_h \rangle - \langle \tilde{\boldsymbol{u}}, \tilde{\boldsymbol{u}} \cdot \nabla \boldsymbol{v}_h \rangle \\
&\quad - \sum_K \langle \tilde{\boldsymbol{u}}, \nu \Delta \boldsymbol{v}_h + \boldsymbol{u}_h \cdot \nabla \boldsymbol{v}_h + \nabla q_h \rangle_K = 0,
\end{aligned} \tag{3.54}$$

where now $\boldsymbol{v}_h \in \mathcal{V}_h^d$ (not just $\mathcal{V}_{h,0}^d$). Considering $d = 3$ and taking for example $\boldsymbol{v}_h = (1, 0, 0)$ and $q_h = 0$, this equation yields

$$\begin{aligned}
&\int_\Omega \left[\partial_t (u_{h,1} + \tilde{u}_1) - u_{h,1} \nabla \cdot \boldsymbol{u}_h \right] d\Omega + \int_\Omega \tilde{\boldsymbol{u}} \cdot \nabla u_{h,1} d\Omega + \int_\Gamma u_{h,1} \boldsymbol{u}_n \cdot \boldsymbol{n} d\Gamma \\
&\qquad = \int_\Omega f_1 \, \mathrm{d}\Omega + \int_\Gamma t_1 d\Gamma,
\end{aligned} \tag{3.55}$$

where now the zero Dirichlet condition for the velocity is not explicitly required. This statement provides *global* momentum conservation if

$$-\int_\Omega u_{h,1}\nabla\cdot\boldsymbol{u}_h d\Omega+\int_\Omega\tilde{\boldsymbol{u}}\cdot\nabla u_{h,1}d\Omega=0. \tag{3.56}$$

This is implied by the continuity equation obtained by taking $\boldsymbol{v}_h=0$

$$(q_h,\nabla\cdot\boldsymbol{u}_h)-\sum_K\langle\tilde{\boldsymbol{u}},\nabla q_h\rangle_K=0, \tag{3.57}$$

provided $\mathcal{V}_h/\mathbb{R}\subseteq\mathcal{Q}_{h,0}$, that is to say, the velocity component $u_{h,1}$ belongs to the pressure space ($u_{h,1}$ can be considered modulo constants, since they do not affect neither the first nor the second terms in (3.56)). This holds, in particular, for the "natural" choice $\mathcal{V}_h/\mathbb{R}=\mathcal{Q}_{h,0}$, that is to say, equal velocity-pressure interpolations. For the standard Galerkin method, *this condition is impossible to be satisfied*, since equal interpolation does not satisfy the inf-sup condition. As a conclusion, *the term* $\langle\tilde{\boldsymbol{u}}\cdot\nabla\boldsymbol{u}_h,\boldsymbol{v}_h\rangle$ *provides global momentum conservation*, since without it in the discrete momentum equation, we would have obtained $-\int_\Omega u_{h,1}\nabla\cdot\boldsymbol{u}_h\,\mathrm{d}\Omega=0$ instead of (3.56), which is not implied by (3.57).

A door to turbulence

Let us made now some speculative comments on the possibility to simulate turbulent flows using the formulation in (3.44) and on the role of the remaining term $-\langle\tilde{\boldsymbol{u}},\tilde{\boldsymbol{u}}\cdot\nabla\boldsymbol{v}_h\rangle$. In the standard LES approach to solve turbulent flows (see sections 2.5.1 and 4.3.3, see also e.g., [255], [265]) an equation is obtained for the large, filtered scales of the flow, which we will denote with an overbar. This equation includes an extra term when compared with the incompressible Navier-Stokes equations (3.1)-(3.5): the divergence of the so-called *residual stress tensor* or *subgrid scale tensor* $\boldsymbol{\mathcal{R}}:=\overline{\boldsymbol{u}\otimes\boldsymbol{u}}-\bar{\boldsymbol{u}}\otimes\bar{\boldsymbol{u}}$. Tensor $\boldsymbol{\mathcal{R}}$ has to be modelled in terms of $\bar{\boldsymbol{u}}$ to obtain a self-contained equation, a problem known as the *closure problem*, and, once this is done, the resulting LES equation can be solved numerically.

The residual stress tensor, $\boldsymbol{\mathcal{R}}$, is often decomposed into the so-called Reynolds, Cross and Leonard stresses to keep the Galilean invariance of the original Navier-Stokes equation in the LES equation. This invariance is automatically inherited by the formulation presented above and we observe that analogous terms to the various stress types are recovered in a "natural" way from our pure numerical approach (this was also the case in [157]). Let us have a look at this point. We first consider the last four terms in the material derivative (3.45) as they appear in the variational equation (3.44). The term $-\langle\tilde{\boldsymbol{u}},\tilde{\boldsymbol{u}}\cdot\nabla\boldsymbol{v}_h\rangle$ can be rewritten as

$$-\langle\tilde{\boldsymbol{u}},\tilde{\boldsymbol{u}}\cdot\nabla\boldsymbol{v}_h\rangle=-\langle\tilde{\boldsymbol{u}}\otimes\tilde{\boldsymbol{u}},\nabla\boldsymbol{v}_h\rangle\qquad\text{(Reynolds stress)}, \tag{3.58}$$

while the addition of the other three terms becomes, after integration by parts,

$$\langle\boldsymbol{u}_h\cdot\nabla\boldsymbol{u}_h,\boldsymbol{v}_h\rangle-\langle\tilde{\boldsymbol{u}},\boldsymbol{u}_h\cdot\nabla\boldsymbol{v}_h\rangle+\langle\tilde{\boldsymbol{u}}\cdot\nabla\boldsymbol{u}_h,\boldsymbol{v}_h\rangle=$$

$$-\langle\boldsymbol{u}_h\otimes\boldsymbol{u}_h,\nabla\boldsymbol{v}_h\rangle\qquad\text{(Convection of the large scales)} \tag{3.59}$$

$$-\langle\boldsymbol{u}_h\otimes\tilde{\boldsymbol{u}}+\tilde{\boldsymbol{u}}\otimes\boldsymbol{u}_h,\nabla\boldsymbol{v}_h\rangle\qquad\text{(Cross stress)}, \tag{3.60}$$

If we now pay attention to the convective term of the residual in the subscale equation (3.50) and take, for simplicity, $\mathcal{P} = \mathcal{I}$, we observe that

$$\begin{aligned} &\langle (\boldsymbol{u}_h + \tilde{\boldsymbol{u}}) \cdot \nabla \boldsymbol{u}_h, \tilde{\boldsymbol{v}} \rangle = \\ &- \langle \boldsymbol{u}_h \otimes \boldsymbol{u}_h, \nabla \tilde{\boldsymbol{v}} \rangle \qquad \text{(Leonard stress)} \qquad (3.61) \\ &- \langle \boldsymbol{u}_h \otimes \tilde{\boldsymbol{u}}, \nabla \tilde{\boldsymbol{v}} \rangle. \qquad (3.62) \end{aligned}$$

Hence, we can effectively conclude that the modifications introduced by the presence of the divergence of $\boldsymbol{\mathcal{R}}$ in the LES equations are somehow automatically included in our subgrid scale stabilised finite element approach. So far we have given an interpretation to (3.59)-(3.62) as contributions from the Galerkin, stabilisation and conservation of momentum terms and also from the equation driving the dynamic evolution of the subscales (3.50). In the present formulation, the remaining Reynolds stress term, (3.58), is then considered to account for the *direct* subscale "turbulent effects" onto the large, resolvable, scales.

How good our formulation will work as a turbulent model will mainly depend on the validity of the approximation made to derive the evolution equation for the subscales (3.50), being the ASGS or the OSS methods two available possibilities. In order to check this performance, benchmark problems for turbulent flows should be used. The model should be able to reproduce the Kolmogorov energy cascade in the wavenumber Fourier space that displays an inertial range where $E(k,t) \sim C_K \varepsilon_{\text{mol}}^{2/3} k^{-5/3}$ (ε_{mol} being the energy dissipation rate, k the wavenumber modulus, C_K the Kolmogorov constant in energy space and E the kinetic energy, see e.g., [186, 232, 255]). Analogously , the pressure spectrum fulfills $E_{pp}(k,t) \sim C_P \varepsilon_{\text{mol}}^{4/3} k^{-7/3}$ ([9, 245] c.f. [203]). The model should be also able to capture the appropriate decay in time of the kinetic energy, the enstrophy and other related statistical variables. Other more intricate questions such as if the model allows for backscatter or if the dimension of the global attractor is properly reproduced could be also addressed. We remind that the heuristic estimate for this dimension is $\mathcal{N} \sim (L/\lambda_K)^3 \sim \text{Re}^{\frac{9}{4}}$ (where λ_K is the Kolmogorov length scale) and that the closest estimate analytically proved is (roughly) $(L/\lambda_K)^{4.8}$ (see [97]). Another standard test for turbulence is the turbulent channel flow. In this case the model should be able to approximate the turbulent boundary layer that, according to Prandtl theory, exhibits a log behavior after the laminar sublayer. Finally, we should mention that in an attempt to find a more mathematical foundation for the LES approach to turbulence, the concept of *suitable approximations* to the Navier-Stokes equations has been introduced in [112, 114], see sections 4.2.3 and 4.3.3. It is expected that approximate solutions converge (in a weak sense) to *suitable solutions*. This seems to be the case for low order finite elements and the *standard Galerkin method* [109]. Hopefully, the above presented *enhanced formulations* will have this property.

Let us conclude noting that the term $-\langle \tilde{\boldsymbol{u}}, \tilde{\boldsymbol{u}} \cdot \nabla \boldsymbol{v}_h \rangle$ has been identified with the *direct* contribution of the subscale turbulent effects onto the large scales. However, all terms involving the subscales are indirectly affected by the turbulence effects because the subscales are obtained from the non-linear equation (3.50) that involves (3.61)-(3.62). In fact, it is argued in [26] that $-\langle \tilde{\boldsymbol{u}}, \tilde{\boldsymbol{u}} \cdot \nabla \boldsymbol{v}_h \rangle$ has a little influence in the results. Let us

also mention that instead of using an expression of $\tilde{\boldsymbol{u}}$ in terms of the residual, turbulence modelling can be attempted by giving directly an expression of $\tilde{\boldsymbol{u}} \otimes \tilde{\boldsymbol{u}}$ in terms of $\boldsymbol{u}_h$ in the spirit of Smagorinsky's model (see [157] and also [104] for a review).

The possibility of using the SGS formulations as appropriate models for the simulation of turbulent flows will be the subject of Chapter 4. Although some numerical examples will be provided, the main effort will be placed in showing by means of heuristic reasoning, that this is precisely the right way to proceed, rather than performing physical LES modelling. Results of statistical fluid mechanics in combination with numerical developments will be used to do so.

3.5.4 A SGS stabilised finite element method for the inhomogeneous Helmholtz equation

We will now apply the SGS approach to solve the third step of the proposed CAA methodology, i.e. to solve the Helmholtz equation weak form (3.25). We will proceed as usual by performing the space splitting $\mathcal{W} = \mathcal{W}_h \oplus \tilde{\mathcal{W}}$, $\mathcal{W}_0 = \mathcal{W}_{h,0} \oplus \tilde{\mathcal{W}}_0$, which respectively allow the decompositions $\hat{p}' = \hat{p}'_h + \widetilde{\hat{p}'}$, $w = w_h + \tilde{w}$ for the acoustic pressure and test function. Substitution in (3.25) yields the large scale and small scale equations. The former is given by [39, 106]

$$\begin{aligned}(\nabla \hat{p}'_h, \nabla w_h) - k^2 (\hat{p}'_h, w_h) - ik (\hat{p}'_h, w_h)_{\Gamma_B} \\ + \sum_{\Omega_{el}} \langle \widetilde{\hat{p}'}, \nabla^2 w_h + k^2 w_h \rangle_{\Omega_{el}} \\ = \langle \hat{s}_h, w_h \rangle + (\hat{g}, w_h)_{\Gamma_B} ,\end{aligned} \tag{3.63}$$

where the first line contains the Galerkin terms already found in (3.39) and the second one accounts for the stabilisation terms that take into account the influence of the small scales into the large ones. The small scales can be approximated as (see e.g., [39, 106])

$$\widetilde{\hat{p}'} = \tau_{ac} r_{\hat{p}',h} = \tau_{ac} \left(-\nabla^2 \hat{p}'_h - k^2 \hat{p}'_h - \hat{s}_h \right). \tag{3.64}$$

The stabilisation parameter τ_{ac} can be obtained from a dispersion analysis. The stencil of (3.63), with (3.64) inserted in it, is considered for a particular mesh, e.g. a structured mesh of bilinear quadrilateral nodes. Then a plane wave solution is assumed at each node and a dispersion relation follows, from which a value for the stabilisation parameter can be derived. This procedure was applied in [106] to find τ_{ac} for the convected Helmholtz equation in two dimensions. For the case of zero Mach number flow, the parameter thus obtained reduces to minus the one found in [287] using the Galerkin least-squares (GLS) stabilised finite element method for the Helmholtz equation. τ_{ac} is given in this case by

$$\begin{aligned}\tau_{ac} &= -\frac{1}{k^2} + \frac{6}{k^4 h^2} \frac{(4 - f_x - f_y - 2 f_x f_y)}{(2 + f_x)(2 + f_y)}, \\ f_x &= \cos\left[k \cos(\theta) h\right], \\ f_y &= \cos\left[k \sin(\theta) h\right],\end{aligned} \tag{3.65}$$

where θ is the angle of propagation of the plane wave and h is the characteristic mesh element size. Eventhough the parameter τ_{ac} depends on the direction θ and on the particular mesh considered to derive it, numerical experiments [106, 287] show that the choice $\theta = 0$ provides stabilisation for a considerable variety of problems, involving waves propagating in many directions. Moreover, (3.65) can be also shown to provide stabilisation for non-structured meshes of quadrilateral and triangular elements [106].

Equation (3.63), together with the subscales in (3.64) and the stabilisation parameter from (3.65), clearly diminish the pollution error found in the Galerkin approximation to the problem and constitute the strategy adopted in this chapter to compute the acoustic field. Obviously, (3.65) limits the acoustic pressure computation to two-dimensional cases and a more general value for τ_{ac} should be found for full three dimensional problems.

In Chapter 5, the above questions are analysed in full detail and a general framework is given relating the Helmholtz and convected Helmholtz equations. A stabilisation SGS method is proposed for the latter [106].

3.6 Numerical examples

3.6.1 Aeolian tone generated by a single cylinder at $\mathrm{Re} = 500$

We consider the case of a two-dimensional cylinder with diameter D embedded in a flow with free stream velocity in Cartesian coordinates $(U_0, 0)$. We define the Reynolds number based on these variables as $\mathrm{Re} = \rho_0 U_0 D/\mu$, being ρ_0 the fluid density. When the Reynolds number is increased from low to large values, the solutions to the Navier-Stokes equations change their configuration following a process of symmetry breaking (bifurcations), until a fully developed turbulent flow is achieved at very high Reynolds numbers (see section 4.3.1).

We will concentrate here in the case where the flow looses its steadiness as well as its up-and-down symmetry and a wake of alternating vortices is formed behind the cylinder. The set of these shed vortices is known as the von Kármán vortex street. Vortex shedding induces lift fluctuations on the cylinder (drag fluctuations also occur although they are much smaller, see [102, 248] c.f. [145, 169]), which lead to the radiation of sound having a dipole pattern. The frequency of the radiated sound is the same as the vortex shedding frequency and is given by

$$f = \mathrm{S_t} \frac{U_0}{D} \tag{3.66}$$

where $\mathrm{S_t}$ is the Strouhal number that has a Reynolds number dependency [145]

$$\mathrm{S_t} = 0.198 \left(1 - \frac{19.7}{\mathrm{Re}}\right), \quad \mathrm{Re} \leq 5 \times 10^5. \tag{3.67}$$

The radiated sound is known as an aeolian tone. In practical cases the cylinder can often vibrate as a reaction to changes in lift. This motion tends to correlate the vortex

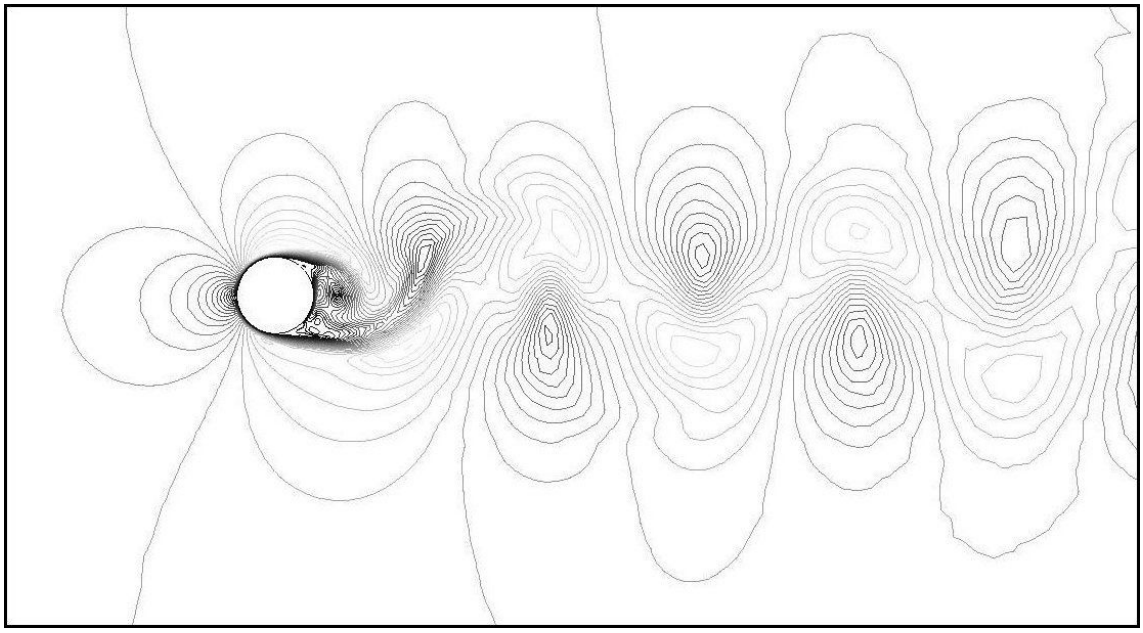

Figure 3.2: Von Kármán vortex street at the lee of the cylinder for Re = 500 (Isovelocity contourlines).

shedding along the length of the cylinder (three-dimensional case) resulting in a high level of radiated noise. If, in addition, the frequency of the vortex shedding coincides with a natural mode of vibration of the cylinder, the mechanism is further reinforced. This mechanism is responsible, for instance, of wire whistles in power transmission lines when wind is blowing and it is also of importance in other industrial problems such as the aerodynamic noise radiated by train pantographs, or by tubular heat exchangers.

For this first numerical example we have chosen a case corresponding to Re = 500. The two-dimensional incompressible Navier-Stokes equations have been solved using the methodology described in section 3.4.2, in an unstructured mesh of linear triangular elements ($n_e = 50\ 054$, $n_p = 25\ 636$). The mesh element size, h, ranges from $3 \times 10^{-3} D$ near the cylinder to $30D$ at the far field. The ASGS-NLTT (ASGS stabilisation with time tracking and all non-linear terms in the equations) described in section 3.4.2 has been used in the simulation. We remind that this approach allows to use equal interpolation for the velocity and the pressure. On the other hand, 10 Picard non-linearity iterations have been performed at each time step. The time step size used in the computation is $\delta t = 0.00025\ s$. A Crank-Nicolson scheme has been used for the large scales time evolution, while a first order scheme has been used for the tracking of the subscales.

The Strouhal number according to (3.67) is $\mathrm{S_t} \approx 0.19$. We have taken the values $D = 0.0049\ m$ and $U_0 = 1.512\ m/s$ so that the expected frequency from (3.66) is $f \approx 58.7\ Hz$.

As a result of the simulation, a periodic flow is established with a von Kármán vortex street developing at the lee of the cylinder (see Fig. 3.2). The lift and drag coefficients of

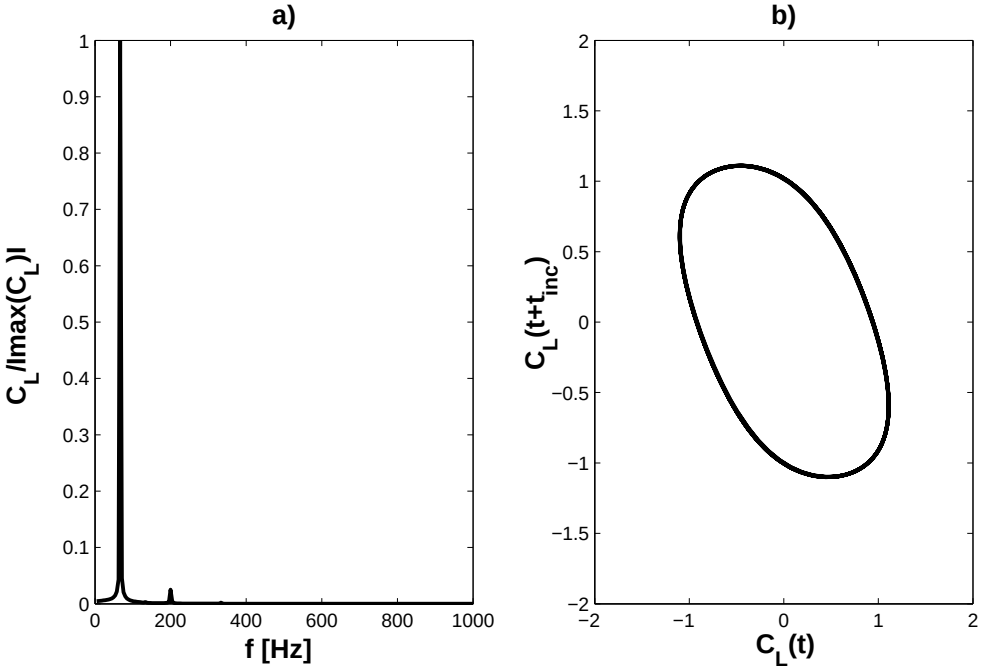

Figure 3.3: Re = 500. a) Normalized lift coefficient spectrum. b) Phase space limit cycle.

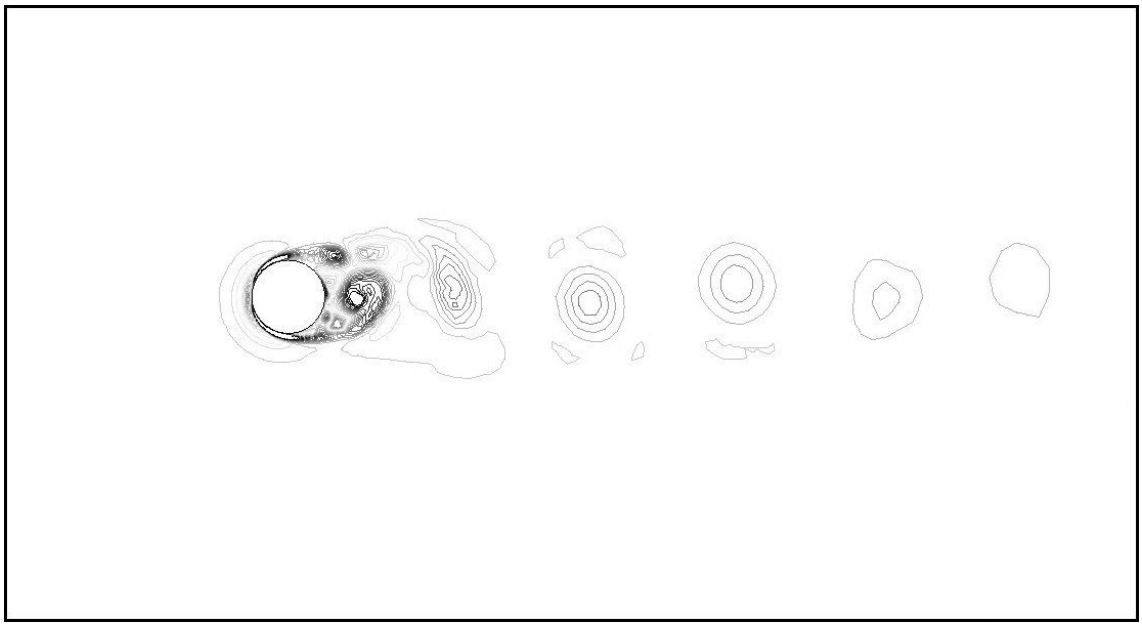

Figure 3.4: Acoustic source term: snaphshot of Reynolds tensor double divergence for Re = 500.

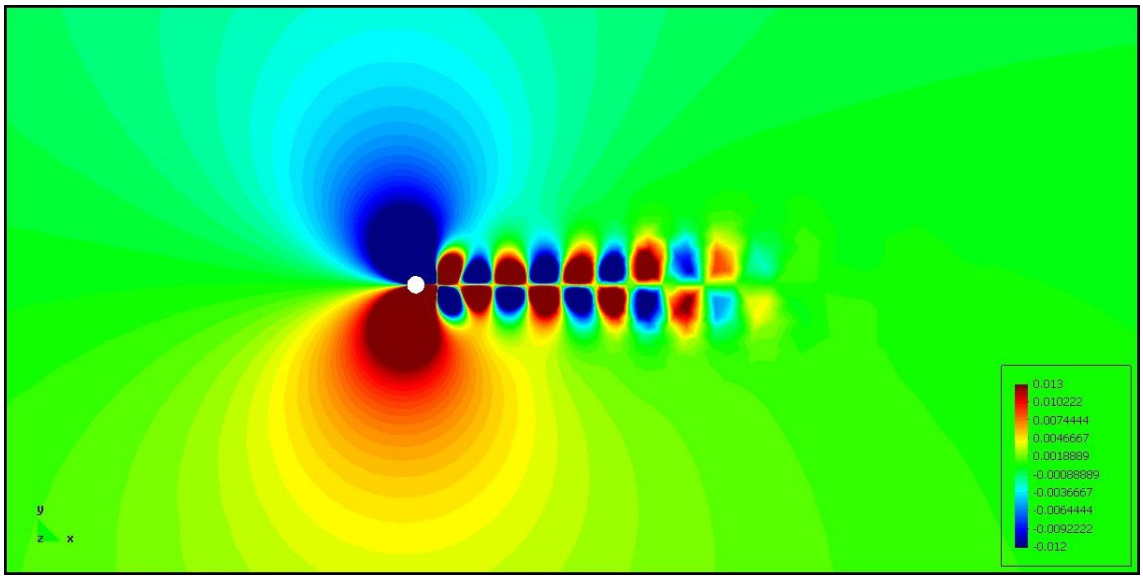

Figure 3.5: Dipole pattern of $Re\left(\hat{p}'_h\right)$ at $f = 66Hz$ for Re $= 500$.

the cylinder, C_L and C_D, have been computed and present a time sinusoidal behaviour. C_L has an amplitude of 1.1 and oscillates at the computed vortex shedding frequency of 66 Hz ($\mathrm{S_t} = 0.21$). The mean value for C_D is 1.39 with an amplitude of 0.12 and a frequency that is twice the vortex shedding one (132 Hz). The discrepancy between the computed frequency and the theoretical one is not strange if we take into account that (3.66)-(3.67) are valid for three dimensional flows and that 3D effects become apparent for Re > 300 (see Ref. [229]).

In Fig. 3.3a we have plotted the normalized spectrum of the lift coefficient. As expected, it only shows a single peak at $66Hz$. In Fig. 3.3b, we have presented a plot of $C_L\left(t\right)$ versus $C_L\left(t + t_{inc}\right)$ with $t_{inc} = 0.05\,s$. According to the Whitney-Takens theorem, the resulting graph is topologically equivalent to a phase space graph and we can observe that Fig. 3.3b effectively shows the characteristic limit cycle of a periodic dynamics.

In Fig. 3.4 a snapshot of the acoustic source term in (3.6), $s\left(\boldsymbol{x}, t\right) = \rho_0 \left(\nabla \otimes \boldsymbol{u}\right) : \left(\nabla \otimes \boldsymbol{u}\right)^{\top}$, is shown. This term rapidly decreases to zero when moving away from the cylinder. This fact is of crucial importance because it actually justifies the acoustic analogy approaches, which are based on a separation between an acoustic source region and a wave propagating one [53, 55].

The acoustic field has been computed according to the methodology described in section 3.4.4. In Fig. 3.5 the real part of the acoustic pressure, $Re\left(\hat{p}'_h\right)$, is plotted. Although some acoustic sources can be identified at the wake of the cylinder (see Fig. 3.4), the far field acoustic field is clearly dominated by the lift fluctuations on the cylinder, which generate outward propagating waves having a clear dipole pattern (see section 2.2.6).

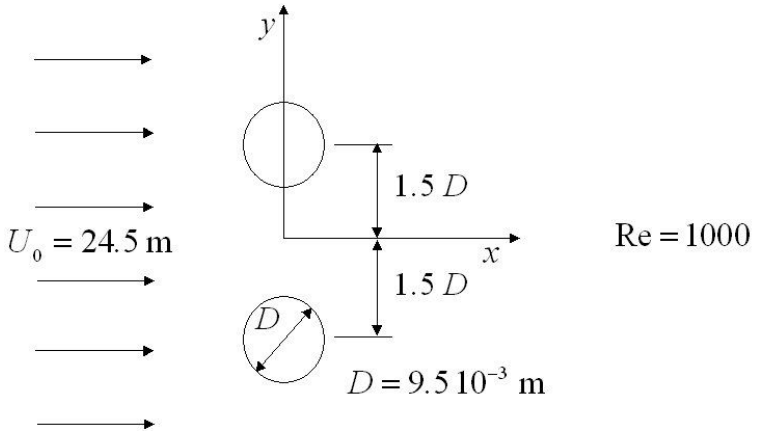

Figure 3.6: Aerodynamic noise generated by cylinders in parallel arrangement at Re = 1000.

3.6.2 Aerodynamic noise generated by parallel cylinders at Re = 1000

As a second numerical example, we address the computation of the aerodynamic sound generated by a viscous flow past two parallel cylinders, according to the configuration in Fig. 3.6. As observed in this figure, two cylinders of diameter $D = 9.5 \times 10^{-3}$ m are immersed in a flow moving at speed $U_0 = 24.5$ m. The characteristic Reynolds number of the problem is given by $\mathrm{Re} = \rho_0 U_0 D/\mu = 1000$. We will show that vortices are periodically shed behind the two cylinders. However, due to the fact that these vortices become antiphase from one cylinder to the other, the resulting acoustic field will considerably differ from the single cylinder case.

The CFD simulation has been performed in a structured mesh of $n_e = 51\ 485$ elements ($n_p = 51\ 881$ nodes) strongly refined at the cylinder boundaries. The squared computational domain has a diagonal of $\sim 1000D$. Again, the ASGS-NLTT stabilised finite element method has been used for the CFD calculation, with 10 Picard non-linearity iterations being performed at each time step. The time step size used in the computation is $\delta t = 0.00008$ s. A second order Crank-Nicolson scheme has been used for the large scales time evolution, while a first order scheme has been used for the tracking of the subscales.

Once the initial transients have been surpassed, an almost periodic flow is established with vortices being shed past both cylinders. The vortices are antiphase from one to the other i.e., when a vortex having positive vorticity detaches from the upper cylinder, an equal strength vortex detaches from the bottom cylinder having negative vorticity, and being located at a symmetric location with respect to the $x-$axis. This can be clearly observed in Figs. 3.7a and b where the isovorticity and isovelocity contours of the flow have been plotted. It is worthwhile to comment that although the wake sometimes looses its symmetry downstream as time evolves, the vortex shedding remains periodic and antiphase between both cylinders. This is no longer true for higher Reynolds numbers,

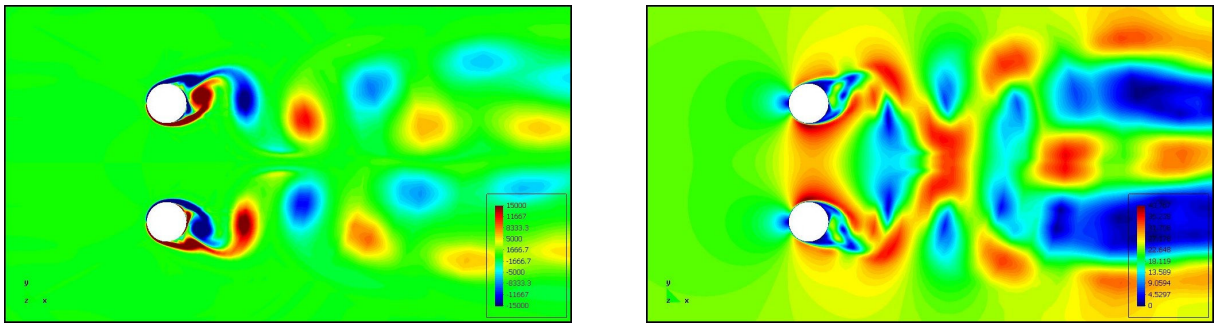

a) Isovorticity contours b) Isovelocity contours

Figure 3.7: Vortices shed behind two cylinders in parallel arrangement at Re = 1000. (Isovorticity and isovelocity contours)

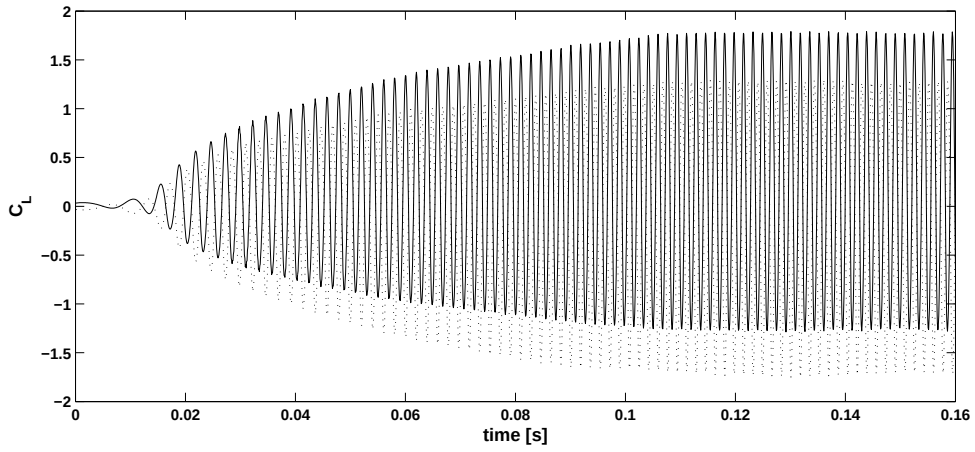

Figure 3.8: Time evolution of the cylinder lift coefficients. Continuous line: upper cylinder. Dotted line: bottom cylinder. Re = 1000.

where eventually the two cylinders can emit vortices in phase, although in the mean the shedding is antiphase.

In Fig. 3.8 we have plotted the time evolution for the lift coefficients C_{Lu} and C_{Lb} of the two cylinders. Once the flow is fully developed, their mean values are ~ 0.19 for the upper cylinder and ~ -0.19 for the one in the bottom. Their amplitudes are respectively ± 1.6. In what concerns the drag coefficients, they are obviously almost identical for both cylinders having a mean value of ~ 1.53 and an amplitude of ~ 0.23. In Figs. 3.9a and b we show the normalised spectra for the lift and drag coefficients of the upper cylinder. C_{Lu} presents a clear maximum at 588 Hz ($\mathrm{S_t} = 0.22$) to be compared with the values 500 Hz ($\mathrm{S_t} = 0.19$) arising from (3.66)-(3.67). The relative error has now increased when compared with the previous single cylinder numerical example probably for two reasons: first, the Reynolds number is now higher and second, equations (3.66)-(3.67) are intended for single cylinders whereas now the wake e.g., of the upper cylinder is clearly influenced by

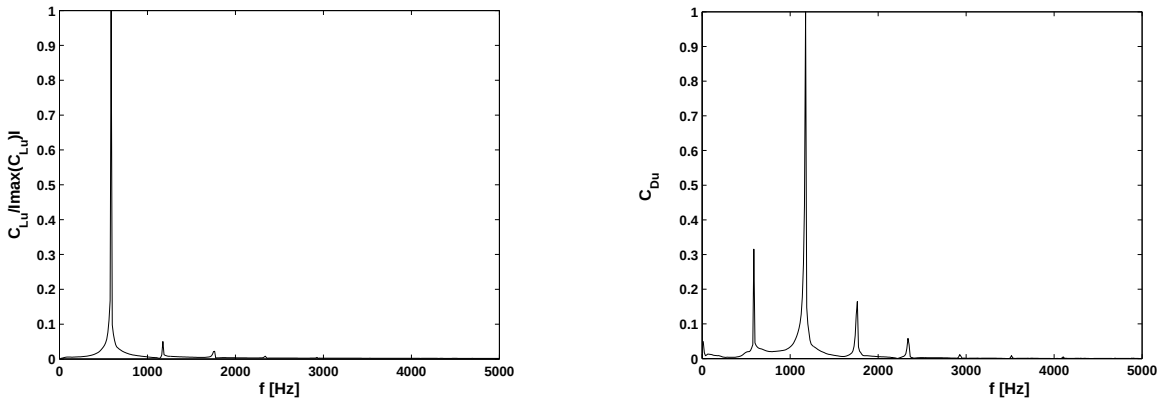

a) Lift coefficient b) Drag coefficient

Figure 3.9: Normalized lift and drag coefficient spectra for the upper cylinder. Re = 1000.

the wake of the bottom cylinder (see Fig. 3.7b). We actually do not know if the presence of the second cylinder may alter the vortex shedding frequency when comparing with an analogous single cylinder case, but it certainly increases the complexity of the simulation. On the other hand, note that the normalised spectrum for the drag coefficient in Fig. 3.9b presents the expected maximum at 1176 Hz (twice the lift coefficient frequency) but it also presents a first subharmonic (lift coefficient frequency), a first harmonic and the first harmonic of fractional order. It is obvious that the drag coefficient is harder to compute given that it has twice the lift coefficient frequency. However, for the present simulation it still has more than ten time steps per wavelength. The appearance of the "extra" frequencies in Fig. 3.9b is attributed to the fact that there is no perfect symmetry between the flow at the upper and bottom cylinders. In addition and as has been commented, the wake breaks downstream loosing also its symmetry. These facts can easily be responsible for the excitation of harmonics and subharmonics. Note that although the lift coefficient seems less affected by these questions, the second and third harmonics also insinuate in Fig. 3.9a.

In what concerns the acoustic field, it has again been computed using the procedure described in section 3.4.4. and using the same mesh intended for the CFD computation. In Fig. 3.10 we have plotted the real part of the acoustic pressure, $Re\,(\hat{p}'_h)$, for $f = 588\,Hz$. As seen in the figure, two dipole radiating patterns can be clearly identified at each cylinder corresponding to the lift fluctuations. A dipole pattern corresponding to the overall drag fluctuations is also present. While the drag dipole is negligible when compared to the lift dipole in the problem of aeolian tones generated by a single cylinder, it acquires a central importance in the present problem when analysing the far field acoustic field. This is due to the fact that the two lift dipoles tend to compensate each other radiating as a longitudinal quadrupole, which is known to be a less efficient radiator than the dipole of a single cylinder. On the contrary the cylinder drag dipoles tend to reinforce each other

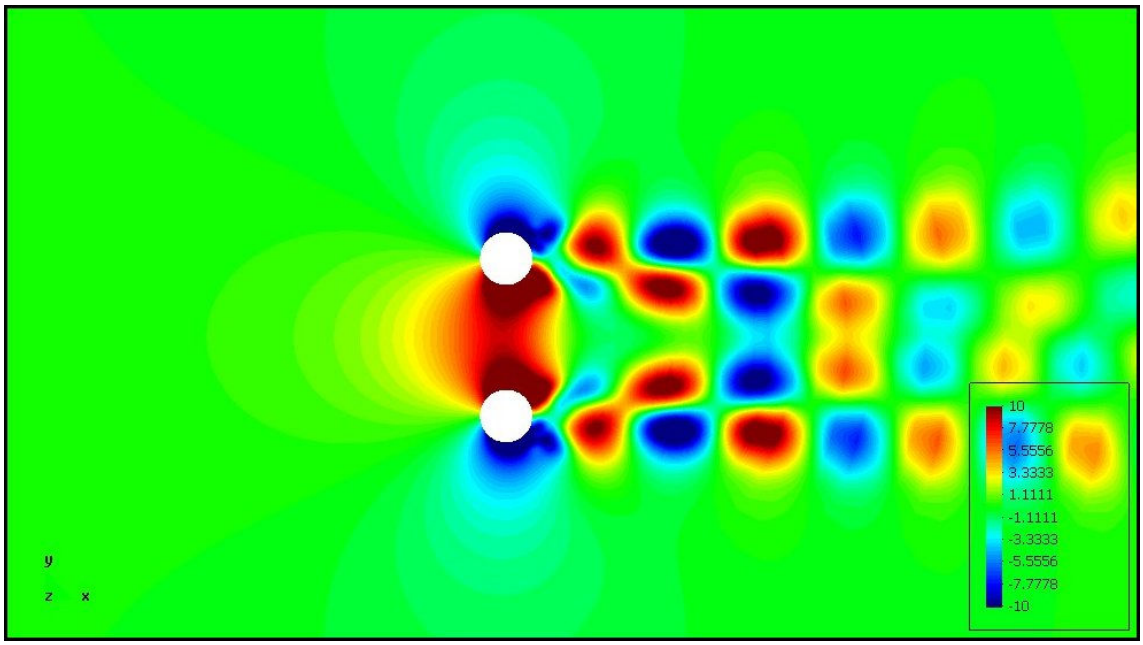

Figure 3.10: Acoustic near field. Cylinders in tandem arrangement at Re = 1000.

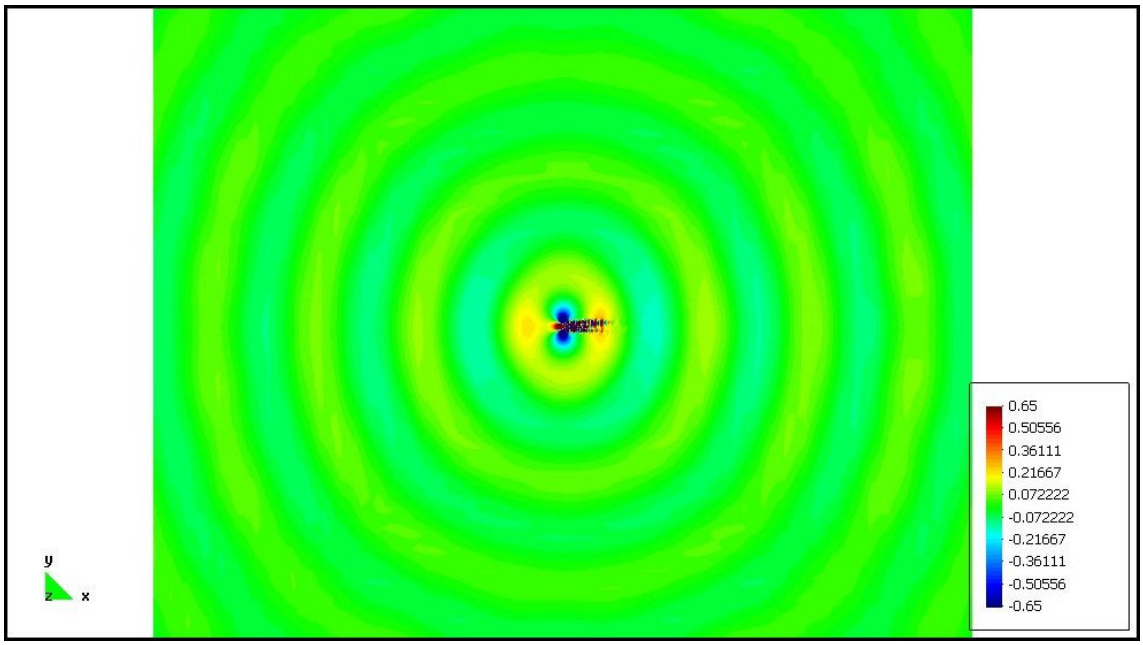

Figure 3.11: Acoustic far field. Cylinders in tandem arrangement at Re = 1000.

resulting in a stronger overall drag dipole. This situation can be observed in Fig. 3.11 where it becomes apparent that the waves generated by the drag dipole at $f = 588\ Hz$ are more intense than the ones generated by the overall lift dipole. It should be noted, however, that as long as the Reynolds number of the problem is increased the breaking of symmetry in the wake will become more important. As previously mentioned, the two cylinders can then eventually radiate in phase for some short periods of time, which will tend to reinforce the radiation of the overall lift dipole in front of the drag one. On the other hand, note that the wavelength of the acoustic waves in Fig. 3.11 have the expected value of $\lambda = c_0/f \sim 0.58$ m.

3.7 Conclusions

This chapter has been devoted to the presentation, development and numerical implementation of a three-step methodology to solve Computational Aeroacoustics (CAA) problems.

We have started by presenting the methodology main points and the initial and boundary value differential problems associated to it. Then, after setting up the functional framework that will be used throughout the thesis, we have stated the variational form of the two differential equations that need to be solved, namely the incompressible Navier-Stokes equation that accounts for the evolution of the aerodynamic field, and the inhomogeneous Helmholtz equation that accounts for the acoustic field. After discretising the first one in time, we have proceeded to both equations spatial discretisation using the Galerkin finite element method (FEM). The different numerical instabilities inherent to the Galerkin FEM approach to both problems have been commented and the Subgrid Scale (SGS) stabilised finite element strategy to avoid them has been introduced.

The SGS stabilisation methods are based on performing a scale splitting of the continuous variables into large scales, that can be resolved by the computational mesh and hence belong to the corresponding finite element space, and small scales that cannot be captured by the mesh, so that their influence onto the large scales has to be somehow modelled. Concerning the Navier-Stokes equations, a very recently developed SGS strategy has been implemented, one of its main features being that the subscales are tracked in time. Moreover, the method accounts for some interesting physical properties and may open a door to the simulation of turbulent flows without resorting to more classical Large Eddy Simulation (LES) approaches. This important issue will be analysed in detail in next chapter. In what refers to the inhomogeneous Helmholtz equation, a SGS strategy has been also implemented that coincides with the more classical Galerkin Least Squares (GLS) stabilisation method with appropriate redefinition of the stabilisation parameter. The later is often found in computational acoustics from a dispersion analysis. The extension of this procedure to the convected Helmholtz equation will be the subject of Chapter 5.

We have ended the chapter by showing that the proposed CAA methodology is able to properly reproduce the multipolar character of the acoustic field. To do so, two numerical

examples have been presented dealing with aeolian tones generated by flow past a single cylinder and with aerodynamic noise generated by flow past two cylinders in parallel arrangement. It has already been checked that the directivity and wavelength of the resulting acoustic fields have been correctly computed, showing the good possibilities of the proposed CAA approach.

Chapter 4

The aerodynamic field

In this chapter we will concentrate on the first step of the proposed methodology to perform computational aeroacoustics of low speed flows, namely the computational fluid dynamics step. Special emphasis will be placed on some aspects concerning the simulation of incompressible turbulent flows. First, some classical results of the existence theory of the Navier-Stokes equations will be reviewed as well as some aspects of the Kolmogorov theory for turbulent flows. Then, the Large Eddy Simulation (LES) computational approach will be presented and some of its drawbacks outlined. Analysing the energy balance equations of the Navier-Stokes and LES equations, as well as their Galerkin and Orthogonal Subgrid Scale (OSS) numerical approximations, it will be shown by means of heuristic reasoning that the use of LES models is in fact redundant, if an appropriate discretisation scheme of the Navier-Stokes equations is carried out. This will be the main result of the chapter, i.e., we will give support to the idea that a purely numerical approach should be followed in the simulation of turbulent flows. Some numerical tests reinforcing this option will be also included.

4.1 Introduction

As explained in Chapter 3, the proposed methodology to face CAA problems involves a first CFD simulation of unsteady and/or turbulent flows in order to find Lighthill's tensor (see Fig. 3.1 and section 3.2). Two parallel lines have been followed in the past years to simulate incompressible turbulent flows that can be of engineering interest. On one side, the drawbacks of RANS (Reynolds Averaged Navier-Stokes) models combined with the impossibility to perform DNS (Direct Numerical Simulation) computations for large Reynolds number problems led to the development of a somehow in-between approach, the LES (Large Eddy Simulation) strategy (see e.g. [265]). On the other side, the numerical problems that arise when trying to solve the discrete differential or weak versions of CDR (Convection-Diffusion-Reaction) equations have motivated the development of several stabilisation strategies to mitigate them. A landmark in the development of these stabilisation methods was the appearance of the *subgrid scale* (SGS) stabilisation approach or, as originally termed, the *variational multiscale* method (VMM),

in the framework of finite element methods [150, 153]. Both approaches, LES and SGS applied to fluid dynamics, share some features like being based on a scale decomposition of the continuous velocity and pressure fields of the Navier-Stokes equations. However, in the former case this scale separation is performed at the continuous level while in the latter it is inherently carried out in the discretisation process. The relation between both methods is not fully understood at present and it is not clear whether they should be used together or independently in the simulation of turbulent flows. In this chapter we will aim at giving some support to the idea that no LES physical model should be used if an appropriate discrete stabilisation scheme is implemented.

The key idea of LES is to perform an explicit computation of the large scales of motion of the flow, which depend on the flow geometry and inputs, while modelling the effects of the small scales (which are assumed to have a universal behaviour [186], c.f. e.g., [255]) on the large ones. LES was originally motivated by meteorological applications [211,272] but has been extended to a large variety of fields involving complex fluid dynamics problems such as astrophysics [27], or a large variety of engineering applications [126, 236, 273, 274, 291].

LES can be performed either in the physical domain or in the wavenumber domain. Only the former case will be considered here. The standard LES approach can be thought as consisting of four main steps (see [255] and also Fig. 4.1):

1. The definition of a filtering operation, usually by means of a convolution operator.
2. Filtering the Navier-Stokes equations, with the appearance of the divergence of the residual stress tensor, and non-commutability terms.
3. Solving the closure problem by modelling the residual stress tensor.
4. Finding a numerical solution of the closed filtered equations.

Let us expand these points in some detail:

1. The filtering operation in the first step is usually performed by means of a convolution of the velocity and pressure fields with a low pass filter operator, $\overline{(\cdot)} : v \longmapsto \overline{v}$, so that the decomposition $[\boldsymbol{u}, p\,] = [\overline{\boldsymbol{u}}, \overline{p}\,] + [\boldsymbol{u}', p']$ is obtained (see e.g., [201] cf. [255], [265]). $[\overline{\boldsymbol{u}}, \overline{p}\,]$ stands for the large, filtered, scales while $[\boldsymbol{u}', p']$ represent the small, residual, scales. The filtering operation can be either performed explicitly (specially in dynamic models) or implicitly assumed (e.g. in standard eddy-viscosity models such as the celebrated Smagorinsky model [272]). Several possibilities can be considered, including differential filters [90, 91] or the most widely implemented convolution with a box, sinc or Gaussian functions. A Taylor development of the convolution operations allows a differential interpretation of the filters, which yields simplified and local filtering operators [265].

   A filter is said to be homogeneous if its width does not depend on the spatial position, while it is inhomogeneous if it does so. As the filter width is related to

the mesh element width, filtering in non-structured meshes correspond to the latter case. Under these circumstances, the differentiation and the filtering operations do not commute. This has to be taken into account when filtering the Navier-Stokes equations. On the other hand, it is worthwhile to mention that implementing explicit filters has received since now little attention in the FEM framework (see [170, 283] for exceptions).

2. The second step of the LES approach consists in filtering the Navier-Stokes equations. As these equations are to be solved in a bounded domain and, in the most general case an unstructured mesh will be used, new terms will appear in the filtered equations. That is to say, filtering in the most general case not only leads to the appearance of the divergence of the so called *residual stress* tensor (arising from filtering the non-linear convective term) but to the appearance of two additional terms: the first one due to the non-commutability of the differential and filter operators and the second one due to the finiteness of the computational domain. These terms have been usually ignored since recently. In this sense see [81, 94, 96] for a complete derivation of the LES equations, [96, 289] for attempts in finding commutative filters and [64] for an analysis of the commutation error due to the domain finite size.

3. The closure problem i.e., finding a model for the residual stress tensor, $\boldsymbol{\mathcal{R}} := \overline{\boldsymbol{u} \otimes \boldsymbol{u}} - \overline{\boldsymbol{u}} \otimes \overline{\boldsymbol{u}}$, has been since nowadays the leitmotiv of LES research. $\boldsymbol{\mathcal{R}}$ can be rearranged in order to depend only on filtered variables [201] and to maintain some of the invariant properties (such as Galilean invariance) of the non-filtered equations [91, 275]. There exist a large amount of different closure models for the terms appearing in $\boldsymbol{\mathcal{R}}$ and only an overview of some of them will be cited here. Closure modelling can be divided in two general groups, namely functional modelling and structural modelling [265]. Functional modelling aims at simulating the energy transfer among the large and small scales. Hence it does not aim at modelling $\boldsymbol{\mathcal{R}}$ but rather its effects on the large scales. On the contrary, structural modelling aims at finding a model for $\boldsymbol{\mathcal{R}}$ usually by means of a formal series expansions, or the use of some scale similarity hypothesis [7, 225]. Mixed models (functional + structural) are frequently used too (see e.g., [29, 37]).

   The most celebrated functional model is, without any doubt, the Smagorinsky model [272]. However, this model suffers of some drawbacks, specially concerning its behaviour near walls and the fact that it does not allow backscatter (energy transfer in the opposite direction of the energy cascade, i.e., from the small scales to the large scales). The problem of backscatter has been addressed by means of the addition of white noise [33] (c.f. [255]) and by the development of dynamic models [28, 92, 212, 250, 255]. These models require an explicit filtering process and aim at finding an optimum local value for the so-called Smagorinsky constant. Some refinements have been given by the localised dynamic model [95] and the Lagrangian dynamic model [226].

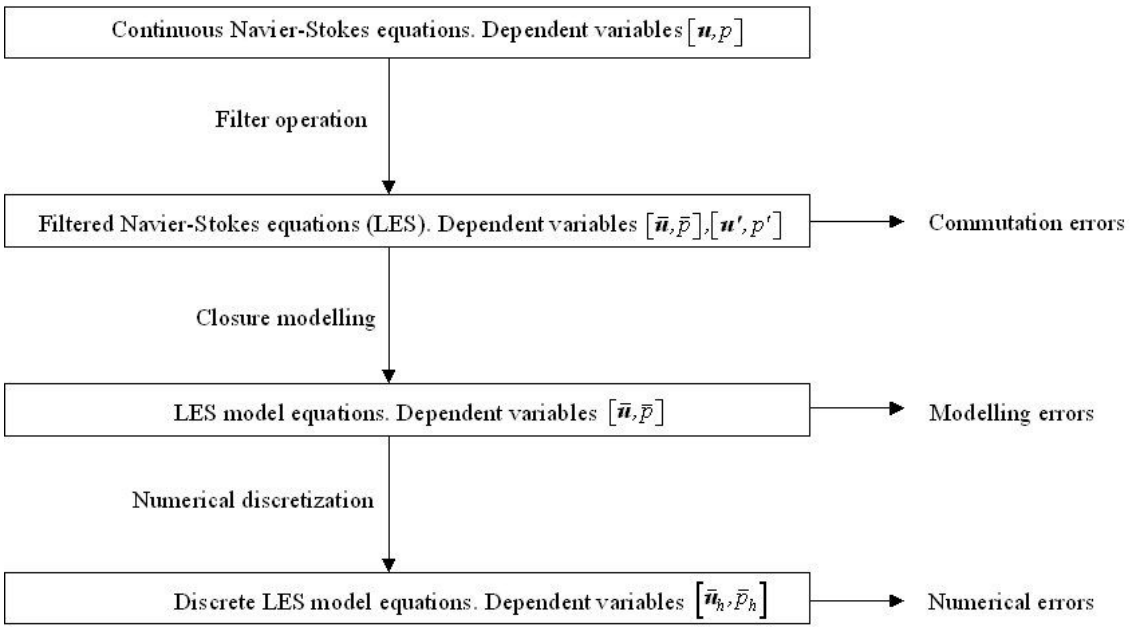

Figure 4.1: Scheme of LES approach to the Navier-Stokes equations.

In what concerns structural models, only reference will be made to those based on formal series expansions of the soft deconvolution problem [265, 277, 278]. The deconvolution approach aims at reconstructing the unfiltered field from the filtered one by inverting the filter operator (in fact an approximation to the inverse can only be achieved). Well-known models such as the gradient or Clark model [37] based on a Taylor series development of the filtered quantities can be embedded in this framework. Another model based on a subdiagonal Padé series development instead of a Taylor one is the rational LES model [16, 85]. A comparison between both methods can be found in [168].

4. The last step of LES consists in solving the filtered equations using a numerical method such as the finite difference method or the finite element method (remember that we concentrate here on LES in the physical domain). The simulations and testing of the closure models cited above are usually performed for simple geometry flows, which allow comparison with DNS simulations (see e.g., [234, 295]) and experimental data (see e.g., [30, 216, 224]). Isotropic turbulence is frequently used [82, 194] as well as plane and rotating turbulent channels [167, 250–252, 295] and wakes and jets [221, 247, 291].

A very detailed book dealing exclusively with LES is [265]. The subject is also treated extensively in [255] and some review papers on the subject are [204, 225, 231].

The above described standard approach to LES presents several difficulties that have motivated a more mathematical approach to the subject in recent years (see e.g. [196–198]). Some of these difficulties are such as evaluating the error introduced when

the commutation between the filtering and differentiation operators is assumed, knowing which should be the appropriate choice for the LES boundary conditions or knowing which should be the appropriate relation between the filter width and the mesh element characteristic size. In addition, and what is probably more important, one should be able to know which is the relation between the errors introduced by the physical LES model and by the numerical discretisation procedure.

Some of these subjects have been addressed both from an analytical (see e.g., [17,171]) and numerical point of view (see e.g., [35,93,185,200,283]). In [112] a review of several LES models was performed and some interesting conclusions were drawn out such as the fact that filtering is not indispensable to achieve LES models, that aiming at an exact closure for the residual stress tensor is a paradoxic program and that some LES models have the remarkable propriety of regularising the original Navier-Stokes equations, leading to well-posed problems. In this sense, it was concluded that a LES model should fulfil with two main requisites, namely, it should regularize the Navier-Stokes equations yielding to well posed problems and it should lead to *suitable* weak solutions (i.e., physically acceptable solutions). In an attempt to provide a first step towards a mathematical definition of LES, the notion of *suitable approximations* to the Navier-Stokes equations was then introduced in [114]. In this context, it is worthwhile to mention that a DNS using the Galerkin method with low order finite elements constitutes a suitable approximation to the Navier-Stokes equations, which may justify the fact that sometimes better results are achieved for low-order methods when no LES model is employed [109].

The second main research line that has very recently resulted in a plausible option to simulate turbulent flows initiated in the framework of stabilised finite element methods. As explained in Chapter 3, stabilised methods are needed to circumvent some of the numerical difficulties that arise when discretising a differential equation or its weak counterpart. The stabilisation procedure started with the work of Von Neumann [290] (c.f. [39]) who realised that the discrete version of the scalar convection-diffusion-reaction (CDR) equation was indeed infradiffusive. That is, the discrete version of the scalar CDR equation using a centred finite difference scheme corresponds to the continuous one with a lower coefficient of diffusion. To solve the problem, Von Neumann added some artificial extra diffusivity to the discrete equation. However, this sometimes resulted in an excessive diffusion. The procedure was improved in the beginning of the 80's [151, 178] by adding diffusion only along the streamlines. The results were less overdiffusive but in the FEM framework the approach was not consistent. This was so because the convective term of the equation was weighted with a modified test function, while the original one was used for the remaining terms. To achieve consistency all the terms in the weak form of the problem were finally weighted with the modified test function giving place to the final form of the SUPG (Stream-Upwind Petrov-Galerkin) method [23].

On the other hand, it was found in [154] that the pressure gradient in the Stokes problem could be viewed as a convective term. This made possible to apply the SUPG strategy to it and hence to avoid using different interpolations for the velocity and the pressure in order to satisfy the inf-sup condition. Initially, the velocity test function was perturbed with a term proportional to the gradient of the pressure test function but soon

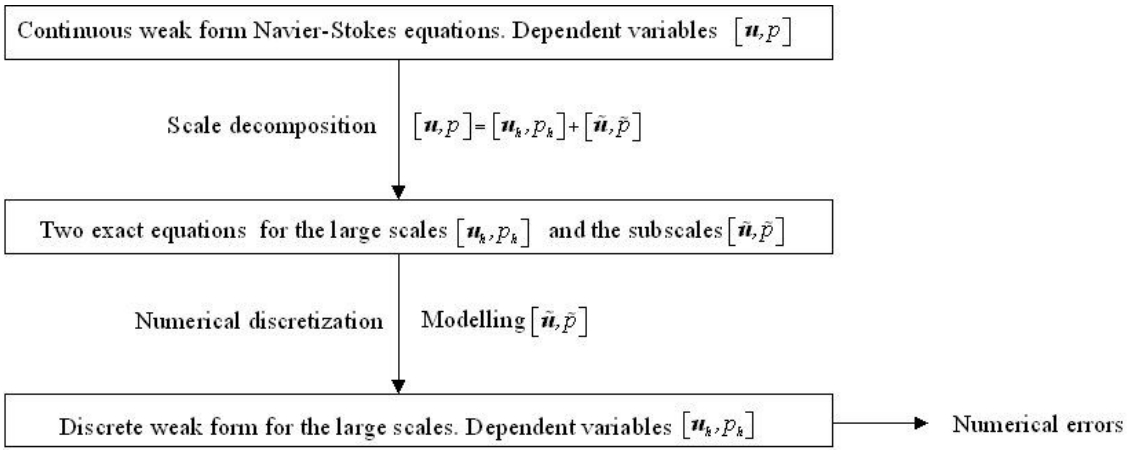

Figure 4.2: Scheme of the SGS or VMM approach to the Navier-Stokes equations.

the whole Stokes operator was applied to the test functions [78,155] (c.f. [39]), [156]. This yielded the Galerkin/Least-Squares (GLS) stabilising method, which is often used within a space-time FEM approach (see [39] and references therein).

A conceptually revolutionary approach to the stabilising procedure was the appearance of the Subgrid Scale (SGS) or Variational Multiscale (VMM) methodology that has been described in the previous chapter. As explained, the SGS approach ([149,150,153]) is based on a scale decomposition between scales that are resolvable by the mesh and unresolvable scales. This scale separation is done by means of a projection onto the finite element space. The original weak form of the problem becomes then split in two equations: one equation governs the dynamics of the subgrid scales and its solution has to be somehow modelled, while the second equation governs the dynamics of the resolvable scales and its solution can be numerically computed. The approximated solution to the first equation is introduced in the second equation in order to account for the effects of the subgrid scales on the resolvable ones.

The SGS approach gives a general framework where to place the stabilisation problem. Several well-known stabilised methods can be then embedded in this framework, their differences mainly depending on how the approximated solution for the subscale equation is found. The easiest solution for the subscales is obtained from an algebraic approach to them, which was first derived in [153] using an approximation to the Green's function for the subgrid equation. Several options are possible e.g., the use of bubble functions [76], or the orthogonal decomposition in [41, 42, 44].

Other stabilisation methods exist such as the Characteristic-Galerkin method (see [61,218,253] (c.f. [39]), [296]) suitable for scalar equations or the Taylor-Galerkin method [60] based on adapting the finite difference Lax-Wendroff scheme in the FEM framework. However, these methods will not be used in this work so no further details on them will be given.

It is worthwhile to remark that the final effect of almost all the stabilisation methods

cited above consists in the addition of a common type term in the discrete weak form of the problem. A complete comparison in the framework of the CDR equation is given in [39].

Let us focus now on the SGS or VMM approach. When first applied to the Navier-Stokes equations, its initial motivation was to solve some numerical problems such as the necessity to satisfy the *inf-sup* condition (which implies the use of different interpolation spaces for the velocity and pressure fields) or the numerical instabilities appearing for convective dominated flows. Consequently, when the SGS was first applied to the simulation of turbulent flows a physical LES model (Smagorinsky model [272]) was still included although solely acting on the subgrid scale equation [157–159] (see also [170,198]). The idea that the stabilisation terms in the SGS approach could be sufficient to simulate turbulent flows was pointed out in the framework of orthogonal subgrid scale (OSS) stabilisation methods [44] (see also [47]) as a natural extension to that work (see Fig. 4.2 for a general scheme to be compared with Fig. 4.1). This idea was later re-introduced in [26,160] and further elaborated in [152]. Very good results were obtained for transitional and fully developed turbulent flows in a channel giving support to the purely numerical approach to solve turbulent flows. Excellent results with the sole stabilisation approach can also be found in [12, 130, 266]. Actually, and as far as we know, this "numerical" line of thinking initiated with the MILES (Monotone Integrated LES) approach [20] c.f. [284] (see also [265] and references therein).

In this chapter a further argument supporting the non physical modelling approach will be given. An important point a closure LES model should satisfy is that the rate of kinetic energy transferred from the filtered large scales to the small ones should equal the physical dissipation rate at the Kolmogorov length scale (see e.g., [211,255]). This is so for the filter width lying in the inertial subrange of the flow under study. Considering the OSS stabilised finite element method [42–44], it will be herein shown that the contribution to the energy balance equation from the stabilisation terms that arise in the discrete weak Navier-Stokes from purely numerical considerations, is in fact already proportional to the physical dissipation rate (for a fine enough computational mesh so that its characteristic element size lies in the inertial subrange of the considered turbulent flow). Consequently, the inclusion of an extra physical LES model seems somewhat redundant and unnecessary.

The chapter is organized as follows. In section 4.2 we review some results of the classical mathematical theory of the Navier-Stokes equations. Some standard modifications of these equations for which uniqueness can be guaranteed are introduced. Section 4.3 is devoted to turbulent flows. The issues of transition and a brief overview of Kolmogorov's theory are presented. Standard LES as well as the notion of *suitable approximations* to the Navier-Stokes equations [112, 114] are reviewed. In section 4.4 the energy balance equations for the continuous Navier-Stokes and LES problems are presented together with their discrete counterparts using the Galerkin and OSS stabilised finite element methods. The main problem we would like to address in the chapter is established, and the OSS stabilisation terms accounting for the energy transfer to subscales that should be proportional to the physical dissipation rate are identified. In section 4.5 we proceed to the explicit discretisation of these terms, showing that their ensemble

average can be written as products of geometrical factors and two point second and fourth-order nodal velocity correlations, as well as triple-order velocity pressure correlations. In section 4.6, results from fluid statistical mechanics are used to relate these correlations to the physical dissipation rate. In section 4.7 some numerical simulations are provided and conclusions are finally drawn in section 4.8.

4.2 The Navier-Stokes equations

4.2.1 Problem statement

Strong or differential form

The mathematical problem we are facing is that of solving the incompressible Navier-Stokes equations for a flow in a bounded domain, $\Omega \subset \mathbb{R}^d$, $d = 2, 3$. As seen in section 3.2, these equations are obtained from the mass and momentum conservation equations assuming a constant density, ρ, and using the hypothesis of *Newtonian* fluid in the constitutive equation. This last equation relates the Cauchy stress tensor with the rate-of-strain tensor. The resulting equations are

$$\partial_t \boldsymbol{u} + \boldsymbol{u} \cdot \nabla \boldsymbol{u} - \nu \Delta \boldsymbol{u} + \nabla p = \boldsymbol{f} \quad \text{in} \quad \Omega \times (0, T) \tag{4.1}$$

$$\nabla \cdot \boldsymbol{u} = 0 \quad \text{in} \quad \Omega \times (0, T) \tag{4.2}$$

with $\boldsymbol{u}$ standing for the velocity vector, p for the pressure[1], ν is the kinematic viscosity and $\boldsymbol{f}$ represents the external force applied to the fluid. Equation (4.2) that corresponds to the continuity equation (mass conservation) is usually known as the *incompressibility constraint*. Equation (4.1) (momentum conservation) together with the constraint (4.2) shows a large variety of intricate solutions thanks to the presence of the non linear term $\boldsymbol{u} \cdot \nabla \boldsymbol{u}$. This results in very complex physics such as those exhibited by turbulent flows.

Equations (4.1) and (4.2) are to be complemented with appropriate boundary and initial conditions. In what follows we will limit to homogeneous Dirichlet conditions for the sake of simplicity. In case of the domain Ω being the cube $\mathcal{T} := (0, 2\pi)^d$, periodic conditions will be also addressed. Hence, we will consider

$$\boldsymbol{u}(\boldsymbol{x}, t) = 0 \quad \text{on} \quad \Gamma \equiv \partial\Omega \quad \text{Dirichlet conditions} \tag{4.3}$$

$$\boldsymbol{u}, p \text{ periodic} \quad \text{in} \quad \Omega = \mathcal{T} := (0, 2\pi)^d \quad \text{Periodic conditions} \tag{4.4}$$

$$\boldsymbol{u}(\boldsymbol{x}, 0) = \boldsymbol{u}_0(\boldsymbol{x}) \quad \text{on} \quad \Omega \quad \text{Initial conditions.} \tag{4.5}$$

The system of equations (4.1)-(4.2) together with the boundary conditions (4.3) or (4.4), and the initial condition (4.5) constitute the *classical* or *strong* formulation of

[1] Actually, for (4.1)-(4.2) the pressure satisfies the Poisson equation $\Delta p = -\rho \partial_j u_i \partial_i u_j$ at each time instant, which is a necessary and sufficient condition to fulfil the incompressibility constraint and determines ∇p with independence of the flow earliest evolution. In other words, at each instant of time the velocity field determines the pressure field.

the Navier-Stokes problem to be compared with the *weak* or *variational* formulation introduced in section 3.3.2. The latter will be next reviewed and some variations introduced.

Weak or variational form

Use will be made of the functional framework in section 3.2 to introduce the weak formulation of the Navier-Stokes problem. Moreover, we will also use some functional spaces incorporating the incompressibility constraint (4.2) and boundary conditions (4.3)-(4.4). Let $\boldsymbol{H}_0^1(\Omega)$ and $\boldsymbol{H}_{\text{per}}^1(\Omega)$ be subspaces of $\boldsymbol{H}^1(\Omega)$ that respectively satisfy the Dirichlet (4.3) and periodic (4.4) boundary conditions of the Navier-Stokes problem (4.1)-(4.2). We then define the functional spaces

$$\boldsymbol{X}(\Omega) := \begin{cases} \boldsymbol{H}_0^1(\Omega) & \text{for Dirichlet conditions} \\ \boldsymbol{H}_{\text{per}}^1(\Omega) & \text{for periodic conditions} \end{cases} \tag{4.6}$$

$$\boldsymbol{V}(\Omega) := \{\boldsymbol{u} \in \boldsymbol{X}(\Omega) | \nabla \cdot \boldsymbol{u} = 0\} \tag{4.7}$$

$$\boldsymbol{H}(\Omega) := \overline{\boldsymbol{V}}(\Omega)^{L^2} \quad (\text{Closure of } \boldsymbol{V}(\Omega) \text{ in } L^2(\Omega)). \tag{4.8}$$

We will also consider the space of infinitely differentiable d-dimensional functions of compact support in Ω, $\boldsymbol{C}_0^\infty(\Omega) \equiv (C_0^\infty(\Omega))^d$. Equipped with this space, we build the space of *test functions* $\mathcal{V} := \{\boldsymbol{v} \in \boldsymbol{C}_0^\infty(\Omega) | \nabla \cdot \boldsymbol{v} = 0\}$.

The weak formulation of the Navier-Stokes problem can be then obtained as usual by multiplying (4.1)-(4.2) by a test function and integrating over the whole domain Ω. After integrating by parts the viscous term, the weak problem can be formulated as: find $\boldsymbol{u}(\boldsymbol{x}, t) \in \boldsymbol{V}(\Omega)$ for every $t > 0$ such that

$$\frac{d}{dt}(\boldsymbol{u}, \boldsymbol{v}) + b(\boldsymbol{u}, \boldsymbol{u}, \boldsymbol{v}) + \nu(\nabla \boldsymbol{u}, \nabla \boldsymbol{v}) = \langle \boldsymbol{f}, \boldsymbol{v} \rangle, \ \forall \boldsymbol{v}(\boldsymbol{x}) \in \mathcal{V} \ (\text{or } \boldsymbol{V}(\Omega)), \tag{4.9}$$

in the distributional sense in $(0, T)$ or $(0, \infty)$ and with initial condition $\boldsymbol{u}(\boldsymbol{x}, 0) = \boldsymbol{u}_0(\boldsymbol{x})$. In (4.9), $b(\cdot, \cdot, \cdot)$ represents the trilinear form

$$b(\boldsymbol{u}, \boldsymbol{w}, \boldsymbol{v}) := \int_\Omega \boldsymbol{v} \cdot (\boldsymbol{u} \cdot \nabla \boldsymbol{w}) d\boldsymbol{x}. \tag{4.10}$$

Note that with this formulation the pressure is no longer an explicit variable of the problem so that $\boldsymbol{u}(\boldsymbol{x}, t)$ is required to directly satisfy the incompressibility constraint.

It is also possible to formulate the weak problem keeping the pressure as an explicit variable and giving the weak form of the incompressibility constraint, like it was done in section 3.3.2. Unfortunately, it is only known for the time behaviour of the pressure to exist in a distributional sense. However, in practice we may expect a more regular behaviour and, for instance, state the weak problem as that of finding $[\boldsymbol{u}(\boldsymbol{x}, t), p(\boldsymbol{x}, t)] \in L^2(0, T; \boldsymbol{X}(\Omega)) \times L^1(0, T; L^2(\Omega)/\mathbb{R})$ such that

$$\frac{d}{dt}(\boldsymbol{u}, \boldsymbol{v}) + b(\boldsymbol{u}, \boldsymbol{u}, \boldsymbol{v}) + \nu(\nabla \boldsymbol{u}, \nabla \boldsymbol{v}) - (p, \nabla \boldsymbol{v}) = \langle \boldsymbol{f}, \boldsymbol{v} \rangle, \tag{4.11}$$

$$(q, \nabla \boldsymbol{u}) = 0, \tag{4.12}$$

$\forall [\boldsymbol{v}(\boldsymbol{x}), q(\boldsymbol{x})] \in \boldsymbol{X}(\Omega) \times L^2(\Omega)/\mathbb{R}$ and satisfying the initial condition $\boldsymbol{u}(\boldsymbol{x}, 0) = \boldsymbol{u}_0(\boldsymbol{x})$ in the weak sense.

4.2.2 Existence and uniqueness theorems

The classical results on existence and uniqueness for the strong problem (4.1)-(4.2) and its weak version (4.9) in the three-dimensional case ($d = 3$) are given by the following two theorems (see e.g., [75, 285]):

Theorem 4.1 (Existence of weak solutions) *For any* $\boldsymbol{u}_0 \in \boldsymbol{H}(\Omega)$, $\boldsymbol{f} \in L^2\left(0, T; \boldsymbol{H}^{-1}(\Omega)\right)$ *and* $T > 0$, *problem (4.9) has at least one weak solution such that* $\boldsymbol{u}$,$\nabla \boldsymbol{u} \in \boldsymbol{L}^2(\Omega \times (0, T))$ *and* $\boldsymbol{u}$ *is weakly continuous from* $[0, T]$ *in* $\boldsymbol{H}(\Omega)$, *(i.e.,* $\forall \boldsymbol{v} \in \boldsymbol{H}(\Omega)$, $t \mapsto (\boldsymbol{u}(\boldsymbol{x}, t), \boldsymbol{v}(\boldsymbol{x}))$ *is a continuous scalar function) . Moreover, the following energy inequality is satisfied* (Leray's inequality)*:*

$$\frac{1}{2}\|\boldsymbol{u}(\boldsymbol{x}, t)\|_2^2 + \nu \int_0^t \|\nabla \boldsymbol{u}(\boldsymbol{x}, s)\|_2^2 \, ds \leq \frac{1}{2}\|\boldsymbol{u}(\boldsymbol{x}, 0)\|_2^2 + \int_0^t \langle \boldsymbol{f}(\boldsymbol{x}, s), \boldsymbol{u}(\boldsymbol{x}, s)\rangle ds, \qquad (4.13)$$

from which it turns out that $\boldsymbol{u} \in L^2(0, T; \boldsymbol{V}(\Omega)) \cap L^\infty(0, T; \boldsymbol{H}(\Omega))$.

Theorem 4.2 (Existence and uniqueness of classical or strong solutions) *For any* $\boldsymbol{u}_0 \in \boldsymbol{V}(\Omega)$, $\boldsymbol{f} \in L^2(0, T; \boldsymbol{H}(\Omega))$ *and* $T > 0$, *there exists* $T_*\,(0 < T_* < T)$, *depending on data* $(\Omega, \nu, \boldsymbol{f}, \boldsymbol{u}_0$ *and* $T)$, *such that there is a unique solution to problem (4.1)-(4.2) in the time interval* $[0, T_*)$ *that fulfils* $\boldsymbol{u}$, $\partial_t \boldsymbol{u}$, $\nabla \boldsymbol{u}$, $\nabla \cdot (\nabla \boldsymbol{u}) \in \boldsymbol{L}^2(\Omega \times (0, T))$ *with* $\boldsymbol{u}$ *continuous from* $[0, T_*)$ *in* $\boldsymbol{V}$.

The proof of existence and uniqueness of classical solutions in a finite time interval $[0, T_*)$ is due to Leray [202], who was the first to initiate the development of the mathematical theory of the Navier-Stokes equations. In his pioneering works, Leray also proved the existence of weak solutions in $\mathbb{R}^3$ [202]. In fact, he was the first one to introduce the concept of weak form of a partial differential equation long before the theory of distributions was built, or the functional framework of Sobolev spaces established. Leray's proof is based on the construction of approximated solutions to a modified Navier-Stokes equation where the convective term is convolved with a function of class $\boldsymbol{C}_0^\infty$ (see section 3.2 and section 4.2.4 below). Lately, Hopf [133] (c.f. [286]) made use of the Galerkin method to prove the existence of weak solutions in Ω bounded in $\mathbb{R}^3$.

Theorem 4.1 predicts the existence of weak solutions that fulfil the energy inequality (4.13). In fact, weak solutions that do not satisfy this inequality could exist and this is the reason why solutions that do comply (4.13) are often called Leray-Hopf weak solutions. As opposite, (4.13) becomes an equality for classical solutions. This point can be easily shown from direct manipulation of the differential Navier-Stokes equations and the result simply states the energy conservation in the fluid. It is worthwhile to mention that the convective term vanishes in the global energy balance. Its main role is that of being responsible for the energy transfer between eddies of different sizes (between modes in

the Fourier representation). We will come back to this point later on when describing Kolmogorov's theory on turbulent flows.

For flows in $\Omega \subseteq \mathbb{R}^2$ things are much more satisfactory than in the three-dimensional case. The problem is well-posed in the sense that existence and uniqueness of weak solutions and of classical solutions can be guaranteed for enough regular data. A physical explanation is at the core of these differences between the two and three-dimensional situations. If we take the curl of equation (4.1) and make use of some standard vector identities we can obtain an equation for the flow vorticity evolution, $\boldsymbol{\omega}$,

$$\partial_t \boldsymbol{\omega} + \boldsymbol{u} \cdot \nabla \boldsymbol{\omega} - \nu \Delta \boldsymbol{\omega} - \boldsymbol{\omega} \cdot \nabla \boldsymbol{u} = \nabla \times \boldsymbol{f} \quad \text{in} \quad \Omega \times (0,T)\,, \tag{4.14}$$

where the term $\boldsymbol{\omega} \cdot \nabla \boldsymbol{u}$ is responsible for the phenomenon of *vortex stretching*. In two dimensions this term identically vanishes whereas in three dimensions it acts as a vorticity amplifier. Making use of the so-called *ladder theorem* for the Navier-Stokes equations, it can be seen that it is precisely the presence of the vortex stretching term what precludes the possibility of finding a regularity proof in three dimensions [59].

The above presented theorems 4.1 and 4.2 together with their counterparts in two dimensions constitute the kernel of the classical theory of the Navier-Stokes equations. In this context two main problems are still to be solved: the uniqueness of weak solutions and the existence of classical solutions at any instant of time. The importance of these two questions has been reflected with their considerations as one of the seven "Millenium Problems" proposed by the Clay Mathematics Institute [235].

Several additional regularity results for the Navier-Stokes equations exist that are out of the scope of this presentation (the interested reader can find an extensive bibliography in [286]). In next section we will briefly outline some regularity results that are directly linked with the central subject of this chapter, namely the numerical simulation of turbulent flows using a LES or stabilised FEM approach.

4.2.3 Partial regularity and suitable solutions

Singularity set

Even though in its original work Leray already initiated the study of the size of the time singularity set of weak solutions, it was not until the 70's that Scheffer [268] proposed the study of the time-space singularity set of the solutions. It is said that $(\boldsymbol{x},t)$ is a *singular* point of the solution $\boldsymbol{u}(\boldsymbol{x},t)$ *iff*, $\boldsymbol{u}(\boldsymbol{x},t) \notin L^\infty(D)$ for any neighbourhood D of $(\boldsymbol{x},t)$ [25] (the remaining points are called *regular* points). Probably, Scheffer's most outstanding result was to prove that there exists a weak solution of (4.1) such that, under certain conditions, its set of singular points, $\mathcal{S}:= \{(\boldsymbol{x},t) \subset \Omega \times (0,T) \mid \boldsymbol{u}(\boldsymbol{x},t) \notin L^\infty(D)\, \forall\, D \,|\, (\boldsymbol{x},t) \in D\}$, satisfies $\mathcal{H}^{\frac{5}{3}}(\mathcal{S}) = 0$, where $\mathcal{H}^k$ denotes the k-dimensional Hausdorff measure[2]. We remind for completeness that the Hausdorff k-dimensional

[2]In fact Scheffer showed $D^{\frac{5}{3}}_{\mathcal{H}}(\mathcal{S}) < \infty$ but a minor modification of his arguments yields $D^{\frac{5}{3}}_{\mathcal{H}}(\mathcal{S}) = 0$ (see e.g., [79]).

measure of a set A is given by

$$\mathcal{H}^k(A) := \lim_{r \longrightarrow 0} \left(\inf \left\{ \sum_{n=1}^{N} r_n^k \middle| A \subset \cup_{n=1}^{N} B_n, \right. \right.$$
$$\left. \left. \text{with } B_n \text{ an open ball of radius } r_n \leq r \right\} \right). \tag{4.15}$$

(4.15) allows to define the Hausdorff dimension of A (which is one of the possible fractal dimensions) as

$$D_{\mathcal{H}}(A) := \inf \left\{ d > 0 | \, \mathcal{H}^d(A) = 0 \right\}. \tag{4.16}$$

Caffarelli, Kohn and Nirenberg [25] (see also [213]) improved Scheffer's results and obtained the best partial regularity result known up to date, $\mathcal{H}^1(\mathcal{S}) = 0$. In other words, the size of the set of singular points $\mathcal{S}$ of a weak solution of the Navier-Stokes equations has to be lower than the dimension of a smooth curve.

Dissipative or suitable solutions

Apart from hypotheses concerning the regularity of the initial conditions and the force datum, the main condition used in the proofs by Scheffer and Caffarelli *et al.* was the fulfilment of a local energy condition, which motivated the definition of *suitable* solutions to the Navier-Stokes equations [25, 268]. Consequently, the result $\mathcal{H}^1(\mathcal{S}) = 0$ is not valid for any weak solution but for those satisfying the following suitability condition (it has to be pointed out that very recently it has been shown [127] that $\mathcal{H}^1(\mathcal{S}) = 0$ is also valid for the more general Leray-Hopf weak solutions).

Definition 4.1 *A weak solution of the Navier-Stokes equations,* $[\boldsymbol{u}, p]$*, is* suitable *iff* $\boldsymbol{u} \in L^2(0,T;\boldsymbol{X}(\Omega)) \cap L^\infty\left(0,T;\boldsymbol{L}^2(\Omega)\right)$*,* $p \in L^{\frac{5}{4}}(\Omega \times (0,T))$ *and the following local energy inequality is satisfied in the distributional sense*

$$\partial_t \left(\frac{1}{2}\boldsymbol{u}^2 \right) + \nabla \cdot \left(\boldsymbol{u} \left(\frac{1}{2}\boldsymbol{u}^2 + p \right) \right) - \nu \Delta \left(\frac{1}{2}\boldsymbol{u}^2 \right) + \nu (\nabla \boldsymbol{u})^2 + \boldsymbol{f} \cdot \boldsymbol{u} \leq 0. \tag{4.17}$$

The proof of existence of suitable weak solutions to the Navier-Stokes equations in $\mathbb{R}^3$ and in a bounded domain $\Omega \subset \mathbb{R}^3$ can be respectively found in [268] and [25]. There is some hope that suitable solutions may play a relevant role in the resolution of the outstanding problem of uniqueness of weak solutions and blowing up at finite time of strong solutions. Although the relation among suitable, weak and classical solutions is not fully understood (Are suitable solutions unique? If this was the case, are they classical? Are Leray-Hopf weak solutions suitable?) it is expected that the former may help to distinguish *physically acceptable* solutions [63, 112, 114]. In this sense, Duchon and Robert [63] analysed the explicit form of the distribution $D(\boldsymbol{u})$ lacking in (4.17) to obtain

an equality. Making use of periodic boundary conditions and neglecting the force term for simplicity, they considered the local energy equation in the distribution sense

$$\partial_t \left(\frac{1}{2}\boldsymbol{u}^2\right) + \nabla \cdot \left(\boldsymbol{u}\left(\frac{1}{2}\boldsymbol{u}^2 + p\right)\right) - \nu\Delta\left(\frac{1}{2}\boldsymbol{u}^2\right) + \nu\left(\nabla\boldsymbol{u}\right)^2 + D\left(\boldsymbol{u}\right) = 0,$$

and observed that $D(\boldsymbol{u})$ vanishes for smooth enough flows but has a non trivial expression for non regular solutions. Hence, the lack of local kinetic energy conservation is not only due to viscous dissipation but also to the lack of regularity of the solution. Solutions $D(\boldsymbol{u}) \geq 0$ were considered *physically acceptable* as they do not allow local energy creation and they are termed *dissipative* solutions. Dissipative solutions coincide with the notion of suitable solutions introduced by Scheffer and Caffarelli *et al.*, and they are expected to be more regular than Leray-Hopf weak solutions, which fulfil the global energy inequality (4.13). This point seems to be confirmed by the fact that solutions of the regularised Navier-Stokes equations (e.g., Leray's convolution model in next section) satisfy $D(\boldsymbol{u}) \geq 0$.

Later on it will be shown that the notion of suitable solutions is at the basis of nowadays attempts to give a precise mathematical definition of LES. This relies on the notion of *suitable approximations* to the Navier-Stokes equations.

4.2.4 Looking for uniqueness: modification of the original equations

We could now question what should be done in order to guarantee uniqueness of the Navier-Stokes weak solutions so as to allow them to become a classical deterministic system. On one hand, we could wonder what should be proved to have a unique solution for equation (4.1) and, on the other hand, we could attempt at modifying the original equations to achieve uniqueness. The answer to the first query is rather amazing given that the difference between what has to be proved to achieve uniqueness and what has yet been proved seems very small. Unfortunately, this small difference remains unbeatable. For instance, using the ladder theorem for the Navier-Stokes equations, it can be checked that for (4.1) with periodic boundary conditions it would suffice to prove $\boldsymbol{u} \in L^2\left(0,T;\boldsymbol{H}^1_{\rm per}(\Omega)\right) \cap L^\infty\left(0,T;\boldsymbol{L}^{3+\varepsilon}(\Omega)\right)$ for ε as small as wanted [59]. However, what has been proved up to date is that $\boldsymbol{u} \in L^2(0,T;\boldsymbol{H}^1_{\rm per}(\Omega)) \cap L^\infty(0,T;\boldsymbol{L}^2(\Omega))$ (see Theorem 4.1). In the case of Dirichlet conditions in a bounded domain Ω it would be enough to see that $\boldsymbol{u} \in L^2\left(0,T;\boldsymbol{H}^1(\Omega)\right) \cap L^\infty\left(0,T;\boldsymbol{L}^4(\Omega)\right)$, or that $\boldsymbol{u} \in L^2\left(0,T;\boldsymbol{H}^2(\Omega)\right) \cap L^\infty\left(0,T;\boldsymbol{L}^2(\Omega)\right)$ (see e.g., [285]).

Concerning the second question, there exist several reguralisation techniques that yield modified Navier-Stokes equations with the advantage of having a unique and suitable weak solution. Probably, the most celebrated ones are Leray's convolution model, Lion's hyperviscosity model and the Ladyženskaja and Kaniel non-linear viscosity model that will be next presented.

Leray's convolution model. Leray [202] (see e.g., [114]) proposed a model consisting on a reguralisation of (4.1)-(4.2) by convolving the convective term with a non-negative,

infinitely differentiable function of compact support in $\mathbb{R}^3$. Let $B(\mathbf{0},\varepsilon)$ be the open ball of radius ε with centre at $\mathbf{0}$ and let ψ_ε be a function such that

$$\psi_\varepsilon \in C_0^\infty\left(\mathbb{R}^3\right),\ \operatorname{supp}(\psi_\varepsilon) \subset B(\mathbf{0},\varepsilon),\ \psi_\varepsilon > 0,$$
$$\int_\Omega \psi_\varepsilon(\boldsymbol{x})\, d\boldsymbol{x} = 1 \quad \text{and} \quad \psi_\varepsilon(\boldsymbol{x}) = \frac{1}{\varepsilon}\psi_\varepsilon\left(\frac{\boldsymbol{x}}{\varepsilon}\right).$$

Denoting with $*$ the convolution product, we have, $\psi_\varepsilon * \omega(\boldsymbol{x}) = \int_\Omega \psi_\varepsilon(\boldsymbol{x}-\boldsymbol{y})\,\omega(\boldsymbol{y})\, d\boldsymbol{y}$. For the tridimensional torus $\mathcal{T} = (0,2\pi)^3$, the reguralised model proposed by Leray can be written as

$$\left.\begin{array}{l} \partial_t \boldsymbol{u}_\varepsilon + (\psi_\varepsilon * \boldsymbol{u}_\varepsilon)\cdot\nabla\boldsymbol{u}_\varepsilon - \nu\Delta\boldsymbol{u}_\varepsilon + \nabla p_\varepsilon = \psi_\varepsilon * \boldsymbol{f} \\ \nabla\cdot\boldsymbol{u}_\varepsilon = 0 \\ \boldsymbol{u}_\varepsilon \ \text{ periodic} \\ \boldsymbol{u}_\varepsilon|_{t=0} = \psi_\varepsilon * \boldsymbol{u}_0. \end{array}\right\} \tag{4.18}$$

The following theorem is satisfied [114] (see also [63, 202]):

Theorem 4.3 *For any $\boldsymbol{u}_0 \in \boldsymbol{H}(\Omega)$, $\boldsymbol{f} \in \boldsymbol{H}(\Omega)$ and for every $\varepsilon > 0$, problem (4.18) has a unique solution in $\boldsymbol{C}^\infty(\Omega)$ for every t. The velocity is uniformly bounded in $L^2(0,T;\boldsymbol{V}(\Omega)) \cap L^\infty(0,T;\boldsymbol{H}(\Omega))$ and there exists a subsequence that converges weakly in $L^2(0,T;\boldsymbol{V}(\Omega))$. Moreover the limit of the solution for $\varepsilon \to 0$ is a suitable weak solution of the Navier-Stokes equations.*

The Lions hyperviscosity model. Lions [214, 215] (cf. [114]) proposed to alter the Navier-Stokes equations through the inclusion of an additional viscosity term and obtained

$$\left.\begin{array}{l} \partial_t \boldsymbol{u}_\varepsilon + \boldsymbol{u}_\varepsilon\cdot\nabla\boldsymbol{u}_\varepsilon - \nu\Delta\boldsymbol{u}_\varepsilon + \varepsilon^{2\alpha}(-\Delta)^\alpha \boldsymbol{u}_\varepsilon + \nabla p_\varepsilon = \boldsymbol{f} \quad \text{in} \quad \Omega\times(0,T) \\ \nabla\cdot\boldsymbol{u}_\varepsilon = 0 \quad \text{in} \quad \Omega\times(0,T) \\ \boldsymbol{u}_\varepsilon|_\Gamma = 0,\ \partial_{\boldsymbol{n}}\boldsymbol{u}_\varepsilon|_\Gamma = 0,\ \partial_{\boldsymbol{n}}^{\alpha-1}\boldsymbol{u}_\varepsilon\big|_\Gamma = 0 \quad \text{or} \quad \boldsymbol{u}_\varepsilon \ \text{ periodic} \\ \boldsymbol{u}_\varepsilon|_{t=0} = \boldsymbol{u}_0. \end{array}\right\} \tag{4.19}$$

The following theorem is then fulfilled [114] (see also [113, 214, 215]):

Theorem 4.4 *Consider $\boldsymbol{f} \in L^2(0,T;\boldsymbol{V}(\Omega))$ and $\boldsymbol{u}_0 \in \boldsymbol{H}^\alpha(\Omega)\cap\boldsymbol{X}(\Omega)$. Then, problem (4.19) has a unique solution $\boldsymbol{u}_\varepsilon \in L^\infty(0,T;\boldsymbol{H}^\alpha(\Omega)\cap\boldsymbol{X}(\Omega))$ for any $T>0$ if $\alpha \geq \frac{d+2}{4}$. Moreover, there exists a subsequence such that $\boldsymbol{u}_\varepsilon$ weakly converges towards a weak solution $\boldsymbol{u}$ of (4.1) in $L^2(0,T;\boldsymbol{X}(\Omega))$. For periodic boundary conditions the solution is suitable.*

The Ladyženskaja and Kaniel non-linear viscosity model Ladyženskaja and Kaniel ([175, 190, 191], cf. [114]) proposed to reguralise the Navier-Stokes equations using a non-linear viscosity term in contrast with the hypothesis of Newtonian fluid, in order to deal with large velocity gradients.

Let $\boldsymbol{T} : \mathbb{R}^3\times\mathbb{R}^3 \longrightarrow \mathbb{R}^3\times\mathbb{R}^3$ be a tensor function satisfying the next conditions

a) $\boldsymbol{T}$ is continuous and there exists $\mu \geq \frac{1}{4}$ such that $\forall \boldsymbol{\xi} \in \mathbb{R}^3\times\mathbb{R}^3$ it follows $|\boldsymbol{T}(\boldsymbol{\xi})| \leq c\left(1+|\boldsymbol{\xi}|^{2\mu}\right)|\boldsymbol{\xi}|$.

b) $\boldsymbol{T}$ is coercive in the sense that $\forall \boldsymbol{\xi} \in \mathbb{R}^3 \times \mathbb{R}^3$ it follows $\boldsymbol{T}(\boldsymbol{\xi}) : \boldsymbol{\xi} \geq c\,|\boldsymbol{\xi}|^2\,(1 + c'\,|\boldsymbol{\xi}|^{2\mu})$, where : stands for the double contraction of two tensors.

c) $\boldsymbol{T}$ has the following monocity propriety: there exists a constant $c > 0$ such that for any solenoidal vector fields $\boldsymbol{\xi}$, $\boldsymbol{\eta} \in W^{1,2+2\mu}(\Omega)$ having identical or periodic conditions on Γ, it holds

$$\int_\Omega \left(\boldsymbol{T}\left(\nabla\boldsymbol{\xi}\right) - \boldsymbol{T}\left(\nabla\boldsymbol{\eta}\right)\right) : \left(\nabla\boldsymbol{\xi} - \nabla\boldsymbol{\eta}\right) \geq c \int_\Omega \left|\nabla\boldsymbol{\xi} - \nabla\boldsymbol{\eta}\right|^2 .$$

An explicit expression for the tensor $\boldsymbol{T}$ that fulfils the above conditions is given by

$$\boldsymbol{T}\left(\boldsymbol{\xi}\right) = \beta\left(\left|\boldsymbol{\xi}\right|^2\right)\boldsymbol{\xi} \tag{4.20}$$

with $\beta\left(\tau\right)$ being a monotonically growing function of $\tau \geq 0$, such that for large τ values satisfies $c\tau^\mu \leq \beta\left(\tau\right) \leq c'\tau^\mu$ for $\mu \geq \frac{1}{4}$ and $c, c' > 0$.

The Ladyženskaja and Kaniel model is obtained taking $\boldsymbol{\xi} = \nabla\boldsymbol{u}$ in (4.20) and including tensor $\boldsymbol{T}\left(\nabla\boldsymbol{u}\right)$ in the viscous term. We get (see [114, 190, 191] and [175]):

$$\left.\begin{array}{l} \partial_t \boldsymbol{u}_\varepsilon + \boldsymbol{u}_\varepsilon \cdot \nabla\boldsymbol{u}_\varepsilon - \left(\nu + \varepsilon^{2\mu+1}\beta\left(\left|\nabla\boldsymbol{u}_\varepsilon\right|^2\right)\right)\Delta\boldsymbol{u}_\varepsilon + \nabla p_\varepsilon = \boldsymbol{f} \\ \nabla \cdot \boldsymbol{u}_\varepsilon = 0 \\ \boldsymbol{u}_\varepsilon|_\Gamma = 0 \quad \text{o} \quad \boldsymbol{u}_\varepsilon \ \text{ periodic} \\ \boldsymbol{u}_\varepsilon|_{t=0} = \boldsymbol{u}_0. \end{array}\right\} \tag{4.21}$$

Theorem 4.5 *Consider $\boldsymbol{f} \in L^2\left(0, \infty; \boldsymbol{L}^2\left(\Omega\right)\right)$ and $\boldsymbol{u}_0 \in \boldsymbol{H}(\Omega)$. If the above conditions a), b) and c) are satisfied, problem (4.21) has a unique weak solution for every $T > 0$ in $L^{2+2\mu}\left(]0, T[\,; \boldsymbol{W}^{1,2+2\mu}(\Omega) \cap \boldsymbol{V}(\Omega)\right) \cap C^0\left([0, T]\,; \boldsymbol{H}(\Omega)\right)$. In the case of periodic boundary conditions there exists a subsequence such that $(\boldsymbol{u}_\varepsilon, p_\varepsilon)$ tends towards a suitable solution of (4.1).*

In summary, we have seen from the above three examples that slight modifications of the original equations (4.1)-(4.2) yield unique and suitable solutions (with some restrictions on the data regularity as seen from theorems 4.3, 4.4 and 4.5). This can be achieved either by "smoothing" the convective term, by including a hyperviscosity term or by using a non-linear viscosity. This fact has posed some doubts on the validity of the Navier-Stokes equations as a model to describe turbulent flows. Does any of the above modified equations account for a better description? Although this is a possibility to consider, there is a certain general agreement that this it is not the case. Effectively, it is nowadays believed that the original Navier-Stokes equations suffice to account for all flow physical phenomena, including turbulence.

4.3 Turbulence and Large Eddy Simulation

4.3.1 Transition to turbulence: dependence with Re

We have previously commented that the Navier-Stokes equations have a large variety of complex solutions and we have just seen that it is nowadays agreed that they suffice to

describe all fluid intricate behaviour, including the phenomenology of turbulent flows. The process by which a dynamical system such as (4.1) transitions from a simple solution (e.g., the laminar flow over a body) to a complex solution (e.g., the turbulent flow over the body) is qualitatively described by the *bifurcation theory*. We will briefly describe by means of an example how this process works.

Dimensionless equations

First of all, and for the sake of simplicity, we will write the Navier-Stokes equations in dimensionless form. Being respectively U_0 and L a characteristic problem velocity and length, the independent dimensionless position $\boldsymbol{x}' = \boldsymbol{x}/L$ and time $t' = U_0 t/L$ can be defined. Moreover, we can also define the dependent dimensionless velocity $\boldsymbol{u}'(\boldsymbol{x}, t) = \boldsymbol{u}(\boldsymbol{x}, t)/U_0$ and pressure $p'(\boldsymbol{x}, t) = p(\boldsymbol{x}, t)/(\rho U_0^2)$. Substituting them in (4.1) yields

$$\partial_t \boldsymbol{u}' + \boldsymbol{u}' \cdot \nabla \boldsymbol{u}' - \frac{1}{\mathrm{Re}} \Delta \boldsymbol{u} + \nabla p' = \boldsymbol{f}' \quad \text{a} \quad \Omega \times (0, T), \tag{4.22}$$

where $\mathrm{Re} := U_0 L/\nu$ is the Reynolds number, which as known expresses when a flow is dominated by convection (large Re) o by viscosity (small Re). The Reynolds number states the relative significance between the inertial and the viscous terms in (4.22).

Note that with the above procedure we have just simplified the parametric dependence of the Navier-Stokes equations to a single parameter dependence, Re. Consequently, flows with different combinations of U_0, L i ν but equal Re will behave identically. This propriety is referred to as Reynolds number *similarity*.

Stability and Reynolds number

The nature of system (4.22) solutions varies depending on Re. For values of the Reynolds number in certain intervals, the solutions do not significantly change when Re is slightly modified. In such cases the system (4.22) is said to be *structurally stable*. However, for some values of Re this is no longer valid and substantial changes occur. The system becomes *structurally unstable* and *bifurcates*. Without getting into technical details, we will describe how a flow can transition from a laminar to a turbulent state through a process of successive bifurcations using a simple example.

We consider the case already addressed in chapter 3 of flow past a circular cylinder [62]. For $\mathrm{Re} \approx 0$ we have a Stokes flow and the configuration is totally symmetric: the flow is steady, time reversal and has up-and-down as well as fore-and-aft symmetries. When $\mathrm{Re} \approx 10$, the fore-and-aft symmetry visibility breaks down and two steady recirculating vortices appear at the lee of the cylinder. These vortices grow in size for increasing Re. When $\mathrm{Re} \approx 45$ the flow becomes unstable and a Hopf bifurcation [62] takes place (two complex eigenvalues of the linearised system associated to (4.22) cross the imaginary axis). For a point in the fluid, the solution has changed from a fix point to a limit cycle in the phase space and its time Fourier transform presents a single non-null frequency. The flow has lost its steadiness as well as its up-and-down symmetry and a wake of alternating vortices is formed behind the cylinder. The set of these shed vortices is known as the

von Kármán vortex street. The system remains structurally stable for growing Re until values of order Re $\simeq 200$ are reached. Then, another Hopf bifurcation occurs associated to wake three-dimensional instabilities. The spectrum of the solution at a given point now presents two discrete frequencies and the phase space dynamics takes place on a two-dimensional torus (quasiperiodic flow). For Re $\simeq 260$ there is a further bifurcation and finally, after one or two more bifurcations, the flow behaviour becomes *chaotic* and we describe it as turbulent. The spectrum of a fluid point solution is no longer discrete but continuous and the phase space torus breaks down being replaced by a *strange attractor*. The corresponding Poincaré sections have now a Hausdorff dimension $D_{\mathcal{H}} > 1$.

The described behaviour for the flow past a cylinder can be generalized to many other cases. If we consider a point $\boldsymbol{x} \in \Omega$ and analyse the velocity vector $\boldsymbol{u}(\boldsymbol{x}, t)$ when $t \to \infty$ for *growing* Re, the following states can be distinguished:

1. $\boldsymbol{u}(\boldsymbol{x}, t)$ converges to $\boldsymbol{u}(\boldsymbol{x})$ *(fix point).*

2. $\boldsymbol{u}(\boldsymbol{x}, t)$ converges (with t) to a *periodic state*, characterized by a time Fourier transform with a single non-null amplitude *(periodic flow).*

3. The time Fourier transform of $\boldsymbol{u}(\boldsymbol{x}, t)$ has a discrete spectrum with more than one non-null frequency *(quasiperiodic flow).*

4. The time Fourier transform of $\boldsymbol{u}(\boldsymbol{x}, t)$ has a continuous spectrum and the Poincaré sections have a Hausdorff dimension $D_{\mathcal{H}} > 1$ *(chaotic flow).*

The above description corresponds to one of the possible *scenarios* or *routes* of transition to chaos and turbulence. To be precise, it corresponds to the Ruelle-Takens-Newhouse scenario [239, 264] (cf. [62, 65]). However, other possibilities exist where transition does not involve Hopf bifurcations, but others. In this sense it is worthwhile to mention the *period doubling* or Feigenbaum scenario, associated to pitchfork bifurcations (see [70], cf. [62, 65]), the *intermitence* scenario associated with saddle point bifurcations (see [254], cf. [62, 65]) and the *subcritical instability* scenario [62]. The bifurcation theory establishes a general mathematical framework that provides a qualitative explanation of the transition to turbulence, although details may substantially vary from one flow to another [62].

4.3.2 Turbulent flows: Kolmogorov's theory, Statistical Fluid Mechanics and Navier-Stokes equations

Let us now focus on flows with *fully developed turbulence*, i.e., flows in phase 4 of the route to chaos described in the previous section. Without any doubt, the most well-known and successful theory describing the behaviour of a turbulent flow is Kolmogorov's theory formulated in 1941 [186] (cf. [255]), henceforth referred to as K41. This theory is described in detail in many books (see e.g., [59, 75, 80, 255]) and only its basis and some results will be presented here.

The Kolmogorov theory (K41).

The turbulent flow is considered to be composed by eddies of different sizes taking into account that the region occupied by one eddy can include eddies of smaller sizes. The various eddies are characterized by a length ℓ and a velocity U. For a flow with Reynolds number $\mathrm{Re} := U_0 L/\nu$, the largest eddies have a characteristic length $\ell \sim L$ and a characteristic velocity, $U \sim U_0$. The symbol $A \sim B$ will be used here and in the sequel to indicate that A is of "the same order" of B, or that A "behaves" as B.

Energy is transferred from the largest eddies to the smallest ones following a process known as the *energy cascade*, first proposed by Richardson [262], cf. [255]. According to this process, large eddies become unstable and break up transferring their energy to smaller eddies. In turn, these eddies also become unstable with time and follow the break-up process transmitting energy to yet smaller eddies. Hence, a cascade mechanism transferring energy to smaller and smaller eddies is established until eddies having a size such that a Reynolds number $\mathrm{Re}(\ell) := U\ell/\nu$ small enough for them to be stable is achieved. At this stage viscosity is able to dissipate kinetic energy. This mechanism of transfer and dissipation of kinetic energy is continuously fed by the energy supplied by the flow external forces, which will be assumed to only act at the large scales of the flow for simplicity. The energy cascade takes place without loss of energy as dissipation takes action at the end of the process. Consequently, the time mean rate of kinetic energy that has been input into the flow has to equal the time mean dissipation rate $\varepsilon_{\mathrm{mol}}$, at the smallest scales.

From the previous description, we can conclude that there exists a certain interval, SI, such that eddies with $\ell \in SI$ are neither influenced by the anisotropy of the largest eddies of the flow, nor by the dissipation that takes place at the smallest scales. This interval is known as the *inertial subrange* and experiments show that is more or less given by $SI \simeq [l_{DI}, l_{EI}] := [60\eta, L/6]$, with η standing for the *Kolmogorov scale*, or *Kolmogorov dissipation length*, which will be defined in short. In the inertial subrange, the spectrum of the energy density in the wavenumber domain is given by

$$E(k,t) := \frac{L}{2\pi} \sum_{|\boldsymbol{k}|_\infty = k} \frac{1}{2} |\hat{\boldsymbol{u}}(\boldsymbol{k},t)|^2 \tag{4.23}$$

and can only depend on $\varepsilon_{\mathrm{mol}}$ and k, i.e., $E(k,t) \sim \varepsilon_{\mathrm{mol}}^a k^b$. From dimensional analysis it is quite straightforward to show that $a = 2/3$ and $b = -5/3$, so that the celebrated Kolmogorov spectrum for local isotropic turbulence is recovered

$$E(k,t) \sim C_K \varepsilon_{\mathrm{mol}}^{2/3} k^{-5/3}. \tag{4.24}$$

In (4.24) C_K stands for a dimensionless universal constant (i.e., valid for any turbulent flow). Using dimensional analysis, it can also be proved that the pressure spectrum behaves as (see [9, 245] c.f. [203])

$$E_{pp}(k,t) \sim C_P \varepsilon_{\mathrm{mol}}^{4/3} k^{-7/3}, \tag{4.25}$$

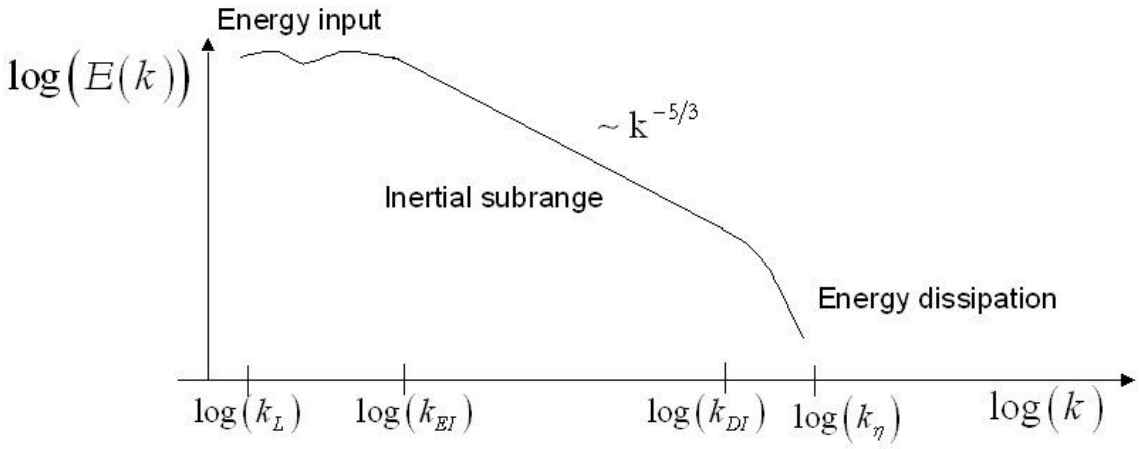

Figure 4.3: Energy cascade mechanism in wavenumber space.

with C_P standing again for a non-dimensional constant. It follows that $C_P \approx 1.33 C_K^2$, see [232].

On the other hand, Kolmogorov's dissipation length, η, corresponds to the length scale where $\mathrm{Re}\,(\eta) = 1$ (convection equals dissipation). From this relation and using (4.24) we arrive at

$$\eta = c_K \left(\frac{\nu^3}{\varepsilon} \right)^{\frac{1}{4}}, \tag{4.26}$$

which is the unique length scale that can be built from ν and ε. It follows that $c_K = 2\pi \left(3C_K/2\right)^{3/4}$. Making use again of dimensional analysis it is possible to relate η with the flow Reynolds number. Using (4.26) and observing that $\varepsilon_{\mathrm{mol}}$ has to behave as $L^{-1}U^3$ yields

$$\frac{\eta}{L} \sim \mathrm{Re}^{-\frac{3}{4}}. \tag{4.27}$$

Let us denote by k_{EI} and k_{DI} the wavenumbers respectively associated with the extreme lengths l_{EI} and l_{DI} of the inertial subrange. Then, the spectrum of the energy density in terms of the wavenumber k presents three distinguishable zones (see Fig. 4.3):

1. For $k < k_{EI}$, $E(k,t)$ corresponds to the energy of the flow macroscopic patterns (eddies).

2. For $k_{EI} \leq k \leq k_{DI}$, it follows that $E(k,t) \propto k^{-5/3}$.

3. For $k > k_{DI}$, even though Re is large (very small ν), viscous effects take place and energy is dissipated.

Kolmogorov was able to state the above framework and further results with the sole use of three main hypotheses concerning the statistics of the flow [186] (c.f. [255]). These are [255]:

1. *Hypothesis of local isotropy.* For high enough Reynolds number, the small-scale turbulent motions ($\ell < l_{EI}$) are statistically isotropic (i.e., they are locally homogeneous and invariant under rotations and reflections of the coordinate axes).

2. *First similarity hypothesis.* For any turbulent flow at sufficiently high Reynolds number, the statistics of the small-scale motions ($\ell < l_{EI}$) have a universal form uniquely determined by ν and ε_{mol}.

3. *Second similarity hypothesis.* For any turbulent flow at sufficiently high Reynolds number, the statistics of the motions of scale ℓ in the range $l_{DI} < \ell < l_{EI}$ have a universal form uniquely determined by ε_{mol} and independent of ν.

In 1962, Kolmogorov himself modified the above outlined K41 theory to adjust some differences detected in the prediction of high order moments of the velocity field ([187,246] cf. [255]). These discrepancies are associated to rare fluctuations or bursts of vorticity away from its mean value. This phenomenon is known as *intermittency* and allows for the possibility that during the bursts, some characteristic flow lengths smaller than Kolmogorov length may occur [59].

Statistical fluid mechanics

In the preceding section we have presented some K41 results that can be derived from Kolmogorov's hypotheses using dimensional analysis and heuristic reasoning. Actually Kolmogorov's hypotheses are inherently based on a statistical description of turbulent flows and were originally formulated in terms of an N-point distribution in the four-dimensional $\boldsymbol{x} - t$ space. Statistical fluid mechanics has become extremely useful in the description of turbulent flows and has probably produced the main landmark results in the field.

The fact that a probabilistic approach suits well for the description of the solutions of a deterministic system, like the Navier-Stokes equations, could look amazing at first sight. However, we have explained in section 4.3.1 how the solutions to the Navier-Stokes problem present increasingly complex behaviour when the Reynolds number is augmented. For sufficiently large Reynolds numbers, the velocity field becomes essentially random in nature and a statistical approach to describe it appears as a very reasonable option. That is, the Navier-Stokes equations exhibit what is known as *deterministic chaos*. The values of the solutions are extremely sensitive to the initial conditions, so that in the long term two close initial conditions may give place to completely different solutions.

It should be pointed out that statistical theory is not of immediate application to the Navier-Stokes. For instance, the ergodic assumption that replaces ensemble averaging by time averaging faces with the difficulty of the local existence of classical solutions. The subject is rather technical and certainly out of the scope of this work. The reader is referred to [75] for extensive information on the subject. In what follows we will limit to briefly review some basic concepts of statistical fluid mechanics that are to be used in forthcoming sections. We will follow [255] (to be consulted for details) and see how statistical tools combined with Kolmogorov's hypothesis can yield very powerful results.

We remind that for a scalar random function U, the probability of any event is characterised by the *cumulative distribution function* (CDF) defined by

$$F(V) := P\left(U < V\right) \tag{4.28}$$

where P denotes the probability (in this case of U being smaller than V). The CDF has three main proprieties, namely $F(-\infty) = 0$, $F(\infty) = 1$ and $F(V_2) \geq F(V_1)$ for $V_2 > V_1$.

The *probability density function* (PDF) is defined as the derivative of the CDF function and it accounts for the probability per unit distance in the sample space,

$$f(V) := \frac{dF(V)}{dV}. \tag{4.29}$$

$f(V)$ is a non-negative function and it is normalised to unity ($\int_{\mathbb{R}} f(V)dV = 1$) with $f(-\infty) = 0$, $f(\infty) = 0$. The PDF (also the CDF) completely characterises a random variable in the sense that two random variables having the same PDF are *statistically identical*.

For any function $Q(U)$ we can define its mean value as

$$\langle Q(U)\rangle := \int_{\mathbb{R}} Q(V)f(V)dV, \tag{4.30}$$

with the particular case of $Q(U) = U$ corresponding to the *mean* value or *expectation* of U. Fluctuations in U are given by $u' := U - \langle U\rangle$ and the n*th central moment* is defined by

$$\mu_n \equiv \langle u^n\rangle := \int_{\mathbb{R}} \left(V - \langle U\rangle\right)^n f(V)dV, \tag{4.31}$$

with $\mu_0 = 1$, $\mu_1 = 0$ and $\mu_2 = \mathrm{var}(U)$ (var standing for the variance).

In the case of turbulent flows we will be interested in statistics concerning the velocity field $\boldsymbol{u}(\boldsymbol{x}, t)$. Our interest can either involve statistics at a single point or at several points (N-point statistics). In the former case the one-point one-time joint CDF is given by

$$F(\boldsymbol{v}, \boldsymbol{x}, t) := P\left(u_i\left(\boldsymbol{x}, t\right) < v_i,\ i = 1, 2, 3\right) \tag{4.32}$$

with joint PDF

$$f(\boldsymbol{v}; \boldsymbol{x}, t) := \frac{\partial^3 F(\boldsymbol{v}, \boldsymbol{x}, t)}{\partial v_1 \partial v_2 \partial v_3}. \tag{4.33}$$

The semi-colon in (4.33) indicates that f is a *density* with respect to $\boldsymbol{v}$ and a function with respect to $\boldsymbol{x}$ and t (see [255]). Analogously to (4.30), the mean velocity field is given by

$$\langle \boldsymbol{u}\left(\boldsymbol{x}, t\right)\rangle := \int_{\mathbb{R}^3} \boldsymbol{v} f(\boldsymbol{v}; \boldsymbol{x}, t)d\boldsymbol{v}, \tag{4.34}$$

and the fluctuation is defined as $\boldsymbol{u}'(\boldsymbol{x},t) := \boldsymbol{u}(\boldsymbol{x},t) - \langle \boldsymbol{u}(\boldsymbol{x},t)\rangle$. Of special interest concerning one-point statistics are the one-point one-time covariances $\left\langle u_i' u_j' \right\rangle$ (dependence on $(\boldsymbol{x},t)$ is understood) known as *Reynolds stresses*.

We will be also interested in N-point N-time joint PDFs relating velocities at different points and instants of time. If $\{\boldsymbol{x}^n, t^n\}$ with $n = 1, 2, \ldots, N$ denote a set of N positions and times, a joint PDF for the velocity $\boldsymbol{u}(\boldsymbol{x},t)$ at these points can be build

$$f_N(\boldsymbol{v}^1, \boldsymbol{v}^2, \ldots, \boldsymbol{v}^N; \boldsymbol{x}^1, t^1, \boldsymbol{x}^2, t^2, \ldots, \boldsymbol{x}^N, t^N). \tag{4.35}$$

In what concerns the work in the remaining of this chapter, we will focus in statistics for the case $N = 2$ that relates the velocity field at a given instant and at two different points, say $\boldsymbol{x}^a$ and $\boldsymbol{x}^b$, separated a distance $r^{ab} = \left\| \boldsymbol{x}^a - \boldsymbol{x}^b \right\|$. Of special interest to us will be the two-point velocity correlation function

$$B_{ij}^{ab} = \left\langle u_i'^a u_j'^b \right\rangle, \tag{4.36}$$

the two-point fourth order velocity correlation function

$$B_{ij,kl}^{ab} = \left\langle u_i'^a u_j'^a u_k'^b u_l'^b \right\rangle, \tag{4.37}$$

and the two-point velocity pressure correlation function

$$B_{p,ij}^{ab} = \left\langle p'^a u_i'^b u_j'^b \right\rangle, \tag{4.38}$$

with p' standing for pressure fluctuations.

On the other hand, the so-called *structure functions* are another quantity of crucial importance in statistical fluid mechanics. The second-order velocity structure function for points $\boldsymbol{x}^a$ and $\boldsymbol{x}^b$ is defined as the covariance of the difference in velocity between these two points

$$D_{ij}^{ab} = \left\langle \left(u_i^b - u_i^a\right)\left(u_j^a - u_j^b\right) \right\rangle. \tag{4.39}$$

It will be next shown how Kolmogorov's hypotheses can be applied to these statistics to obtain predictions that agree fairly well with experimental data. We have chosen this example because the herein shown results, as well as the reasoning employed to derive them, will be used in subsequent sections.

A first consequence of Kolmogorov's hypothesis of local isotropy is that D_{ij}^{ab} is an isotropic function of $\boldsymbol{r}^{ab} = \boldsymbol{x}^a - \boldsymbol{x}^b$ (see [232, 255] for details). The only second-order tensors that can be build from $\boldsymbol{r}^{ab}$ (to within scalar multiples) are δ_{ij} and $r_i^{ab} r_j^{ab}$, so that D_{ij}^{ab} can be written as

$$D_{ij}^{ab} = D_{NN}^{ab}\left(r^{ab}\right)\delta_{ij} + \left[D_{LL}^{ab}\left(r^{ab}\right) - D_{NN}^{ab}\left(r^{ab}\right)\right]\frac{r_i^{ab} r_j^{ab}}{\left(r^{ab}\right)^2}. \tag{4.40}$$

In (4.40) the subscript L in the scalar function D_{LL}^{ab} stands for longitudinal, while D_{NN}^{ab} is the normal or transverse structure function. If the coordinate frame is such that $\boldsymbol{r}^{ab}$ is

in the x_1 direction, it follows that $D_{ij}^{ab} = 0$ for $i \neq j$ and $D_{11}^{ab} = D_{LL}^{ab}$, $D_{22}^{ab} = D_{33}^{ab} = D_{NN}^{ab}$, which make apparent the meaning of D_{LL}^{ab} and D_{NN}^{ab}.

It is a consequence of the incompressibility constraint that for homogeneous turbulence with zero mean value

$$\partial_{r_i} D_{ij}^{ab} = 0. \tag{4.41}$$

Differentiating (4.40) and taking into account (4.41) it follows that

$$D_{NN}^{ab} = D_{LL}^{ab} + \frac{1}{2} r^{ab} \partial_{r^{ab}} D_{LL}^{ab} \tag{4.42}$$

so that for isotropic turbulence D_{ij}^{ab} is solely determined by the scalar function D_{LL}^{ab}.

We can next apply Kolmogorov's first similarity hypothesis. According to it, for $\ell < l_{EI}$ D_{ij}^{ab} is uniquely determined by ν and ε_{mol}. D_{ij}^{ab} can be made dimensionless by means of $\left(\varepsilon_{\text{mol}} r^{ab}\right)^{2/3}$ that has dimensions of squared velocity. There only exists one independent non-dimensional group that can be formed from r^{ab}, ε_{mol} and ν, which can be taken to be $r^{ab} \varepsilon_{\text{mol}}^{1/4} \nu^{-3/4} = r^{ab} \eta^{-1}$. Hence there is a universal non-dimensional function $\hat{D}_{LL}^{ab}\left(r^{ab}/\eta\right)$ such that

$$D_{LL}^{ab} = \left(\varepsilon_{\text{mol}} r^{ab}\right)^{2/3} \hat{D}_{LL}^{ab}\left(r^{ab}/\eta\right). \tag{4.43}$$

Now, according to Kolmogorov's second similarity hypothesis, for $l_{DI} < \ell < l_{EI}$ (large values of $r^{ab}\eta^{-1}$) D_{LL}^{ab} does not depend on the viscosity ν. Given that there is no non-dimensional group that can be formed from r^{ab} and ε_{mol}, in the inertial subrange D_{LL}^{ab} will behave as

$$D_{LL}^{ab} = C\left(\varepsilon_{\text{mol}} r^{ab}\right)^{2/3}, \tag{4.44}$$

with C being a universal constant such that $\hat{D}_{LL}^{ab} \to C$ for large $r^{ab}\eta^{-1}$.

Substituting (4.44) in (4.42) we obtain the value for the transverse structure function D_{NN}^{ab}

$$D_{NN}^{ab} = \frac{4}{3} C\left(\varepsilon_{\text{mol}} r^{ab}\right)^{2/3}, \tag{4.45}$$

and inserting (4.44), (4.45) in (4.40) we get an expression for D_{ij}^{ab} in the inertial subrange,

$$D_{ij}^{ab} = C\left(\varepsilon_{\text{mol}} r^{ab}\right)^{2/3} \left(\frac{4}{3}\delta_{ij} - \frac{1}{3}\frac{r_i^{ab} r_j^{ab}}{\left(r^{ab}\right)^2}\right). \tag{4.46}$$

Consequently, we observe that the Kolmogorov hypotheses have allowed to express the second order structure function in the inertial subrange solely in terms of ε_{mol}, r^{ab} and the universal constant C. Experimental results show very close results to those predicted by (4.46) (see e.g., [255]).

Relation between K41 and the Navier-Stokes equations

One of the most surprising things about the K41 theory (apart from its experimental success) is that it does not consider at all the Navier-Stokes equations. Kolmogorov builds his theory from some basic hypothesis and heuristic reasoning, and using some statistical fluid mechanics results and dimensional analysis as working tools. However, we have seen in preceding sections that it is widely accepted that the Navier-Stokes equations are able to describe the behaviour of turbulent flows. If this is the case, it should be possible to obtain the K41 results directly from the Navier-Stokes equations. Unfortunately this is not an easy task. As previously mentioned, a first difficulty appears given that classical solutions only exist for very short periods of time (see theorem 4.2). However, we are dealing with fully developed turbulent flows (stage 4 in section 4.3.1) and thus considering long time behaviour.

A first approximation to relate K41 with the Navier-Stokes equations can be obtained from the spatial Fourier transform of the latter. Effectively, equations (4.1)-(4.2) in the wavenumber space become (for periodic boundary conditions)

$$\begin{aligned} &\partial_t \hat{\boldsymbol{u}}(\boldsymbol{k},t) - \frac{\mathrm{i}}{L^3}\left(\boldsymbol{I} - \frac{\boldsymbol{k}\boldsymbol{k}}{k^2}\right)\cdot \sum_{\boldsymbol{k}'+\boldsymbol{k}''=\boldsymbol{k}} \hat{\boldsymbol{u}}(\boldsymbol{k}',t)\cdot \boldsymbol{k}''\hat{\boldsymbol{u}}(\boldsymbol{k}'',t) \\ &\qquad + \nu k^2 \hat{\boldsymbol{u}}\left(\boldsymbol{k},t\right) = \hat{\boldsymbol{f}}\left(\boldsymbol{k}\right), \\ &\boldsymbol{k}\cdot\hat{\boldsymbol{u}}\left(\boldsymbol{k},t\right) = 0, \end{aligned} \tag{4.47}$$

with $i=\sqrt{-1}$, $\boldsymbol{I}$ being the identity tensor and $\boldsymbol{I}-\boldsymbol{k}\boldsymbol{k}/k^2$ being the projector to divergence-free vector fields. We can observe that (4.47) gives further insight to the fact that the convective term is responsible for the coupling between modes and consequently for the transfer of energy among them, according to the energy cascade description. This term does not play a role in the global energy balance (4.13), see section 4.4. below. On the other hand, the energy balance (Leray's inequality) suggests to define the time mean rate of energy dissipation per unit mass, $\varepsilon_{\mathrm{mol}} \equiv \varepsilon^{t2}_{\mathrm{mol}}$, as

$$\varepsilon^{t2}_{\mathrm{mol}} := \frac{\nu}{L^3}\left\langle \|\nabla \boldsymbol{u}\|_2^2 \right\rangle \tag{4.48}$$

(the brackets stand here for an ensemble average, or time average under the ergodic hypothesis).

It is already known that the flow kinetic energy is bounded so Leray's inequality guarantees that $\varepsilon^{t2}_{\mathrm{mol}}$ in (4.48) will be also bounded. On the other hand, we can observe that the viscous term in (4.47) contains a k^2 factor, which makes $\nu k^2 \hat{\boldsymbol{u}}\left(\boldsymbol{k},t\right)$ larger for high wavenumbers (small lengths). This is again in accordance with Komogorov's idea that dissipation takes place at the smallest scales of the flow.

The Navier-Stokes equations also play an important role in the derivation of some important equations of statistical fluid mechanics such as the *Kármán-Howarth* equation, which is viewed as an indirect validation for them. However, to recover the K41 results in a rigorous manner, neither this last result nor the above global image from (4.47) suffice

and new approaches are required. In this sense, it is worthwhile to mention that the main mechanisms of the Richardson-Kolmogorov energy cascade have been recently proved in a rigorous way starting from the Navier-Stokes equations [74] (see also [75]).

On the other hand, a central role in K41 is played by the Kolmogorov dissipation length η. It has been attempted to obtain the value of this scale from the dimension of the Navier-Stokes equations *global* or *universal attractor*[3]. The key idea goes as follows: for a three-dimensional flow with characteristic length scale L, we will need according to K41 (see (4.27)),

$$\mathcal{N} \sim \left(\frac{L}{\eta}\right)^3 \sim \mathrm{Re}^{\frac{9}{4}} \tag{4.49}$$

degrees of freedom to solve it, given that there will be no active eddies for $\ell < \eta$. Therefore we can consider, for instance, to represent the flow using the spatial Fourier transform components ranging from $1/L$ to $1/\eta$ sampled each $1/L$. On the other hand, we can identify the number of a system degrees of freedom, $\mathcal{N}$, with the dimension of its global attractor [59]. If (4.49) represents the attractor dimension of a turbulent flow according to K41, what we need is to find the global attractor of the Navier-Stokes equations and check if the same characteristic scale η is recovered.

The first problem of such a procedure concerns again the local character of classical solutions (theorem 4.2) that does not ensure the existence of a global attractor. Up to nowadays (4.49) has not been achieved, but very close results have been encountered. The most precise ones are those in [97] where it has been shown that the dimension of the attractor can be bounded by $(L/\eta)^{4.8}$ (actually, the bound in [97] does not contain η but a length that can be related to it). The desired value of 3 for the exponent can be recovered if more spatial regularity is assumed so that $\nabla \boldsymbol{u} \in L^1(0,T;L^\infty(\Omega))$ [50]. The statement of the problem of bounding the dimension of the Navier-Stokes attractor can be found, for example, in [59, 97].

4.3.3 LES: Large Eddy Simulation

Up to now we have reviewed some aspects of the mathematical theory for the Navier-Stokes equations and outlined some of its connections with the physical description of turbulence. Given that in general it is not possible to solve these equations analytically, numerical methods have become a very useful tool to understand several aspects of turbulent flows such as the transition process to chaos or the complex physics of fully developed turbulent flows. Numerical methods have become also an indispensable tool to address many engineering problems involving turbulence.

We have already commented in sections 2.5.1 and in the introduction of Chapter 4 that there exist three main possibilities to perform Computational Fluid Dynamics (CFD) of turbulent flows in the spatial domain (see e.g., [255,265]) namely RANS, DNS and LES

[3] A possible definition for the global attractor, $\mathcal{A}$, is the set of points in phase space that can be arrived at from an initial condition at an arbitrary long time in the past i.e., $\mathcal{A} = \cup_{\rho>0} \cap_{t>0} B_\rho(t)$, with $B_\rho(t)$ being a ball of radius ρ of initial conditions in phase space.

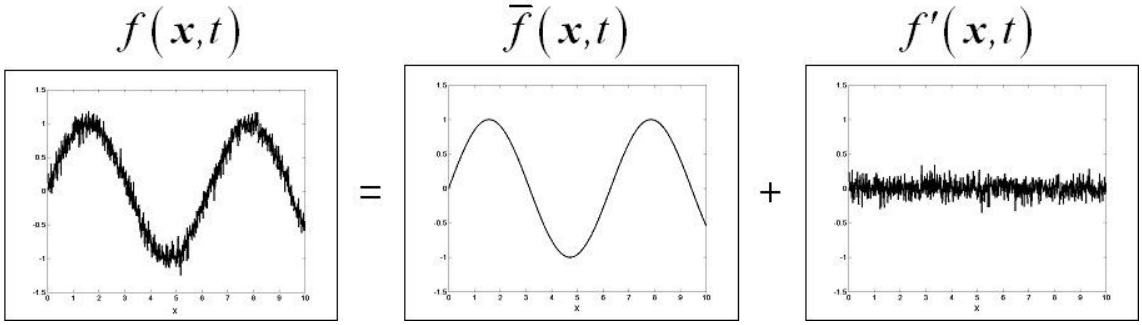

Figure 4.4: Scale decomposition in large and small scales in LES.

methods. It has been argued that the later turns to be the appropriate approach for the kind of problems we aim to solve and we will concentrate on it in this section. We remind that the key idea of standard LES is to decompose the velocity and pressure fields at the continuum level, so that $[\boldsymbol{u}, p\,] = [\overline{\boldsymbol{u}}, \overline{p}\,] + [\boldsymbol{u}', p']$, with $[\overline{\boldsymbol{u}}, \overline{p}\,]$ representing the large scales of the flow that can be computed, whereas $[\boldsymbol{u}', p'\,]$ accounts for the non-resolvable small scales. As mentioned, the key point in LES consists in properly modelling the effects of the non-computable small scales into the large ones.

Filtered Navier-Stokes equations

As stated in the introduction, the scale decomposition between large and small scales (see Fig. 4.4) has been done traditionally by means of a filtering process (see e.g., [201] cf. [255], [265]). Without detailing the possible low-pass filter operations [255, 265] and assuming that the filter $\overline{(\cdot)} : v \longmapsto \overline{v}$ commutes with the differential operators, we can filter the Navier-Stokes equations (4.1)-(4.2), with boundary conditions (4.3) or (4.4) and initial condition (4.5), to obtain the system

$$\partial_t \overline{\boldsymbol{u}} + \overline{\boldsymbol{u}} \cdot \nabla \overline{\boldsymbol{u}} - \nu \Delta \overline{\boldsymbol{u}} + \nabla \overline{p} = \boldsymbol{f} - \nabla \cdot \boldsymbol{\mathcal{R}} \quad \text{in} \quad \Omega \times (0, T) \tag{4.50}$$

$$\nabla \cdot \overline{\boldsymbol{u}} = 0 \quad \text{in} \quad \Omega \times (0, T) \tag{4.51}$$

$$\overline{\boldsymbol{u}} = 0 \quad \text{or} \quad \overline{\boldsymbol{u}} \ \text{periodic on} \quad \Gamma \tag{4.52}$$

$$\overline{\boldsymbol{u}}\,(\boldsymbol{x}, 0) = \overline{\boldsymbol{u}}_0\,(\boldsymbol{x}) \quad \text{in} \quad \Omega. \tag{4.53}$$

In (4.50), the tensor $\boldsymbol{\mathcal{R}} := \overline{\boldsymbol{u} \otimes \boldsymbol{u}} - \overline{\boldsymbol{u}} \otimes \overline{\boldsymbol{u}}$ is known as the *residual stress tensor, subscale tensor* or *subgrid scale tensor*. In order for (4.50)-(4.53) to be a closed system of equations for $[\overline{\boldsymbol{u}}, \overline{p}\,]$, it is needed to express $\boldsymbol{\mathcal{R}}$ solely in terms of $\overline{\boldsymbol{u}}$. This question is known as the *closure problem*. The various choices for $\boldsymbol{\mathcal{R}}$ give place to different LES models. Once a model has been chosen, the last step of LES consists in the discretisation of (4.50)-(4.53) and in finding its numerical solution.

One could wonder about the possibility of finding an exact closure for (4.50)-(4.53) so that $\boldsymbol{\mathcal{R}}$ could be expressed in terms of $\overline{\boldsymbol{u}}$, without making any approximation. This is in

fact possible if we make use of the Helmholtz filter that obtains $\overline{\boldsymbol{u}}$ from the solution of the Helmholtz equation, $\overline{\boldsymbol{u}} - \varepsilon^2\Delta\overline{\boldsymbol{u}} = \boldsymbol{u}$. It follows that $\overline{\boldsymbol{u}} := (\boldsymbol{I} - \varepsilon^2\Delta)^{-1}\boldsymbol{u}$, with $\varepsilon > 0$ standing for the cut-off scale [90, 91, 112]. Taking into account that $\boldsymbol{u}\otimes\boldsymbol{u} = (\overline{\boldsymbol{u}} - \varepsilon^2\Delta\overline{\boldsymbol{u}})\otimes(\overline{\boldsymbol{u}} - \varepsilon^2\Delta\overline{\boldsymbol{u}})$ and applying the filter to $\overline{\boldsymbol{u}}\otimes\overline{\boldsymbol{u}}$, we get $\overline{\boldsymbol{u}}\otimes\overline{\boldsymbol{u}} = \overline{\overline{\boldsymbol{u}}\otimes\overline{\boldsymbol{u}}} - \varepsilon^2\Delta\overline{\overline{\boldsymbol{u}}\otimes\overline{\boldsymbol{u}}}$. Inserting these relations into the subgrid scale tensor we obtain

$$\begin{aligned}
\mathcal{R}_{ij} &= \overline{(\overline{u}_i - \varepsilon^2\Delta\overline{u}_i)(\overline{u}_j - \varepsilon^2\Delta\overline{u}_j)} - \overline{u}_i\overline{u}_j \\
&= \overline{\overline{u}_i\overline{u}_j} - \varepsilon^2\overline{\overline{u}_j\Delta\overline{u}_i} - \varepsilon^2\overline{\overline{u}_i\Delta\overline{u}_j} + \varepsilon^4\overline{\Delta\overline{u}_i\Delta\overline{u}_j} - \overline{u}_i\overline{u}_j \\
&= \varepsilon^2\Delta\overline{(\overline{u}_i\overline{u}_j)} - \varepsilon^2\overline{\overline{u}_j\Delta\overline{u}_i} - \varepsilon^2\overline{\overline{u}_i\Delta\overline{u}_j} + \varepsilon^4\overline{\Delta\overline{u}_i\Delta\overline{u}_j} \\
&= 2\varepsilon^2\overline{\nabla\overline{u}_i\cdot\nabla\overline{u}_j} + \varepsilon^4\overline{\Delta\overline{u}_i\Delta\overline{u}_j}. \qquad (4.54)
\end{aligned}$$

This expression[4] effectively allows to write $\boldsymbol{\mathcal{R}}$ in terms of $\overline{\boldsymbol{u}}$ without making any approximation or ad hoc hypotheses. However, it is to be remarked that the Helmholtz filter establishes an isomorphism between $L^\infty(0,T;\boldsymbol{H}(\Omega))$ and $L^\infty\left(0,T;\boldsymbol{H}(\Omega)\cap\boldsymbol{H}^2(\Omega)\right)$, and between $L^2(0,T;\boldsymbol{V}(\Omega))$ and $L^2\left(0,T;\boldsymbol{V}(\Omega)\cap\boldsymbol{H}^3(\Omega)\right)$. Consequently, the exact closure (4.54) has only served to build an isomorphism between the weak solutions of (4.1)-(4.2) and the weak solutions of (4.50)-(4.53) [112]. Hence, the number of degrees of freedom needed to solve both problems remains the same. This result can be generalised to any exact closure of equations (4.50)-(4.53), so making LES under these circumstances is as much involved as performing DNS. At first sight this may look as a paradoxic fact given that finding an exact closure seems a reasonable goal. However, this is not the case and LES is only meaningful for a non-exact closure so that flow information is lost in the subscale modelling.

Some drawbacks of LES

As commented in the introduction of the chapter, LES presents several problems and unsolved questions. The key subject still concerns finding a good model for the subgrid scale tensor. However, it has just been pointed out that achieving an exact closure is a paradoxic program, so this cannot be a motivation to find subscale models. On the other hand, many of the existing LES models are based on physical and numerical approximations and heuristic arguments, which perform more or less well depending on the problem where they are applied. Generalisations are difficult to find although it is recommended that the subscales satisfy certain properties such as to conserve the invariance under transformations of the original Navier-Stokes equations. However, it is not fully clear which should be the characteristics of a good LES model (apart from the obvious fact that it should properly reproduce experimental data).

Another important question concerns the relation/interaction between errors arising from the physical LES model and from numerical methods used to solve the discretised problem [35, 93, 185, 200, 283]. It is also not clear which should be the relation between the filter support ε and the characteristic mesh element size h [35, 93]. In addition, the

[4] A first order approximation on ε^2 yields $\mathcal{R}_{ij} \simeq 2\varepsilon^2\overline{\nabla\overline{u}_i\cdot\nabla\overline{u}_j}$ that is the de Clark et al. [37] modelling for the *Leonard stresses* plus the *cross stresses* into which the subgrid scale tensor can be decomposed [90].

problem of the commutation error of the filtering and differentiation operations needs also to be addressed [64, 96, 289].

In summary, we could say that nowadays a satisfactory mathematical theory of LES still does not exist although steps towards this direction are being carried out (see e.g. [17, 171, 196–198]).

Suitable approximations to the Navier-Stokes equations

Recently, a detailed analysis of several LES models has been performed in an attempt to clarify the situation somehow [112]. From this analysis several interesting conclusions have been derived. For instance, it is observed that those models in section 4.2.4 presenting uniqueness of solutions can be written in the form of LES equations. Effectively,

Leray's convolution model. Without considering initial and boundary conditions for brevity, Leray's model (4.18) can be rewritten in the form (4.50)

$$\partial_t \boldsymbol{u} + \boldsymbol{u} \cdot \nabla \boldsymbol{u} - \nu \Delta \boldsymbol{u} + \nabla p = (\boldsymbol{\psi}_\varepsilon * \boldsymbol{f}) - \nabla \cdot \boldsymbol{\mathcal{R}}_{Le}, \tag{4.55}$$

$$\boldsymbol{\mathcal{R}}_{Le} := \boldsymbol{u} \otimes (\boldsymbol{\psi}_\varepsilon * \boldsymbol{u}) - \boldsymbol{u} \otimes \boldsymbol{u}. \tag{4.56}$$

This model has the inconvenience that is not invariant under transformations of the coordinate axis although it can be rearranged to achieve this propriety [112]. The resulting model is known as the *Navier-Stokes alpha model* (NS-α) [111].

The Lions hyperviscosity model. In this case we have

$$\partial_t \boldsymbol{u} + \boldsymbol{u} \cdot \nabla \boldsymbol{u} - \nu \Delta \boldsymbol{u} + \nabla p = \boldsymbol{f} - \nabla \cdot \boldsymbol{\mathcal{R}}_{Li},$$

$$\boldsymbol{\mathcal{R}}_{Li} := \varepsilon^{2\alpha} (-\nabla)^{2\alpha - 1} \boldsymbol{u}. \tag{4.57}$$

The Ladyženskaja and Kaniel non-linear viscosity model For this model we obtain

$$\partial_t \boldsymbol{u} + \boldsymbol{u} \cdot \nabla \boldsymbol{u} - \nu \Delta \boldsymbol{u} + \nabla p = \boldsymbol{f} - \nabla \cdot \boldsymbol{\mathcal{R}}_{La}, \tag{4.58}$$

$$\boldsymbol{\mathcal{R}}_{La} := -\varepsilon^{2\mu+1} \beta \left| \nabla \boldsymbol{u} \right|^2 \nabla \boldsymbol{u}. \tag{4.59}$$

It is worthwhile to mention that the most celebrated LES model, the Smagorinsky model [272] (cf. [255]) has the same structure as (4.58) taking $\mu = 1/2$, $\beta(\tau) = \tau^\mu$, and $\boldsymbol{\xi} = \boldsymbol{\mathcal{S}}$ in (4.20), with $\boldsymbol{\mathcal{S}} := 1/2 \left(\nabla \boldsymbol{u} + \nabla \boldsymbol{u}^T \right)$. It follows $\boldsymbol{\mathcal{R}}_{Sm} := -\varepsilon^2 \left| \boldsymbol{\mathcal{S}} \right| \boldsymbol{\mathcal{S}}$.

Hence, we can conclude that it is possible to obtain LES models with the remarkable attribute of leading to well posed mathematical problems. Moreover, we can observe that filtering is not the only way to attain LES models as shown e.g., for the Ladyženskaja and Kaniel model. Even the celebrated Smagorinsky model can be recovered without filtering in contrast to what is usually performed in literature.

Further models were analysed in [112] such as spectral viscosity models, subgrid viscosity models, variational multiscales models, similarity models, etc. Although it does

not seem possible to build a general mathematical framework for the whole of these models, it was concluded that a LES model should satisfy at least two main requisites: first, it should lead to a well-posed system of equations. Second, it should select physical relevant solutions i.e., *suitable* in the sense specified in section 4.2.3 (see Definition 4.1).

In view of the above considerations, the notion of *suitable approximations* to the Navier-Stokes equations was proposed in [114] as a first step towards a mathematical definition of LES .

Definition 4.2 *A sequence* $[\boldsymbol{u}_\gamma, p_\gamma]$, *with* $\gamma > 0$ *and* $\boldsymbol{u}_\gamma \in L^2(0,T;\boldsymbol{X}(\Omega)) \cap L^\infty\left(0,T;\boldsymbol{L}^2(\Omega)\right)$ *and* $p_\gamma \in \mathcal{D}'(]0,T[, L^2(\Omega)/\mathbb{R})$, *is said to be a suitable approximation to the Navier-Stokes equations (4.1)-(4.5) iff*

1. *There exist two finite dimensional vector spaces* $\boldsymbol{X}_\gamma(\Omega) \subset \boldsymbol{X}(\Omega)$ *and* $M_\gamma(\Omega) \subset \boldsymbol{L}^2(\Omega)/\mathbb{R}$ *such that* $\boldsymbol{u}_\gamma \in C^0([0,T];\boldsymbol{X}_\gamma(\Omega))$ *and* $p_\gamma \in \boldsymbol{L}^2(]0,T[, M_\gamma(\Omega))$.

2. *The sequence* $\{\boldsymbol{u}_\gamma, p_\gamma\}$ *(or a subsequence) converges to a weak solution of (4.1)-(4.5), i.e.,* $\boldsymbol{u}_\gamma \rightharpoonup \boldsymbol{u}$ *(weak convergence) in* $L^2(0,T;\boldsymbol{X}(\Omega))$ *and* $p_\gamma \to p$ *in* $\mathcal{D}'(]0,T[, L^2(\Omega)/\mathbb{R})$.

3. *The weak solution* $[\boldsymbol{u}, p]$ *is suitable.*

Note that two parameters are involved in the definition 4.2: the parameter h associated to the smallest scale in $\boldsymbol{X}_\gamma(\Omega)$ (the dimension of $\boldsymbol{X}_\gamma(\Omega)$ will be of order $(L/h)^3$) and the parameter ε associated to the cut-off scale (or to the diameter of the filter support). This scale corresponds to the size of the smallest active eddies in the flow. The parameter γ in the definition stands for a combination of h and ε to be determined in each case. It is understood that $\gamma \to 0$ for $\varepsilon \to 0$ and $h \to 0$.

The following three step strategy is proposed in [114] for the practical construction of suitable approximations.

1. *Elaboration of a* pre-LES *model.* This step consists in reguralising the Navier-Stokes equations to obtain a well-posed problem and introduces the parameter ε. For $\varepsilon \to 0$ the pre-LES model has to converge to a suitable solution of the Navier-Stokes equations. Hence, the pre-LES model corresponds to the process of obtaining the filtered equations (4.50) in standard LES but, with the additional requisite that once closed, the resulting equations have to be well-posed. That is to say, the problem needs to have a unique solution that converges to a suitable weak solution of the Navier-Stokes equations.

2. *Discretisation of the pre-LES model.* In this step we introduce the approximated functions for the velocity and pressure fields, the finite dimensional spaces $\boldsymbol{X}_\gamma(\Omega)$ and $M_\gamma(\Omega)$, and the parameter h.

3. *Determining the relation between* ε *and* h. The relation between ε and h cannot be arbitrary given that when taking the limits $\varepsilon \to 0$ and $h \to 0$, the solution has to converge to a suitable solution of the Navier-Stokes equations.

It can be checked that the Leray, (NS-α), Lions and Ladyženskaja-Kaniel models yield suitable approximations of the Navier-Stokes equations [112]. Nevertheless, although suitable approximations constitute a first substantial step towards a mathematical definition of LES some problems remain. This is the case e.g., of the unknown relation between errors induced by the pre-LES model and those of the discretisation. In this sense it is worthwhile to wonder which is the role played by DNS in all this context. In other words and to be precise, given $\boldsymbol{X}_\gamma(\Omega) \subset \boldsymbol{X}(\Omega)$ and $M_\gamma(\Omega) \subset \boldsymbol{L}^2(\Omega)/\mathbb{R}$, we wonder if $\forall t \in [0,T]$ the Galerkin approximation

$$\begin{array}{rcl} (\partial_t \boldsymbol{u}_h, \boldsymbol{v}) + b(\boldsymbol{u}_h, \boldsymbol{u}_h, \tilde{\boldsymbol{v}}) + \nu(\nabla \boldsymbol{u}_h, \nabla \boldsymbol{v}) - (p_h, \nabla \boldsymbol{v}) & = & \langle \boldsymbol{f}, \tilde{\boldsymbol{v}} \rangle \quad \forall \boldsymbol{v} \in \boldsymbol{X}_\gamma(\Omega) \\ (q, \nabla \boldsymbol{u}_h) & = & 0 \quad \forall q \in M_\gamma(\Omega) \\ (\boldsymbol{u}_h(\boldsymbol{x}, 0), \boldsymbol{v}) & = & (\boldsymbol{u}_0, \boldsymbol{v}) \quad \forall \boldsymbol{v} \in \boldsymbol{X}_\gamma(\Omega) \end{array} \tag{4.60}$$

with $\boldsymbol{u}_h(\cdot, t) \in \boldsymbol{X}_\gamma(\Omega)$ and $p_h(\cdot, t) \in M_\gamma(\Omega)$, is suitable. It has been proved that this is in fact the case for the solution of (4.60) with periodic boundary conditions, and using low order finite element spaces having a discrete commutation property and satisfying an appropriate inf-sup condition [109]. Recently, the result has been extended for the case of Dirichlet boundary conditions [110]. These results may justify somehow the fact that, for low order finite elements, sometimes better results are obtained when no physical LES modelling is used.

4.3.4 SGS versus LES

In the preceding section we have introduced the standard LES approach to solve turbulent flows as well as some recent developments aiming to establish a mathematical definition and framework for LES. On the other hand, in Chapter 3 a SGS (or VMM) stabilised finite element method was introduced (in particular the OSS method with time tracking and inclusion of all non-linear terms), and we claimed that SGS may constitute a valid alternative for the simulation of turbulent flows.

Even though the final goal of LES consists of a numerical simulation, its statement *precedes* this simulation. Starting from the description of the dynamics of the original problem, LES modelling aims at stating a problem with similar behaviour for some *macro scales*, obtained after a filter operation and a closure for the subgrid scale tensor. In contrast, SGS models are numerical formulations without previous manipulation of the original problem. From the comparison of both approaches it follows that:

- There is no filter operation in SGS but a closed expression for the subscales. The different ways to obtain this expression give place to the different SGS models.

- There is no ambiguity in the SGS definition of a subscale: we would like that $\boldsymbol{u}_h = P_h(\boldsymbol{u})$ for a projection P_h onto the discrete space, from which $\boldsymbol{u}' = \boldsymbol{u} - P_h(\boldsymbol{u})$. There is no closure problem except for the necessity to find an expression for P_h.

- According to the definition 4.2, in SGS $\varepsilon = h$, i.e., the reguralisation term is introduced by the numerical approximation. In other words, in SGS there is not pre-LES model and the reguralisation comes from the effects of the numerical subscales.
- Whether for the SGS solution $\boldsymbol{u}_h \rightharpoonup \boldsymbol{u}, p_h \rightharpoonup p$ and $[\boldsymbol{u}, p]$ is a suitable solution is still an open problem and it will depend on the model for the subscales. Convergence to a weak solution of the continuous problem is however guaranteed by the Hopf technique [133], in combination with stability results.
- The SGS stabilisation terms can be also written in terms of Reynolds, Leonard and cross stresses. Moreover the SGS formulation retains the invariants of the original Navier-Stokes equations.

From these observations we may conjecture that

- Probably, *SGS is LES*, according to the definition of suitable approximations ...
- ... But having SGS is LES necessary?
- In other words, turbulence needs to be a physical or a numerical model?

In Chapter 3 we have seen some properties of the SGS approach that make it a proper candidate for the simulation of turbulence. In the next sections we will use a totally different line of reasoning to give further support to the idea that no physical LES model should be used in the simulation of turbulent flows [108]. It will be heuristically shown that the rate of transfer of subgrid kinetic energy provided by the stabilisation terms of the Orthogonal Subgrid Scale (OSS) finite element method is already proportional to the molecular physical dissipation rate (for an appropriate choice of the stabilisation parameter). This precludes the necessity of including an extra LES physical model to achieve this behaviour and somehow justifies the purely numerical approach to solve turbulent flows. The argumentation is valid for a fine enough mesh with characteristic element size, h, so that h lies in the inertial subrange of a turbulent flow.

4.4 Energy balance equations

4.4.1 Energy balance equation for the Navier-Stokes problem

The strong formulation of the Navier-Stokes equations problem in a domain $\Omega \subset \mathbb{R}^3$ has been stated in (4.1)-(4.2), with boundary conditions (4.3)-(4.4) and initial condition (4.5). This problem can be rewritten in conservative form for the case of homogeneous Dirichlet conditions on the boundary ($\partial\Omega \equiv \Gamma_D$) as

$$\partial_t \boldsymbol{u} - 2\nabla \cdot [\nu \boldsymbol{\mathcal{S}}(\boldsymbol{u})] + \nabla \cdot (\boldsymbol{u} \otimes \boldsymbol{u}) + \nabla p = \boldsymbol{f} \qquad \text{in } \Omega \times (0,T), \tag{4.61}$$

$$\nabla \cdot \boldsymbol{u} = 0 \qquad \text{in } \Omega \times (0,T), \tag{4.62}$$

$$\boldsymbol{u}(\boldsymbol{x},0) = \boldsymbol{u}_0(\boldsymbol{x}) \qquad \text{in } \Omega,\ t = 0, \tag{4.63}$$

$$\boldsymbol{u}(\boldsymbol{x},t) = 0 \qquad \text{on } \Gamma_D \times (0,T), \tag{4.64}$$

where as usual $\boldsymbol{u}$ stands for the flow velocity, p for the pressure, ν represents the kinematic fluid viscosity (taken constant hereafter), $\boldsymbol{\mathcal{S}}(\boldsymbol{u}) := \frac{1}{2}\left(\nabla\boldsymbol{u} + \nabla\boldsymbol{u}^T\right)$ the rate of strain tensor, $\boldsymbol{f}$ the external force and $(0,T)$ is the time interval of analysis.

Using the functional framework introduced in section 3.2, we can formulate the weak form associated to problem (4.61)-(4.64) as: find $[\boldsymbol{u},p] \in \boldsymbol{L}^2(0,T;\boldsymbol{H}^1_0(\Omega)) \times L^1(0,T;L^2(\Omega)/\mathbb{R})$ (for example) such that

$$(\partial_t\boldsymbol{u},\boldsymbol{v}) + 2\nu(\boldsymbol{\mathcal{S}}(\boldsymbol{u}),\boldsymbol{\mathcal{S}}(\boldsymbol{v})) + \langle\nabla\cdot(\boldsymbol{u}\otimes\boldsymbol{u}),\boldsymbol{v}\rangle - (p,\nabla\cdot\boldsymbol{v}) = \langle\boldsymbol{f},\boldsymbol{v}\rangle, \tag{4.65}$$

$$(q,\nabla\cdot\boldsymbol{u}) = 0, \tag{4.66}$$

for all $[\boldsymbol{v},q] \in \boldsymbol{H}^1_0(\Omega) \times L^2(\Omega)/\mathbb{R}$, and satisfying the initial condition in a weak sense.

In what follows we will assume the solutions to be classical, which allows setting $\boldsymbol{v} = \boldsymbol{u}$, $q = ct$ (constant) in (4.65)-(4.66) for each $t \in (0,T)$. Taking into account that we have limited the analysis to homogeneous Dirichlet boundary conditions, we obtain the energy balance equation

$$\frac{d}{dt}\left(\frac{1}{2}\|\boldsymbol{u}\|^2\right) = -2\nu\|\boldsymbol{\mathcal{S}}(\boldsymbol{u})\|^2 + \langle\boldsymbol{f},\boldsymbol{u}\rangle. \tag{4.67}$$

Equation (4.67) states that the time variation of the flow kinetic energy depends on two factors, namely, the molecular dissipation due to viscosity (which is clearly negative) and the power exerted by the external force that can be either positive or negative. Identifying the pointwise kinetic energy as $k := \boldsymbol{u}\cdot\boldsymbol{u}/2$, the pointwise molecular dissipation as $\varepsilon_{\text{mol}} := 2\nu[\boldsymbol{\mathcal{S}}(\boldsymbol{u}) : \boldsymbol{\mathcal{S}}(\boldsymbol{u})]$ and the pointwise power of the external force as $P_f := \boldsymbol{f}\cdot\boldsymbol{u}$ we can rewrite (4.67) as

$$\int_\Omega \frac{dk}{dt}d\Omega = -\int_\Omega \varepsilon_{\text{mol}}d\Omega + \int_\Omega P_f d\Omega. \tag{4.68}$$

According to the Kolmogorov description of the energy cascade in turbulent flows described earlier [186] cf. [255], the flow can be viewed as driven by the external forces acting at the large scales (low wave numbers) and generating kinetic energy, which is transferred to the low scales (high wave numbers) by non-linear processes. When the Kolmogorov length is reached, the viscous dissipation, ε_{mol}, in the r.h.s of (4.68) takes part transforming the flow kinetic energy into internal energy (heat is released).

4.4.2 Energy balance equation for a Large Eddy Simulation model

We have shown in section 4.3.3 that in the standard Large Eddy Simulation (LES) of turbulent flows, a scale separation between large and small scales for the velocity and pressure fields in the Navier-Stokes equations is carried out. This yields $[\boldsymbol{u},p] = [\overline{\boldsymbol{u}},\overline{p}] + [\boldsymbol{u}',p']$, with $[\overline{\boldsymbol{u}},\overline{p}]$ standing for the large, filtered, scales and $[\boldsymbol{u}',p']$ representing the small, residual, ones. Considering the same assumptions used to derive (4.50)-(4.53),

we get the filtered incompressible Navier-Stokes equations in conservative form:

$$\partial_t \overline{\boldsymbol{u}} - 2\nabla \cdot [\nu \boldsymbol{\mathcal{S}}(\overline{\boldsymbol{u}})] + \nabla \cdot (\overline{\boldsymbol{u}} \otimes \overline{\boldsymbol{u}}) + \nabla \overline{p} = \boldsymbol{f} - \nabla \cdot \boldsymbol{\mathcal{R}} \qquad \text{in } \Omega \times (0,T), \tag{4.69}$$

$$\nabla \cdot \overline{\boldsymbol{u}} = 0 \qquad \text{in } \Omega \times (0,T), \tag{4.70}$$

$$\overline{\boldsymbol{u}}(\boldsymbol{x},0) = \overline{\boldsymbol{u}}_0(\boldsymbol{x}) \qquad \text{in } \Omega,\ t=0, \tag{4.71}$$

$$\overline{\boldsymbol{u}}(\boldsymbol{x},t) = 0 \qquad \text{on } \Gamma_D \times (0,T), \tag{4.72}$$

which are analogous to (4.61)-(4.64) except for the divergence of the *residual stress tensor* $\boldsymbol{\mathcal{R}} := \overline{\boldsymbol{u} \otimes \boldsymbol{u}} - \overline{\boldsymbol{u}} \otimes \overline{\boldsymbol{u}}$ appearing in the r.h.s of (4.69). As already mentioned, an expression for the latter in terms of $\overline{\boldsymbol{u}}$ is needed to close the system of equations (4.69)-(4.72).

The weak formulation of problem (4.69)-(4.72) can be stated as: find $[\overline{\boldsymbol{u}}, \overline{p}] \in \boldsymbol{L}^2(0,T;\boldsymbol{H}_0^1(\Omega)) \times L^1(0,T;L^2(\Omega)/\mathbb{R})$ such that

$$(\partial_t \overline{\boldsymbol{u}}, \boldsymbol{v}) + 2\nu(\boldsymbol{\mathcal{S}}(\overline{\boldsymbol{u}}), \boldsymbol{\mathcal{S}}(\boldsymbol{v})) + \langle \nabla \cdot (\overline{\boldsymbol{u}} \otimes \overline{\boldsymbol{u}}), \boldsymbol{v} \rangle - (\overline{p}, \nabla \cdot \boldsymbol{v}) = \langle \overline{\boldsymbol{f}}, \boldsymbol{v} \rangle + \langle \boldsymbol{\mathcal{R}}, \nabla \boldsymbol{v} \rangle, \tag{4.73}$$

$$(q, \nabla \cdot \overline{\boldsymbol{u}}) = 0, \tag{4.74}$$

for all $[\boldsymbol{v}, q] \in \boldsymbol{H}_0^1(\Omega) \times L^2(\Omega)/\mathbb{R}$, and satisfying the initial condition in a weak sense. Taking into account that $\boldsymbol{\mathcal{R}}$ is symmetric, we can rewrite the second term in the r.h.s of (4.73) as $\langle \boldsymbol{\mathcal{R}}, \nabla \boldsymbol{v} \rangle = \langle \boldsymbol{\mathcal{R}}, \boldsymbol{\mathcal{S}}(\boldsymbol{v}) \rangle$. In addition, and without loss of generality, we will consider $\boldsymbol{\mathcal{R}}$ deviatoric, its volumetric part being absorbed in the pressure term.

If we next set $\boldsymbol{v} = \overline{\boldsymbol{u}}$, $q = ct$, for each $t \in (0,T)$ in (4.73)-(4.74) we can obtain an energy balance for the filtered Navier-Stokes equations:

$$\frac{d}{dt}\left(\frac{1}{2}\|\overline{\boldsymbol{u}}\|^2\right) = -2\nu \|\boldsymbol{\mathcal{S}}(\overline{\boldsymbol{u}})\|^2 + \langle \boldsymbol{\mathcal{R}}, \boldsymbol{\mathcal{S}}(\overline{\boldsymbol{u}}) \rangle + \langle \overline{\boldsymbol{f}}, \overline{\boldsymbol{u}} \rangle. \tag{4.75}$$

We can now define the filtered pointwise kinetic energy $\overline{k} := \overline{\boldsymbol{u}} \cdot \overline{\boldsymbol{u}}/2$, the pointwise filtered molecular dissipation $\overline{\varepsilon}_{\text{mol}} := 2\nu [\boldsymbol{\mathcal{S}}(\overline{\boldsymbol{u}}) : \boldsymbol{\mathcal{S}}(\overline{\boldsymbol{u}})]$, the rate of production of residual kinetic energy $\overline{\mathcal{P}}_r := -\boldsymbol{\mathcal{R}} : \boldsymbol{\mathcal{S}}(\overline{\boldsymbol{u}})$ and the pointwise power of the external filtered force $\overline{P}_f := \overline{\boldsymbol{f}} \cdot \overline{\boldsymbol{u}}$, so that we can rewrite (4.75) as

$$\frac{d}{dt}\int_\Omega \overline{k} d\Omega = -\int_\Omega \overline{\varepsilon}_{\text{mol}} d\Omega - \int_\Omega \overline{\mathcal{P}}_r d\Omega + \int_\Omega \overline{P}_f d\Omega. \tag{4.76}$$

For a fully developed turbulent flow with the filter width in the inertial subrange, the filtered field accounts for almost all the kinetic energy of the flow. Thus, $\int_\Omega \overline{k} d\Omega \approx \int_\Omega k d\Omega$ and the first terms in (4.68) and (4.76) become nearly equal. If the external force mainly acts on the large scales of the flow, it will also happen that $\int_\Omega \overline{\mathcal{P}}_f d\Omega \approx \int_\Omega \mathcal{P}_f d\Omega$. On the other hand, the energy dissipated by the filtered field, $\overline{\varepsilon}_{\text{mol}}$ is relatively small and can be neglected [255]. Consequently, comparing equation (4.76) with equation (4.68), we observe that in order for the LES model to behave correctly it should happen that $\int_\Omega \overline{\mathcal{P}}_r d\Omega \approx \int_\Omega \varepsilon_{\text{mol}} d\Omega$. That is, the rate of production of residual kinetic energy should equal, in the mean, the energy dissipated by viscous processes at the very small scales (Kolmogorov length), which is the point of view expressed by Lilly [211].

In the case of some celebrated LES models, such as the Smagorinsky model [272], $\overline{\mathcal{P}}_r$ is always positive and there is no backscatter, i.e., the energy is always transferred from the filtered scales to the residual ones, but not vice versa. It is quite customary then to term $\overline{\mathcal{P}}_r$ as *subgrid* or *residual dissipation* and to denote it by ε_{SGS}, see e.g., [283]. However, this may lead to confusion, especially when introducing the discrete stabilised numerical version of the original and filtered Navier-Stokes equations, so we will keep the notation $\overline{\mathcal{P}}_r$ in this work.

4.4.3 Energy balance equations in discrete problems: stabilised numerical approach of the original and filtered Navier-Stokes equations

Galerkin finite element approach

Following section 3.3.3 in the previous chapter we can state the Galerkin finite element approximation to problem (4.65)-(4.66) as: given the finite dimensional spaces $\mathcal{V}_{0,h}^d \subset \boldsymbol{H}_0^1(\Omega)$ and $\mathcal{Q}_{0,h} \subset L^2(\Omega)/\mathbb{R}$ find $[\boldsymbol{u}_h(t), p_h(t)] \in \boldsymbol{L}^2(0,T;\mathcal{V}_{0,h}^d) \times L^1(0,T;\mathcal{Q}_{0,h})$ such that

$$(\partial_t \boldsymbol{u}_h, \boldsymbol{v}_h) + 2\nu(\boldsymbol{\mathcal{S}}(\boldsymbol{u}_h), \boldsymbol{\mathcal{S}}(\boldsymbol{v}_h)) + \langle \nabla \cdot (\boldsymbol{u}_h \otimes \boldsymbol{u}_h), \boldsymbol{v}_h \rangle$$
$$-(p_h, \nabla \cdot \boldsymbol{v}_h) = \langle \boldsymbol{f}, \boldsymbol{v}_h \rangle, \tag{4.77}$$
$$(q_h, \nabla \cdot \boldsymbol{u}_h) = 0, \tag{4.78}$$

for all $[\boldsymbol{v}_h, q_h] \in \mathcal{V}_{0,h}^d \times \mathcal{Q}_{0,h}$.

Note that equations (4.77)-(4.78) are still continuous in time. However, for the developments to be presented hereafter time discretisation will be not required, so no explicit expression for it will be given. Anyway, and whatever time discrete scheme is used, it has been explained in section 3.4.2 that the Galerkin finite element approach (4.77)-(4.78) presents several difficulties. We remind that numerical instabilities are encountered when the non-linear convective term in the equation dominates the viscous one at high Reynolds number problems. Moreover, the *inf-sup* condition is required to control the pressure term and does not allow to use equal order interpolations to approximate the velocity and pressure fields. In addition, numerical instabilities are also found when small time steps are used.

In the introduction of this chapter we have referenced several stabilisation strategies that have been developed to circumvent the above numerical instabilities of the Galerkin finite element solution to the Navier-Stokes equations. We will focus in what follows on the SGS approach. In particular, we will concentrate on the orthogonal subgrid scale (OSS) approach developed in [42–44, 47], see section 3.5.2. This will simplify some of the forthcoming analysis although the developments could be possibly extended to other methods.

Orthogonal subgrid scale stabilisation

The subgrid scale finite element stabilisation method applied to the present problem has been already described in section 3.4.2, and we remind that it consists in first splitting the continuous spatial spaces where the solution is found as $\boldsymbol{H}_0^1(\Omega) = \mathcal{V}_{h,0}^d \oplus \tilde{\mathcal{V}}_0^d$ and $L^2(\Omega)/\mathbb{R} = \mathcal{Q}_{h,0} \oplus \tilde{\mathcal{Q}}_0$, with $\tilde{\mathcal{V}}_0^d$ and $\tilde{\mathcal{Q}}_0$ being any infinite dimensional spaces that respectively complete the finite element spaces $\mathcal{V}_{h,0}^d$ and $\mathcal{Q}_{h,0}$ in $\boldsymbol{H}_0^1(\Omega)$ and $L^2(\Omega)/\mathbb{R}$. The velocity and pressure fields can then be decomposed as $\boldsymbol{u} = \boldsymbol{u}_h + \tilde{\boldsymbol{u}}$ and $p = p_h + \tilde{p}$ (the same holds for the test functions $\boldsymbol{v} = \boldsymbol{v}_h + \tilde{\boldsymbol{v}}$, $q = q_h + \tilde{q}$).

The weak form of the Navier-Stokes equations can now be split into two systems of equations. This is done by first substituting $\boldsymbol{u} = \boldsymbol{u}_h + \tilde{\boldsymbol{u}}$ and $p = p_h + \tilde{p}$ in (4.65)-(4.66) and taking $[\boldsymbol{v}, q] = [\boldsymbol{v}_h, q_h]$, which corresponds to projecting (4.65)-(4.66) onto the finite element spaces. Then, a second equation is obtained by projecting (4.65)-(4.66) onto the finite element complementary spaces by setting $[\boldsymbol{v}, q] = [\tilde{\boldsymbol{v}}, \tilde{q}]$.

After integrating some terms by parts and neglecting terms involving integrals over interelement boundaries, the equation corresponding to the large scales (projection onto the finite element spaces) becomes [44, 47],

$$
\begin{aligned}
&(\partial_t \boldsymbol{u}_h, \boldsymbol{v}_h) + 2\nu(\boldsymbol{\mathcal{S}}(\boldsymbol{u}_h), \boldsymbol{\mathcal{S}}(\boldsymbol{v}_h)) + \langle \nabla \cdot (\boldsymbol{u}_h \otimes \boldsymbol{u}_h), \boldsymbol{v}_h \rangle \\
&\qquad - (p_h, \nabla \cdot \boldsymbol{v}_h) + (q_h, \nabla \cdot \boldsymbol{u}_h) \\
&\qquad - \sum_e \langle \tilde{\boldsymbol{u}}, 2\nu \nabla \cdot \boldsymbol{\mathcal{S}}(\boldsymbol{v}_h) + \nabla \cdot (\boldsymbol{u}_h \otimes \boldsymbol{v}_h) + \nabla q_h \rangle_{\Omega_e} \\
&\qquad + (\partial_t \tilde{\boldsymbol{u}}, \boldsymbol{v}_h) + \langle \nabla \cdot (\tilde{\boldsymbol{u}} \otimes \boldsymbol{u}_h), \boldsymbol{v}_h \rangle \\
&\qquad + \langle \tilde{\boldsymbol{u}} \cdot \nabla \tilde{\boldsymbol{u}}, \boldsymbol{v}_h \rangle \\
&\qquad - (\tilde{p}, \nabla \cdot \boldsymbol{v}_h) = \langle \boldsymbol{f}, \boldsymbol{v}_h \rangle .
\end{aligned}
\tag{4.79}
$$

The meaning of the various terms (4.79) was already explained in section 3.4.2, although we reproduce it here for the sake of completeness of the chapter. As mentioned there, the first two lines of (4.79) contain the Galerkin terms previously found in (4.77)-(4.78). The third line includes terms that are already obtained in the stabilisation of the linearised and stationary version of the Navier-Stokes equations [42, 43] (Oseen problem). These terms avoid the convection instabilities of the Galerkin formulation and also allow to use equal interpolations for the velocity and the pressure. The first term in the fourth line accounts for the time derivative of the subscales, while the second term provides global momentum conservation [47]. The term in the fifth line has a second order dependence on the velocity subscales and it is argued in [26] that has very little influence on the results. Consequently it will be neglected in what follows, which will simplify the analysis. Finally, the term in the sixth line accounts for the effects of the pressure subscales.

To solve (4.79) we need some expressions for the velocity and pressure subscales $[\tilde{\boldsymbol{u}}, \tilde{p}]$. These expressions can be found from the solution of the small subgrid scale equation (projection onto the finite element complementary spaces). Given that the latter equation cannot be solved exactly, an approximation for its solution is required. We will use here the orthogonal subgrid scale (OSS) approach, which is based on choosing

the spaces orthogonal to the finite element ones as the complimentary spaces in the above formulation. Moreover *quasi-static* subscales will be considered (this correspond to neglecting the time derivatives in (3.50)-(3.51)), leading to the approximation [42, 43]:

$$\tilde{\boldsymbol{u}} \approx \tau_1 \boldsymbol{r}_{u,h}, \tag{4.80}$$

$$\tilde{p} \approx \tau_2 r_{p,h}, \tag{4.81}$$

where $\boldsymbol{r}_{u,h}$ and $r_{p,h}$ represent the orthogonal projection of the residuals of the finite element components $\boldsymbol{u}_h$ and p_h

$$\begin{aligned} \boldsymbol{r}_{u,h} &= -\Pi_h^{\perp}[\partial_t \boldsymbol{u}_h - 2\nu\nabla\cdot\boldsymbol{\mathcal{S}}(\boldsymbol{u}_h) + \nabla\cdot(\boldsymbol{u}_h\otimes\boldsymbol{u}_h) + \nabla p_h - \boldsymbol{f}] \\ &= -\Pi_h^{\perp}[-2\nu\nabla\cdot\boldsymbol{\mathcal{S}}(\boldsymbol{u}_h) + \nabla\cdot(\boldsymbol{u}_h\otimes\boldsymbol{u}_h) + \nabla p_h], \qquad (4.82) \\ r_{p,h} &= -\Pi_h^{\perp}[\nabla\cdot\boldsymbol{u}_h]. \qquad (4.83) \end{aligned}$$

$\Pi_h^{\perp}$ in the above equations stands for the orthogonal projection, $\Pi_h^{\perp} := \mathcal{I} - \Pi_h$, with $\mathcal{I}$ being the identity and Π_h the L^2 projection onto the appropriate finite element space. In fact, the numerical analysis of the stationary and linearised problem is greatly simplified if this projection is weighted elementwise by the stabilisation parameters, as shown in [45]. However, this is not essential for the following developments.

In the second line of (4.82) we have used precisely the fact that, once discretised, $\partial_t \boldsymbol{u}_h \subset \mathcal{V}_{h,0}^d$. We have also considered that the external force belongs to $\mathcal{V}_{h,0}^d$ i.e., it only acts at the large scales of the flow in accordance with the simplified vision of the energy cascade presented at the end of section 2.1. We have also introduced another simplification in the expressions for the velocity residual as only the finite element component has been considered in the advective velocity term. Note, in addition, that no implicit time dependence of the subscales has been considered (*quasi-static* approach). On the other hand, the viscous term in the above equations has to be evaluated elementwise.

The stabilisation parameters appearing in (4.80)-(4.81) can be obtained from arguments based on a Fourier analysis for the subscales [44] that yield,

$$\tau_1 = \left[\left(c_1\frac{\nu}{h^2}\right)^2 + \left(c_2\frac{|\boldsymbol{u}_h|}{h}\right)^2\right]^{-1/2}, \tag{4.84}$$

$$\tau_2 = \frac{h^2}{c_1\tau_1}\,. \tag{4.85}$$

c_1 and c_2 in (4.84)-(4.85) are algorithmic parameters with recommended values of $c_1 = 4$ and $c_2 = 2$ for linear elements [41], while h stands for a characteristic mesh element size. Again, we have neglected the subscale contribution in the advective velocity of τ_1 (compare with the parameter expressions (3.52)-(3.53)). The choice (4.84)-(4.85) for the stabilisation parameters guarantees that the kinetic energy of the modelled subscales approximates the kinetic energy of the exact subscales [44]. In the forthcoming analysis we will consider τ_1 and τ_2 constant within each element and typified by a characteristic element velocity to be defined later on.

Equation (4.79) together with the approximation (4.80)-(4.81) for the subscales constitute a plausible numerical approach to solve the incompressible Navier-Stokes equations. It will be argued that this scheme should also be valid for the simulation of turbulent flows without the necessity to perform a LES scale separation at the continuous level, prior to the numerical discretisation.

Energy balance for the orthogonal subgrid scale finite element approach to the Navier-Stokes problem

In order to find an energy balance equation for the OSS numerical approach to the Navier-Stokes equations we can now set $\boldsymbol{v}_h = \boldsymbol{u}_h$ and $q_h = ct$ in (4.79). This yields (no approximation for the subscales is considered for the moment)

$$\begin{aligned}
&\frac{1}{2}\frac{d}{dt}\left\|\boldsymbol{u}_h\right\|^2 = -2\nu\left\|\boldsymbol{S}\left(\boldsymbol{u}_h\right)\right\|^2 \\
&-\sum_e \langle \tilde{\boldsymbol{u}}, 2\nu\boldsymbol{\mathcal{S}}\left(\boldsymbol{u}_h\right) + \nabla\cdot\left(\boldsymbol{u}_h\otimes\boldsymbol{u}_h\right)\rangle_{\Omega_e} + \sum_e \left(\tilde{p}, \nabla\cdot\boldsymbol{u}_h\right)_{\Omega_e} + \langle \boldsymbol{f}, \boldsymbol{u}_h\rangle,
\end{aligned} \tag{4.86}$$

where Ω_e denotes the domain of the e-th element. Here and below, the summations with index e are assumed to be extended over all elements.

If we now consider the subscale approximation (4.80)-(4.83) in (4.86) we obtain

$$\begin{aligned}
&\frac{1}{2}\frac{d}{dt}\left\|\boldsymbol{u}_h\right\|^2 = -2\nu\left\|\boldsymbol{S}\left(\boldsymbol{u}_h\right)\right\|^2 + \langle \boldsymbol{f}_h, \boldsymbol{u}_h\rangle \\
&-\sum_e \tau_1\big(\Pi_h^{\perp}\big[-2\nu\nabla\cdot\boldsymbol{\mathcal{S}}\left(\boldsymbol{u}_h\right) + \nabla\cdot\left(\boldsymbol{u}_h\otimes\boldsymbol{u}_h\right) + \nabla p_h\big], \\
&2\nu\nabla\cdot\boldsymbol{\mathcal{S}}\left(\boldsymbol{u}_h\right) + \nabla\cdot\left(\boldsymbol{u}_h\otimes\boldsymbol{u}_h\right)\big)_{\Omega_e} - \sum_e \tau_2\left(\Pi_h^{\perp}\left(\nabla\cdot\boldsymbol{u}_h\right), \nabla\cdot\boldsymbol{u}_h\right)_{\Omega_e}.
\end{aligned} \tag{4.87}$$

Since we are interested in high Reynolds numbers, all the stabilisation terms multiplied by the viscosity will be neglected, from where we obtain the following energy balance equation for the OSS stabilised finite element approach to the Navier-Stokes equations:

$$\begin{aligned}
&\frac{1}{2}\frac{d}{dt}\left\|\boldsymbol{u}_h\right\|^2 = -2\nu\left\|\boldsymbol{S}\left(\boldsymbol{u}_h\right)\right\|^2 + \langle \boldsymbol{f}_h, \boldsymbol{u}_h\rangle \\
&-\sum_e \tau_1\left(\Pi_h^{\perp}\left[\nabla\cdot\left(\boldsymbol{u}_h\otimes\boldsymbol{u}_h\right) + \nabla p_h\right], \nabla\cdot\left(\boldsymbol{u}_h\otimes\boldsymbol{u}_h\right)\right)_{\Omega_e} \\
&-\sum_e \tau_2\left(\Pi_h^{\perp}\left(\nabla\cdot\boldsymbol{u}_h\right), \nabla\cdot\boldsymbol{u}_h\right)_{\Omega_e}.
\end{aligned} \tag{4.88}$$

Let us define the pointwise numerical kinetic energy of the flow as $k^h := \frac{1}{2}\left|\boldsymbol{u}_h\right|^2$, the pointwise molecular numerical dissipation for the large scales as $\varepsilon^h_{\mathrm{mol}} := 2\nu\boldsymbol{S}\left(\boldsymbol{u}_h\right) : \boldsymbol{S}\left(\boldsymbol{u}_h\right)$ and the pointwise numerical power for the external force as $P_f^h := \boldsymbol{f}_h\cdot\boldsymbol{u}_h$. We will also identify $\mathcal{P}_r^{h\tau}$ within each element with

$$\mathcal{P}_r^{h\tau} := \tau_1\mathcal{P}_r^{h\tau_1} + \tau_2\mathcal{P}_r^{h\tau_2} \tag{4.89}$$

where

$$\mathcal{P}_r^{h\tau_1} := \Pi_h^{\perp}\left[\nabla\cdot(\boldsymbol{u}_h\otimes\boldsymbol{u}_h)+\nabla p_h\right]\cdot\left[\nabla\cdot(\boldsymbol{u}_h\otimes\boldsymbol{u}_h)\right] \tag{4.90}$$

$$\mathcal{P}_r^{h\tau_2} := \Pi_h^{\perp}\left(\nabla\cdot\boldsymbol{u}_h\right)\left(\nabla\cdot\boldsymbol{u}_h\right). \tag{4.91}$$

Equipped with these definitions, equation (4.88) can be rewritten as

$$\frac{d}{dt}\int_\Omega k^h d\Omega = -\int_\Omega \varepsilon_{\mathrm{mol}}^h d\Omega - \sum_e \int_{\Omega_e} \mathcal{P}_r^{h\tau} d\Omega_e + \int_\Omega P_f^h d\Omega\,, \tag{4.92}$$

which can be compared with the energy balance equation of the continuous problem (4.68), using similar arguments to those in section 2.2.

It is clear that k^h will account for nearly the whole pointwise kinetic energy of the flow so that $\int_\Omega k^h d\Omega \approx \int_\Omega k d\Omega$. On the other hand, it will also occur that $\int_\Omega P_f^h d\Omega \approx \int_\Omega P_f d\Omega$, given that the force only acts at the large scales. In addition the numerical molecular dissipation of the large scales will be negligible, so that $\int_\Omega \varepsilon_{\mathrm{mol}}^h d\Omega \approx 0$.

The next, crucial, question is if it should happen that $\sum_e \int_{\Omega_e} \mathcal{P}_r^{h\tau} d\Omega \approx \int_\Omega \varepsilon_{\mathrm{mol}} d\Omega$ for the OSS formulation to be a good numerical approach for the Navier-Stokes equations, in the case of fully developed turbulence. Actually, this should not be necessarily the case for all the terms in $\mathcal{P}_r^{h\tau}$, given that they have arisen in the equation motivated by pure numerical stabilisation necessities. However, it is clear that at least some of these terms should account for the appropriate physical behaviour and their domain integration should approximate the mean molecular dissipation in (4.68). It will be one of the main outcomes of this thesis to show, by means of heuristic reasoning, that actually the whole $\mathcal{P}_r^{h\tau}$ satisfies this assumption. It should be also noted that in the definition of $\mathcal{P}_r^{h\tau}$, the approximation for high Reynolds number flows was already performed (stabilisation terms multiplied by the viscosity have been neglected).

Energy balance for the orthogonal subgrid scale finite element approach to a LES model

We could now proceed to discretise the LES equations (4.73)-(4.74) using the OSS approach. The usual way to do so is by simply adding the Navier-Stokes stabilisation terms to the Galerkin discretisation of the LES equations, i.e., terms containing the residual stress tensor, $\boldsymbol{\mathcal{R}}$, are not included in the stabilisation terms (see e.g., [283]). This approach is in fact non consistent unless linear elements are used. However, in the OSS method this approach still makes sense given that the consistency error becomes optimal (see [45]).

The following discrete energy balance equation for the LES model analogous to (4.92) is obtained

$$\int_\Omega \frac{d\overline{k}^h}{dt} d\Omega = -\int_\Omega \overline{\varepsilon}_{\mathrm{mol}}^h d\Omega - \sum_e \int_{\Omega_e} \overline{\mathcal{P}}_r^{h\tau} d\Omega - \int_\Omega \overline{\mathcal{P}}_r^h d\Omega + \int_\Omega \overline{P}_f^h d\Omega\,, \tag{4.93}$$

with $k^h := \frac{1}{2}|\overline{\boldsymbol{u}}_h|^2$, $\overline{\varepsilon}^h_{\rm mol} := 2\nu \boldsymbol{S}(\overline{\boldsymbol{u}}_h) : \boldsymbol{S}(\overline{\boldsymbol{u}}_h)$, $\overline{P}^h_f := \overline{\boldsymbol{f}}_h \cdot \overline{\boldsymbol{u}}_h$, $\overline{\mathcal{P}}^h_r := -\boldsymbol{\mathcal{R}} : \boldsymbol{\mathcal{S}}(\overline{\boldsymbol{u}}_h)$ and $\overline{\mathcal{P}}^{h\tau}_r := -\sum_e \tau_1(\Pi^\perp_h[\nabla\cdot(\overline{u}_h\otimes\overline{u}_h)+\nabla\overline{p}_h], \Pi^\perp_h[\nabla\cdot(\overline{u}_h\otimes\overline{u}_h)])_{\Omega_e} - \sum_e \tau_2(\Pi^\perp_h(\nabla\cdot\overline{u}_h), \Pi^\perp_h(\nabla\cdot\overline{u}_h))_{\Omega_e}$. Following the argumentation lines in the above sections it is clear that the kinetic energy term will approximate the one in the exact energy balance equation (4.68). The same will prove true for the external force power and, again, $\overline{\varepsilon}^h_{\rm mol}$ will be negligible. However, we are now left with the curious fact that the two terms involving $\overline{\mathcal{P}}^{h\tau}_r$ and $\overline{\mathcal{P}}^h_r$ should equal, in the mean, the molecular physical dissipation. This seems at least redundant if the term containing $\overline{\mathcal{P}}^{h\tau}_r$ that arises from the discretisation of the original Navier-Stokes equation already presents this behaviour. In other words, the process of first filtering at the continuum level, modelling, and then proceeding to discretisation (LES method) looks unnecessary if an appropriate numerical discretisation scheme is used. Obviously, for an inaccurate discretisation scheme the addition of extra dissipation as that provided by LES may be useful, but this should not be the case. In the following sections we aim at giving support to this idea by means of some heuristic reasoning.

4.5 Subgrid energy transfer in the OSS FEM

4.5.1 Elemental ensemble average of $\mathcal{P}^{h\tau}_r$ for high Reynolds numbers

Stabilisation parameters at high Reynolds numbers

In (4.84) an expression is given for the stabilisation parameter τ_1. In the case of high Reynolds number flows the viscosity term in this expression can be discarded in front of the convective one, yielding

$$\tau_1 \approx \frac{h}{c_2\,|\boldsymbol{u}_h|}\ . \tag{4.94}$$

On the other hand, using (4.94) in the expression for the parameter τ_2 in (4.85) we get

$$\tau_2 \approx \frac{c_2}{c_1} h\,|\boldsymbol{u}_h|\ . \tag{4.95}$$

When using the above stabilisation parameters in a finite element implementation, h represents a characteristic element length of Ω_e, while $\boldsymbol{u}_h$ stands for a characteristic velocity at each element of the partition. Several options exist for the latter giving place to different OSS stabilisation methods. One could take for example the velocity mean value at the element or its root mean square value. Whatever choice is made the key point for the forthcoming results is that τ_1 should depend inversely on this characteristic velocity while τ_2 should be proportional to it. This behaviour will allow us to relate $\mathcal{P}^{h\tau}_r$ with the molecular dissipation rate $\varepsilon_{\rm mol}$, a fact that can be inversely be viewed as a confirmation of the right choice for τ_1 and τ_2 in (4.94)-(4.95).

As mentioned in the introduction, for a given computational mesh we will consider the case of the characteristic element size h being fine enough so as to lay in the inertial subrange. The inertial subrange can be thought as having limiting values $[l_{DI}, l_{EI}]$ with $l_{DI} \approx 60\eta$ and $l_{EI} \approx L/6$. η represents the Kolmogorov length where dissipation takes place and L corresponds to the flow scale typical of the largest, anisotropic eddies (see e.g., [255]). Let us denote by U the ensemble average (or time average under the ergodic assumption) of the chosen characteristic velocity at a given mesh element, to be used in the expressions for the stabilisation parameters. Kolomogorov's second similarity hypothesis then guarantees that for an eddy of size ℓ, such that $\ell \in [l_{DI}, l_{EI}]$, U can only depend on ε_{mol} and ℓ, actually $U \sim (\varepsilon_{\text{mol}}\ell)^{1/3}$. It then follows that the elemental stabilisation parameters become

$$\tau_{1,ae} \sim \frac{h}{U} \sim \frac{h}{(\varepsilon_{\text{mol}}\ell)^{1/3}}\,, \tag{4.96}$$

$$\tau_{2,ae} \sim hU \sim h\,(\varepsilon_{\text{mol}}\ell)^{1/3}\,, \tag{4.97}$$

where all constants have been included inside U. As previously mentioned, the symbol $\sim$ is used here to denote *behaves as*, that is, the terms related by this symbol are approximately equal up to constants. However, we will abuse of language and in what follows the equality sign will be frequently employed in expressions containing approximated terms of the type (4.96)-(4.97).

Elemental ensemble average of $\mathcal{P}_r^{h\tau_1}$

Let us denote by $\Pi_i^h\big[\nabla\cdot(\boldsymbol{u}_h\otimes\boldsymbol{u}_h)+\nabla p_h\big]$ the i-th component of the projector in the definition of the numerical subgrid kinetic energy transfer term $\mathcal{P}_r^{h\tau_1}$ in (4.90) and denote the i-th velocity component by u_{hi}.

We consider a finite element partition of the domain Ω having n_p pressure nodes, n_u velocity nodes and n_e elements. Following similar lines of what is done in [49] (although with a very different objective) we define the average value in a mesh element Ω_e of $\mathcal{P}_r^{h\tau_1}$ in (4.90) as

$$\begin{aligned}\mathcal{P}_{r,e}^{h\tau_1} &= \frac{1}{V_e}\int_{\Omega_e}\big(\mathcal{P}_r^{h\tau_1}\big)\,d\Omega_e \\ &= \frac{1}{V_e}\int_{\Omega_e}\Pi_i^{h,\perp}\big[\nabla\cdot(\boldsymbol{u}_h\otimes\boldsymbol{u}_h)+\nabla p_h\big]\cdot\big[\nabla\cdot(\boldsymbol{u}_h\otimes\boldsymbol{u}_h)\big]\,d\Omega_e.\end{aligned} \tag{4.98}$$

An ensemble average (or time average under the ergodic assumption) of this quantity can be performed to obtain

$$\big\langle\mathcal{P}_{r,e}^{h\tau_1}\big\rangle = \frac{1}{V_e}\left\langle\int_{\Omega_e}\Pi_i^{h,\perp}\big[\nabla\cdot(\boldsymbol{u}_h\otimes\boldsymbol{u}_h)+\nabla p_h\big]\cdot\big[\nabla\cdot(\boldsymbol{u}_h\otimes\boldsymbol{u}_h)\big]\,d\Omega_e\right\rangle \tag{4.99}$$

(Brackets are used in this section to denote ensemble average instead of duality pairing). We next identify the terms $\big\langle\mathcal{P}_{r,e}^{h\tau_1}\big\rangle_U$ and $\big\langle\mathcal{P}_{r,e}^{h\tau_1}\big\rangle_P$ in (4.99) that will be treated

independently in the analysis. We have

$$\begin{aligned}\left\langle \mathcal{P}_{r,e}^{h\tau_1} \right\rangle_U &:= \frac{1}{V_e} \left\langle \int_{\Omega_e} \Pi_i^{h,\perp} \big[\nabla \cdot (\boldsymbol{u}_h \otimes \boldsymbol{u}_h) \big] \cdot \big[\nabla \cdot (\boldsymbol{u}_h \otimes \boldsymbol{u}_h) \big] d\Omega_e \right\rangle \\ &= \frac{1}{V_e} \left\langle \int_{\Omega_e} \partial_i \left(u_i^h u_j^h \right) \partial_k \left(u_k^h u_j^h \right) d\Omega_e \right\rangle \\ &- \frac{1}{V_e} \left\langle \int_{\Omega_e} \Pi_i^h \big[\nabla \cdot (\boldsymbol{u}_h \otimes \boldsymbol{u}_h) \big] \partial_j \left(u_j^h u_i^h \right) d\Omega_e \right\rangle \end{aligned} \tag{4.100}$$

and

$$\begin{aligned}\left\langle \mathcal{P}_{r,e}^{h\tau_1} \right\rangle_P &:= \frac{1}{V_e} \left\langle \int_{\Omega_e} \Pi_i^{h,\perp} \big(\nabla p_h \big) \cdot \big[\nabla \cdot (\boldsymbol{u}_h \otimes \boldsymbol{u}_h) \big] d\Omega_e \right\rangle \\ &= \frac{1}{V_e} \left\langle \int_{\Omega_e} \partial_i p_h \partial_j \left(u_j^h u_i^h \right) d\Omega_e \right\rangle \\ &- \frac{1}{V_e} \left\langle \int_{\Omega_e} \Pi_i^h \big(\nabla p_h \big) \partial_j \left(u_j^h u_i^h \right) d\Omega_e \right\rangle , \end{aligned} \tag{4.101}$$

Above and in the following, summation is understood over spatial repeated indexes.

Obviously, we have

$$\left\langle \mathcal{P}_{r,e}^{h\tau_1} \right\rangle = \left\langle \mathcal{P}_{r,e}^{h\tau_1} \right\rangle_U + \left\langle \mathcal{P}_{r,e}^{h\tau_1} \right\rangle_P . \tag{4.102}$$

Elemental ensemble average of $\mathcal{P}_r^{h\tau_2}$

Proceeding analogously to what has been done in the previous section but for the $\mathcal{P}_r^{h\tau_2}$ term defined in (4.91), it can readily be checked that the elemental ensemble average of $\mathcal{P}_r^{h\tau_2}$ becomes

$$\begin{aligned}\left\langle \mathcal{P}_{r,e}^{h\tau_2} \right\rangle &:= \frac{1}{V_e} \left\langle \int_{\Omega_e} \Pi^{h,\perp} \big(\nabla \cdot \boldsymbol{u}_h \big) \big(\nabla \cdot \boldsymbol{u}_h \big) d\Omega_e \right\rangle \\ &= \frac{1}{V_e} \left\langle \int_{\Omega_e} \left(\partial_i u_i^h \right)^2 d\Omega_e \right\rangle - \frac{1}{V_e} \left\langle \int_{\Omega_e} \Pi^h \big(\nabla \cdot \boldsymbol{u}_h \big) \left(\partial_i u_i^h \right) d\Omega_e \right\rangle . \end{aligned} \tag{4.103}$$

Elemental ensemble average of $\mathcal{P}_r^{h\tau}$

From (4.89) and using the elemental stabilisation parameters (4.96)-(4.97) as well as (4.99) and (4.103), we can define the ensemble average of the rate of production of kinetic energy $\mathcal{P}_r^{h\tau}$ for high Reynolds numbers as

$$\left\langle \mathcal{P}_{r,e}^{h\tau} \right\rangle := \tau_{1,ae} \left\langle \mathcal{P}_{r,e}^{h\tau_1} \right\rangle + \tau_{2,ae} \left\langle \mathcal{P}_{r,e}^{h\tau_2} \right\rangle . \tag{4.104}$$

4.5.2 FEM solution and treatment of the L^2 projection in $\left\langle \mathcal{P}_{r,e}^{h\tau} \right\rangle$

FEM solution for the velocity and pressure fields and L^2 projection

The components of the discrete velocity field $\boldsymbol{u}_h$ can be expanded as usual for a mesh having n_u nodes as

$$u_i^h(\boldsymbol{x}) = \sum_{a=1}^{n_u} N_u^a(\boldsymbol{x})\, U_i^a, \tag{4.105}$$

where the velocity shape functions $\{N_u^a(\boldsymbol{x}), a = 1, \ldots, n_u\}$ are a basis of $\mathcal{V}_{0,h}^d$ and U_i^a are the velocity nodal values, i.e., at the nodal points, $\boldsymbol{x}^b$, $b = 1, \ldots, n_u$, it holds that

$$u_i^h(\boldsymbol{x}^b) = U_i^b. \tag{4.106}$$

In case of $\boldsymbol{u}_h$ being the finite element interpolant, the nodal values are exact and

$$u_i^h(\boldsymbol{x}^b) = U_i^b = u_i(\boldsymbol{x}^b) \equiv u_i^b. \tag{4.107}$$

Let us also assume the following interpolation for the Reynolds stresses (see e.g., [40])

$$u_i^h u_j^h(\boldsymbol{x}) = \sum_{b=1}^{n_u} N_u^b(\boldsymbol{x})\, U_i^b U_j^b \tag{4.108}$$

in order to have simpler expressions and to make some of the forthcoming results useful from a computational point of view.

Concerning the discrete pressure field, p_h, it will be expanded as

$$p_h(\boldsymbol{x}) = \sum_{a=1}^{n_p} N_p^a(\boldsymbol{x})\, P^a, \tag{4.109}$$

where the pressure shape functions $\left\{N_p^a(\boldsymbol{x}), a = 1, \ldots, n_p\right\}$ are a basis of $\mathcal{Q}_{h,0}$ and P^a denotes the pressure nodal value at node $\boldsymbol{x}^a$. We note that one of the advantages of using a stabilised finite element method such as the OSS in section 2.3.2 is that one can choose $N_u^a = N_p^a \equiv N^a$, hence circumventing the necessity of using different interpolations for the velocity and pressure fields as demanded by the *inf-sup* condition (see e.g. [42–44, 150, 153]).

On the other hand, it will be necessary to give explicit expressions for the projected terms $\Pi_i^h\left[\nabla\cdot(\boldsymbol{u}_h \otimes \boldsymbol{u}_h)\right]$ and $\Pi_i^h\left(\nabla p_h\right)$ appearing in (4.100), (4.101) and (4.103). This can be done as follows. Consider a function ψ_h computed from the finite element interpolation, not necessarily continuous. Its L^2 projection onto $\mathcal{V}_{h,0}^d$ can be written as

$$\Pi(\psi_h) = \sum_{a=1}^{n_u} N^a(\boldsymbol{x})\, \Pi^a, \tag{4.110}$$

with the coefficients Π^a being given by the solution of the linear system

$$\sum_{a=1}^{n_u} M^{ba}\Pi^a = \int_\Omega N^b \psi_h d\Omega, \quad b = 1, \ldots, n_u \tag{4.111}$$

$$M^{ba} := \int_\Omega N^b N^a d\Omega. \tag{4.112}$$

The mass matrix $\boldsymbol{M}$ in (4.112) can be approximated by means of a diagonal matrix $\mathrm{diag}(\mathcal{M}_{11}, \ldots, \mathcal{M}_{n_u n_u})$ using a standard nodal quadrature rule. In this case

$$\Pi^b = \mathcal{M}_{bb}^{-1} \int_\Omega N^b \psi_h d\Omega, \tag{4.113}$$

so (4.112) becomes

$$\Pi(\psi_h) = \sum_{a=1}^{n_u} \mathcal{M}_{aa}^{-1} N^a \int_\Omega N^a \psi_h d\Omega\,. \tag{4.114}$$

$\left\langle \mathcal{P}_{r,e}^{h\tau} \right\rangle$ in terms of the finite element velocity and pressure fields

We next have to substitute the above expansions for the discrete velocity and pressure fields in the expressions for $\left\langle \mathcal{P}_{r,e}^{h\tau_1} \right\rangle_U$, $\left\langle \mathcal{P}_{r,e}^{h\tau_1} \right\rangle_P$ and $\left\langle \mathcal{P}_{r,e}^{h\tau_2} \right\rangle$, respectively given by equations (4.100), (4.101) and (4.103).

Convective term $\left\langle \mathcal{P}_{r,e}^{h\tau_1} \right\rangle_U$ corresponding to the velocity subscales (4.100). We will first address the term in the second line of (4.100), which will be denoted by $\left\langle \mathcal{P}_{r,e}^{h\tau_1} \right\rangle_{U,1}$. Substituting (4.108) in this term yields

$$\begin{aligned}\left\langle \mathcal{P}_{r,e}^{h\tau 1} \right\rangle_{U,1} &= \frac{1}{V_e}\left\langle \int_{\Omega_e} \left[\sum_a \partial_i N^a U_i^a U_j^a \sum_b \partial_k N^b U_k^b U_j^b \right] d\Omega_e \right\rangle \\ &= \frac{1}{V_e}\left[\sum_{a,b} \left\langle U_i^a U_j^a U_k^b U_j^b \right\rangle \int_{\Omega_e} \partial_i N^a \partial_k N^b d\Omega_e \right].\end{aligned} \tag{4.115}$$

The term in the third line of (4.100) will be denoted by $\left\langle \mathcal{P}_{r,e}^{h\tau_1} \right\rangle_{U,2}$. After substituting (4.108) and (4.114) in it, we get

$$\begin{aligned}\left\langle \mathcal{P}_{r,e}^{h\tau_1} \right\rangle_{U,2} &= -\frac{1}{V_e}\left\langle \int_{\Omega_e} \left[\sum_{a,c} \mathcal{M}_{cc}^{-1} N^c \int_\Omega N^c \partial_i N^a U_i^a U_j^a d\Omega \sum_b \partial_k N^b U_k^b U_j^b \right] d\Omega_e \right\rangle \\ &= -\frac{1}{V_e}\left\{ \sum_{a,b} \left\langle U_i^a U_j^a U_k^b U_j^b \right\rangle \int_{\Omega_e} \left[\partial_k N^b \sum_c \mathcal{M}_{cc}^{-1} N^c \int_\Omega N^c \partial_i N^a d\Omega \right] d\Omega_e \right\}.\end{aligned} \tag{4.116}$$

To facilitate the notation in expressions (4.115) and (4.116) we define the geometric factors

$$I_{ij}^{ab} := \int_{\Omega_e} \partial_j N^b \partial_i N^a d\Omega_e \tag{4.117}$$

and

$$G_{ij}^{ab} := \int_{\Omega_e} \left[\partial_j N^b \sum_c \mathcal{M}_{cc}^{-1} N^c \int_{\Omega} N^c \partial_i N^a d\Omega \right] d\Omega_e. \tag{4.118}$$

Both factors depend on the element Ω_e. However, while I_{ij}^{ab} has a *local* character in the sense that it only depends on the shape functions and the type of element being used, G_{ij}^{ab} has a *global* character because it involves an integration over the whole computational domain Ω. This global character is due to the fact that a projection is involved in $\left\langle \mathcal{P}_{r,e}^{h\tau_1} \right\rangle_{U,2}$.

Using the notation in (4.36)-(4.37) for the velocity correlation function

$$B_{ij}^{ab} = \left\langle U_i^a U_j^b \right\rangle. \tag{4.119}$$

and for the two point fourth moment of the velocity field

$$B_{ij,kl}^{ab} = \left\langle U_i^a U_j^a U_k^b U_l^b \right\rangle, \tag{4.120}$$

we can insert (4.117)-(4.120) in equations (4.115) and (4.116), to obtain the following expansion for the convective term $\left\langle \mathcal{P}_{r,e}^{h\tau_1} \right\rangle_U$:

$$\left\langle \mathcal{P}_{r,e}^{h\tau_1} \right\rangle_U = \left\langle \mathcal{P}_{r,e}^{h\tau_1} \right\rangle_{U,1} + \left\langle \mathcal{P}_{r,e}^{h\tau_1} \right\rangle_{U,2} = \frac{1}{V_e} \sum_{a,b} B_{ij,kj}^{ab} \left(I_{ik}^{ab} - G_{ik}^{ab} \right). \tag{4.121}$$

Summation on the spatial dimension indexes i, j, k is assumed in (4.121), whereas summation on nodes will be explicitly indicated throughout the text for the sake of clarity.

Pressure term $\left\langle \mathcal{P}_{r,e}^{h\tau_1} \right\rangle_P$ corresponding to the velocity subscales (4.101). It will be next found an expression similar to (4.121) but for the pressure term $\left\langle \mathcal{P}_{r,e}^{h\tau_1} \right\rangle_P$. Making use of (4.108) and (4.109) in (4.101), we get for the term in the second line of (4.101), which we denote $\left\langle \mathcal{P}_{r,e}^{h\tau_1} \right\rangle_{P,1}$,

$$\begin{aligned} \left\langle \mathcal{P}_{r,e}^{h\tau_1} \right\rangle_{P,1} &= \frac{1}{V_e} \left\langle \int_{\Omega_e} \left[\sum_a \partial_i N^a P^a \sum_b \partial_j N^b U_j^b U_i^b \right] d\Omega_e \right\rangle \\ &= \frac{1}{V_e} \left[\sum_{a,b} \left\langle P^a U_j^b U_i^b \right\rangle \int_{\Omega_e} \partial_i N^a \partial_j N^b d\Omega_e \right]. \end{aligned} \tag{4.122}$$

Using now (4.108), (4.109) and (4.114) in the third line of (4.101), we obtain

$$\begin{aligned} \left\langle \mathcal{P}_{r,e}^{h\tau_1} \right\rangle_{P,2} &= -\frac{1}{V_e} \left\langle \int_{\Omega_e} \left[\sum_{a,c} \mathcal{M}_{cc}^{-1} N^c \int_{\Omega} N^c \partial_i N^a P^a d\Omega \sum_b \partial_j N^b U_j^b U_i^b \right] d\Omega_e \right\rangle \\ &= -\frac{1}{V_e} \left\{ \sum_{a,b} \left\langle P^a U_j^b U_i^b \right\rangle \int_{\Omega_e} \left[\partial_j N^b \sum_c \mathcal{M}_{cc}^{-1} N^c \int_{\Omega} N^c \partial_i N^a d\Omega \right] d\Omega_e \right\}. \end{aligned} \tag{4.123}$$

Given the geometric factors (4.117)-(4.118) and using the notation (4.38) for the two point triple velocity-pressure correlation

$$B^{ab}_{p,ij} = \left\langle P^a U^b_i U^b_j \right\rangle, \tag{4.124}$$

we can rewrite $\left\langle \mathcal{P}^{h\tau_1}_{r,e} \right\rangle_P$ as

$$\left\langle \mathcal{P}^{h\tau_1}_{r,e} \right\rangle_P = \left\langle \mathcal{P}^{h\tau_1}_{r,e} \right\rangle_{P,1} + \left\langle \mathcal{P}^{h\tau_1}_{r,e} \right\rangle_{P,2} = \frac{1}{V_e} \sum_{a,b} B^{ab}_{p,ij} \left(I^{ab}_{ij} - G^{ab}_{ij} \right), \tag{4.125}$$

with summation implied on indexes i, j.

Divergence term $\left\langle \mathcal{P}^{h\tau_2}_{r,e} \right\rangle$ corresponding to the pressure subscales (4.103). It can be readily checked that the expression analogous to (4.121) and (4.125) for the term $\left\langle \mathcal{P}^{h\tau_2}_{r,e} \right\rangle$ in (4.103) is given by

$$\left\langle \mathcal{P}^{h\tau_2}_{r,e} \right\rangle_P = \frac{1}{V_e} \sum_{a,b} B^{ab}_{ij} \left(I^{ab}_{ij} - G^{ab}_{ij} \right), \tag{4.126}$$

with B^{ab}_{ij} being the second-order velocity correlations (4.119).

Finite element expression for $\left\langle \mathcal{P}^{h\tau}_{r,e} \right\rangle$. Using the developments (4.121), (4.125) and (4.126) in equations (4.102) and (4.104) we obtain the finite element expression for the ensemble average of the rate of production of subgrid kinetic energy

$$\begin{aligned} \left\langle \mathcal{P}^{h\tau}_{r,e} \right\rangle &= \tau_{1,ae} \left\langle \mathcal{P}^{h\tau_1}_{r,e} \right\rangle + \tau_{2,ae} \left\langle \mathcal{P}^{h\tau_2}_{r,e} \right\rangle \\ &= \frac{1}{V_e} \sum_{a,b} \left[\tau_{1,ae} \left(B^{ab}_{ij,kj} + B^{ab}_{p,ik} \right) + \tau_{2,ae} B^{ab}_{ik} \right] \left(I^{ab}_{ik} - G^{ab}_{ik} \right). \end{aligned} \tag{4.127}$$

4.6 Numerical energy transfer and physical dissipation

4.6.1 Two point fourth-order velocity correlations for $\left\langle \mathcal{P}^{h\tau_1}_{r,e} \right\rangle_U$

Given that I^{ab}_{ij} and G^{ab}_{ij} in (4.117)-(4.118) are pure geometric factors, in order to relate the expression (4.127) for $\left\langle \mathcal{P}^{h\tau}_{r,e} \right\rangle$ with the physical molecular dissipation, ε_{mol}, we will have to relate the various second-order and fourth-order velocity correlations B^{ab}_{ij}, $B^{ab}_{ij,kl}$ and the two point triple velocity-pressure correlation $B^{ab}_{p,ij}$ to it.

To do so, use will be made in what follows of some results of statistical fluid mechanics and in particular of statistics concerning homogeneous isotropic turbulence. Although the various correlations B^{ab}_{ij}, $B^{ab}_{ij,kl}$ and $B^{ab}_{p,ij}$ do not involve the whole velocity and pressure fields at the nodes, but their OSS finite element approximation, we will consider that the results from statistical fluid mechanics can be still applied to them. Note that in the case of $[\boldsymbol{u}_h, p_h]$ being the interpolant, see (4.107), no approximation would be needed. We then

guess that the velocity and pressure from the OSS finite element solution will not differ substantially from the interpolant, at least in what concerns their statistical behaviour. This is also implicitly assumed in practical implementations of the results in [49].

Let us start with the two point fourth moment velocity correlation $B^{ab}_{ij,kl}$, which by virtue of its definition (4.120) fulfills

$$B^{ab}_{ij,kl} = B^{ab}_{ji,kl} = B^{ab}_{ji,lk} = B^{ab}_{ij,lk}. \tag{4.128}$$

Use can be made of the *quasi-normal* approximation (*Millionshchikov zero-fourth-cumulant hypothesis*, see e.g., [232]) in order to relate the fourth-order velocity correlations with second-order velocity correlations. For the particular case of velocities being considered at just two points, the quasi-normal approximation for the exact velocity field establishes

$$\left\langle u^a_i u^a_j u^b_k u^b_l \right\rangle = \left\langle u^a_i u^a_j \right\rangle \left\langle u^b_k u^b_l \right\rangle + \left\langle u^a_i u^b_k \right\rangle \left\langle u^a_j u^b_l \right\rangle + \left\langle u^a_i u^b_l \right\rangle \left\langle u^a_j u^b_k \right\rangle. \tag{4.129}$$

Assuming that this relation holds true for the finite element velocity field, we can rewrite it using the notation (4.119)-(4.120) to obtain

$$B^{ab}_{ij,kl} = B^{aa}_{ij} B^{bb}_{kl} + B^{ab}_{ik} B^{ab}_{jl} + B^{ab}_{il} B^{ab}_{jk}. \tag{4.130}$$

In our case, the two-point fourth-order velocity correlation in (4.121) and (4.127) is contracted on the second and fourth indexes so that

$$B^{ab}_{ij,kj} = B^{aa}_{ij} B^{bb}_{kj} + B^{ab}_{ik} B^{ab}_{jj} + B^{ab}_{ij} B^{ab}_{jk}. \tag{4.131}$$

The second-order velocity correlations can be related to the second-order velocity structure function D^{ab}_{ij} in (4.39) now given by

$$D^{ab}_{ij} = \left\langle \left(U^b_i - U^a_i\right) \left(U^b_j - U^a_j\right) \right\rangle. \tag{4.132}$$

Developing (4.132) and under the assumption of homogeneous isotropic turbulence (which implies that $B^{ab}_{ij} = B^{ba}_{ij}$, $B^{aa}_{ij} = B^{bb}_{ij}$, see for example [232]) it is straightforward to see that

$$B^{ab}_{ij} = B^{aa}_{ij} - \frac{1}{2} D^{ab}_{ij} = \frac{1}{3} \left|\boldsymbol{U}\right|^2 \delta_{ij} - \frac{1}{2} D^{ab}_{ij}, \tag{4.133}$$

with $\boldsymbol{U}$ representing the ensemble average of the velocity either at node a or b, since both must be the same.

Substituting (4.133) into (4.131) yields

$$B^{ab}_{ij,kj} = \frac{5}{9} \left|\boldsymbol{U}\right|^4 \delta_{ik} - \frac{5}{6} \left|\boldsymbol{U}\right|^2 D^{ab}_{ik} - \frac{1}{6} \left|\boldsymbol{U}\right|^2 \delta_{ik} D^{ab}_{jj} + \frac{1}{4} \left(D^{ab}_{jj} D^{ab}_{ik} + D^{ab}_{ij} D^{ab}_{jk}\right). \tag{4.134}$$

The first term in (4.134) can be neglected in what follows given that it will vanish when finally inserted in (4.121). This is so because it can be factorized out of the summation

on nodes in this expression. The summation can be carried inside the integrals in (4.117)-(4.118), which will then contain terms of the type $\partial_i \left(\sum_a N^a\right)$. Given that the shape functions form a partition of unity, $\sum_a N^a = 1$ and the derivative of this term is obviously zero (velocity boundary conditions need not to be considered at this point).

As previously mentioned, a computational mesh with its characteristic length h lying in the inertial subrange $[\, l_{DI}, l_{EI}]$ is considered. Combining the Kolmogorov first and second similarity hypothesis, an expression for the second order structure function D_{ij}^{ab} can be found solely in terms of ε_{mol} and the distance between nodes $\boldsymbol{x}^a$ and $\boldsymbol{x}^b$, $r^{ab} = \left\|\boldsymbol{x}^a - \boldsymbol{x}^b\right\|$, for $r^{ab} \in [\, l_{DI}, l_{EI}]$ (see section 4.3.2). The expression is given by (4.46), which we rewrite for convenience as

$$D_{ij}^{ab} = 2C \left(\varepsilon_{\text{mol}} r^{ab}\right)^{2/3} \mathcal{D}_{ij}^{ab}, \quad \mathcal{D}_{ij}^{ab} := \frac{1}{6}\left(4\delta_{ij} - \frac{r_i^{ab} r_j^{ab}}{(r^{ab})^2}\right). \tag{4.135}$$

Substituting (4.135) in (4.134) gives

$$\begin{aligned} B_{ij,kj}^{ab} = -\frac{11}{18}\left|\boldsymbol{U}\right|^2 C \left(\varepsilon_{\text{mol}} r^{ab}\right)^{2/3} \delta_{ik} + \Bigg[-\frac{5}{3}\left|\boldsymbol{U}\right|^2 C \left(\varepsilon_{\text{mol}} r^{ab}\right)^{2/3} \\ + \frac{11}{6} C^2 \left(\varepsilon_{\text{mol}} r^{ab}\right)^{4/3} \Bigg] \mathcal{D}_{ik}^{ab} + C^2 \left(\varepsilon_{\text{mol}} r^{ab}\right)^{4/3} \mathcal{D}_{ij}^{ab} \mathcal{D}_{jk}^{ab}. \end{aligned} \tag{4.136}$$

We can now make use again of Kolmogorov's second similarity hypothesis, which as explained in section 3.1.1 states that for an eddy of size $\ell \in [l_{DI}, l_{EI}]$ (i.e. lying in the inertial subrange) all velocity scales are proportional to $\left(\varepsilon_{\text{mol}}\ell\right)^{1/3}$. Since $|\boldsymbol{U}|$ is a velocity, it follows that

$$\left|\boldsymbol{U}\right| \sim \left(\varepsilon_{\text{mol}}\ell\right)^{1/3} \tag{4.137}$$

and substituting in (4.136)

$$\begin{aligned} B_{ij,kj}^{ab} = C\varepsilon_{\text{mol}}^{4/3} \Bigg\{ -\frac{11}{18}\ell^{2/3} \left(r^{ab}\right)^{2/3} \delta_{ik} + \Bigg[-\frac{5}{3}\ell^{2/3} \left(r^{ab}\right)^{2/3} \\ + \frac{11}{6} C \left(r^{ab}\right)^{4/3} \Bigg] \mathcal{D}_{ik}^{ab} + C \left(r^{ab}\right)^{4/3} \mathcal{D}_{ij}^{ab} \mathcal{D}_{jk}^{ab} \Bigg\} =: \varepsilon_{\text{mol}}^{4/3} \mathcal{K}_{ik}^{ab}, \end{aligned} \tag{4.138}$$

where $\mathcal{K}_{ik}^{ab}$ has been defined in the last line of (4.138).

In view of (4.138), equation (4.121) for $\left\langle \mathcal{P}_{r,e}^{h\tau_1} \right\rangle_U$ can be rewritten as

$$\left\langle \mathcal{P}_{r,e}^{h\tau_1} \right\rangle_U = \frac{1}{V_e} \varepsilon_{\text{mol}}^{4/3} \sum_{a,b} \mathcal{K}_{ik}^{ab} \left(I_{ik}^{ab} - G_{ik}^{ab}\right). \tag{4.139}$$

4.6.2 Two point triple-order velocity pressure correlations for $\left\langle \mathcal{P}_{r,e}^{h\tau_1} \right\rangle_P$

It is our aim now to find an expression analogous to (4.139) but relating the two point triple-order velocity-pressure correlation $B_{p,ij}^{ab}$ with the rate of physical dissipation ε_{mol}.

To do so we will closely follow [232] although with some particularities. We will abuse of notation and use $B^{ab}_{p,ij}$ to denote the triple-order velocity-pressure correlations of either the exact velocity field or the finite element approximated one. Whether equations are valid for one or the other, or for both of them, can be easily determined by the context. Likewise, we will identify $r \equiv r^{ab}$, being clear that this is the distance between nodes $\boldsymbol{x}^a$ and $\boldsymbol{x}^b$.

The tensor of second rank $B^{ab}_{p,kl}$ for the isotropic case can be written as

$$B^{ab}_{p,kl} = P_1(r)\, r_k r_l + P_2(r)\, \delta_{kl}, \tag{4.140}$$

where

$$P_1(r) = \frac{1}{r^2}\left[B^{ab}_{p,LL} - B^{ab}_{p,NN}\right], \quad P_2(r) = B^{ab}_{p,NN}, \tag{4.141}$$

with the subscript L standing again for *longitudinal* and designating the direction of the vector $\boldsymbol{r}^{ab}$ and N standing for *normal* and designating any perpendicular direction to it.

Consider the Poisson equation for the pressure at node a

$$\Delta p = -\rho \partial_{r_i} \partial_{r_j} \left(u^a_i u^a_j\right) \tag{4.142}$$

where Δ is the Laplacian operator that for functions only depending on r becomes

$$\Delta = \frac{d^2}{dr^2} + \frac{2}{r}\frac{d}{dr}. \tag{4.143}$$

Multiplying both sides of (4.142) by $u^b_k u^b_l$ and performing an ensemble average of the results yields

$$\Delta B^{ab}_{p,kl} = -\rho \partial_{r_i} \partial_{r_j} \left(B^{ab}_{ij,kl}\right). \tag{4.144}$$

In the case of homogeneous isotropic turbulence, the tensor in the r.h.s of (4.144) is an isotropic symmetric tensor of second rank that can be expressed as

$$\partial_{r_i} \partial_{r_j} \left(B^{ab}_{ij,kl}\right) = Q_1(r)\, r_k r_l + Q_2(r)\, \delta_{kl}. \tag{4.145}$$

Inserting (4.140) and (4.145) in (4.144) and equating the coefficients of $r_k r_l$ and δ_{kl} on both sides yields two differential equations for the unknowns P_1 and P_2:

$$\frac{d^2 P_1}{dr^2} + \frac{6}{r}\frac{dP_1}{dr} = -\rho Q_1. \tag{4.146}$$

$$\frac{d^2 P_2}{dr^2} + \frac{2}{r}\frac{dP_2}{dr} + 2P_1 = -\rho Q_2. \tag{4.147}$$

These equations can be uncoupled defining a new function P_3 such that

$$P_3(r) = r^2 P_1(r) + 3P_2(r) = B^{ab}_{p,LL} + 2B^{ab}_{p,NN}. \tag{4.148}$$

Multiplying (4.146) by r^2 and adding the result to (4.147) multiplied by 3 gives the following equation for P_3:

$$\frac{d^2P_3}{dr^2} + \frac{2}{r}\frac{dP_3}{dr} = -\rho Q_3, \tag{4.149}$$

where

$$Q_3(r) = r^2 Q_1(r) + 3Q_2(r). \tag{4.150}$$

In order to find the two point triple-order velocity-pressure correlation $B^{ab}_{p,kl}$ in (4.140) we need the values of P_1 and P_2, which can be obtained from the solutions of the equations (4.146) and (4.149) together with (4.148). However, to solve these equations we first need a value for their inhomogeneous terms Q_1 and Q_3. To do so, the use of the quasi-normal approximation and of Kolmogorov's similarity hypotheses will prove very useful again. We remind that our interest is in finding the results for r in the inertial subrange $[l_{DI}, l_{EI}]$.

Making use of the quasi-normal approximation (4.130) in (4.145) and taking into account that due to the incompressibility constraint $\partial_{r_i} B^{ab}_{ij} = \partial_{r_j} B^{ab}_{ij} = 0$ (see [232]), it follows that

$$Q_1(r)\, r_k r_l + Q_1(r)\, \delta_{kl} = \partial_{r_i}\partial_{r_j}\left(B^{ab}_{ij,kl}\right) = 2\partial_{r_j} B^{ab}_{ik}\partial_{r_i} B^{ab}_{jl} \tag{4.151}$$

and given that the second-order velocity correlation tensor B^{ab}_{ij} for homogeneous isotropic turbulence can be expressed as [232]

$$B^{ab}_{ij} = -\partial_r B^{ab}_{LL}(r)\frac{r_i r_j}{r} + \left[B^{ab}_{LL}(r) + \frac{r}{2}\partial_r B^{ab}_{LL}\right], \tag{4.152}$$

we can obtain the following expressions for Q_1, Q_2 and Q_3 solely in terms of the longitudinal second-order velocity correlation B^{ab}_{LL}:

$$Q_1(r) = \frac{6}{r^2}\left[\frac{d}{dr}B^{ab}_{LL}(r)\right]^2 + \frac{1}{r}\frac{d}{dr}B^{ab}_{LL}(r)\frac{d^2}{dr^2}B^{ab}_{LL}(r), \tag{4.153}$$

$$Q_2(r) = -3\left[\frac{d}{dr}B^{ab}_{LL}(r)\right]^2 - r\frac{d}{dr}B^{ab}_{LL}(r)\frac{d^2}{dr^2}B^{ab}_{LL}(r), \tag{4.154}$$

$$Q_3(r) = -\frac{1}{r^2}\frac{d}{dr}\left\{r^3\left[\frac{d}{dr}B^{ab}_{LL}(r)\right]^2\right\}. \tag{4.155}$$

Use has been made of (4.150) to obtain the expression for Q_3.

Up to know we have followed [232], which should be consulted for details. We can next use (4.133) to relate B^{ab}_{LL} with the longitudinal velocity structure function D^{ab}_{LL} and the rate of dissipation ε_{mol}:

$$B^{ab}_{LL} = B^{aa}_{LL} - \frac{1}{2}D^{ab}_{LL} = B^{aa}_{LL} - \frac{C}{2}\left(\varepsilon_{\text{mol}} r\right)^{2/3}. \tag{4.156}$$

Substituting (4.156) in (4.153) and (4.155) results in

$$Q_1(r) = \frac{17}{27} C^2 \varepsilon_{\text{mol}}^{4/3} r^{-8/3}, \tag{4.157}$$

$$Q_3(r) = -\frac{7}{27} C^2 \varepsilon_{\text{mol}}^{4/3} r^{-2/3}. \tag{4.158}$$

The solutions to equations (4.146) and (4.149) with the inhomogeneous terms given by (4.157) and (4.158) and appropriate boundary conditions can be found using the Green's function approach. This is the procedure we will follow next.

We will first address the problem of finding the solution $P_1(r)$ of the inhomogeneous equation (4.146). The solutions to the homogeneous counterpart of (4.146) are 1 and r^{-5} so that the problem Green's function will be of the type

$$G_1(r, r_0) = \begin{cases} A + Br^{-5} \equiv G_1^{<}(r, r_0) & l_{DI} < r < r_0 \\ \\ C + Dr^{-5} \equiv G_1^{>}(r, r_0) & r_0 < r < l_{EI}\ . \end{cases} \tag{4.159}$$

To determine the values of A, B, C and D we impose the boundary conditions at the inertial range threshold values $[\, l_{DI}, l_{EI}]$

$$G_1(l_{DI}, r_0) = K_{D1}, \tag{4.160}$$

$$G_1(l_{EI}, r_0) = K_{E1}, \tag{4.161}$$

with K_{D1}, K_{E1} constants. We also impose the continuity conditions

$$G_1^{>}\left(r_0^{+}, r_0\right) - G_1^{<}\left(r_0^{-}, r_0\right) = 0 \tag{4.162}$$

$$\partial_r G_1^{>}\left(r_0^{+}, r_0\right) - \partial_r G_1^{<}\left(r_0^{-}, r_0\right) = -1 \tag{4.163}$$

with $G_1^{\gtrless}\left(r_0^{\pm}, r_0\right) \equiv \lim_{\substack{r \to r_0 \\ r \gtrless r_0}} G_1^{\gtrless}(r, r_0)$. Defining the constants

$$L_{\Delta E} := \frac{l_{EI}^5}{l_{EI}^5 - l_{DI}^5}, \quad L_{\Delta D} := \frac{l_{DI}^5}{l_{EI}^5 - l_{DI}^5}, \quad L_{ED} := \frac{l_{EI}^5 l_{DI}^5}{l_{EI}^5 - l_{DI}^5}, \tag{4.164}$$

as well as

$$A_{01} := L_{\Delta E} K_{E1} - L_{\Delta D} K_{D1}, \quad A_{11} := -L_{ED}\left(K_{E1} - K_{D1}\right), \quad A_{21} := -\frac{L_{ED}}{l_{EI}^5 l_{DI}^5}, \tag{4.165}$$

it can readily be checked that the following expression is obtained for the Green function in (4.159)

$$G_1(r, r_0) = \begin{cases} \left(A_{01} + A_{11} r^{-5}\right) + \frac{1}{5}\left(L_{\Delta E} - L_{ED} r^{-5}\right) r_0 \\ \quad + \frac{1}{5}\left(A_{21} + L_{\Delta D} r^{-5}\right) r_0^6 & l_{DI} < r < r_0 \\ \\ \left(A_{01} + A_{11} r^{-5}\right) + \frac{1}{5}\left(L_{\Delta D} - L_{ED} r^{-5}\right) r_0 \\ \quad + \frac{1}{5}\left(A_{21} + L_{\Delta E} r^{-5}\right) r_0^6 & r_0 < r < l_{EI}\ . \end{cases} \tag{4.166}$$

Using (4.166) and the inhomogeneous term $Q_1(r)$ given by (4.157), $P_1(r)$ can be found as

$$\begin{aligned} P_1(r) &= -\rho \int_{l_{DI}}^{r} G_1^{>}(r,r_0)\, Q_1(r_0)\, dr_0 - \rho \int_{r}^{l_{EI}} G_1^{<}(r,r_0)\, Q_1(r_0)\, dr_0 \\ &= -\frac{17}{27}\rho C^2 \varepsilon_{\text{mol}}^{4/3} \left[F_{01}\frac{1}{r^5} + F_{11}\frac{1}{r^{2/3}} + F_{21} \right] =: -\frac{17}{27}\rho C^2 \varepsilon_{\text{mol}}^{4/3} F_1^{ab}(r)\,, \end{aligned} \tag{4.167}$$

where

$$\begin{aligned} F_{01} &:= -\frac{3}{5}\left(l_{EI}^{-5/3} - l_{DI}^{-5/3}\right) A_{11} + \frac{3}{10}\left(l_{EI}^{-2/3} - l_{DI}^{-2/3}\right) L_{ED} \\ &\quad + \frac{3}{65}\left(L_{\Delta D} l_{EI}^{13/3} - L_{\Delta E} l_{DI}^{13/3}\right), \end{aligned} \tag{4.168}$$

$$F_{11} := \frac{33}{130}\left(L_{\Delta E} - L_{\Delta D}\right), \tag{4.169}$$

$$\begin{aligned} F_{21} &:= -\frac{3}{5}\left(l_{EI}^{-5/3} - l_{DI}^{-5/3}\right) A_{01} + \frac{3}{65}\left(l_{EI}^{13/3} - l_{DI}^{13/3}\right) A_{21} \\ &\quad + \frac{3}{10}\left(L_{\Delta D} l_{DI}^{-2/3} - L_{\Delta E} l_{EI}^{-2/3}\right), \end{aligned} \tag{4.170}$$

and we have defined $F_1^{ab}(r)$ in the last line of (4.167).

We can now proceed analogously to find the solution $P_3(r)$ to equation (4.149). The solutions for the homogeneous counterpart of this equation are 1 and r^{-1} so that the Green function will behave as

$$G_3(r,r_0) = \begin{cases} A + Br^{-1} \equiv G_3^{<}(r,r_0) & l_{DI} < r < r_0 \\ \\ C + Dr^{-1} \equiv G_3^{>}(r,r_0) & r_0 < r < l_{EI}\,. \end{cases} \tag{4.171}$$

To find A, B, C and D in (4.171) we impose the boundary conditions

$$G_3(l_{DI}, r_0) = K_{D3}, \tag{4.172}$$

$$G_3(l_{EI}, r_0) = K_{E3}, \tag{4.173}$$

as well as the continuity conditions

$$G_3^{>}\left(r_0^+, r_0\right) - G_3^{<}\left(r_0^-, r_0\right) = 0 \tag{4.174}$$

$$\partial_r G_3^{>}\left(r_0^+, r_0\right) - \partial_r G_3^{<}\left(r_0^-, r_0\right) = -1. \tag{4.175}$$

Defining the new constants

$$\ell_{\Delta E} := \frac{l_{EI}}{l_{EI} - l_{DI}}, \quad \ell_{\Delta D} := \frac{l_{DI}}{l_{EI} - l_{DI}}, \quad \ell_{ED} := \frac{l_{EI} l_{DI}}{l_{EI} - l_{DI}}, \tag{4.176}$$

and

$$A_{03} := \ell_{\Delta E} K_{E3} - \ell_{\Delta D} K_{D3}, \quad A_{13} := -\ell_{ED}\left(K_{E3} - K_{D3}\right), \quad A_{23} := -\frac{\ell_{ED}}{l_{EI} l_{DI}}, \tag{4.177}$$

the Green function (4.171) can be written as

$$G_3(r,r_0)=\begin{cases}(A_{03}+A_{13}r^{-1})+(\ell_{\Delta E}-\ell_{ED}r^{-1})\,r_0 & \\ +(A_{23}+\ell_{\Delta D}r^{-1})\,r_0^2 & l_{DI}<r<r_0\\ & \\ (A_{03}+A_{13}r^{-1})+(\ell_{\Delta D}-\ell_{ED}r^{-1})\,r_0 & \\ +(A_{23}+\ell_{\Delta E}r^{-1})\,r_0^2 & r_0<r<l_{EI}\ .\end{cases} \tag{4.178}$$

We can now find $P_3(r)$ using (4.178) and the inhomogeneous term $Q_3(r)$ in (4.158)

$$\begin{aligned}P_3(r)&=\rho\int_{l_{DI}}^{r}G_3^{>}(r,r_0)\,Q_3(r_0)\,dr_0+\rho\int_{r}^{l_{EI}}G_3^{<}(r,r_0)\,Q_3(r_0)\,dr_0\\&=\frac{7}{27}\rho C^2\varepsilon_{\rm mol}^{4/3}\left[F_{03}\frac{1}{r}+F_{13}+F_{23}r^{4/3}\right]=:\frac{1}{27}\rho C^2\varepsilon_{\rm mol}^{4/3}F_3^{ab}(r)\,,\end{aligned} \tag{4.179}$$

where

$$\begin{aligned}F_{03}&:=3\left(l_{EI}^{1/3}-l_{DI}^{1/3}\right)A_{13}-\frac{3}{4}\left(l_{EI}^{4/3}-l_{DI}^{4/3}\right)\ell_{ED}\\&\quad+\frac{3}{7}\left(\ell_{\Delta D}l_{EI}^{7/3}-\ell_{\Delta E}l_{DI}^{7/3}\right)\,,\end{aligned} \tag{4.180}$$

$$\begin{aligned}F_{13}&:=3\left(l_{EI}^{1/3}-l_{DI}^{1/3}\right)A_{03}+\frac{3}{7}\left(l_{EI}^{7/3}-l_{DI}^{7/3}\right)A_{23}\\&\quad-\frac{3}{4}\left(\ell_{\Delta D}l_{DI}^{4/3}-\ell_{\Delta E}l_{EI}^{4/3}\right)\,,\end{aligned} \tag{4.181}$$

$$F_{21}:=-\frac{9}{28}\left(\ell_{\Delta E}-\ell_{\Delta D}\right)\,, \tag{4.182}$$

and $F_3^{ab}(r)$ has been defined in the last line of (4.179).

Once we have $P_1(r)$ from (4.167) and $P_3(r)$ from (4.179), we can next obtain $P_2(r)=B_{p,NN}^{ab}(r)$ substituting (4.167) and (4.179) into (4.148):

$$\begin{aligned}P_2(r)&:=\frac{1}{81}\rho C^2\varepsilon_{\rm mol}^{4/3}\Big\{17F_{01}r^{-3}+7F_{03}r^{-1}+7F_{13}\\&\quad+\left[17F_{11}+7F_{23}r^{4/3}\right]+17F_{21}r^2\Big\}=:\frac{1}{81}\rho C^2\varepsilon_{\rm mol}^{4/3}F_{NN}^{ab}(r)\,,\end{aligned} \tag{4.183}$$

where F_{NN}^{ab} has been defined in the last step.

Inserting (4.167) and (4.183) in (4.140) we find the expression for the two-point triple order velocity-pressure correlation $B_{p,ij}^{ab}$ we were looking for:

$$\begin{aligned}B_{p,ij}^{ab}&=P_1(r)\,r_ir_j+P_2(r)\,\delta_{ij}\\&=\frac{1}{27}\rho C^2\varepsilon_{\rm mol}^{4/3}\left[17F_1^{ab}(r)\,r_ir_j+\frac{1}{3}F_{NN}^{ab}(r)\,\delta_{ij}\right]\\&=:\varepsilon_{\rm mol}^{4/3}\mathcal{F}_{ij}^{ab}(r)\,,\end{aligned} \tag{4.184}$$

$\mathcal{F}_{ij}^{ab}(r)$ being defined in the last line.

Finally, we can find an expression for the numerical kinetic energy transfer term $\left\langle \mathcal{P}_{r,e}^{h\tau_1} \right\rangle_P$ in equation (4.125). Substituting (4.184) in (4.125) yields

$$\left\langle \mathcal{P}_{r,e}^{h\tau_1} \right\rangle_P = \frac{1}{V_e} \varepsilon_{\text{mol}}^{4/3} \sum_{a,b} \mathcal{F}_{ij}^{ab} \left(I_{ij}^{ab} - G_{ij}^{ab} \right). \tag{4.185}$$

4.6.3 Two point second-order velocity correlations for $\left\langle \mathcal{P}_{r,e}^{h\tau_2} \right\rangle$

The last term that has to be dealt with is $\left\langle \mathcal{P}_{r,e}^{h\tau_2} \right\rangle$ in (4.126) arising from the pressure subscale stabilisation. As previously seen, (4.126) only involves the second-order velocity correlation tensor B_{ij}^{ab}. From (4.133) and (4.135) it can readily be checked that the expression analogous to (4.139) and (4.185) for the term $\left\langle \mathcal{P}_{r,e}^{h\tau_2} \right\rangle$ in (4.126) is given by

$$\begin{aligned} \left\langle \mathcal{P}_{r,e}^{h\tau_2} \right\rangle_P &= \frac{2C}{V_e} \varepsilon_{\text{mol}}^{2/3} \sum_{a,b} r^{2/3} \mathcal{D}_{ij}^{ab} \left(I_{ij}^{ab} - G_{ij}^{ab} \right) \\ &=: \frac{1}{V_e} \varepsilon_{\text{mol}}^{2/3} \sum_{a,b} \widetilde{\mathcal{D}}_{ij}^{ab} \left(I_{ij}^{ab} - G_{ij}^{ab} \right), \end{aligned} \tag{4.186}$$

with $\widetilde{\mathcal{D}}_{ij}^{ab} := 2Cr^{2/3}\mathcal{D}_{ij}^{ab}$.

4.6.4 Relation between $\left\langle \mathcal{P}_{r,e}^{h\tau} \right\rangle$ and the rate of dissipation ε_{mol}

From equations (4.139), (4.185) and (4.186) substituted in (4.127) we get

$$\left\langle \mathcal{P}_{r,e}^{h\tau} \right\rangle = \frac{1}{V_e} \sum_{a,b} \left[\tau_{1,ae} \varepsilon_{\text{mol}}^{4/3} \left(\mathcal{K}_{ik}^{ab} + \mathcal{F}_{ik}^{ab} \right) + \tau_{2,ae} \varepsilon_{\text{mol}}^{2/3} \widetilde{\mathcal{D}}_{ik}^{ab} \right] \left(I_{ik}^{ab} - G_{ik}^{ab} \right) \tag{4.187}$$

and finally inserting expressions (4.96)-(4.97) for the stabilisation parameters in (4.187) we obtain the final expression we were looking for

$$\left\langle \mathcal{P}_{r,e}^{h\tau} \right\rangle = \varepsilon_{\text{mol}} \left\{ \frac{h}{V_e} \sum_{a,b} \left[\ell^{-1/3} \left(\mathcal{K}_{ik}^{ab} + \mathcal{F}_{ik}^{ab} \right) + \ell^{1/3} \widetilde{\mathcal{D}}_{ik}^{ab} \right] \left(I_{ik}^{ab} - G_{ik}^{ab} \right) \right\}, \tag{4.188}$$

which states that the average value of $\mathcal{P}_r^{h\tau}$ on a mesh element is directly related to the molecular physical dissipation by means of a factor that only depends on the mesh geometry and the interpolation spaces used to approximate the continuous ones.

4.6.5 Discussion

In section 4.4.3 (Orthogonal Subgrid stabilisation paragraph) we wondered about the possibility that some terms in $\mathcal{P}_r^{h\tau}$ integrated over the whole computational domain

equated the overall physical dissipation in the energy balance equation. It was argued that this should not necessarily be the case for all the stabilisation terms in $\mathcal{P}_r^{h\tau}$, given that they arise from purely numerical considerations rather than physical ones. However, we have found in (4.188) that when using the OSS stabilised finite element method all terms in the ensemble average of $\mathcal{P}_r^{h\tau}$ are proportional to the dissipation $\varepsilon_{\rm mol}$. This would not have been the case, for instance, for the Algebraic Subgrid Scale (ASGS) method (see e.g. [39]). In this case, there would be a contribution of an extra stabilisation term in the energy balance equation arising from time derivative of the velocity. This term would be related to the dissipation $\varepsilon_{\rm mol}$ raised to a power different from one.

As observed from (4.188) the proportionality factor between $\left\langle \mathcal{P}_{r,e}^{h\tau} \right\rangle$ and $\varepsilon_{\rm mol}$ is a rather complicated function depending on the element and mesh geometry, as well on the chosen finite element interpolation spaces. Although one could be tempted to think that its optimum value should equal unity in order to have the desired physical behaviour, we have no basis to assess this point given that, as stated, the terms in (4.188) have to account not only for appropriate physical behaviour, but also for circumventing purely numerical difficulties (e.g., to allow the use of equal interpolation spaces for the velocity and the pressure).

In any case, what seems to follow from the above analysis is that it makes somehow redundant and unnecessary the use of LES models. Effectively, should we have done the above analysis for the energy balance equation (4.93), a result of the type $\overline{\mathcal{P}}_r^{h\tau} = \alpha\varepsilon_{\rm mol}$ (with α being a proportionality function analogous to the one in (4.188)) would have been obtained. On the other hand, the term arising from the LES model would also behave as $\overline{\mathcal{P}}_r^{h} = \beta\varepsilon_{\rm mol}$ so that its effects, if any, could be included in the $\overline{\mathcal{P}}_r^{h\tau}$ term with appropriate redefinition of the proportionality factor. Hence, if a good enough discretisation of the Navier-Stokes equations is performed, the somehow artificial fact of filtering and modelling at the continuous level should be unnecessary. In other words, the problem of simulating turbulence is probably a purely numerical problem of correctly discretising the Navier-Stokes equations rather than a problem of LES physical modelling. Whether the OSS or other finite element methods are good enough to simulate turbulent flows has to be tested by means of numerical experiments. In this sense, and as previously mentioned, very good results have been recently obtained [12, 26, 130, 152, 160, 266].

Finally it is also worthwhile to mention that the results of the above analysis can be viewed as a confirmation of the right choice for the stabilisation parameters τ_1 and τ_2 in the OSS formulation.

4.7 Numerical Examples

Following the suggestion in [44], slightly extended in section 3.5.3 (see [47]), and in view of the results of the preceding sections, it is certainly necessary to test the feasibility of the presented SGS stabilisation strategies as alternatives to LES by means of numerical examples (see also, e.g. [26]). In this section we present a first step towards this goal. We will first address the simulation of decaying two-dimensional turbulence using several

ASGS approaches (standard ASGS, ASGS with subscale time tracking and ASGS with subscale time tracking and full nonlinear terms). It will be shown how the main physical features of this problem are well reproduced without needing to resort to extra LES models. Next, the three dimensional problem of a turbulent flow impinging on a plate will be considered. Again, it will be seen how the OSS method analysed in the previous section, complemented with time tracking, is able to properly reproduce the turbulent pressure spectrum on the plate without the inclusion of extra LES terms. Moreover, we will see the advantage of using the subscale time tracking in front of the standard ASGS and OSS approaches.

4.7.1 Decay of two-dimensional incompressible turbulence

Introduction

Two dimensional turbulence is of importance in some areas of physics involving geophysical flows, such as oceanography or meteorology. It may be also useful to test ideas and theories regarding some aspects of three-dimensional turbulence, given that they share some common phenomena [280]. However, there is an essential difference between two-dimensional and three-dimensional turbulence: the lack of vortex stretching in the former. That is, the term $\boldsymbol{\omega} \cdot \nabla \boldsymbol{u}$ in (4.14) identically vanishes for a two-dimensional flow. This fact is of crucial importance for the following two reasons, among others.

On the mathematical side, and as already quoted in section 4.2.2, the presence of $\boldsymbol{\omega} \cdot \nabla \boldsymbol{u}$ does not allow to find a regularity proof for the Navier-Stokes equations in three dimensions, whereas existence and uniqueness of weak solutions can be proved in $\Omega \subseteq \mathbb{R}^2$. On the physical side, the vanishing of $\boldsymbol{\omega} \cdot \nabla \boldsymbol{u}$ pose severe constraints to two-dimensional flows. Note for instance, that if $\boldsymbol{f} = 0$ in (4.14), conservation of vorticity follows in the inviscid case. This additional constraint had posed some doubts in the past concerning the possibility of existence of two-dimensional turbulence. However, it is nowadays accepted that two-dimensional weakly-viscous flows share typical behaviours compatible with a possible definition of turbulence, such as *mixing* and *unpredictability* [203, 280].

Two landmark papers on two-dimensional turbulence are those of Kraichnnan [188] and Batchelor [11]. The first one establishes energy and enstrophy cascade mechanisms in forced two-dimensional turbulence, while the second addresses the free decaying of homogeneous two-dimensional turbulence. It should be pointed out that while the forced and unforced cases behave almost identically in three-dimensional turbulence, this is not the case in two dimensions. Actually and in what concerns turbulence, two-dimensional flows present a much larger variety of behaviours than three-dimensional flows as they involve several types of cascades and turbulence. As stated in [280], "there is no life for turbulence outside the direct energy cascade" in three dimensions (Kolmogorov cascade [186]).

In what follows, we will concentrate on the simulation of free decaying homogeneous two-dimensional turbulence. Given that in two dimensions the number of degrees of freedom needed for a complete description of the flow is of $\mathcal{O}(\mathrm{Re})$ (to be compared with

$\mathcal{O}\left(\mathrm{Re}^{9/4}\right)$ in three dimensions) detailed Direct Numerical Simulations of two-dimensional turbulence have been performed in the past [21, 38, 195, 220]. Closure models such as the EDQNM (Eddy-Damped Quasi-Normal Markovian) model have been often used too [203]. In the next section, we will see that using the subgrid scale stabilised finite element method presented in chapter 3 we will be able to reproduce some basic qualitative and quantitative behaviour of decaying two-dimensional turbulence, using relatively coarse meshes.

Numerical results

We consider the problem of solving the incompressible Navier-Stokes equations in the two-dimensional domain $\Omega = (0,1)^2$ with periodic boundary conditions on $\partial\Omega$. The differential problem is written as

$$\partial_t \boldsymbol{u} - \nu\Delta\boldsymbol{u} + \boldsymbol{u}\cdot\nabla\boldsymbol{u} + \nabla p = 0 \qquad \text{in } \Omega,\ t \in]0,T[, \tag{4.189}$$

$$\nabla\cdot\boldsymbol{u} = 0 \qquad \text{in } \Omega,\ t \in]0,T[, \tag{4.190}$$

$$\boldsymbol{u} \text{ periodic} \qquad \text{on } \partial\Omega,\ t \in]0,T[, \tag{4.191}$$

$$\boldsymbol{u} = 0.05\left[\cos\left(8\pi x\right), \cos\left(8\pi y\right)\right] \qquad \text{in } \Omega\cup\partial\Omega,\ t = 0. \tag{4.192}$$

The integral-scale Reynolds number of the problem is given by $\mathrm{Re} = UL/\nu$, with U standing for the rms velocity of the initial flow field (4.192). In our case $\mathrm{Re} = 5000$.

Problem (4.189)-(4.192) has been solved in three different regular meshes of quadrilaterals of 50×50, 100×100 and 200×200 elements and using three different finite element stabilised formulations namely, the ASGS (Algebraic Subgrid Scale), the ASGS-TT (Algebraic Subgrid Scale with Time Tracking) and the ASGS-NLTT (Algebraic Subgrid Scale with Non-linear subscales and Time Tracking). The second order Crank-Nicolson scheme has been used for the time integration of the finite element solution while a first order scheme has been used for the subscales. As already mentioned, this choice is justified in [46] and it still keeps the second order of accuracy in time of the finite element solution. A time step of $\Delta t = 1$ s has been taken. Five Picard non-linear iterations have been performed for each time step (three for the subscales) and a direct solver has been employed to solve all algebraic matrix systems.

From a phenomenological point of view all methods and meshes have yielded similar results. The decay of isotropic two-dimensional turbulence is characterized by the singular fact that coherent structures emerge and prevail on the long time. The time evolution of the flow dynamics can be thought as consisting of different time events. In a first phase, the initial flow field gets rapidly distorted with independence of the initial condition being an ordered flow field like (4.192), a field of Gaussian vortices or a random vorticity field. The early dynamics of vorticity is characterized by sheetlike structures rolling up around emerging centres of concentrated vorticity. The resulting vortices may either form pairings (merging of vortices of the same sign) or dipoles (vortices of opposite sign). The situation is shown in Figs. 4.5a-4.6a, where we have plotted the modulus of vorticity at $t = 25$ s. The number of vortices is constantly reduced as time evolves due to vortex merging following the scenario described in [222]. This can be clearly observed in Fig. 4.5b-4.6b,

corresponding to $t = 60$ s, where less and larger vortices than in Figs. 4.5a are present. As time continues to evolve fewer and fewer coherent vortices remain as seen in Figs. 4.5c-4.6c ($t = 100$ s) where there are only three vortices. The two central vortices having equal sign will tend to merge as shown in Figs. 4.5d-4.6d and Figs. 4.5e-4.6e ($t = 150$, 200 s) before the final state is achieved (see Figs. 4.5f-4.6f).

The quasiuniversal final state consists of two vortices of opposite sign with nearly circular cross sections and with their maximums lying on the diagonal of the periodic domain. The maximums are placed at the equilibrium positions of a two-dimensional Ewald potential [220]. In Fig. 4.7a we have plotted the stream function corresponding to Fig. 4.5d. We can observe that the flow is clearly dominated by just two patterns. In Fig. 4.7b the flow has nearly achieved the final state. Hence, from the above description we can see that decaying two-dimensional is able to generate a highly ordered state from an initial "chaotic" state and thus constitutes a beautiful example of a self-organized system.

Although some issues of two-dimensional turbulence remain unsolved, several general properties are well understood and satisfactory theories account for them [280]. For instance, and contrary to what happens in the three-dimensional case, it is well known that enstrophy decreases with time in the case of low viscosity, while energy remains essentially constant. Whereas enstrophy is transferred from large to small scales, there is no viscous sink of energy at the small scales in two-dimensional turbulence. Roughly speaking, and with due care, one can say that in two-dimensional turbulence, enstrophy plays somehow the role played by energy in three-dimensional turbulence.

As previously mentioned, the enstrophy and energy cascade mechanisms were respectively described by Kraichnnan for the forced case [188] and by Batchelor for the free decaying case [11]. Batchelor predicted an energy spectra $E(k) \sim k^{-3}$ for the flow in the initial decay phase (see Fig. 4.5a), where k represents the modulus of the wavenumber vector $\boldsymbol{k} = (k_x, k_y)$. In Fig. 4.8a we have plotted the energy spectrum $E(k_x, k_y)$ for the initial condition ($t = 0$ s). Obviously only the wavenumber (k_x, k_y) corresponding to (4.192) has a non-null value. In Fig. 4.8b we have plotted $E(k_x, k_y)$ for $t = 25$ s, which corresponds to the velocity field whose vorticity has been plotted in Fig. 4.5a. As seen, almost all wavenumbers have been excited by this time.

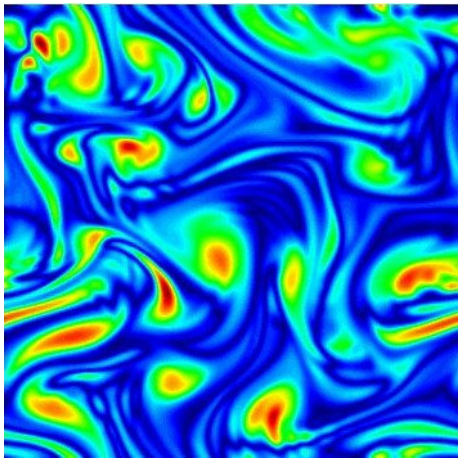

a) $t = 25$ s

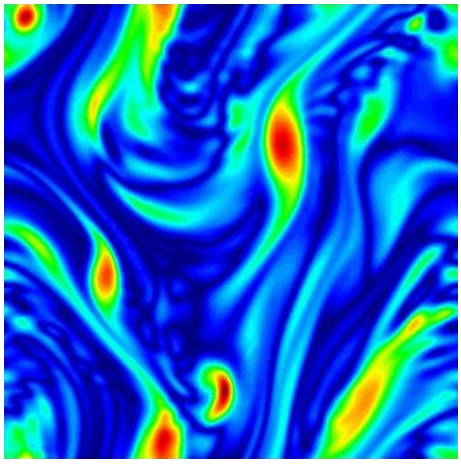

b) $t = 60$ s

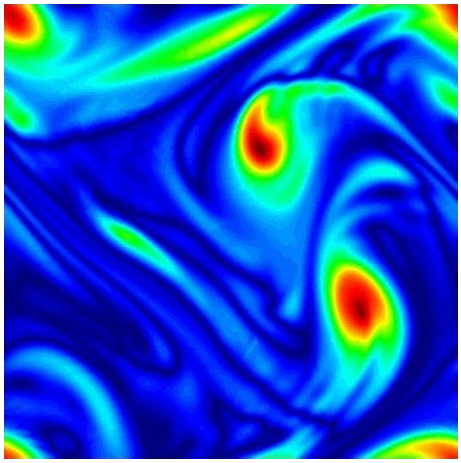

c) $t = 100$ s

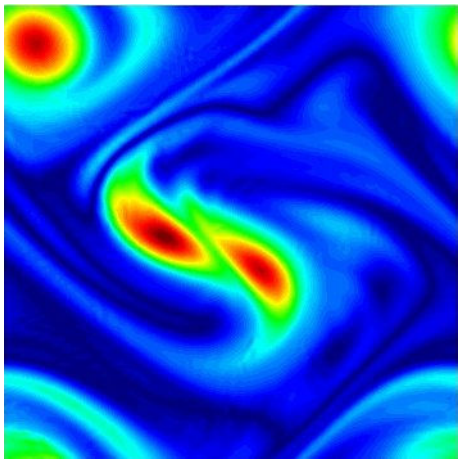

d) $t = 150$ s

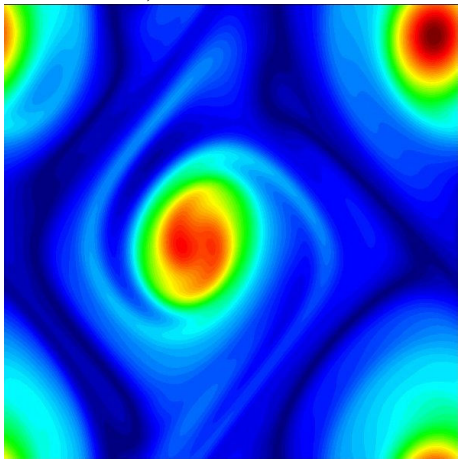

e) $t = 200$ s

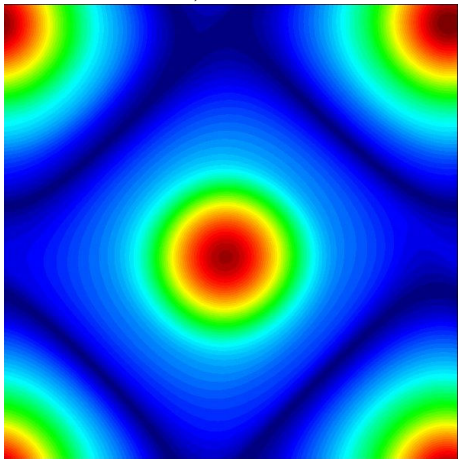

f) $t = 350$ s

Figure 4.5: Vorticity modulus field at different time steps. a) $t = 25$ s, b) $t = 60$ s, c) $t = 100$ s, and d) $t = 150$ s, e) $t = 200$ s and f) $t = 350$ s. Results corresponding to the 200×200 mesh and the ASGS-TT finite element method. The colour scale has been changed from plot to plot for a better visualization of the flow.

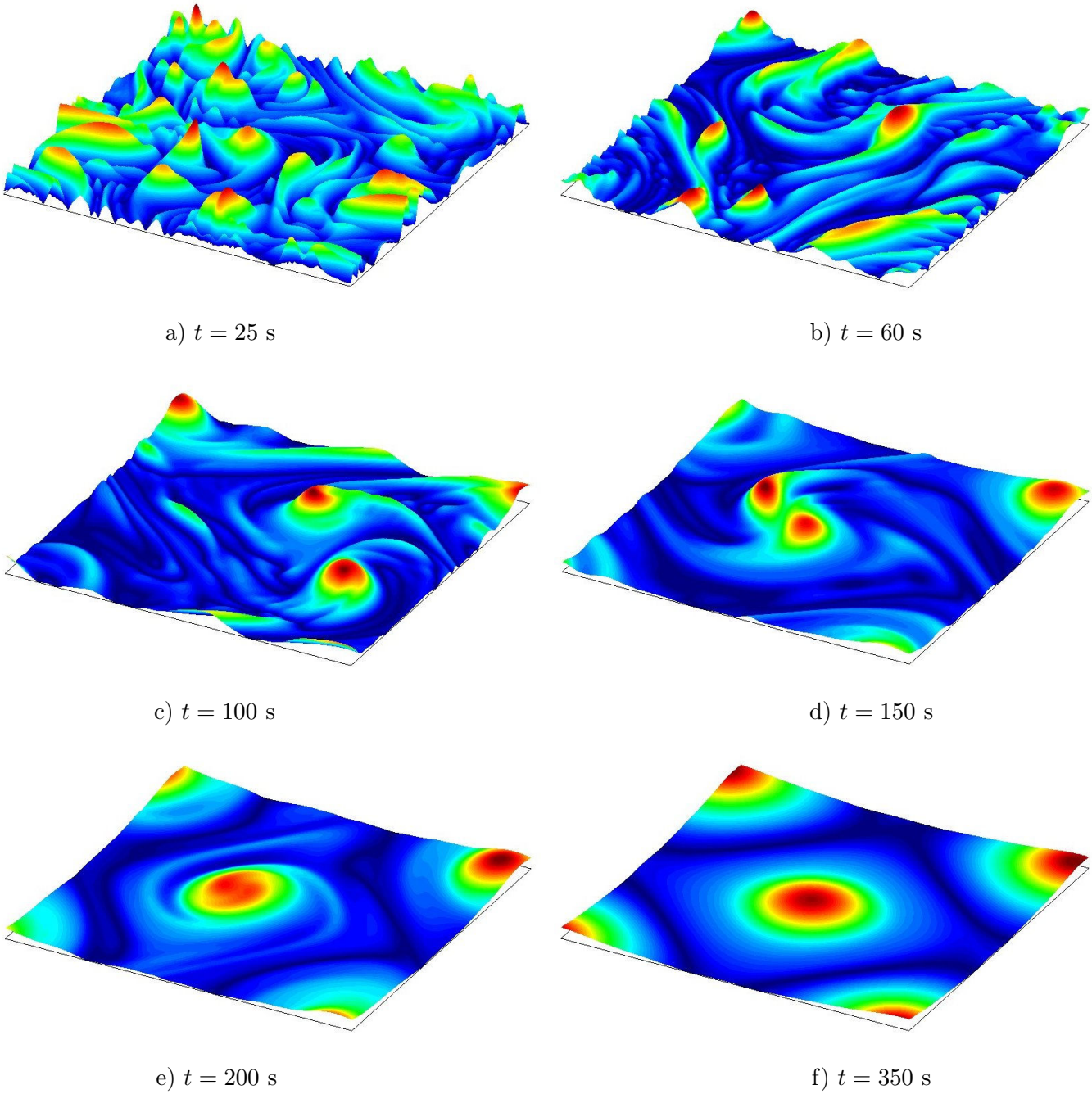

a) $t = 25$ s

b) $t = 60$ s

c) $t = 100$ s

d) $t = 150$ s

e) $t = 200$ s

f) $t = 350$ s

Figure 4.6: Vorticity surfaces at different time steps. a) $t = 25$ s, b) $t = 60$ s, c) $t = 100$ s, and d) $t = 150$ s, e) $t = 200$ s and f) $t = 350$ s. These results are those of Fig. 4.5 but showing elevation surfaces.

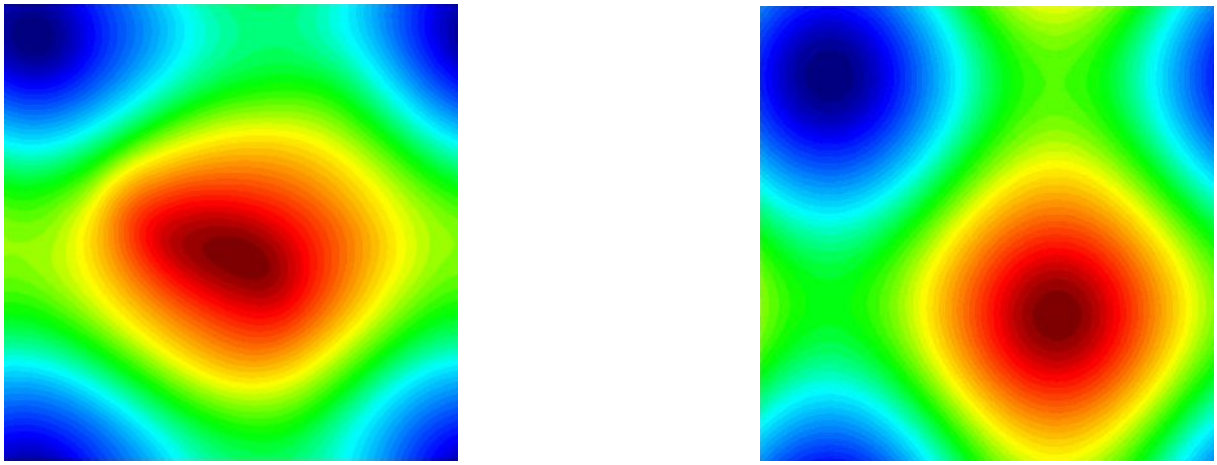

a) $t = 150$ s b) $t = 350$ s

Figure 4.7: Stream function at different time steps. a) $t = 150$ s, b) $t = 350$ s. Results corresponding to the 200×200 mesh and the ASGS-TT finite element method. The colour scale has been changed from plot to plot for a better visualization of the flow.

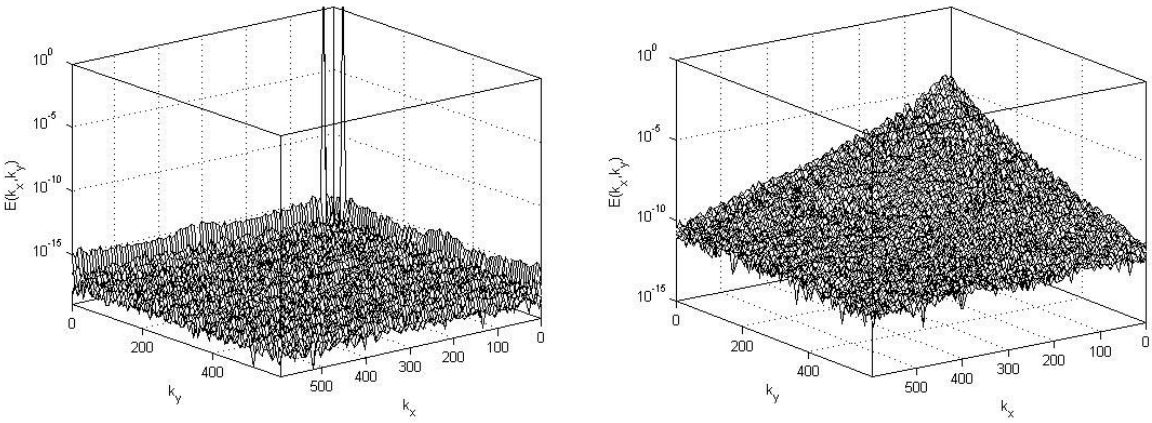

a) $t = 0$ s b) $t = 25$ s

Figure 4.8: Energy spectra $E(k_x, k_y)$ at different time steps. a) Initial condition $t = 0$ s, b) $t = 25$ s.

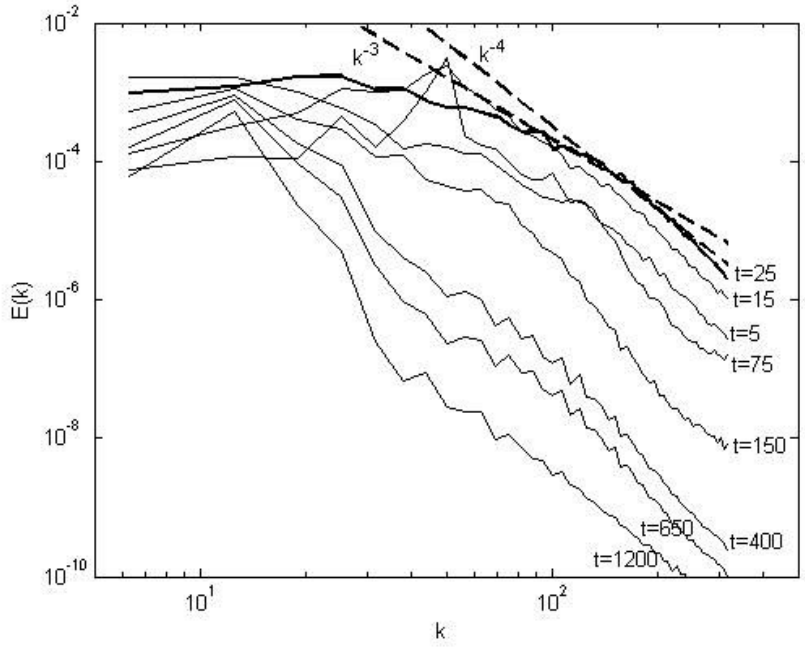

Figure 4.9: Energy spectra $E(k)$ for various time steps. 100×100 mesh using the ASGS finite element method.

In Fig. 4.9 we have plotted the energy spectrum $E(k)$ for different time steps together with the k^{-3} and k^{-4} slopes. The results of this figure have been obtained using the ASGS finite element method with a mesh of 100×100 elements. We observe that for $t = 25$ s (bold line) the expected k^{-3} energy spectrum dependence is achieved for a certain wavenumber interval, although for the largest wavenumbers the spectrum decays with a k^{-4} dependence. Actually, an energy spectrum $\sim k^{-4}$ is what is more often observed in simulations of free decaying turbulence (see e.g., [200,203,280]). As time evolves and fewer and larger coherent structures emerge, the slope becomes steeper and energy concentrates near the wavenumber that corresponds to the quasiuniversal final state.

In Fig. 4.10 we present a comparison of $E(k)$ at $t = 25$ s for various meshes and stabilised finite element methods. It can be observed that all spectra follow the expected k^{-3} law, at least for a considerable range of wavenumbers. The energy spectra of the ASGS-TT and ASGS-NLTT finite element methods are very similar and no remarkable differences can be detected between them, except for the latter being slightly more dissipative at high wavenumbers for the finer meshes. The spectrum corresponding to the ASGS method is also similar to the remaining ones but their values for high wavenumbers are clearly larger than the ASGS-TT and ASGS-NLTT ones. That is to say the latter methods are more dissipative, which make them possible candidates for the proper simulation of three-dimensional turbulence, where dissipation at small scales (high wavenumbers) is crucial.

As a conclusion and in accordance with the results found in [200], it seems that the

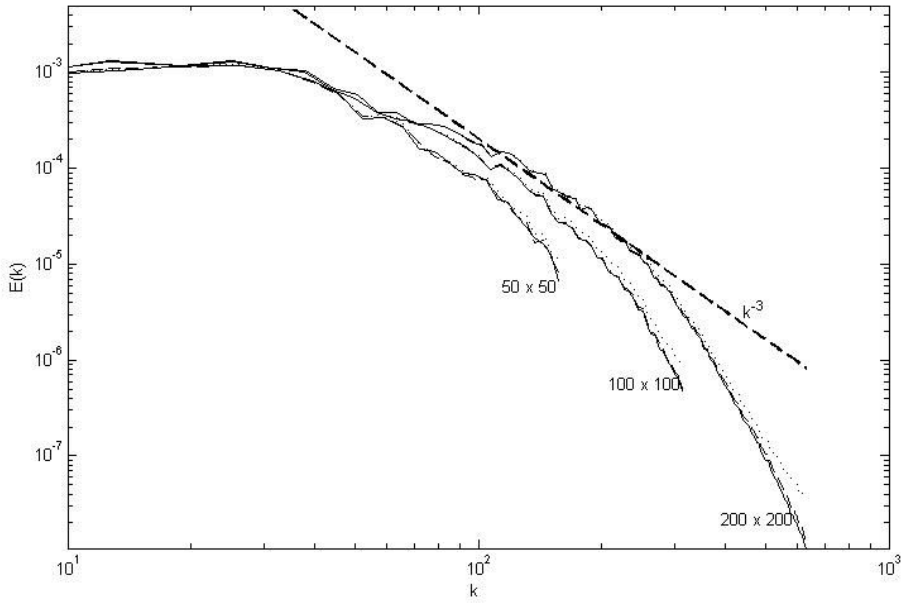

Figure 4.10: Energy spectra $E(k)$ for various meshes and stabilised finite element methods. Dotted lines: ASGS, Dashed lines: ASGS-TT and Continuous lines: ASGS-NLTT

ASGS method suffices for a correct reproduction of the general behaviour of free decaying two-dimensional turbulence. The ASGS-TT and the ASGS-NLTT methods perform also well and might be appropriate options to simulate three dimensional turbulence given that they are more dissipative than the ASGS approach (which does not suffice in the three dimensional case [200]). In any case, what looks apparent from the above simulations is that no extra LES model seems necessary to yield good results if an appropriate spatial and time discretisation schemes are used.

4.7.2 Three-dimensional turbulent flow impinging on a plate

As a second numerical example to test the feasibility of the SGS stabilisation strategy to simulate turbulent flows, the case of a three-dimensional flow impinging on a plate has been considered. The mathematical problem to address consists in solving the incompressible Navier-Stokes equations (4.1)-(4.2) for the flow over the plate, in a given computational wind tunnel Ω, with boundary $\partial\Omega$, once some initial and boundary conditions have been imposed. The problem Reynolds number according to the plate diameter $D = 0.5$ m and the maximum initial velocity $U_0 = 10$ m/s is $\mathrm{Re} \sim 2.75 \times 10^5$.

Some simulations using different SGS stabilised finite element methods have been carried out. The case of the quite standard approach of combining SGS with the Smagorinsky LES model has been also addressed. The result we are interested in consists in reproducing the pressure spectrum at the central point of the plate. According to

(4.25) in section 4.3.2, it should happen that $E_{pp}(k) \sim k^{-7/3}$. Experimental data exist for the present plate problem confirming that the point pressure spectra in the frequency domain fulfils $E_{pp}(f) \sim f^{-7/3}$, where f is the frequency. Results for the energy spectrum dependence in the wavenumber domain can be transformed to results in the frequency domain making use of *Taylor's hypothesis*, also known as the *frozen-turbulence approximation* (the same follows from the spatial to the time domain, see e.g., [129,255]).

The main computational features of the simulations are listed below:

- The computational wind tunnel is a rectangular hexahedral domain with dimensions $\Omega = 9 \times 2.5 \times 1.8$ m^3 that guarantees no influence of the far field boundaries in the numerical solution.
- An unstructured mesh of 1.336.823 elements (1.318.883 tetrahedral elements + 17.940 surface triangular elements) corresponding to 240.351 nodes (961.404 d.o.f) has been used. The mesh has been strongly refined near the plate contours.
- Equal linear interpolation functions have been used for the velocity and the pressure as allowed by the SGS stabilised finite element approach.
- In what concerns the spatial discretisation, use has been made of a nodal based-implementation scheme [40] that allows to save a large amount of computational time. This is so because all integrals involving combinations of shape function products and their corresponding derivatives are carried out at the first stage of the computation, which avoids to recompute the volume and surface integrals anymore.
- 5 linearisation Picard iterations have been used for each time step.
- A GMRES solver has been used to solve all matrix systems.
- The second order accurate in time Crank-Nicholson scheme has been used (see section 3.4.1). The time incremental has been $\Delta t = 0.0015$ s.
- In order to surpass the initial transients, the Smagorinsky model (4.58) has been used with a constant $C_S^2 = 0.01$ to obtain extra dissipation. We note however, that $C_S^2 = 0.01$ corresponds to a Smagorinsky constant of $C_S = 0.1$, which is smaller than the standard value of $C_S = 0.17$ that yields the relevant value in the simulation $C_S^2 \sim 0.03$ (three times the used one).

Computational domain and boundary conditions

The computational domain is shown in Fig. 4.11, where we have plotted some general and detailed views. The inner domain between the external rectangular parallelepiped and the plate surface is required for an appropriate mesh transition size. The plate in Fig. 4.11d has a slope of 18° with respect to the x-axis.

The Dirichlet boundary is built from $\Gamma_D = \overline{\Gamma_i^a \cup \Gamma^p}$ (with Γ^p standing for the plate surface), while the mixed boundary is given by $\Gamma_M = \overline{\Gamma_u^a \cup \Gamma_d^a \cup \Gamma_o^a \cup \Gamma_{lat1}^a \cup \Gamma_{lat2}^a}$. The corresponding boundary conditions are given by:

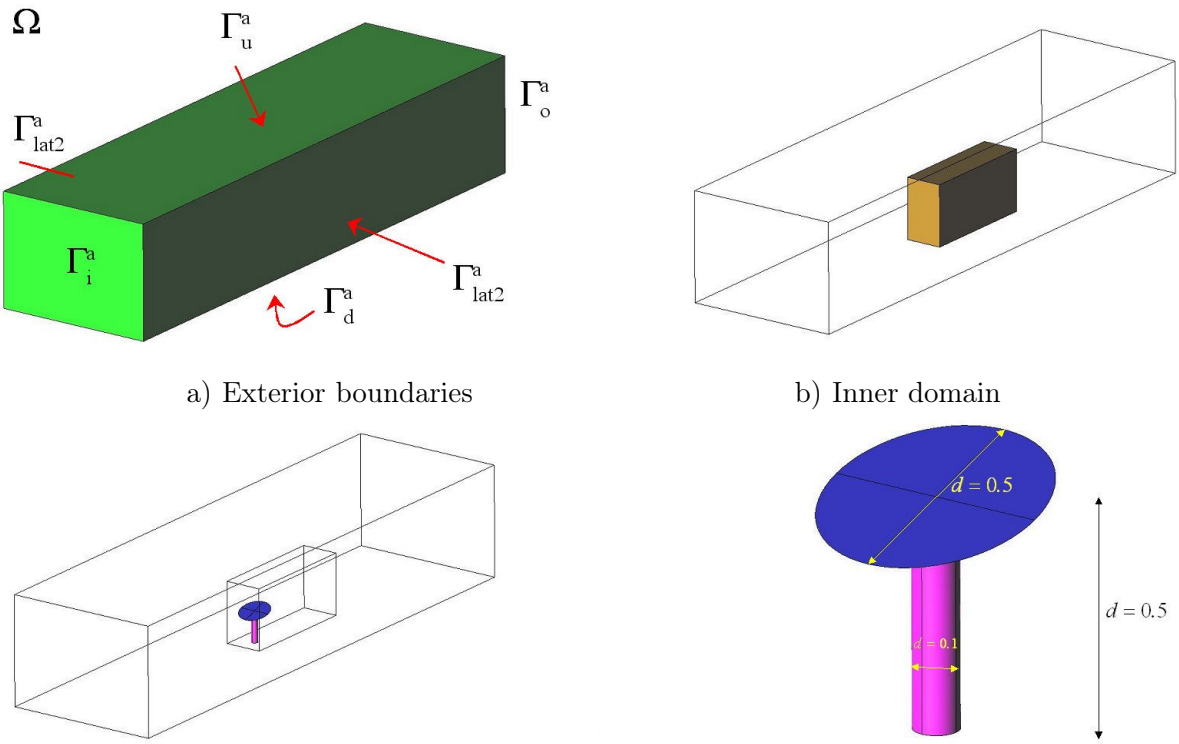

a) Exterior boundaries

b) Inner domain

c) Plate boundary

d) Plate dimensions

Figure 4.11: Wind tunnel computational domain. General and detailed views.

Dirichlet boundary Γ_D*:*

$$\boldsymbol{u}_D = (u_x, u_y, u_z)^\top = \begin{cases} (3.0864y^2, 0, 0)^\top \ m/s \ \text{ on } \ \Gamma^a_i \\ (0,0,0)^\top \ m/s \ \text{ on } \ \Gamma^p \end{cases} \tag{4.193}$$

Mixed boundary Γ_M*:*

$$\left.\begin{matrix} t_x, t_y = 0 \\ u_z = 0 \end{matrix}\right\} \ \text{on} \ \ \Gamma^a_u, \Gamma^a_d \qquad \left.\begin{matrix} t_x, t_z = 0 \\ u_y = 0 \end{matrix}\right\} \ \text{on} \ \ \Gamma^a_{lat1}, \Gamma^a_{lat2} \tag{4.194}$$

$$\boldsymbol{t}_M = (t_x, t_y, t_z)^\top = (0,0,0)^\top \ \text{ on } \ \Gamma^a_o \tag{4.195}$$

with $\boldsymbol{t}_M$ standing for the traction at the mixed boundary.

In Fig. 4.12 we show some mesh details and it can be clearly observed that the mesh has been strongly refined on the plate surface.

Pressure and velocity fields

For the present example we have tested the standard ASGS method, the OSS method the OSS-TT (OSS method including time tracking, see section 3.4.2) and the LES

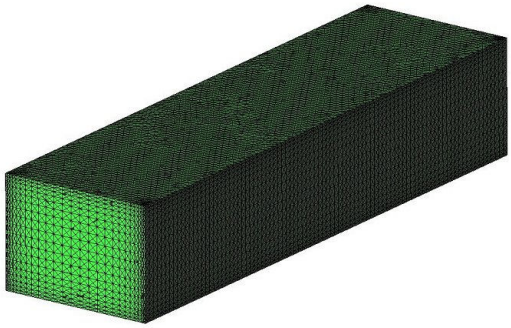

a) Exterior boundaries

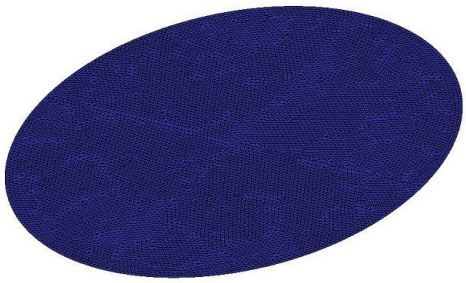

b) Plate surface

Figure 4.12: Plate mesh: General and detailed views.

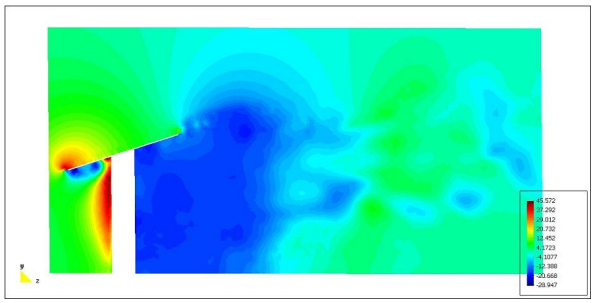

a) Isopressure surfaces on the plane $x = 0$

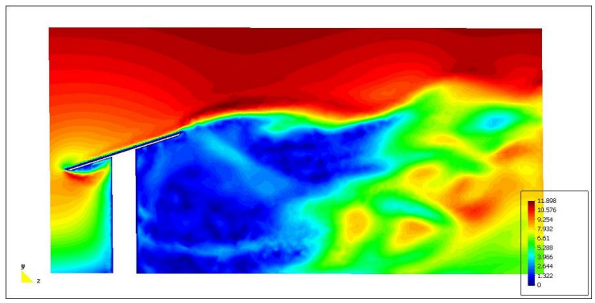

b) Isovelocity surfaces on the plane $x = 0$

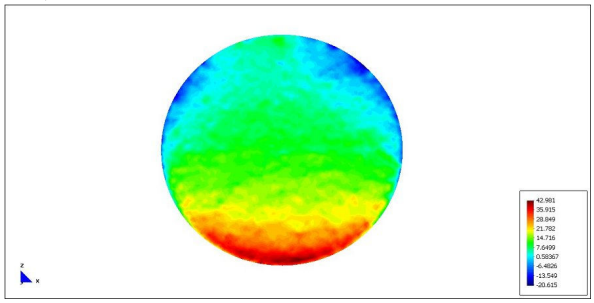

c) Pressure on the plate surface

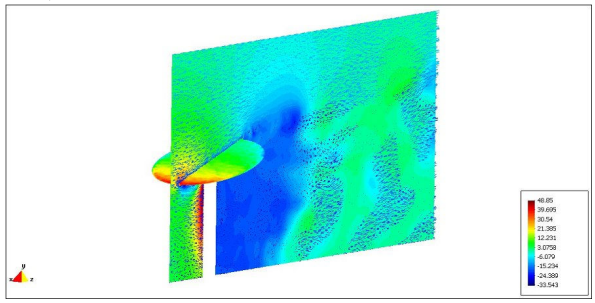

d) Isopressure and velocity vectors

Figure 4.13: Pressure and velocity fields at a given time step.

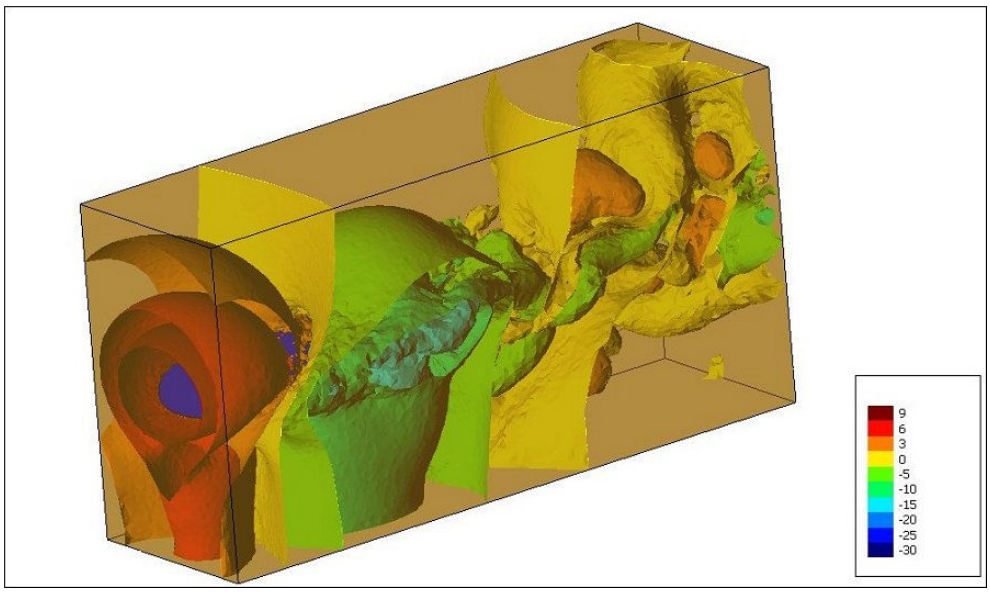

a) Isopressure flat surfaces

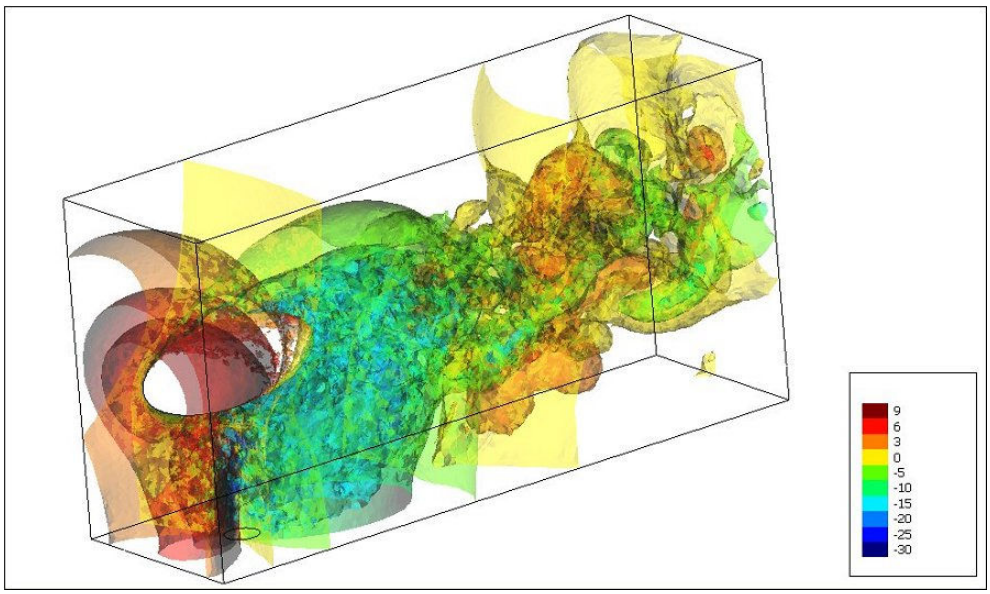

b) Isopressure transparent surfaces

Figure 4.14: Isopressure surfaces in the inner domain for a given time snapshot.

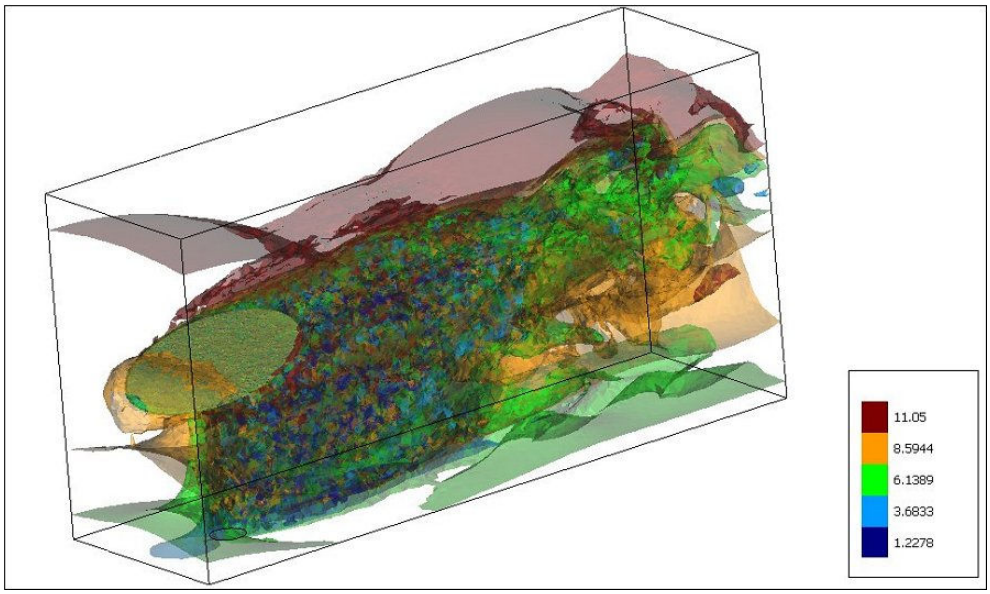

Figure 4.15: Isovelocity surfaces in the inner domain for a given time snapshot.

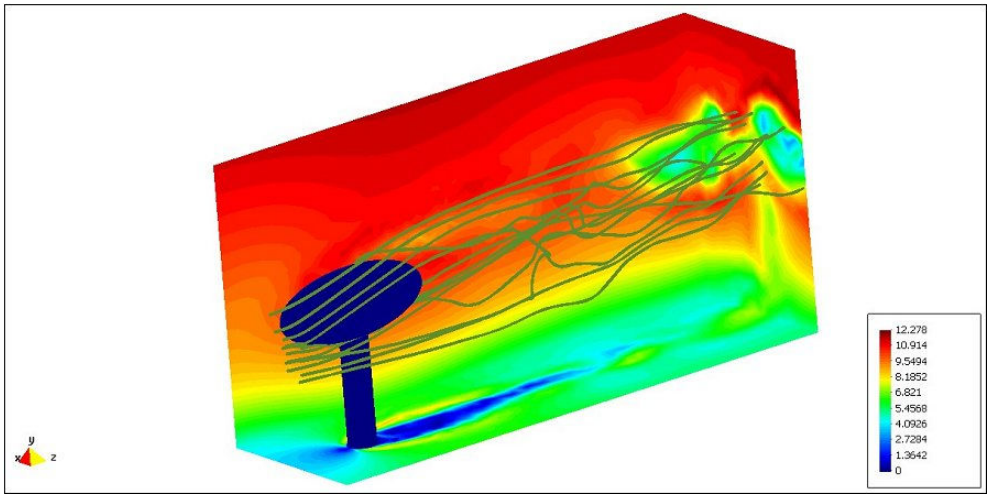

Figure 4.16: Stream lines.

Smagorinsky model combined with ASGS stabilisation. The first two methods have turned to be non robust for the used mesh and the solutions have blown up after some hundred computational steps. However, and as expected (see [44,46,47]), the OSS-TT approach has shown better stabilisation properties and has yielded a fairly promising solution. Actually, from a phenomenological point of view, the OSS-TT and the Smagorinsky methods have shown similar results so we will not compare their qualitative performance until next section. We will limit here to present the general behaviour of the pressure and velocity fields.

It can be clearly observed from Figs. 4.13a,b and d, that a complex flow pattern develops past the plate, involving the formation of large vortices. The pressure becomes maximum on the upper leading edge of the plate (minimum under the plate) and decreases on the surface, the minimum being reached at the rear edge where flow separates (see Figs. 4.13a and c). In turn, the velocity becomes minimum at the leading edge and the flow accelerates reaching maximum speed values when it leaves the surface (see Figs. 4.13b and d). Large vortices are shed leading to a fully developed turbulent flow.

The intricate flow behaviour can also be observed in Figs. 4.14a and b, where we have plotted the isopressure surfaces for the inner domain at a given time instant. In Fig. 4.15 we have plotted the isovelocity surfaces for the same time value, while in Fig. 4.16 the stream lines for different points are plotted. As it can be observed, while some stream lines smoothly follow the plate profile and leave it unaltered, others present a quite erratic and chaotic path.

Point pressure spectrum and time evolution

As previously mentioned, experimental results performed in a wind tunnel exist for the plate problem we are addressing. The experimental point pressure spectrum at the plate's central point is presented in Fig. 4.17. As seen, for the frequency range that comprises from 10 Hz to 1000 Hz the spectrum clearly exhibits a $f^{-7/3}$ slope in accordance to the predicted pressure spectrum for isotropic turbulence (with the additional assumption of Taylor's hypothesis).

The spectra resulting from the computations are plotted in Fig. 4.18. According to the computational time step, results are only to be expected up to $\sim$ 330 Hz. In Fig. 4.18 we can observe that the Smagorinsky model (blue line) quickly depicts the $f^{-7/3}$ expected slope, although for the spectrum higher frequency range it is more dissipative than the OSS-TT solution (green line). The latter closely matches the $f^{-7/3}$ line from 80 Hz to 330 Hz. In fact it should be noted that the low frequency spectrum is not of great importance in the present simulations given that they have been started from previous and different fully developed solutions.

In Fig. 4.19 we have plotted a zoomed interval of the pressure time evolution. We can observe that the OSS-TT solution has a higher mean value than the Smagorinsky one. This is an expected result given that the OSS-TT is intended to be less dissipative than the Smagorinsky model. In addition, it can be observed that the OSS-TT curve also exhibits more intricate dynamics than those of the Smagorinsky solution. In view of these

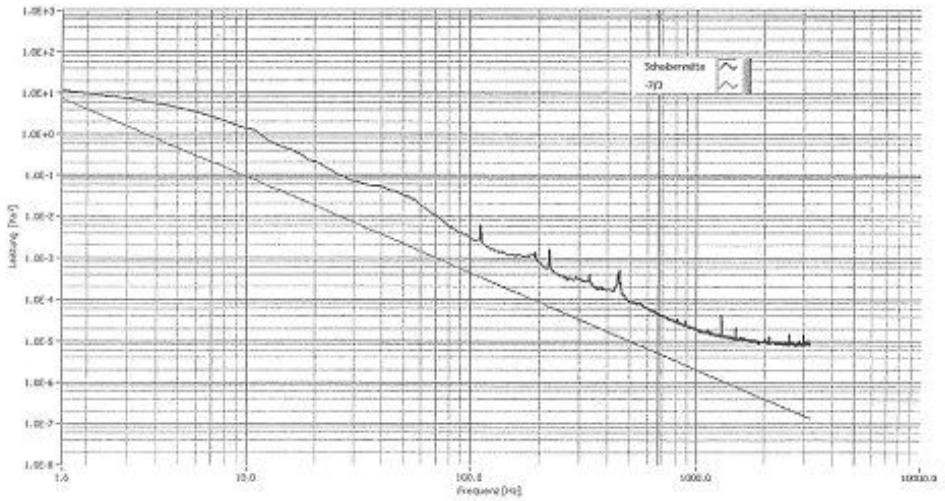

Figure 4.17: Experimental pressure spectrum at the plate's central point. Courtesy of GBF Aachen, Dipl. Ing. Ralf Haase.

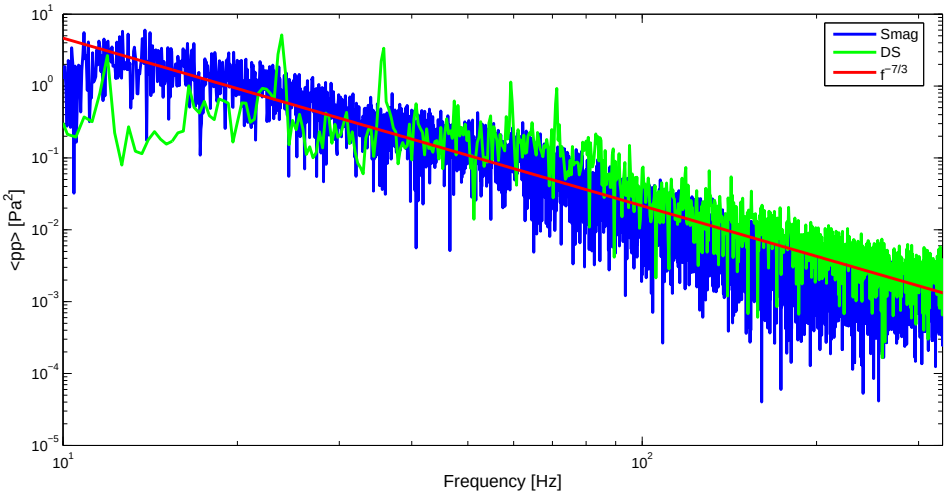

Figure 4.18: Computed pressure spectrum at the plate's central point. Smagorinsky (blue line), OSS-TT (green line) and $f^{-7/3}$ (red line)

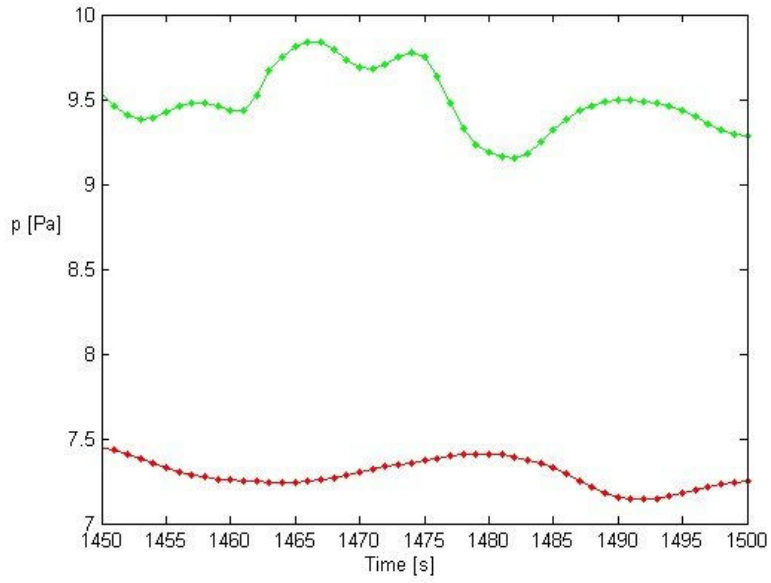

Figure 4.19: Zoom of the pressure time evolution at the plate's central point. Smagorinsky (red line), OSS-TT (green line)

results, one could expect a higher value for the dimension of the OSS-TT final attractor than for the Smagorinsky one. Checking this fact constitutes a future research line that would be worthwhile to explore.

It should be noted that the performance of the various SGS methods may strongly depend on the mesh being used for the simulations. In [162], for instance, it was shown that for very coarse meshes the dynamic Smagorinsky model performed better than the VMM approach (the VMM in this reference still included a Smagorinsky model for the finer scales). However for a more refined mesh, the latter exhibited a clearly better behaviour. This type of mesh dependence analysis has not been performed here due its high computational cost. In any case, what seems clear from the present example is that a purely numerical approach to the problem with no use of physical LES models can yield excellent results.

4.8 Conclusions

In this chapter we have reviewed some basic results of the classical mathematical theory for the Navier-Stokes equations. We have commented on its main drawbacks, essentially the lack of a proof for the uniqueness of weak solutions and for the existence of strong solutions in the long time. Despite of the mathematical technicalities needed to assert it, it is commonly accepted that the Navier-Stokes equations suffice to describe the behaviour of any incompressible isentropic flow, including fully developed turbulent flows. On the other hand, we have also reviewed Kolmogorov's theory that precisely presents a totally different

approach for the description of turbulent flows, based on statistical fluid mechanics and heuristic reasoning.

Equipped with these mathematical and physical grounds, we then have focused on the numerical simulation of turbulent flows, and in particular on the Large Eddy Simulation (LES) method. We have reviewed recent attempts to give a precise mathematical definition of LES that have led to the notion of *suitable approximations* to the Navier-Stokes equations. This mathematical approach to LES poses some restrictions on the possible modifications to the original Navier-Stokes equations in order to be able to simulate turbulent flows. It also allows to address some unsolved questions of the "standard" LES approach. Moreover, and in the same framework, one can also consider the possibility of performing a non physical LES modelling approach. That is, if an appropriate discretisation scheme is used, the simulation of turbulence could be made without the addition of an extra LES model for the residual stress tensor. It has been explained that an adequate discretisation scheme to do so could be that provided by Subgrid Scale (SGS) stabilised finite element methods.

Then, our aim has been to explore the latter idea combining some results of numerical mathematics with some results of statistical fluid mechanics. For a fine enough computational mesh, it has been heuristically proved that the contribution to the energy balance equation of the stabilisation terms of the Orthogonal Subgrid Scale (OSS) stabilised finite element method is already proportional to the physical dissipation rate for an appropriate choice of the stabilisation parameters. This has been done with the sole use of the quasi-normal approximation for two point fourth-order velocity correlations and using Kolmogorov's first and second similarity hypotheses. It has been also assumed that several statistical fluid mechanics results, which are valid for the exact velocity field, hold true for the approximated finite element velocity field. Taking into account that the stabilisation terms in the OSS method arise from pure numerical necessities it is a noteworthy fact that they have the correct physical behaviour in the inertial subrange of a turbulent flow. This somehow supports the idea that no extra physical LES modelling should be added to the equations to achieve this behaviour, if an appropriate stabilisation method is used. That is to say, the simulation of turbulence should probably rely on optimum numerical modelling rather than in physical one.

Finally, some numerical examples have been presented showing the performance of some SGS methods in the simulation of turbulent flows. The case of decaying isotropic turbulence in two dimensions and the case of a three-dimensional turbulent flow impinging on a plate have been considered. The obtained results give further support to the previous heuristic proof, in the line that a pure numerical approach to turbulence can be possible.

Chapter 5

The acoustic field

In this chapter we address the computation of the acoustic field generated by known flow motion. This implies solving an inhomogeneous Helmholtz equation and in some cases, its convected counterpart. When this is done by means of the standard Galerkin finite element method, the solution is known to present the so called pollution error for large wave numbers. The same problem appears in the case of the convected Helmholtz equation. In order to avoid this situation, several numerical strategies have been proposed with predominance of stabilised finite element approaches. In this line, we will propose here an algebraic subgrid scale (ASGS) stabilised finite element method to improve the accuracy of the Galerkin finite element solution to the two dimensional convected Helmholtz equation. The method is formally equivalent to the Galerkin Least-Squares (GLS) method and, in the case of no convection, the well known GLS results for the Helmholtz equation are recovered. As an application, we have considered again the case of aerodynamic sound radiated by incompressible flow past a two-dimensional cylinder, but now taking into account the convected case. Following Lighthill's acoustic analogy, we have used the time Fourier transform of the double divergence of the Reynolds stress tensor as a source term for the Helmholtz and convected Helmholtz equations and showed the benefits of using the subgrid scale stabilisation.

5.1 Introduction

Acoustic waves propagating in a stationary background media are solutions of the well-known wave equation. Acoustic waves are generated by sound sources, which may be considered as regions of space in contact with the fluid (or subregions in motion of the fluid itself) where energy of any origin is transformed into acoustic energy to be propagated outward as sound waves. The wave equation can be easily derived from the continuity and Euler equations for an isentropic flow, assuming quiescence and neglecting all non-linear terms (see section 2.2.3 in Chapter 2). In the case of waves propagating in a flow with uniform mean speed, a convected wave equation can be derived that is valid for arbitrary values of the Mach number, up to transonic flows (see e.g. [101, 145] and references therein). The convected wave equation becomes of importance in many

practical problems in aeroacoustics involving aerodynamic sound generated by aircraft engine fans and compressors [101, 145]. It is also worthwhile to mention that wave equations are crucial in many other areas of physics such as electromagnetism, geophysics, meteorology or general relativity.

Just as significant as the wave equation is its time Fourier transform: the Helmholtz equation, which gives the spatial distribution of the acoustic field for a given wavenumber. Analogously, the time Fourier transform of the convected wave equation describes the spatial distribution of acoustic waves propagating in a background uniform flow. This equation, known as the time-reduced version of the convected wave equation, will be hereafter referred to as the convected Helmholtz equation.

When facing problems involving complex geometries, analytic solutions to the above equations can hardly be found and one has to resort to numerical methods, such as the finite element method (FEM). Finding a FEM solution to the Helmholtz and convected Helmholtz equations is not a trivial task and two main difficulties have to be overcome (see e.g. [118,163]). The first one appears when solving unbounded exterior acoustic problems in finite computational domains (see Fig. 5.1). Some kind of absorbing boundary condition (ABC) has to be placed at the boundary of the computational domain to account for outward radiating waves. The second difficulty arises when dealing with wave phenomena at high wave numbers (short wave lengths). In this case the discrete wave propagates with a phase lag with respect to the exact one, see Fig. 5.2, and a pollution error appears in the numerical solution of the problem (even if keeping the number of nodes per wave length constant).

In what concerns the first problem (ABC) three main strategies have been developed, namely the use of DtN (*Dirichlet-to-Neumann*) operators, the implementation of *infinite* elements and the inclusion of a PML (*Perfectly Matched Layer*) at the domain boundary. The DtN approach [98,177] consists in relating the unknown solution and its derivatives at the computational external boundary Γ_R (see Fig. 5.1) by means of a global operator (DtN operator) built from the analytical exact solution of a Dirichlet outward wave propagating problem. The exact solution used in the DtN operator can be stated in an integral or series representation, which has to be truncated when numerically implemented. The number of terms in the series determines the accuracy of the solution. The second option consists in using *infinite* elements (see e.g. [2,18,88]). In this case the computational domain, Ω_{ac}, is discretised using standard finite elements, while the exterior infinite domain is discretised using the so called *infinite* elements. These elements are a semi analytical construction obtained through the tensor product of finite element shape functions and radial analytic shape functions, for instance of the type $\varphi_n(r) = e^{ikr}/r^n$ in the case of Γ_R being a sphere. At present there are still several questions to be answered concerning the performance of the method, specially in what refers to the convergence of the various formulations and to ill-conditioning problems (see [118] and references therein). The third main approach to solve the ABC problem consists in using the PML method [15,123]. This method was originally developed for the computation of time-dependent electromagnetic waves and it is based on adding an exterior absorbing layer to the computational boundary, Γ_R, so that any incident wave becomes absorbed. This is done by reformulating the original Helmholtz

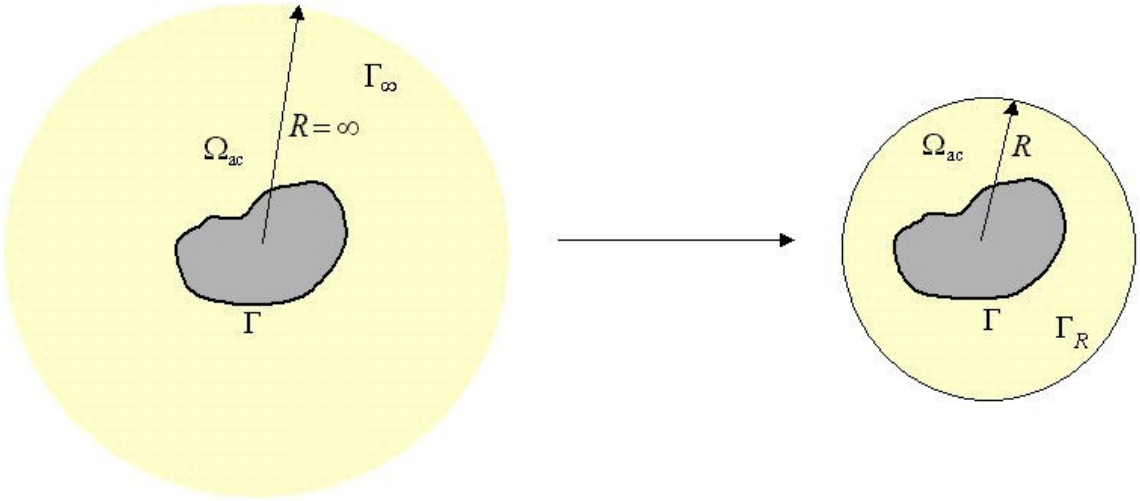

Figure 5.1: The problem of absorbing boundary conditions due to the finite computational domain.

equation so that it includes an absorption term that only differs from zero beyond Γ_R. The PML approach is very popular and widely used although its implementation requires the tunning of several numerical parameters and some stability issues still remain unresolved (see [1, 13, 48, 128] c.f. [118]).

In this work, however, we will not address the ABC problem. All computations will be performed in large enough computational domains that allow the global boundary operators to be replaced by the local Sommerfeld radiation condition (see section 5.2.3). Instead, we will concentrate on the second type of problem appearing in the numerical solution of the Helmholtz equation, namely the appearance of the pollution error for large wave numbers. To be precise, we will aim at finding some procedure to diminish this type of error in the finite element solution of the convected Helmholtz equation.

A large amount of work has been carried out to find non-polluted numerical solutions to the Helmholtz equation using finite element methods. The pollution error stems from the fact that the weak form associated to the Helmholtz equation is non positive definite for large wave numbers, although it satisfies a Gårding inequality that allows Galerkin methods to be applied to it [163]. However, the inf-sup constant has an inverse dependence with the wavenumber k that leads to a deterioration of the stability and to the appearance of the pollution error for large values of k. A dispersion analysis of the weak form interior numerical stencil reveals that this error is related to the fact that discrete waves propagate with a discrete wavenumber, k_h, instead of the continuous one. The difference between both wavenumbers, $k - k_h$, increases for large $k's$ and, as earlier mentioned, a phase error appears in the numerically solved waves (see e.g. [5, 119, 120]). This is illustrated in Fig. 5.2.

In order to avoid this problem several methods have been developed, some of them in the more general context of the CDR (convection-diffusion-reaction) equations. The basic

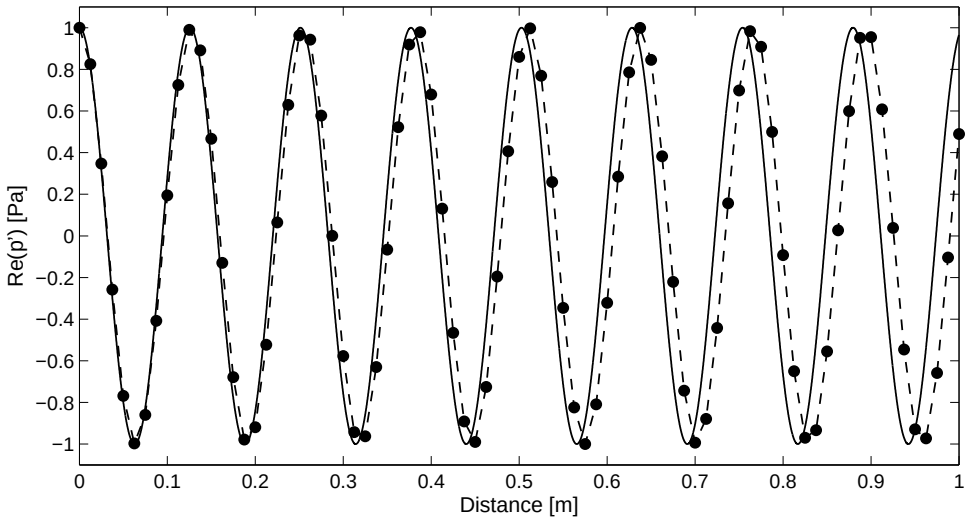

Figure 5.2: Dispersion error: the discrete wave propagates with a wave number, k_h (dot-dashed), that differs from the exact one, k (continuous).

idea of several of these methods is to add a stabilising term to the discrete weak form of the problem that enhances the behaviour of the solution, diminishing the pollution effects. This is the case in [119, 120, 287] where the GLS (Galerkin Least Squares) was applied to the Helmholtz equation in one and two dimensions. An alternative approach is the partition of unity method (PUM) [192, 223] in which the shape functions are multiplied by free space homogeneous solutions of the Helmholtz equation. This is also done in the GFEM (Generalized Finite Element Method) developed in [3, 4, 164], although in this case only the fine scales are multiplied by the free space solutions, while standard shape functions are used for the coarse ones. However, the GFEM is basically suitable for structured meshes. The SGS (Subgrid Scale) approach in [150, 154] has been already detailed in Chapter 3 and was applied to the Helmholtz equation using different models for the subscales in [36, 240]. This method also motivated the inclusion of the element boundary residues into the weak form [242]. Other approaches to find improved numerical solutions for the Helmholtz equation have considered the use of bubble functions [77] or enriching the standard polynomial field by means of plane waves. In the discontinuous enrichment method (DEM) [67] standard shape functions are used for the coarse scales while free space homogeneous solutions are added to them representing the influence of the finer scales. The underlying idea is that particular solutions are properly resolved by the coarse scales while the finer ones should contain solutions from the homogeneous partial differential Helmholtz equation. In [241] and [57] comparisons of the performance of some of these methods can be found and in [118] a recent and complete review of several finite element methods for time harmonic acoustics is provided.

It is the main purpose of this chapter to solve the convected Helmholtz equation for a background flow of constant speed, in the framework of finite element methods (FEM).

In contrast with the Helmholtz equation and as far as we know, the convected Helmholtz equation has received much less attention. In [125], some stabilising methods for the CDR scalar equation were re-adapted to include the case of a production source term and, recently, an analysis of the accuracy of the Galerkin solution to the convected wave equation has been addressed in [83, 84]. Dispersion and amplitude errors for upstream and downstream propagating waves using different finite element types have been studied as well as their dependence on several parameters such as the Mach number magnitude and the wave and flow orientations.

In this chapter, an algebraic subgrid scale finite element method for the convected Helmholtz equation is proposed [106]. A stabilising term is added to the discrete weak form of the problem containing a stabilisation parameter that is determined by means of a dispersion analysis. As we will deal with selfadjoint operators, the herein proposed method coincides with the GLS approach to the problem except for a minus sign that can be included in the definition of the stabilisation parameter [39,118]. The GLS approach is probably the cheapest and simplest way to provide stabilisation to the Helmholtz equation because its implementation is made at almost no computational cost [118]. In [57], it was concluded that the GLS performed superior to residual-free bubbles (only effective in one dimension) but that the QSFEM (Quasi stabilised FEM) or increasing the degree of the polynomial field were clearly better in lowering the dispersion error. However, the QSFEM is rather difficult to adapt to non uniform meshes and irregular boundary conditions, as already quoted in [57]. Some of the methods cited in the above paragraphs can also yield better results than GLS but usually at the cost of more implementation difficulties and higher computational cost. On the other hand, although it is often argued that the GLS has the main drawback of its dependence on the direction of the plane wave used to derive the stabilisation parameter, it has been shown that some standard values for this direction angle yield good results for very general situations [287, 288]. Actually, it has recently been checked by means of numerical experiments that the GLS clearly improves the Galerkin FEM results in intricate acoustic fields such as e.g., the noise radiation in an automotive interior or the scattering from a submarine-shaped obstacle [121]. In addition, the stabilisation parameters usually derived for a particular mesh (e.g., a mesh of bilinear elements) still work when changing to unstructured meshes [121,276]. As a consequence, we may conclude that GLS still becomes an appealing option when considering its easy implementation aspect and low computational cost, together with the clear improvement of the standard Galerkin FEM results. It is worthwhile to mention that recent work on GLS has involved adapting the stabilisation parameter for triangular and distorted elements [122,176].

The work presented in this chapter for the convected Helmholtz equation tends to confirm the general features found in the GLS application to the Helmholtz equation. A stabilisation parameter is derived for a structured mesh of quadrilateral bilinear elements, which yields exact nodal values for a wave propagating at a given direction in a background uniform flow of constant speed. This parameter also performs well if we use, instead, a mesh of unstructured quadrilateral elements. We have decided not to work with many simple problems with analytical solution (the performance of the method in these cases

could be readily outlined from the herein presented results, the analysis in [83, 84] and the GLS application to the Helmholtz equation) but to address a more intricate case in the line of what is done in [121]. Hence the case of aerodynamic sound generated by flow past a two dimensional cylinder has been considered again using the Lighthill acoustic analogy approach (see sections 3.2 and 3.6.1) but now taking also into account the convected Helmholtz equation. Following the proposed three step approach for CAA in section 3.2, a first incompressible computational fluid dynamic simulation has been performed in order to obtain the time evolution of the double divergence of the Reynolds stress. This quantity has been time Fourier transformed to the frequency domain and used as the acoustic source term for the Helmholtz and convected Helmholtz equation. Even though an unstructured mesh of triangular elements has been used in this example, the benefits of using the GLS stability parameter, derived from a quadrilateral bilinear element mesh, become apparent and the dispersion error in the outward generated waves is clearly reduced.

The chapter is organized as follows. In section 5.2 the relations among the wave equation, the Helmholtz equation and their convected counterparts are established. Fourier transform pairs together with Galilean and Lorentz transformations relate these equations. Change of variables by means of these transformations offer a first possibility to solve the convected Helmholtz equation. On the other hand, appropriate boundary conditions are given for the latter and it is shown that this equation corresponds to a particular case of the more general CDR equations. In section 5.3 we present the weak form of the problem and the subgrid scale finite element method proposed to solve it. The dispersion analysis to find the value for the stabilisation parameter is carried out. In section 5.4 we present the numerical examples. We first show how the method yields an exact nodal solution for a wave propagating in a mean flow of constant speed and we then present the case of aerodynamic noise generated by flow past a two dimensional cylinder for the convected Helmholtz equation. Finally, conclusions are drawn in section 5.5.

5.2 Steady and convected wave and Helmholtz equations

5.2.1 Wave equation and convected wave equation

The inhomogeneous wave equation for the propagation of pressure perturbations in a stationary, ideal medium is given by (*acoustic wave equation*, see section 2.2.3)

$$\left(c_0^{-2}\partial_{tt}^2 - \nabla^2\right) p\left(\boldsymbol{x}, t\right) = s\left(\boldsymbol{x}, t\right) \tag{5.1}$$

where $p\left(\boldsymbol{x}, t\right)$ stands for the acoustic pressure, $s\left(\boldsymbol{x}, t\right)$ is the source term, c_0 is the sound speed in the medium and ∇^2 represents the Laplacian operator (throughout this chapter we will use ∇^2 instead of Δ for the Laplacian operator, as it is common practice in acoustics). On the other hand, p will be used in this chapter to designate the acoustic

pressure instead of the p' used in previous chapters, as there will be now no possible confusion with the aerodynamic pressure.

For acoustic waves propagating in an homentropic, irrotational flow, (5.1) is no longer valid and has to be replaced by a linear equation for the time derivative of the velocity potential or for the perturbation velocity potential [145]. However, in the special case of a flow with mean velocity $\boldsymbol{U}_0(\boldsymbol{x})$ at a low Mach number ($M^2 << 1,\ M = \|\boldsymbol{M}\|,\ \boldsymbol{M}(\boldsymbol{x}) := \boldsymbol{U}_0(\boldsymbol{x})/c_0$) variations in the mean density and sound speed can be neglected and the acoustic wave propagation can be described by a relatively simple equation, namely the *convected* wave equation

$$\left[c_0^{-2}\left(\partial_t + \boldsymbol{U}_0(\boldsymbol{x})\cdot\nabla\right)^2 - \nabla^2\right] p(\boldsymbol{x},t) = s(\boldsymbol{x},t). \tag{5.2}$$

It follows that

- If $\boldsymbol{U}_0$ is constant (*uniform flow*) (5.2) becomes valid for Mach numbers up to one (transonic flows). Then, equations (5.1)-(5.2) become equivalent as they are related by a simple Galilean transformation of the coordinate system

$$\boldsymbol{x}' = \boldsymbol{x} + \boldsymbol{U}_0 t. \tag{5.3}$$

  Uniform flow will be assumed from now on throughout the chapter unless specified.

- It is quite customary to use the material derivative $D_t := \partial_t + \boldsymbol{U}_0\cdot\nabla$ to rewrite (5.2) as

$$\left(c_0^{-2}D_{tt}^2 - \nabla^2\right) p(\boldsymbol{x},t) = s(\boldsymbol{x},t) \tag{5.4}$$

  showing the close resemblance with (5.1).

5.2.2 Helmholtz equation and convected Helmholtz equation

The time reduced versions of (5.1)-(5.2) are obtained by taking their Fourier transforms. Assuming time harmonic motion and replacing ∂_t by $-i\omega$ in (5.1) yields the Helmholtz equation (see Chapter 2)

$$\left(-\nabla^2 - k_0^2\right)\hat{p}(\boldsymbol{x},\omega) = \hat{s}(\boldsymbol{x},\omega), \tag{5.5}$$

with $k_0 = \omega/c_0$ being the wavenumber and ω the radian frequency. Analogously, replacing ∂_t by $-i\omega$ in (5.2) yields the convected wave equation

$$-\left[\nabla^2 + \left(k_0 + i\boldsymbol{M}\cdot\nabla\right)^2\right]\hat{p}(\boldsymbol{x},\omega) = \hat{s}(\boldsymbol{x},\omega), \tag{5.6}$$

with $i = \sqrt{-1}$. We identify, for subsequent sections, the Helmholtz and convected Helmholtz differential operators as

$$\mathcal{L}_{\mathcal{H}} := \left(-\nabla^2 - k_0^2\right) \tag{5.7}$$

$$\mathcal{L}_{\mathcal{CH}} := -\left[\nabla^2 + \left(k_0 + i\boldsymbol{M}\cdot\nabla\right)^2\right]. \tag{5.8}$$

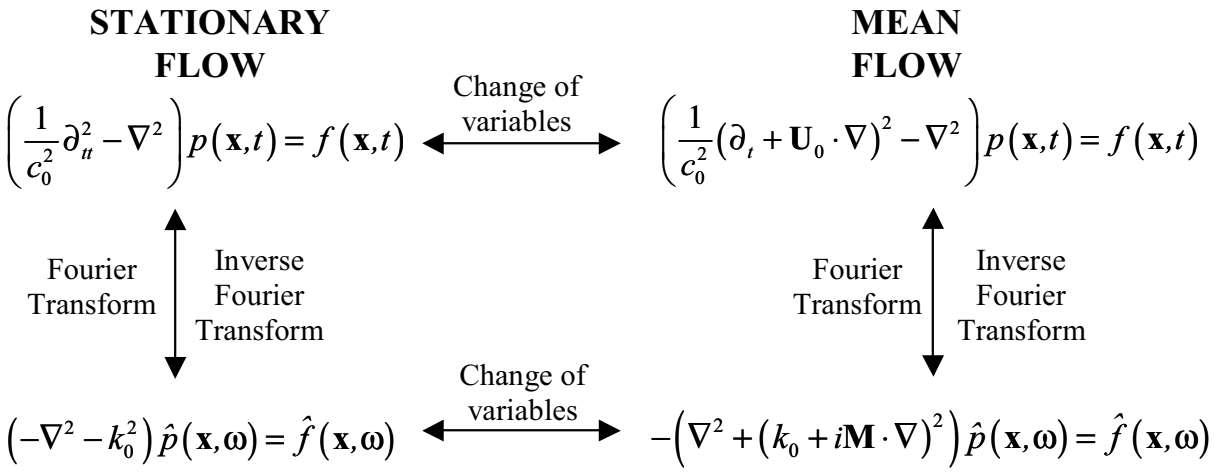

Figure 5.3: Equations framework

Note that, disregarding boundary condition contributions as it is common practice in the present numerical context, both operators are selfadjoint i.e.,

$$\mathcal{L}_{\mathcal{H}}{}^{\dagger} = \mathcal{L}_{\mathcal{H}}, \quad \mathcal{L}_{\mathcal{CH}}{}^{\dagger} = \mathcal{L}_{\mathcal{CH}}. \tag{5.9}$$

As for (5.1)-(5.2), equations (5.5)-(5.6) can also be related but now via a full Lorentz transformation (also known as a Prandtl-Glauert transformation in the aerodynamic context). This offers a first possibility to solve the convected wave equation by first converting it in the more simple Helmholtz equation, then solving for it and finally reverting to the original variables (see Fig. 5.3 for a schematic representation of the relations among all equations (5.1)-(5.2)-(5.5)-(5.6)). The full Lorentz transformation relating (5.5)-(5.6) involves a rotation plus a boost in the x-direction. The idea is to first rotate the coordinates so that the Mach vector $\boldsymbol{M}$ has only an x-component in the new coordinate-system, $\boldsymbol{x}'$, and then to dilate them together with an appropriate change of variables to obtain a Helmholtz equation in a second coordinate-system $\boldsymbol{x}''$. The two changes will be briefly and independently presented for clarity and given in a compact form at the end.

Rotation

Let us denote by $\boldsymbol{R}$ the rotation matrix that transforms the Mach number vector $\boldsymbol{M}$ so that it only has x-component in the new coordinate-system $\boldsymbol{x}'$, i.e., $\boldsymbol{M}' = \boldsymbol{R}\boldsymbol{M}$ with $\boldsymbol{M}' = (M, 0, 0)^{\top}$, or in components

$$\begin{pmatrix} M \\ 0 \\ 0 \end{pmatrix}' = \begin{pmatrix} R_{xx} & R_{xy} & R_{xz} \\ R_{yx} & R_{yy} & R_{yz} \\ R_{zx} & R_{zy} & R_{zz} \end{pmatrix} \begin{pmatrix} M_x \\ M_y \\ M_z \end{pmatrix}. \tag{5.10}$$

If we apply the change of coordinate-system

$$\boldsymbol{x}' = \boldsymbol{R}\boldsymbol{x} \;\Leftrightarrow\; x_i' = R_{ij}x_j \quad \forall i,j = 1 \div d \tag{5.11}$$

to the convected Helmholtz equation, (5.6), and take into account that $\boldsymbol{R}$ is an orthogonal matrix, (i.e., $\boldsymbol{R}^{-1} = \boldsymbol{R}^{\top}$) so that

$$\boldsymbol{R}\boldsymbol{R}^{\top} = \boldsymbol{I} \;\Leftrightarrow\; R_{ij}R_{ik} = \delta_{jk}, \tag{5.12}$$

it follows that the spatial derivatives transform as

$$\partial_i = \partial_i x_k' \partial_k' = R_{ki}\partial_k'. \tag{5.13}$$

Taking into account these results, it is quite straightforward to obtain (5.6) in the new coordinates

$$\begin{aligned} &-\left[\nabla'^2 + \left(k_0 + iM\partial_x'\right)^2\right]\hat{p}\left(\boldsymbol{x}', \omega\right) \\ &= -\left(\nabla'^2 + k_0^2 + 2iMk_0\partial_x' - M^2\partial_{xx}'^2\right)\hat{p}\left(\boldsymbol{x}', \omega\right) = \hat{s}\left(\boldsymbol{R}^{\top}\boldsymbol{x}', \omega\right). \end{aligned} \tag{5.14}$$

Boost in the x-direction

We now perform a boost in the x-direction to (5.14) consisting in taking $\boldsymbol{x}'' = \boldsymbol{D}\boldsymbol{x}'$ with $\boldsymbol{D}$ being the diagonal matrix $\boldsymbol{D} = \mathrm{diag}\left(\beta^{-1}, 1, 1\right)$ (it has inverse $\boldsymbol{D}^{-1} = \mathrm{diag}\left(\beta, 1, 1\right)$) and β being defined as usual by $\beta := \sqrt{1 - M^2}$. We also take $k_0'' = \beta^{-1}k_0$ and $\hat{p}''\left(\boldsymbol{x}'', k_0''\right) = \hat{p}\left(\boldsymbol{x}', k_0\right)\exp\left(ik_0''Mx''\right)$. Again, after some straightforward algebra we can obtain an expression for (5.14) in the new coordinates $\boldsymbol{x}''$:

$$\left(\nabla''^2 + k_0''^2\right)\hat{p}''\left(\boldsymbol{x}'', \omega\right) = e^{\left(ik_0''Mx''\right)}\hat{s}\left(\boldsymbol{R}^{\top}\boldsymbol{D}^{-1}\boldsymbol{x}'', \beta k_0''\right). \tag{5.15}$$

Full Lorentz transformation

From the previous results it should be noted that

- Equation (5.15) is a Helmholtz equation with a source term modified by an exponential factor. As the source term is a known input quantity for the problem, it will have to be expressed in terms of the new coordinates $\boldsymbol{x}''$ to solve (5.15).

- The full Lorentz transformation can be set in a compact form as

$$\begin{aligned} \boldsymbol{x}'' = \boldsymbol{D}\boldsymbol{R}\boldsymbol{x}, \quad k_0'' = \beta^{-1}k_0 \\ \hat{p}''\left(\boldsymbol{x}'', k_0''\omega\right) = \hat{p}\left(\boldsymbol{R}\boldsymbol{x}, \omega\right)\exp\left[i\beta^{-1}k_0\left(\boldsymbol{R}\boldsymbol{M}\right)\cdot\left(\boldsymbol{D}\boldsymbol{R}\boldsymbol{x}\right)\right]. \end{aligned} \tag{5.16}$$

5.2.3 Boundary conditions for the convected Helmholtz problem and strong formulation

In order to solve the Helmholtz and convected Helmholtz equations in a given domain we have to complement them with appropriate boundary conditions. Let us first consider the problem of finding $\hat{p} : \Omega_{ac} \mapsto \mathbb{C}$ for the Helmholtz equation, (5.5), in a domain $\Omega_{ac} \subset \mathbb{R}^d$ with smooth boundary $\partial\Omega_{ac} = \Gamma_D \cup \Gamma_N \cup \Gamma_\infty$ such that

$$-\left(\nabla^2 + k_0^2\right)\hat{p}\left(\boldsymbol{x},\omega\right) = \hat{s}\left(\boldsymbol{x},\omega\right) \quad \text{in } \Omega_{ac} \tag{5.17}$$

$$\hat{p}\left(\boldsymbol{x},\omega\right) = \hat{p}_D\left(\boldsymbol{x},\omega\right) \quad \text{on } \Gamma_D \tag{5.18}$$

$$\nabla\hat{p}\left(\boldsymbol{x},\omega\right)\cdot\boldsymbol{n} = \hat{g}\left(\boldsymbol{x},\omega\right) \quad \text{on } \Gamma_N \tag{5.19}$$

$$\nabla\hat{p}\left(\boldsymbol{x},\omega\right)\cdot\boldsymbol{n} = ik_0\hat{p} \quad \text{on } \Gamma_\infty. \tag{5.20}$$

In (5.19), (5.20) $\boldsymbol{n}$ represents the normal respectively pointing outwards of Γ_N and Γ_∞, $\hat{g} : \Gamma_N \mapsto \mathbb{C}$, represents data prescribed on Γ_N and (5.20) represents the Sommerfeld radiation condition (see section 3.2.3, equation (3.10)).

Let us now find the appropriate boundary conditions for the convected Helmholtz equation. According to (5.17)-(5.20), we can consider the convected problem in the $\boldsymbol{x}''$ coordinate system, i.e. we aim at solving (5.15) in a computational domain Ω''_{ac}. Considering Dirichlet, Neumann and Sommerfeld conditions we are left with the strong or differential form of the Helmholtz problem: find the acoustic pressure $\hat{p}'' : \Omega''_{ac} \mapsto \mathbb{C}$, being $\Omega''_{ac} \subset \mathbb{R}^d$ a bounded domain with smooth boundary $\partial\Omega''_{ac} = \Gamma''_D \cup \Gamma''_N \cup \Gamma''_\infty$, such that

$$\left(\nabla''^2 + k_0''^2\right)\hat{p}''\left(\boldsymbol{x}'',\omega\right) = e^{\left(ik_0''M\boldsymbol{x}''\right)}\hat{s}\left(\boldsymbol{R}^\top\boldsymbol{D}^{-1}\boldsymbol{x}'',\beta k_0''\right) \quad \text{in } \Omega''_{ac} \tag{5.21}$$

$$\hat{p}''\left(\boldsymbol{x}'',\omega\right) = \hat{p}''_D\left(\boldsymbol{R}^\top\boldsymbol{D}^{-1}\boldsymbol{x}'',\beta k_0''\right) \quad \text{on } \Gamma''_D \tag{5.22}$$

$$\nabla''\hat{p}''\left(\boldsymbol{x},\omega\right)\cdot\boldsymbol{n} = \hat{g}\left(\boldsymbol{R}^\top\boldsymbol{D}^{-1}\boldsymbol{x}'',\beta k_0''\right) \quad \text{on } \Gamma''_N \tag{5.23}$$

$$\nabla''\hat{p}''\left(\boldsymbol{x},\omega\right)\cdot\boldsymbol{n} = ik_0\hat{p}''\left(\boldsymbol{x},\omega\right) \quad \text{on } \Gamma''_\infty. \tag{5.24}$$

As previously mentioned, solving (5.21) and reverting to the original coordinate-system and variables is a suitable option to find the solution of the convected Helmholtz equation. However, if we are interested in directly solving this equation we will need appropriate boundary conditions for it. These conditions can be found by reverting the Helmholtz boundary conditions in (5.22)-(5.23)-(5.24) to the original variables and coordinate system through the Lorentz transformation in (5.16). This yields the following results:

Sommerfeld's radiation condition

We start from the Sommerfeld's radiation condition in the $\boldsymbol{x}''$ coordinate system, (5.24), and revert the x-boost by substituting

$$\boldsymbol{x}'' = \boldsymbol{D}\boldsymbol{x}', \tag{5.25}$$

$$k_0'' = \beta^{-1}k_0, \tag{5.26}$$

$$\hat{p}''\left(\boldsymbol{x}'',k_0''\right) = \hat{p}\left(\boldsymbol{x}',k_0\right)\exp\left(ik_0''Mx''\right), \tag{5.27}$$

in this equation. This yields

$$\begin{aligned}&\left(\beta^{-1}n'_x\beta\partial'_x + n'_y\partial'_y + n'_z\partial'_z\right)\left(\hat{p}\left(\boldsymbol{x}', k_0\right)e^{ik_0M\beta^{-2}x'}\right)\\&= \left(\boldsymbol{n}'\cdot\nabla'\right)\left(\hat{p}\left(\boldsymbol{x}', k_0\right)e^{ik_0M\beta^{-2}x'}\right) = i\beta^{-1}k_0\hat{p}\left(\boldsymbol{x}', k_0\right)e^{ik_0M\beta^{-2}x'},\end{aligned} \tag{5.28}$$

from which it follows

$$\boldsymbol{n}'\cdot\left[\nabla'\hat{p} + \left(ik_0M\beta^{-2}\hat{p}, 0, 0\right)\right] = i\beta^{-1}\hat{p}, \tag{5.29}$$

and then

$$\boldsymbol{n}'\cdot\nabla'\hat{p} = ik_0\beta^{-1}\left[1 - M\beta^{-1}\left(\boldsymbol{n}'\cdot\overline{\boldsymbol{M}}'\right)\right]. \tag{5.30}$$

with $\bar{\boldsymbol{M}}$ being the normalised Mach number vector, $\bar{\boldsymbol{M}} = (1/M)\,\boldsymbol{M}$ (in this case in the $\boldsymbol{x}'$ coordinate system).

We can next revert the rotation to finally obtain the Sommerfeld condition for the convected Helmholtz equation in the $\boldsymbol{x}$ coordinate system. Doing so in (5.30) and using the orthogonality of the rotation matrix yields

$$R_{jl}n_lR_{jm}\partial_m\hat{p} = ik_0\beta^{-1}\left[1 - M\beta^{-1}\left(R_{kl}n_lR_{km}\overline{M}_m\right)\right], \tag{5.31}$$

that becomes

$$\nabla\hat{p}\left(\boldsymbol{x}, \omega\right)\cdot\boldsymbol{n} = ik_0\alpha_S\hat{p}\left(\boldsymbol{x}, \omega\right), \tag{5.32}$$

$$\alpha_S := \beta^{-1}\left[1 - M\beta^{-1}\left(\boldsymbol{n}\cdot\bar{\boldsymbol{M}}\right)\right]. \tag{5.33}$$

Neumann boundary condition

The Neumann boundary condition for the convected Helmholtz equation can be found proceeding in an analogous way to what has been done for the Sommerfeld condition so details will not be reproduced. The condition is given by

$$\nabla\hat{p}\left(\boldsymbol{x}, \omega\right)\cdot\boldsymbol{n} = -ik_0\alpha_N\hat{p}\left(\boldsymbol{x}, \omega\right) + \hat{g}\left(\boldsymbol{x}, k_0\right) \tag{5.34}$$

$$\alpha_N := \beta^{-2}\left(\boldsymbol{n}\cdot\bar{\boldsymbol{M}}\right) = \beta^{-1} - \alpha_S. \tag{5.35}$$

Note that, as expected $\alpha_S = 1$, $\alpha_N = 0$ for $\boldsymbol{M} = \boldsymbol{0}$.

Taking into account (5.32)-(5.35), the strong formulation for the convected Helmholtz equation problem can be written as: find the acoustic pressure $\hat{p} : \Omega_{ac} \mapsto \mathbb{C}$, being $\Omega_{ac} \subset \mathbb{R}^d$ a bounded domain with smooth boundary $\partial\Omega_{ac} = \Gamma_D \cup \Gamma_N \cup \Gamma_\infty$, such that

$$-\left[\nabla^2 + \left(k_0 + i\boldsymbol{M}\cdot\nabla\right)^2\right]\hat{p}\left(\boldsymbol{x}, \omega\right) = \hat{s}\left(\boldsymbol{x}, \omega\right) \quad \text{in } \Omega_{ac} \tag{5.36}$$

$$\hat{p}\left(\boldsymbol{x}, \omega\right) = \hat{p}_D\left(\boldsymbol{x}, \omega\right) \quad \text{on } \Gamma_D \tag{5.37}$$

$$\nabla\hat{p}\left(\boldsymbol{x}, \omega\right)\cdot\boldsymbol{n} = ik_0\alpha_S\hat{p} \quad \text{on } \Gamma_\infty \tag{5.38}$$

$$\nabla\hat{p}\left(\boldsymbol{x}, \omega\right)\cdot\boldsymbol{n} = -ik_0\alpha_N\hat{p}\left(\boldsymbol{x}, \omega\right) + \hat{g}\left(\boldsymbol{x}, k_0\right) \quad \text{on } \Gamma_N. \tag{5.39}$$

5.3 Convected Helmholtz equation as a CDR equation

It will be next shown that the Helmholtz and convected Helmholtz equations correspond to particular cases of the more general Convection-Diffusion-Reaction (CDR) equation. Hence, stabilised numerical methods developed for this equation could in principle be applied to the former [39]. The scalar CDR equation is given by

$$\partial_i \left(a_i u\right) - \partial_i \left(k_{ij} \partial_j u\right) + s u = f \quad \text{in } \Omega, \tag{5.40}$$

with $u \in \mathbb{C}$ and $f \in \mathbb{C}$ respectively being the scalar unknown and the scalar force term, a_i the components of the convection velocity vector, k_{ij} the diffusion parameters and s the reaction term. (5.40) is to be completed with appropriate Dirichlet, Neumann or mixed boundary conditions on $\partial\Omega$ for a given problem.

The Helmholtz equation, (5.21), corresponds to (5.40) with

$$a_i = 0 \; \forall i, \qquad k_{ij} = \delta_{ij}, \qquad s = -k_0''^2, \tag{5.41}$$

and with δ_{ij} standing for the Kronecker delta. In order to write the convected Helmholtz equation (5.36) as a scalar CDR equation we expand the squared term in the convected Helmholtz differential operator (5.8)

$$\mathcal{L}_{\mathcal{CH}} = -\left[\nabla^2 + \left(k_0 + i\boldsymbol{M}\cdot\nabla\right)^2\right] = -\nabla^2 - k_0^2 - 2ik_0\boldsymbol{M}\cdot\nabla + \left(\boldsymbol{M}\cdot\nabla\right)\left(\boldsymbol{M}\cdot\nabla\right), \tag{5.42}$$

and take into account that (remember $\boldsymbol{M}$ is constant)

$$\nabla^2 = \nabla\cdot\left(\boldsymbol{I}\cdot\nabla\right), \tag{5.43}$$

$$2ik_0\boldsymbol{M}\cdot\nabla = \nabla\cdot\left(2ik_0\boldsymbol{M}\right), \tag{5.44}$$

$$\left(\boldsymbol{M}\cdot\nabla\right)\left(\boldsymbol{M}\cdot\nabla\right) = M_i\partial_i M_j\partial_j = \nabla\cdot\left(\boldsymbol{M}\otimes\boldsymbol{M}\right). \tag{5.45}$$

We then arrive at the following expression for (5.6)

$$-\nabla\cdot\left(2ik_0\boldsymbol{M}\hat{p}\right) - \nabla\cdot\left\{\left[\boldsymbol{I} - \left(\boldsymbol{M}\otimes\boldsymbol{M}\right)\right]\cdot\nabla\hat{p}\right\} - k_0^2\hat{p} = \hat{s}. \tag{5.46}$$

Equation (5.46) corresponds to equation (5.40) with the following identifications for the convective velocity, dissipative and production terms

$$a_i = -2ik_0M_i, \qquad k_{ij} = \delta_{ij} - M_iM_j, \qquad s = -k_0^2\ . \tag{5.47}$$

If we split the acoustic pressure into its real and imaginary parts, $\hat{p} = \hat{p}_{Re} + i\hat{p}_{Im}$, a CDR real system of two unknowns corresponding to the vector counterpart of (5.40) can be obtained for the Helmholtz and convected Helmholtz equations. These systems are often more practical for computational implementations and will be next given for completeness.

The vectorial CDR equation is written as

$$\partial_i \left(\boldsymbol{A}_i\boldsymbol{u}\right) - \partial_i \left(\boldsymbol{K}_{ij}\partial_j\boldsymbol{u}\right) + \boldsymbol{S}\boldsymbol{u} = \boldsymbol{f} \quad \text{in } \Omega \tag{5.48}$$

where now $\boldsymbol{u}$ and $\boldsymbol{f}$ are vectors of n_{unk} components and $\boldsymbol{A}_i$, $\boldsymbol{K}_{ij}$ and $\boldsymbol{S}$ respectively stand for the $n_{unk} \times n_{unk}$ convection, diffusion and reaction matrices, with $i, j = 1 \div d$.

The Helmholtz equation, (5.21), can be split using $\hat{p} = \hat{p}_{Re} + i\hat{p}_{Im}$ as the system

$$
\begin{aligned}
&- \left[\begin{pmatrix} \partial''^2_{xx} & 0 \\ 0 & \partial''^2_{xx} \end{pmatrix} + \begin{pmatrix} \partial''^2_{yy} & 0 \\ 0 & \partial''^2_{yy} \end{pmatrix} + \begin{pmatrix} \partial''^2_{zz} & 0 \\ 0 & \partial''^2_{zz} \end{pmatrix} + \begin{pmatrix} k''^2_0 & 0 \\ 0 & k''^2_0 \end{pmatrix} \right] \begin{pmatrix} \hat{p}''_{Re} \\ \hat{p}''_{Im} \end{pmatrix} \\
&= \begin{pmatrix} \cos(Mk''_0 x'') & -\sin(Mk''_0 x'') \\ \sin(Mk''_0 x'') & \cos(Mk''_0 x'') \end{pmatrix} \begin{pmatrix} \hat{s}''_{Re} \\ \hat{s}''_{Im} \end{pmatrix} \quad \text{in } \Omega''_{ac}
\end{aligned} \tag{5.49}
$$

with boundary conditions (5.22)-(5.24) transformed written as

$$
\begin{pmatrix} \hat{p}''_{Re} \\ \hat{p}''_{Im} \end{pmatrix} = \begin{pmatrix} \hat{p}''_{DRe} \\ \hat{p}''_{DIm} \end{pmatrix} \quad \text{on } \Gamma''_D \tag{5.50}
$$

$$
\begin{pmatrix} \partial_{\boldsymbol{n}} \hat{p}''_{Re} \\ \partial_{\boldsymbol{n}} \hat{p}''_{Im} \end{pmatrix} = \begin{pmatrix} \hat{g}''_{DRe} \\ \hat{g}''_{DIm} \end{pmatrix} \quad \text{on } \Gamma''_N \tag{5.51}
$$

$$
\begin{pmatrix} \partial_{\boldsymbol{n}} \hat{p}''_{Re} \\ \partial_{\boldsymbol{n}} \hat{p}''_{Im} \end{pmatrix} = \begin{pmatrix} 0 & -k''_0 \\ k''_0 & 0 \end{pmatrix} \begin{pmatrix} \hat{g}''_{Re} \\ \hat{g}''_{Im} \end{pmatrix} \quad \text{on } \Gamma''_\infty. \tag{5.52}
$$

(5.49) corresponds to (5.48) taking

$$
\boldsymbol{A}_i = \boldsymbol{0}, \qquad \boldsymbol{K}_{ij} = \boldsymbol{I}\delta_{ij}, \qquad \boldsymbol{S} = -k''^2_0 \boldsymbol{I} \ . \tag{5.53}
$$

Similarly, for the convected Helmholtz equation, (5.36)-(5.39), we obtain

$$
\begin{aligned}
&- \begin{pmatrix} \partial_i & 0 \\ 0 & \partial_i \end{pmatrix} \begin{pmatrix} 0 & 2k_0 M_i \\ 2k_0 M_i & 0 \end{pmatrix} \begin{pmatrix} \hat{p}_{Re} \\ \hat{p}_{Im} \end{pmatrix} \\
&- \begin{pmatrix} \partial_i & 0 \\ 0 & \partial_i \end{pmatrix} \left[\begin{pmatrix} \delta_{ij} - M_i M_j & M_i M_j \\ M_i M_j & \delta_{ij} - M_i M_j \end{pmatrix} \begin{pmatrix} \partial_j & 0 \\ 0 & \partial_j \end{pmatrix} \begin{pmatrix} \hat{p}_{Re} \\ \hat{p}_{Im} \end{pmatrix} \right] \\
&- \begin{pmatrix} k_0^2 & 0 \\ 0 & k_0^2 \end{pmatrix} \begin{pmatrix} \hat{p}_{Re} \\ \hat{p}_{Im} \end{pmatrix} = \begin{pmatrix} \hat{s}_{Re} \\ \hat{s}_{Im} \end{pmatrix} \quad \text{in } \Omega_{ac}
\end{aligned} \tag{5.54}
$$

with boundary conditions

$$
\begin{pmatrix} \hat{p}_{Re} \\ \hat{p}_{Im} \end{pmatrix} = \begin{pmatrix} \hat{p}_{DRe} \\ \hat{p}_{DIm} \end{pmatrix} \quad \text{on } \Gamma_D, \tag{5.55}
$$

$$
\begin{pmatrix} \partial_{\boldsymbol{n}} \hat{p}_{Re} \\ \partial_{\boldsymbol{n}} \hat{p}_{Im} \end{pmatrix} = \begin{pmatrix} 0 & k_0 \alpha_N \\ -k_0 \alpha_N & 0 \end{pmatrix} \begin{pmatrix} \hat{p}_{Re} \\ \hat{p}_{Im} \end{pmatrix} + \begin{pmatrix} \hat{g}_{Re} \\ \hat{g}_{Im} \end{pmatrix} \quad \text{on } \Gamma_N, \tag{5.56}
$$

$$\begin{pmatrix} \partial_{\boldsymbol{n}}\hat{p}_{Re} \\ \partial_{\boldsymbol{n}}\hat{p}_{Im} \end{pmatrix} = \begin{pmatrix} 0 & -k_0\alpha_S \\ k_0\alpha_S & 0 \end{pmatrix} \begin{pmatrix} \hat{p}_{Re} \\ \hat{p}_{Im} \end{pmatrix} \quad \text{on } \Gamma_\infty. \tag{5.57}$$

Equation (5.54) is a CDR system with

$$\boldsymbol{A}_i = \begin{pmatrix} 0 & 2k_0M_i \\ 2k_0M_i & 0 \end{pmatrix}, \qquad \boldsymbol{K}_{ij} = \begin{pmatrix} \delta_{ij} - M_iM_j & M_iM_j \\ M_iM_j & \delta_{ij} - M_iM_j \end{pmatrix}, \qquad \boldsymbol{S} = -k_0^2\boldsymbol{I} \ . \tag{5.58}$$

5.4 Numerical approximation using the Galerkin FEM

5.4.1 Continuous weak forms

As already stated in section 3.3.2, in order to solve the differential Helmholtz and convected Helmholtz equations by means of a finite element method we first have to obtain their continuous weak forms. This is done as usual multiplying (5.17) by a test function and integrating over the computational domain Ω_{ac}. Following the notation introduced in sections 3.3.1 and 3.3.2, the weak problem for the inhomogeneous Helmholtz equation in (5.17) with boundary conditions given by (5.18)-(5.20) can be stated as: find $\hat{p} \in \mathcal{W}$ such that

$$(\nabla\hat{p}, \nabla w) - k_0^2\,(\hat{p}, w) - ik_0\,(\hat{p}, w)_{\Gamma_\infty} = \langle \hat{s}, w\rangle + (\hat{g}, w)_{\Gamma_N} \tag{5.59}$$

for all $w \in \mathcal{W}_0$. Let us remind that the parenthesis with no subscript in (5.59) stand for the scalar product in $L^2\,(\Omega_{ac})$ and that the scalar products in the equation involve the complex conjugate of the test function, given that the pressure is a complex function. The brackets stand for the duality pair between $H_0^1\,(\Omega_{ac})$ and $H^{-1}\,(\Omega_{ac})$. On the other hand, we have considered $\hat{g}$ in $L^2\,(\Gamma_N)$.

Similarly, the weak problem for the convected Helmholtz equation, (5.36), with boundary conditions given by (5.37)-(5.39) can be formulated as: find $\hat{p} \in \mathcal{W}$ such that

$$\begin{aligned} -2ik_0\,(\boldsymbol{M}\cdot\nabla\hat{p}, \nabla w) + ([\boldsymbol{I} - \boldsymbol{M}\otimes\boldsymbol{M}]\,\nabla\hat{p}, \nabla w) - k_0^2\,(\hat{p}, w) \\ -ik_0\alpha_S\,(\hat{p}, w)_{\Gamma_\infty} + ik_0\alpha_N\,(\hat{p}, w)_{\Gamma_N} = \langle \hat{s}, w\rangle + (\hat{g}, w)_{\Gamma_N} \end{aligned} \tag{5.60}$$

for all $w \in \mathcal{W}_0$. Use of the convected Helmholtz equation in the form of (5.46) has been made in this expression.

5.4.2 Discrete weak forms

The discrete weak form corresponding to the Galerkin finite element approximation of (5.59) can be stated as follows: given a finite element partition of Ω_{ac} (see Chapter 3) with n_e elements and n_p nodes, and the finite dimensional subspaces $\mathcal{W}_h$, $\mathcal{W}_{h,0} \subset \mathcal{W}$, find $\hat{p}_h \in \mathcal{W}_h$ such that

$$(\nabla\hat{p}_h, \nabla w_h) - k_0^2\,(\hat{p}_h, w_h) - ik_0\,(\hat{p}_h, w_h)_{\Gamma_\infty} = \langle \hat{s}_h, w_h\rangle + (\hat{g}, w_h)_{\Gamma_N} \tag{5.61}$$

for all $w_h \in \mathcal{W}_{h,0}$. In (5.61) $\hat{p}_h$ will be of the type

$$\hat{p}_h(\boldsymbol{x}) = \sum_{a=1}^{n_p} N_p^a(\boldsymbol{x})\,\hat{P}^a \tag{5.62}$$

with $N_p^a(\boldsymbol{x})$ being the acoustic pressure shape functions and $\hat{P}^a$ its nodal values.

Let us denote by $\|\cdot\|$ the norm in $L^2(\Omega_{ac})$. If we take $w_h = \hat{p}_h$ in (5.61) and ignore the boundary terms in the sesquilinear form, we are left with the inequality

$$\|\nabla\hat{p}_h\|^2 - k_0^2\,\|\hat{p}_h\|^2 \leq \|\hat{p}_h\|\,\|\hat{s}_h\|\,, \tag{5.63}$$

which states the fact that the discrete weak form (the same follows for the continuous one) may become non positive definite for large wavenumbers. This may lead to the appearance of stability problems and, consequently, to the necessity of using some stabilising techniques to solve the weak form of the Helmholtz equation.

On the other hand, the Galerkin finite element approximation of the convected Helmholtz equation weak form, (5.60), can be stated as: find $\hat{p}_h \in \mathcal{W}_h$ such that

$$\begin{aligned} -2ik_0\,(\boldsymbol{M}\cdot\nabla\hat{p}_h, \nabla w_h) + ([\boldsymbol{I} - \boldsymbol{M}\otimes\boldsymbol{M}]\,\nabla\hat{p}_h, \nabla w_h) - k_0^2\,(\hat{p}_h, w_h) \\ -ik_0\alpha_S\,(\hat{p}_h, w_h)_{\Gamma_\infty} + ik_0\alpha_N\,(\hat{p}_h, w_h)_{\Gamma_N} = \langle\hat{s}_h, w_h\rangle + (\hat{g}, w_h)_{\Gamma_N} \end{aligned} \tag{5.64}$$

for all $w_h \in \mathcal{W}_{h,0}$. If we now set $w_h = \hat{p}_h$ and ignore the boundary terms, it follows the inequality

$$\|\nabla\hat{p}_h\|^2 - \|\boldsymbol{M}\cdot\nabla\hat{p}_h\|^2 - k_0^2\,\|\hat{p}_h\|^2 \leq \|\hat{p}_h\|\,\|\hat{s}_h\|\,, \tag{5.65}$$

which states that there is no control on the convective term and that analogously to (5.63), the weak form can be non positive definite for large wave numbers (remember that $M < 1$ for our purposes). Hence, stability problems may also be expected for the Galerkin finite element solution of the convected Helmholtz equation.

5.4.3 Well-posedness and convergence theorems

In the previous sections we have presented a general mathematical framework for the Helmholtz and convected Helmholtz equations, showing that they correspond to particular cases of the more general CDR (Convection-Diffusion-Reaction) systems. We have shown how these equations can be related via some variable transformations and we have found appropriate boundary conditions for them. In order to solve the equations using finite element methods, we have presented their variational or weak continuous forms in the last section, as well as their Galerkin discrete counterparts. The problems arising in the numerical solution of the latter have been also insinuated, as earlier done in the introduction of the chapter.

In this and next section we precisely aim at gaining some insight on the nature of the numerical errors appearing in the Galerkin finite element solution of the Helmholtz and convected Helmholtz equations. To do so we will first review some general theorems that

assess under which conditions a weak problem is well-posed or not. We remind that a boundary value problem is said to be well-posed if, for a given set of data, the solution exists, is unique and it is stable (i.e., it is bounded by the data). We will also review some convergence theorems that establish error estimates for the finite element approximations of weak problems.

In the preceding chapters, a detailed explanation to justify the appearance of instabilities in the numerical solution of the Navier-Stokes equations was not provided. However, we have considered worthwhile to present such information for the Helmholtz and convected Helmholtz equation, given that the final goal of this chapter precisely consists in developing a a stabilisation procedure to mitigate them. In the presentation we have closely followed the main lines in [163] although making use of some particularisations. On the other hand, we note that bold characters will be used for the variables in the following theorems, accounting for the fact that the complex pressure field might be represented in vector notation.

Well-posedness of positive definite forms

A sesquilinear form $a : \mathcal{V} \times \mathcal{V} \mapsto \mathbb{C}$, with $\mathcal{V}$ being a Hilbert space, is said to be $\mathcal{V}$-*elliptic* or *positive definite* if exists $K > 0$ such that

$$K \left\| \boldsymbol{u} \right\|_{\mathcal{V}}^2 \leq a\left(\boldsymbol{u}, \boldsymbol{u}\right)$$

for all $\boldsymbol{u} \in \mathcal{V}$.

The well-posedness (existence, uniqueness and stability) of positive definite weak forms is established by the Lax-Milgram theorem.

Theorem 5.1 (Lax-Milgram) *Let us consider the abstract variational problem of finding* $\boldsymbol{u} \in \mathcal{V}$ *such that*

$$a\left(\boldsymbol{u}, \boldsymbol{w}\right) = l\left(\boldsymbol{w}\right) \quad \forall \boldsymbol{w} \in \mathcal{V}, \tag{5.66}$$

where $\mathcal{V}$ *is a Hilbert space (in fact it suffices* $\mathcal{V}$ *separable),* $a : \mathcal{V} \times \mathcal{V} \mapsto \mathbb{C}$*, is a sesquilinear form and* $l : \mathcal{V} \mapsto \mathbb{C}$ *is an antilinear functional. The solution to problem (5.66) exists and is unique if the following conditions fulfill:*

a) $a\left(\boldsymbol{u}, \boldsymbol{w}\right)$ *is continuous:*

$$\exists\ N_a > 0 \mid a\left(\boldsymbol{u}, \boldsymbol{w}\right) \leq N_a \left\| \boldsymbol{u} \right\|_{\mathcal{V}} \left\| \boldsymbol{w} \right\|_{\mathcal{V}} \quad \forall \boldsymbol{u}, \boldsymbol{w}\ \in \mathcal{V}$$

b) $l\left(\boldsymbol{w}\right)$ *is continuous:*

$$\exists\ N_l > 0 \mid l\left(\boldsymbol{w}\right) \leq N_l \left\| \boldsymbol{w} \right\|_{\mathcal{V}} \quad \forall \boldsymbol{w}\ \in \mathcal{V}$$

c) $a\left(\boldsymbol{u}, \boldsymbol{w}\right)$ *is* $\mathcal{V}$*-elliptic:*

$$\exists\ K > 0 \mid K \left\| \boldsymbol{u} \right\|_{\mathcal{V}}^2 \leq a\left(\boldsymbol{u}, \boldsymbol{u}\right) \quad \forall \boldsymbol{u}\ \in \mathcal{V} \tag{5.67}$$

Stability follows straightforwardly from conditions b) and c). We can see that

$$\|\boldsymbol{u}\|_{\mathcal{V}} \leq \frac{N_l}{K} \tag{5.68}$$

or alternatively, for $l(\boldsymbol{w}) = \langle \boldsymbol{s}, \boldsymbol{w} \rangle$,

$$\|\boldsymbol{u}\|_{\mathcal{V}} \leq \frac{1}{K} \|\boldsymbol{s}\|_{\mathcal{V}'}$$

with $\mathcal{V}'$ being the dual space of $\mathcal{V}$. Hence, the Lax-Milgram theorem effectively guarantees well-posedness of the variational problem (5.66).

An important property of positive definite forms is that $\mathcal{V}$-ellipticity is inherited by Galerkin discrete weak forms, i.e., if the continuous weak forms of the Helmholtz and convected Helmholtz equations, (5.59)-(5.60), were H^1-elliptic, their discrete counterparts, (5.61),(5.64), would be also H^1-elliptic. Unfortunately, H^1-ellipticity of weak forms (5.59)-(5.60) is only achieved at very low wave numbers. Hence, we cannot make use of the Lax-Milgram theorem to ensure well-posedness for large wave numbers and an alternative theorem dealing with indefinite weak forms is required in this case. On the other hand, note that theorem 5.1 only applies to forms with both arguments belonging to the same space.

Well-posedness of indefinite forms

A generalised form of the Lax-Milgram theorem that establishes under which conditions a variational problem with an indefinite form can be well-posed is given by the Babuška theorem.

Theorem 5.2 (Babuška) *Let us consider the abstract variational problem of finding* $\boldsymbol{u} \in \mathcal{V}$ *such that*

$$a(\boldsymbol{u}, \boldsymbol{w}) = l(\boldsymbol{w}) \quad \forall \boldsymbol{w} \in \mathcal{W}, \tag{5.69}$$

where $\mathcal{V}, \mathcal{W}$ *are Hilbert spaces (it suffices* $\mathcal{V}, \mathcal{W}$ *separables),* $a : \mathcal{V} \times \mathcal{W} \mapsto \mathbb{C}$ *is a sesquilinear form and* $l : \mathcal{W} \mapsto \mathbb{C}$ *is an antilinear functional. The solution to problem (5.67) exists and is unique if the following conditions fulfill:*

a) $a(\boldsymbol{u}, \boldsymbol{w})$ *is continuous:*

$$\exists\ N_a > 0 \mid a(\boldsymbol{u}, \boldsymbol{w}) \leq N_a \|\boldsymbol{u}\|_{\mathcal{V}} \|\boldsymbol{w}\|_{\mathcal{W}} \quad \forall \boldsymbol{u} \in \mathcal{V}, \boldsymbol{w} \in \mathcal{W}$$

b) $l(\boldsymbol{w})$ *is continuous:*

$$\exists\ N_l > 0 \mid l(\boldsymbol{w}) \leq N_l \|\boldsymbol{w}\|_{\mathcal{W}} \quad \forall \boldsymbol{w} \in \mathcal{W}$$

c) inf-sup *condition*[1]*:*

$$\exists\ \beta > 0 \mid \beta \leq \inf_{u \in \mathcal{V}} \sup_{w \in \mathcal{W}} \frac{a\left(\boldsymbol{u}, \boldsymbol{u}\right)}{\|\boldsymbol{u}\|_{\mathcal{V}} \|\boldsymbol{w}\|_{\mathcal{W}}}\ \boldsymbol{u}, \boldsymbol{w} \neq \boldsymbol{0}. \tag{5.70}$$

Note again that stability directly follows from the above conditions b) and c)

$$\|\boldsymbol{u}\|_{\mathcal{V}} \leq \frac{N_l}{\beta} \tag{5.71}$$

and that, for $l\left(\boldsymbol{w}\right) = \langle \boldsymbol{s}, \boldsymbol{w} \rangle$

$$\|\boldsymbol{u}\|_{\mathcal{V}} \leq \frac{1}{\beta} \|\boldsymbol{s}\|_{\mathcal{W}'}$$

with $\mathcal{W}'$ being the dual space of $\mathcal{W}$. Hence, the Babuška theorem ensures well-posedness of the variational problem (5.69).

It should be remarked that, contrary to ellipticity, the inf-sup condition does not carry over from continuous to discrete spaces $\mathcal{V}_h \subset \mathcal{V}$. This is so because the infimum in the inf-sup condition cannot decrease if taken on a subspace $\mathcal{V}_h$. Consequently, a value for the inf-sup constant, β, can be found that may be suitable for the continuous weak forms (5.59)-(5.60) but that it is not appropriate for the discrete weak forms (5.61),(5.64). Hence a specific β_h is needed for each particular discretisation.

One could compare the $\mathcal{V}$-ellipticity constant, K, with the inf-sup constant, β, by taking $\mathcal{V} = \mathcal{W}$ in the Babuška theorem [163]. Taking into account that K is given by

$$K = \inf_{\boldsymbol{u} \in \mathcal{V}} \frac{a\left(\boldsymbol{u}, \boldsymbol{u}\right)}{\|\boldsymbol{u}\|^2},$$

we see that the infimum is taken also over the second argument, whereas in the inf-sup condition the supremum is taken over the second argument. Hence, it will follow that $K \leq \beta$ and it could happen that $K = 0$ but still $\beta > 0$. This is in fact the situation for the Helmholtz equation for large wave numbers. The weak form is non-positive definite but satisfies the inf-sup condition. Actually, it can be shown for one-dimensional Helmholtz problems that the inf-sup constant depends on k as $\beta = \mathcal{O}\left(k^{-1}\right)$. This guarantees existence and uniqueness but from the stability bounds it follows that $\|\boldsymbol{u}\|_{\mathcal{V}} \leq N_l \mathcal{O}\left(k\right)$. For large values of k the stability obviously deteriorates and this is at the origin of the so-called pollution error to be defined in section 5.4.4. On the other hand, we advance that the ASGS stabilised finite element method that will be presented in section 5.5 precisely aims at modifying the discrete weak forms, (5.61), (5.64), so that the resulting ones become unconditionally stable, circumventing the necessity to fulfill the inf-sup condition.

[1]This condition is also known as LBB condition after Ladyzhenskaya-Babuška-Brezzi.

Let us introduce now the concept of $\mathcal{V}$-coercivity. Given a bounded domain, Ω, and the Hilbert space $H^1(\Omega)$, it will be said that the sesquilinear form $a : H^1 \times H^1 \mapsto \mathbb{C}$ is H^1-coercive if it satisfies the Gårding inequality

$$K_G \|\boldsymbol{u}\|^2_{H^1(\Omega)} \leq \left| a(\boldsymbol{u}, \boldsymbol{u}) + C \|\boldsymbol{u}\|^2_{L^2(\Omega)} \right| \quad \forall \boldsymbol{u} \in H^1(\Omega) \tag{5.72}$$

with K_G, C positive constants. Note that this condition can be viewed as the H^1-ellipticity of the modified sesquilinear form $a_M(\boldsymbol{u}, \boldsymbol{v}) := a(\boldsymbol{u}, \boldsymbol{v}) + C(\boldsymbol{u}, \boldsymbol{v})$.

The Helmholtz equation does in general satisfy the Gårding inequality (see [163] for details). Satisfying H^1-coercivity is important due to a convergence theorem to be presented below, which, roughly speaking, ensures convergence of the Galerkin FEM solution at least for fine enough meshes.

Convergence of positive definite forms

Convergence of the Galerkin finite element solution of positive definite problems is established by Céa's Lemma, which states as follows

Theorem 5.3 (Céa's Lemma) *Let us consider the abstract discrete variational problem of finding $\boldsymbol{u}_h \in \mathcal{V}_h \subset \mathcal{V}$ such that*

$$a(\boldsymbol{u}_h, \boldsymbol{w}_h) = l(\boldsymbol{w}_h) \quad \forall \boldsymbol{w}_h \in \mathcal{V}_h. \tag{5.73}$$

Let us assume that the weak form satisfies the assumptions of the Lax-Milgram theorem and respectively denote by $\boldsymbol{u}$ and $\boldsymbol{u}_h$ the exact and approximated solutions. Then the error $\boldsymbol{u} - \boldsymbol{u}_h$ satisfies

$$\|\boldsymbol{u} - \boldsymbol{u}_h\|_{\mathcal{V}} \leq \frac{N_a}{K} \inf_{\boldsymbol{w}_h \in \mathcal{V}_h} \|\boldsymbol{u} - \boldsymbol{w}_h\|_{\mathcal{V}} \tag{5.74}$$

with N_a and K being the continuity and $\mathcal{V}$-ellipticity constants.

Convergence of indefinite forms

Céa's lemma can be generalised for the case of indefinite forms by means of the following theorem.

Theorem 5.4 *Let us consider the abstract discrete variational problem of finding $\boldsymbol{u}_h \in \mathcal{V}_h \subset \mathcal{V}$ such that*

$$a(\boldsymbol{u}_h, \boldsymbol{w}_h) = l(\boldsymbol{w}_h) \quad \forall \boldsymbol{w}_h \in \mathcal{W}_h. \tag{5.75}$$

Let us assume that the weak form satisfies the assumptions of the Babuška theorem and let us denote by $\boldsymbol{u}$ and $\boldsymbol{u}_h$ the exact and approximated solutions. Then the error $\boldsymbol{u} - \boldsymbol{u}_h$ satisfies the estimate

$$\|\boldsymbol{u} - \boldsymbol{u}_h\|_{\mathcal{V}} \leq \left(1 + \frac{N_a}{\beta_h}\right) \inf_{\boldsymbol{w}_h \in \mathcal{V}_h} \|\boldsymbol{u} - \boldsymbol{w}_h\|_{\mathcal{V}} \tag{5.76}$$

with N_a and β_h being the continuity and discrete inf-sup constants.

From the error estimates in the above theorems, (5.74), (5.76), it follows that the convergence of any FEM solution to problems (5.73), (5.75) is accounted for two factors, namely:

- *Approximability*: The factor $\inf_{\boldsymbol{w}_h \in \mathcal{V}_h} \|\boldsymbol{u} - \boldsymbol{w}_h\|_{\mathcal{V}}$ characterises the *approximability* of the exact solution in the discrete space $\mathcal{V}_h$ spanned by the FEM shape functions. We can define the *best approximation* or *optimal approximation* of the exact solution $\boldsymbol{u}$ in $\mathcal{V}_h$ as [5]:
$$\boldsymbol{u}_{ba}^h \equiv \boldsymbol{u}_{opt}^h := \arg \inf_{\boldsymbol{w}_h \in \mathcal{V}_h} \|\boldsymbol{u} - \boldsymbol{w}_h\|_{\mathcal{V}} \tag{5.77}$$
and the error of the best approximation as
$$e_{ba}^h \equiv e_{opt}^h := \left\|\boldsymbol{u} - \boldsymbol{u}_{opt}^h\right\|_{\mathcal{V}}. \tag{5.78}$$
From a geometrical point of view, e_{opt}^h represents the minimum distance between the exact solution $\boldsymbol{u} \in \mathcal{V}$ and the subspace $\mathcal{V}_h$. The optimal error can be related to the interpolation error found when approximating the exact solution with polynomials of degree p. Given the p-th order interpolant of $\boldsymbol{u}$, $\boldsymbol{u}_I$, and a characteristic measure of the mesh element size, h, it follows that
$$\|\boldsymbol{u} - \boldsymbol{u}_I\|_{H^s(\Omega)} \leq C h^{m-s} \|\boldsymbol{u}\|_{H^m(\Omega)} \quad 0 \leq s \leq m. \tag{5.79}$$
with $m = p + 1$. By definition, the optimal error is less or equal the interpolation error so it will also satisfy inequality (5.79).

- *Stability*: The factors N_a/K and $1+N_a/\beta_h$ in (5.74), (5.76) characterise the problem stability. For positive definite problems N_a/K is usually small and *approximability* plays a predominant role in the convergence of the solution. As opposite, and in what concerns the Helmholtz problem for large wave numbers (indefinite problem), the discrete inf-sup constant, β_h, has an $\mathcal{O}(k^{-1})$ dependence as the continuous inf-sup constant, β. Consequently, $1 + N_a/\beta_h$ will have a large value and the error estimate (5.76) will become very poor. In this situation stability will determine the convergence behaviour.

Let us finally introduce a convergence theorem for weak forms satisfying the Gårding inequality, (5.72).

Theorem 5.5 *Consider the variational problem (5.66) with the sesquilinear form* $a : \; H^1 \times H^1 \mapsto \mathbb{C}$ *being* H^1*-coercive (i.e., satisfying (5.72)). Consider in addition a sequence of subspaces satisfying*
$$\mathcal{V}_h^1 \subset \mathcal{V}_h^2 \subset \cdots \subset \mathcal{V}_h^N \subset \cdots \subset \mathcal{V} \tag{5.80}$$
as well as
$$\inf_{\boldsymbol{w}_h \in \mathcal{V}_h^N} |||\boldsymbol{u} - \boldsymbol{w}_h||| \to 0, \; N \to \infty \quad \forall \boldsymbol{u} \in \mathcal{V} \tag{5.81}$$
with $|||\cdot|||$ *standing for the energy norm* $|||\boldsymbol{u}||| := a_M(\boldsymbol{u}, \boldsymbol{u})^{1/2}$, $a_M(\boldsymbol{u}, \boldsymbol{v}) := a(\boldsymbol{u}, \boldsymbol{v}) + C(\boldsymbol{u}, \boldsymbol{v})$. *Then there exists a number* N_0 *such that the discrete variational problem (5.73) has unique solutions* $\boldsymbol{u}_h^N \in \mathcal{V}_h^N$ *for all* $N \geq N_0$ *and* $\left\|\boldsymbol{u} - \boldsymbol{u}_h^N\right\|_{H^1} \to 0$ *as* $N \to \infty$.

It follows from theorem 5.5, that given a sequence of meshes with sizes $\{h\}$ and solutions $\{\boldsymbol{u}_h \in \mathcal{V}_h\}$ there exists a threshold mesh size, h_0, such that for any $h < h_0$ the next error estimate holds

$$\|\boldsymbol{u} - \boldsymbol{u}_h\|_{\mathcal{V}} \leq C \inf_{\boldsymbol{w}_h \in \mathcal{V}_h} \|\boldsymbol{u} - \boldsymbol{w}_h\|_{\mathcal{V}}, \ \forall h < h_0 \tag{5.82}$$

with C being a constant independent of h. We say in this case that the error has a quasioptimal convergence. The estimate (5.82) can also be written as $\left\|e^h\right\|_{\mathcal{V}} \leq C \left\|e^h_{opt}\right\|_{\mathcal{V}}$.

Well-posedness and convergence of the Helmholtz and convected Helmholtz equations

We can summarise the situation for the Helmholtz equation given by the above well-posedness and convergence theorems as follows. For low wave numbers the Helmholtz variational problem (5.59) is well posed thus satisfying the conditions of the Lax-Milgram theorem. Convergence of the Galerkin finite element solution will be optimal for the h-version of the FEM, whenever the resolution is kept constant (number of nodal points per wave length, see next section). Convergence will be controlled by the approximability factor in Céa's lemma.

For large wave numbers the situation is completely different. The weak form (5.59) is no longer positive definite although an inf-sup constant, β, can be found so that existence and uniqueness of the solution is ensured by the Babuška theorem. However, this constant has an $\mathcal{O}(k^{-1})$ behaviour implying that the stability bound will depend on $\mathcal{O}(k)$, which is very poor for large k (see (5.71)). The discrete β_h also varies as $\mathcal{O}(k^{-1})$ so the convergence error estimate (5.76) will be dominated by a rather unuseful large stability factor. For large wave numbers, convergence will hence be driven by stability instead of by approximability. In this situation, the FEM error will be larger than the optimal error, the difference being known as the pollution error. Nevertheless, the Helmholtz weak form also satisfies the Gårding inequality (5.72). Theorem 5.5 then guarantees that refining the mesh we will achieve a threshold value, h_0, beyond which convergence of the FEM solution will be quasioptimal. It can then be seen that for the h-version of the FEM, the FEM solution will present a rather intricate convergence pattern depending on the mesh size h. For coarse meshes the solution will be dominated by the pollution error, while for fine enough meshes quasioptimal convergence will be achieved.

In what concerns the convected Helmholtz equation, a very similar behaviour to the one in the Helmholtz equation is expected to occur. This is so because we can transform the convected Helmholtz equation into the Helmholtz one by means of the full Lorentz transformation, (5.16). That the convected Helmholtz equation presents a similar convergence pattern to the Helmholtz equation has been numerically checked in [83] for the one dimensional case. The two dimensional case is more intricate due to the effects of the mean flow and also presents pollution [84]. In the next section we will study the pattern of convergence for the Helmholtz equation by means of some model problems.

5.4.4 Pollution error and pattern of convergence

One dimensional model problem

In this section we will first make use of numerical simulations to analyse the behaviour of the FEM solution of the following one dimensional model problem.

- *Model problem 1: One dimensional Helmholtz equation*

  We consider the case of free propagation of a one dimensional plane wave, which can be stated as: find the acoustic pressure $\hat{p} : \Omega_{ac} \mapsto \mathbb{C}$, with $\Omega_{ac} = (0, 1)$, such that

$$-d_{xx}^2\hat{p} - k_0^2\hat{p} = 0 \quad \text{in } \Omega_{ac} \tag{5.83}$$

$$\hat{p}(0) = \hat{p}_{ex}(0) = 1 \tag{5.84}$$

$$d_x\hat{p}(1) - ik_0\hat{p}(1) = g := d_x\hat{p}_{ex}(1) - ik_0\hat{p}_{ex}(1) \tag{5.85}$$

  where $d_x \equiv d/dx$ and $\hat{p}_{ex} = \exp(ik_0x)$.

Dispersion and pollution

In the introduction we have mentioned the fact that, for large wave numbers, the FEM discrete waves propagate with a discrete wave number, k_h, which is different from the continuous one, k. This phase lag due to the dispersive character of k_h is at the origin of the pollution error. We can easily see this following [57] and plotting e.g., the real part of the exact, interpolant and Galerkin FEM solutions of model problem 1 for $k_0 = 10$ (see Fig. 5.4a). Denoting by $\hat{p}_I$ the interpolant of the exact acoustic pressure, $\hat{p}$, the interpolant error is defined as $e_{int} := \|\hat{p} - \hat{p}_I\|_{\mathcal{V}}$, which is an upper bound to the best approximation or optimal error. This error has a *local* character and it is sometimes referred to as the *local error*. On the other hand and due to dispersion, the Galerkin FEM solution can have an error, $e_{tot} = \|\hat{p} - \hat{p}_h\|_{\mathcal{V}}$, much larger than the interpolant one. The difference between the FEM error and the interpolation error is what is called the *pollution error*, i.e., $e_{pol} = e_{tot} - e_{int}$ and it is clear from Fig. 5.4a that this error is strongly related to dispersion. The higher the dispersion is, the higher the pollution error will be. In accordance with the results inferred from the well-posedness theorems of the previous sections, we also observe that if the wave number is increased, the pollution error grows. This can be seen in Fig. 5.4b where we have plotted the real part of the exact, interpolant and Galerkin FEM solutions for $k_0 = 15$. It is apparent that the phase lag is higher than for the $k_0 = 10$ case and consequently the pollution error will be also larger. Explicit expressions can be found for the pollution error and for the phase lag dependence with k_0, for one-dimensional Helmholtz problems (see below, [163]). On the other hand, it is important to note that unlike the interpolant error, the pollution error has a *global* character.

In Fig. 5.5 we have plotted the dependence of the total and optimal errors in the H^1-seminorm with the mesh refinement (number of mesh elements). The difference between

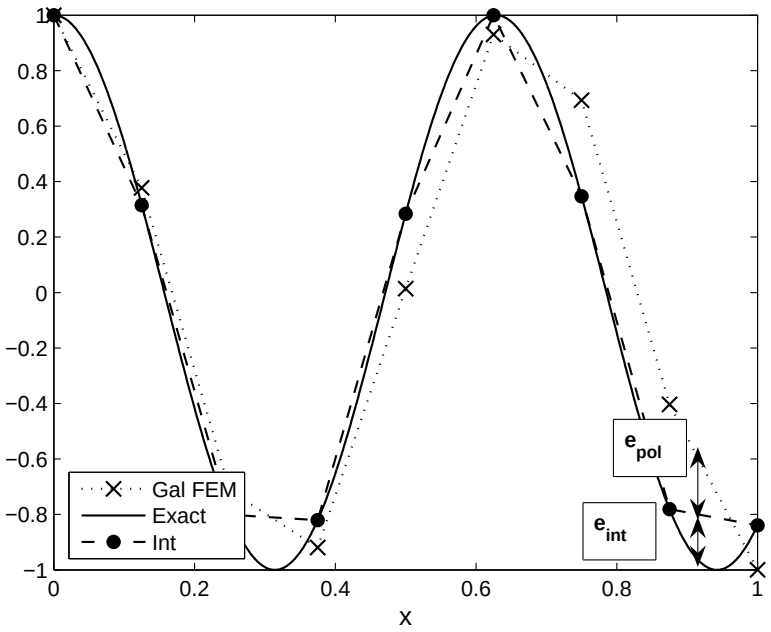

a) Optimal (*local*) error, $e_{int} = \hat{p} - \hat{p}_I$ and pollution (*global*) error, $e_{pol} = \hat{p}_I - \hat{p}_h$. The total error is given by $e_{tot} = \hat{p} - \hat{p}_h = e_{opt} + e_{pol}$. $k_0 = 10$.

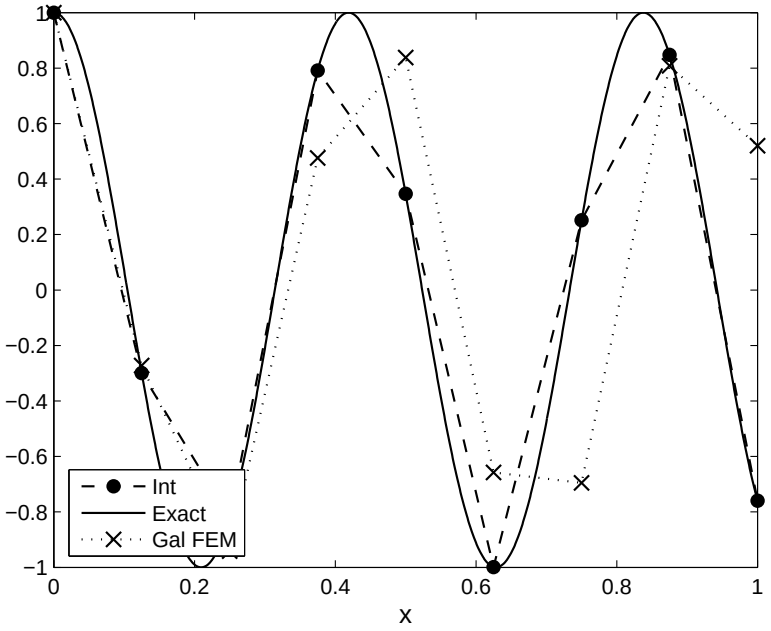

b) Real part of the exact, interpolant and Galerkin FEM solution for the case $k_0 = 15$.

Figure 5.4: Dispersion and pollution error.

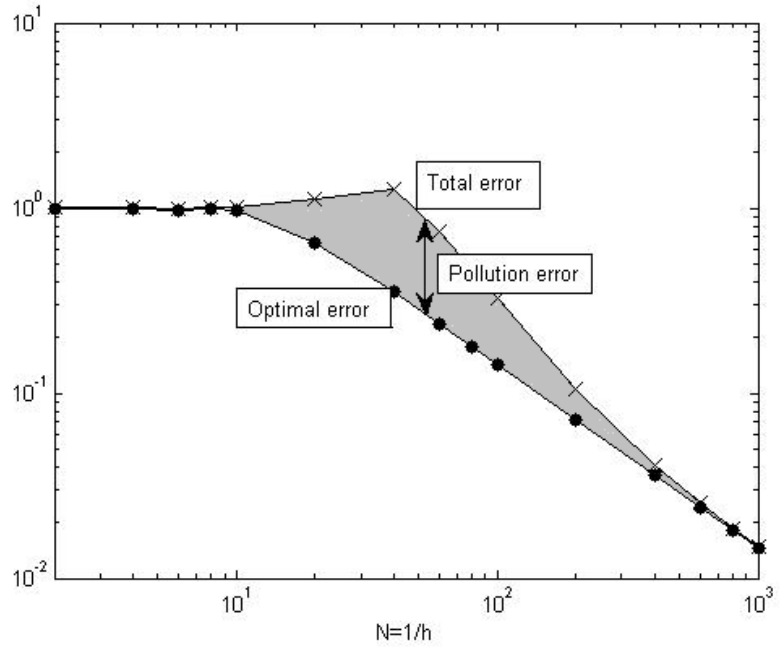

Figure 5.5: Log-log graph of the total and optimal relative errors in the H^1-seminorm for model problem 1, with $k_0 = 50$. Shaded area = pollution error. N = number of elements, h = characteristic mesh element size.

both quantities has been defined as the pollution error (shaded area in the plot). The results correspond to model problem 1 with $k_0 = 50$. In what follows we will analyse the behaviour of this graph (*pattern of convergence*) in some detail.

Pattern of convergence

Let us consider model problem 1 where we have discretised the computational domain $\Omega_{ac} = (0, 1)$ with a mesh of characteristic element size h and number of elements $N = h^{-1}$. For a given wavelength, $\lambda = 2\pi/k_0$, we can define the *mesh resolution* as the number $n_{res} = \lambda/h = N\lambda = 2\pi/(k_0 h) = 2\pi N/k_0$. The limit of resolution corresponds to two points per wavelength ($n_{res} = 2 \Leftrightarrow k_0 h = \pi$) and in practical cases it is usually recommended to take $n_{res} = 10$. It seems quite obvious that n_{res} (and hence $k_0 h$) should be kept constant in the design of a mesh, for a given wave number k_0. That is to say, if we have solved a Helmholtz problem with $n_{res} = 10$, and we want to solve the same problem for the new wave number $k_0' = 2k_0$, we will have to use a new finer mesh with $h' = h/2$ to keep the resolution constant.

In fact, it can be easily shown that the relative interpolation error, $e_{r,int} := \|\hat{p} - \hat{p}_I\|_{\mathcal{V}} / \|\hat{p}\|_{\mathcal{V}}$, for an oscillatory solution is controlled by a term $\mathcal{O}(k_0 h)^{\alpha}$, with $\alpha = 1, 2$, respectively for the H^1-seminorm and L^2-norm [163]. Unfortunately, this is not the case for the total or FEM solution error. We can observe this behaviour in Fig. 5.6 where we

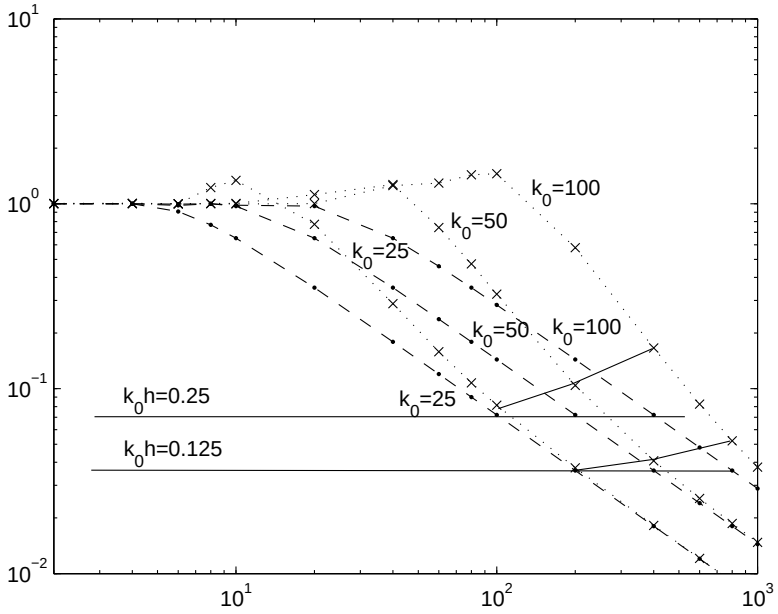

Figure 5.6: Log-log graph of the H^1-seminorm of $e_{r,int}$ (dashed lines) and $e_{r,Gal}$ (cross dotted lines) for $k_0 = \{30, 50, 70\}$. Model problem 1.

have plotted the H^1-seminorm errors of the interpolant and the Galerkin FEM solution using linear shape functions, for wave numbers $k_0 = \{25, 50, 100\}$. If one chooses a fixed value for the product $k_0 h$ (e.g., $k_0 h = \{0.25, 0.125\}$ in Fig. 5.6), it can be checked that $e_{r,int}$ remains constant while $e_{r,Gal}$ does not and increases for growing values of k_0 (see Fig. 5.6). On the other hand, it is clear from the figure that the higher k_0 is, the higher the pollution error becomes.

In what concerns the behaviour of the total or Galerkin FEM error, $e_{r,Gal}$, four clear distinct intervals of convergence can be identified. Let us consider model problem 1 with $k_0 = 30$.

- *First interval of convergence* ($N \leq n_0$)
  This case corresponds to using N mesh elements with N being smaller than the threshold value of two point per wavelength ($n_{res} = 2$). In our case $k_0 = 30 \Rightarrow \lambda \approx 0.2$ and $n_0 = k_0/\pi \approx 9.5$. Hence if less than 9.5 elements are used, both, the optimum relative error, $e_{r,opt}$, and the Galerkin FEM relative error, $e_{r,Gal}$, will be of order 1, see Fig. 5.7a.

- *Second interval of convergence* ($n_0 \leq N \leq N_0$)
  This second interval of convergence comprises from n_0 to $N_0 = (k_0^3/24)^{1/2}$, see Fig. 5.7b. The expression for N_0 is found from heuristic arguments [164] and in our example it takes the value ≈ 33.5. In this interval, $e_{r,opt}$ in the H^1-seminorm

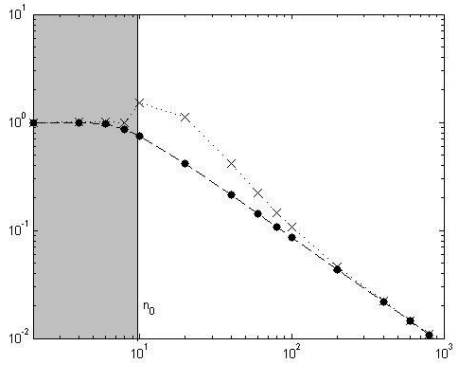

a) First interval $N \leq n_0$

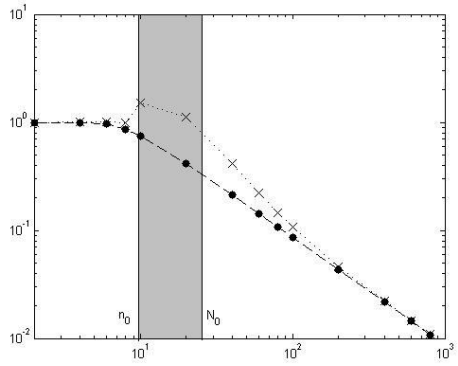

b) Second interval $n_0 \leq N \leq N_0$

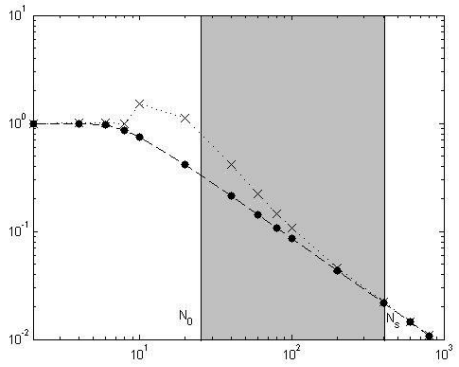

c) Third interval $N_0 \leq N \leq N_s$

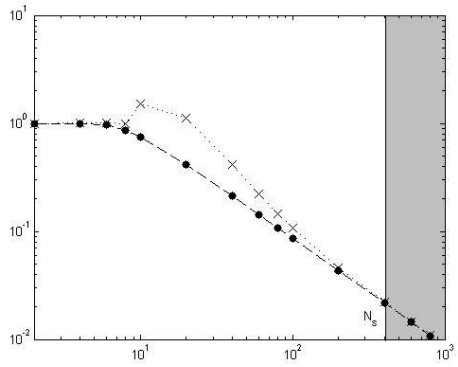

d) Fourth interval $N \geq N_s$

Figure 5.7: Convergence intervals for the H^1-seminorm of $e_{r,int}$ (dashed lines) and $e_{r,Gal}$ (cross dotted lines) for $k_0 = 30$. Model problem 1.

decreases with a slope of -1 as predicted by (5.79) for linear elements. For the recommended resolution of $n_{res} = 10$, $e_{r,opt} \approx 10\%$. It can be shown as mentioned above, that

$$e^{SH^1}_{r,opt} \leq C_1^{opt} h k_0 \tag{5.86}$$

$$e^{L^2}_{r,opt} \leq C_2^{opt} (h k_0)^2 \tag{5.87}$$

with C_1^{opt}, C_2^{opt} being constants. On the contrary the Galerkin FEM error, $e_{r,Gal}$, oscillates with amplitudes larger than 100%. Hence, eventhough the Galerkin FEM solution is well definied, it does not approximate at all the exact solution. The Galerkin FEM solution is dominated in this second interval by the pollution error.

- *Third interval of convergence (Preasymptotic range)* ($N_0 \leq N \leq N_s$)
  The third interval, known as the preasymptotic range (see Fig. 5.7c), comprises from N_0 to N_s where $N_s = k^2/c$, being c a theoretically small constant. In this

interval the Galerkin FEM solution is still dominated by the pollution error. It can be shown, for the H^1-seminorm, that

$$\|\hat{p} - \hat{p}_h\|_{SH^1} \leq \left(1 + Ck_0^2 h\right) \inf_{w_h \in \mathcal{V}_h} \|\hat{p} - w_h\|_{H^1} \tag{5.88}$$

and that the Galerkin FEM relative error, $e_{r,Gal}$, satisfies

$$e_{r,Gal} \leq C_1^{fem} k_0 h + C_2^{fem} k_0^3 h^2, \quad k_0 h < 1, \tag{5.89}$$

with C, C_1^{fem}, C_2^{fem} constants. Comparing (5.89) with (5.86) we observe that the second term in the r.h.s of (5.89) is the responsible for the pollution effect i.e., for the deviation with respect to the interpolant error. For large values of k_0 this term dominates the error, which decays with a dependence N^{-2} (h^2) towards the optimal error, $e_{r,opt}$ (that still decays with a slope of -1).

The preasymptotic range is the most interesting from a practical point of view, because when solving engineering problems at large wave numbers it admits an acceptable balance between the FEM solution error and the size of the mesh needed to solve the problem.

- *Fourth interval of convergence (Asymptotic range)* $(N_s \leq N)$
  In this interval the pollution effect on the Galerkin FEM solution is negligible, see Fig. 5.7d. Numerical experiments have shown that the constant c in the definition of N_s must not be necessarily small and that it suffices that the condition $k_0^2 h \ll 1$ holds, for the Galerkin FEM solution to have a quasioptimal convergence (5.82). From (5.89) it follows that

$$e_{r,Gal} \leq k_0 h \left(C_1^{fem} + C_2^{fem} k_0^2 h\right) \approx C_1^{fem} k_0 h, \quad k_0^2 h \ll 1, \tag{5.90}$$

  so that the Galerkin FEM solution relative error, $e_{r,Gal}$, behaves like the optimal relative error in (5.86). Hence, $e_{r,Gal}$ will also decrease with a slope of -1 for increasing N and the difference with $e_{r,opt}$ will be due to the difference in the constants appearing in (5.90) and (5.86), i.e. to $\log\left(C_1^{fem}/C_1^{opt}\right)$.

  Given that there is no pollution in the asymptotic range, it is clear that this one is the ideal interval where to work. Unfortunately, the condition $k_0^2 h \ll 1$ is very restrictive and implies the use of very fine meshes for large wave numbers. A possible solution to this situation is the use of stabilised finite element methods, which allow to work in the preasymptotic range giving a solution that is very close to the optimal one. This will be the task in section 5.5.

Pollution error definition

In view of the results in the above two subsections, a general definition for the pollution error can be attempted (see [5, 163]).

Definition 5.1 *Consider a Helmholtz problem on a normed space $\mathcal{V}$, with wave number k_0, exact solution $\hat{p} \neq 0 \in \mathcal{V}$ and finite element solution $\hat{p}_h \neq 0 \in \mathcal{V}_h \subset \mathcal{V}$. Suppose that an estimate of the type*

$$\frac{\|\hat{p} - \hat{p}_h\|_{\mathcal{V}}}{\|\hat{p}\|_{\mathcal{V}}} \leq C(k_0) \inf_{w_h \in \mathcal{V}_h} \frac{\|\hat{p} - w_h\|_{\mathcal{V}}}{\|\hat{p}\|_{\mathcal{V}}}, \tag{5.91}$$

holds, which can also be written as

$$e_{r,h} \leq C(k_0)\, e_{r,opt}. \tag{5.92}$$

Then, if the constant $C(k_0)$ has an expression of the type

$$C(k_0) = C_1 + C_2 k_0^{\beta} (k_0^{\alpha} h) \tag{5.93}$$

with $\beta > 0$, $\alpha \geq 0$ and C_1, C_2 being constants independent of k_0 and h, we say that the finite element solution is polluted *and the term $C_2 k_0^{\beta} (k_0^{\alpha} h)$ is called the* pollution term.

Dispersion analysis in 1D

At the beginning of this section we have stated that the fact that the Galerkin FEM solution is dispersive is at the origin of the pollution effect. For completeness, we will see now by means of a very simple dispersion analysis that the discrete FEM wave effectively propagates with a discrete wave number, k_0^h, that differs from the continuous one, k_0.

The a-th equation of the tridiagonal system associated to the discrete weak form of model problem 1, for nodes $a-1$, a and $a+1$, is given by (see e.g. [119])

$$-\hat{P}^{a-1} + 2\hat{P}^a - \hat{P}^{a+1} - 2\alpha^h \left(\hat{P}^{a-1} + 4\hat{P}^a + \hat{P}^{a+1}\right) = 0, \quad \alpha^h := \frac{(k_0 h)^2}{12}, \tag{5.94}$$

where $\hat{P}^a = \hat{p}_h(x_a)$ stands for the nodal value at node $x_a = ha$ and we have assumed linear shape functions. From (5.94) we obtain the stencil

$$\left(2\alpha^h + 1\right)\hat{P}^{a-1} + 2\left(4\alpha^h - 1\right)\hat{P}^a - \left(2\alpha^h + 1\right)\hat{P}^{a+1} = 0. \tag{5.95}$$

We can guess a solution $U^a = \rho^a$ to (5.95). Substituting in (5.95) and dividing by ρ^a we get

$$\left(2\alpha^h + 1\right)\rho^2 + 2\left(4\alpha^h - 1\right)\rho - \left(2\alpha^h + 1\right) = 0, \tag{5.96}$$

which for a propagating wave has the solution

$$\rho = \frac{1 - 4\alpha^h + \sqrt{12\alpha^h(\alpha^h - 1)}}{2\alpha^h + 1}. \tag{5.97}$$

For $\alpha^h > 1$ we have a decaying wave, while for $\alpha^h < 1 \Leftrightarrow k_0 h < \sqrt{12}$ (two points per wave length) we have an oscillating solution, which is the one we are interested in [119].

If we demand that the discrete solution $\hat{p}_h$ becomes exact at the nodes it follows

$$\begin{aligned}\hat{p}_h(x_a) = \hat{P}^a = \hat{p}(x_a) \Rightarrow \rho^a = \exp(ik_0 x_a) = \exp(ik_0 ha) = [\exp(ik_0 a)]^a \\ \Rightarrow \rho = \exp(ik_0 h) = \cos(k_0 h) + i\sin(k_0 h)\,. \end{aligned} \tag{5.98}$$

Assuming a discrete wave number, k_0^h, such that $\rho = \cos\left(k_0^h h\right) + i\sin\left(k_0^h h\right)$, it should hold that $Re\left[\left(1-4\alpha^h\right)/\left(2\alpha^h+1\right)\right] = \cos\left(k_0^h h\right)$. Consequently,

$$k_0^h h = \arccos\left(\frac{1-4\alpha^h}{2\alpha^h+1}\right) \approx k_0 h - \frac{(k_0 h)^3}{24} + 3\frac{(k_0 h)^5}{640} + \ldots\ldots \leq k_0 h \tag{5.99}$$

that implies

$$k^h - k_0 \approx \frac{k_0^3 h^2}{24} + \mathcal{O}\left(k_0^5 h^4\right). \tag{5.100}$$

Hence it is clear that contrary to the optimal and exact solutions, the Galerkin FEM solution is dispersive. Consequently a phase lag appears between the exact wave solution and the discrete one, see Fig. 5.4. Note also that the same dependence on k_h and h has been encountered for the phase lag than for the pollution error in (5.89).

Similar dispersion analysis to the one derived here can be performed for the Helmholtz equation in two and three dimensions [89, 287]. On the other hand, we remind again that very close results to the ones described above for the one dimensional convected equation can be found in [83].

Pattern of convergence for a two dimensional problem

We will end this section by having a look to the pattern of convergence of a two dimensional Helmholtz problem. We advance that a very similar behaviour to the one encountered for the one dimensional case will be observed.

Let us consider the following model problem:

- *Model problem 2: Two dimensional Helmholtz equation*

  We consider the case of free propagation of a two dimensional plane wave, which can be stated as: find the acoustic pressure $\hat{p} : \Omega_{ac} \mapsto \mathbb{C}$, with $\Omega_{ac} = (0,1)\times(0,1)$, such that

$$-\nabla^2\hat{p} - k_0^2\hat{p} = 0 \quad \text{in } \Omega_{ac} \tag{5.101}$$

$$\nabla\hat{p}\cdot\boldsymbol{n} = ik_0\hat{p} + g \quad \text{on } \partial\Omega_{ac}. \tag{5.102}$$

  The wave number is given by $\boldsymbol{k}_0 = (k_{0x}, k_{0y}) = k_0(\cos\theta, \sin\theta)$ and the boundary is $\partial\Omega_{ac} = \Gamma_1 \cup \Gamma_2 \cup \Gamma_3 \cup \Gamma_4$ with

$$\Gamma_1 = [x, 0]\,,\ x \in [0,1] \tag{5.103}$$

$$\Gamma_2 = [1, y]\,,\ y \in (0,1] \tag{5.104}$$

$$\Gamma_3 = [x, 1]\,,\ x \in [0,1) \tag{5.105}$$

$$\Gamma_4 = [0, y]\,,\ y \in (0,1). \tag{5.106}$$

The data g in (5.102) has the values

$$g(x,y) = i(k_0 - k_{0y})\exp(ik_{0x}x) \quad \text{on } \Gamma_1 \tag{5.107}$$
$$g(x,y) = i(k_0 + k_{0x})\exp(ik_{0x} + ik_{0y}y) \quad \text{on } \Gamma_2 \tag{5.108}$$
$$g(x,y) = i(k_0 + k_{0y})\exp(ik_{0x}x + ik_{0y}) \quad \text{on } \Gamma_3 \tag{5.109}$$
$$g(x,y) = i(k_0 - k_{0x})\exp(ik_{0y}y) \quad \text{on } \Gamma_4. \tag{5.110}$$

The exact solution to problem (5.101)-(5.110) is a plane wave propagating in the direction of the wave number vector $\boldsymbol{k}_0$:

$$\hat{p} = \exp(ik_{0x}x + ik_{0y}y). \tag{5.111}$$

Let us solve problem (5.101)-(5.110) for various wavenumbers in a squared structured mesh of $N \times N$ elements (characteristic mesh size $h = 1/N$) using bilinear shape functions. In Fig. 5.8 the optimum relative error for a wave propagating in the $\theta = 45$ direction, and wavenumbers $k_0 = \{5, 10, 50, 100\}$ is plotted for increasing N. As expected, the optimum relative error in the L^2 norm, $e^{L^2}_{r,opt}$, decays with a slope of -2 for diminishing h (increasing N). Instead, the optimum relative error in the H^1-seminorm, $e^{SH^1}_{r,opt}$, decays with a slope -1 for decreasing h. These behaviours are valid for $k_0 h \geq \pi$, i.e., once the resolution threshold of two elements per wavelength has been surpassed. If $k_0 h \leq \pi$ we will have a 100% of optimum relative error as seen in Fig. 5.8 for $k_0 = 50,\ N < 15$ and $k_0 = 100,\ N < 30$. It can also be observed that for a fixed h, the optimum relative error increases with k_0. Moreover, for $k_0 h = const$, $e^{SH^1}_{r,opt}$ has the same value for all cases as seen from the intersection of the horizontal lines, $k_0 h = \{0.1, 0.5\}$, with the $e^{SH^1}_{r,opt}$ curves in Fig. 5.8.

In Fig. 5.9 a comparison between the optimum relative error and the Galerkin-FEM error is given in the H^1-seminorm, for $k_0 = \{10, 50\}$. The pollution error (difference between both types of errors) can be clearly appreciated. As expected, this is larger for $k_0 = 50$ than for $k_0 = 10$.

Let us concentrate now in the $k_0 = 50$ case. Four convergence intervals can be distinguished like in the one dimensional case. First, for $N < 15$ both relative errors become 100% and consequently neither the Galerkin FEM solution nor the interpolant approximate the exact solution of the problem. Second, for $15 < N < (k_0^3/24)^{1/2} \approx 70$ the Galerkin FEM relative error is clearly dominated by the pollution effect, while the optimum relative error decays with a slope of -1. Third, for $70 < N < 2500$ ($N = 2500$ comes from demanding $k_0 h \approx 1$, i.e., $N \approx k_0^2$) we lay in the preasymptotic range. Although the Galerkin FEM error is still influenced by the pollution effect, it rapidly decays with a slope of -2. Fourth, the asymptotic range for $k_0 = 50$ is not observed in Fig. 5.9 because the simulation has a maximum of $N = 200$ elements. However, the asymptotic range can be observed for the case $k_0 = 10$ showing a -1 slope for both, the optimum and the Galerkin FEM relative errors. The difference between the two error lines is due to the difference in the logarithms of their corresponding bounding constants.

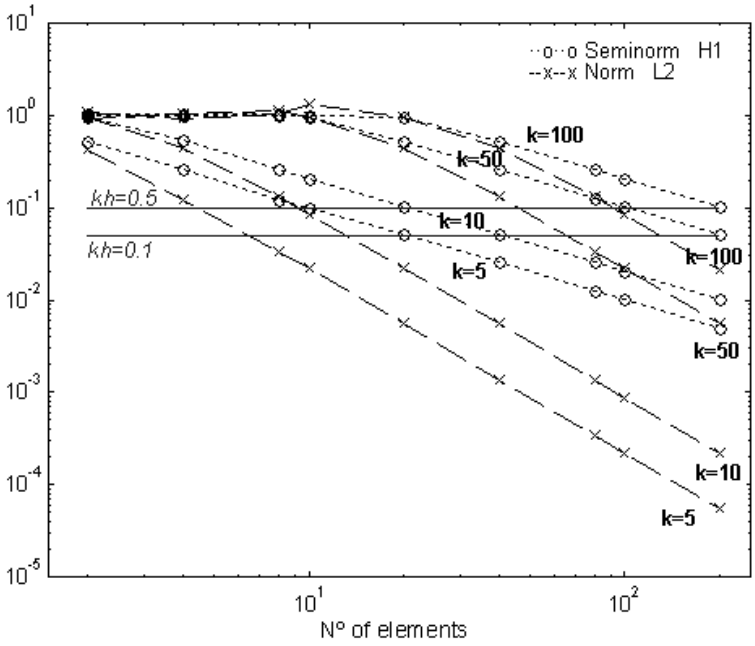

Figure 5.8: Optimal relative errors in the L^2 norm and the H^1-seminorm for $k_0 = \{5, 10, 50, 100\}$ and $\theta = 45$. Model problem 2.

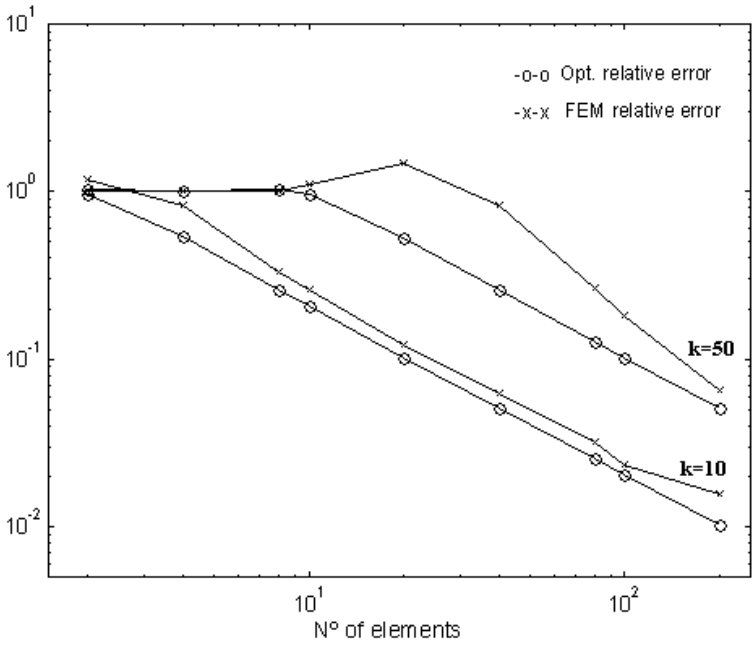

Figure 5.9: Optimal and Galerkin FEM relative errors in the L^2-norm and the H^1-seminorm for $k_0 = \{10, 50\}$ and $\theta = 45$. Model problem 2.

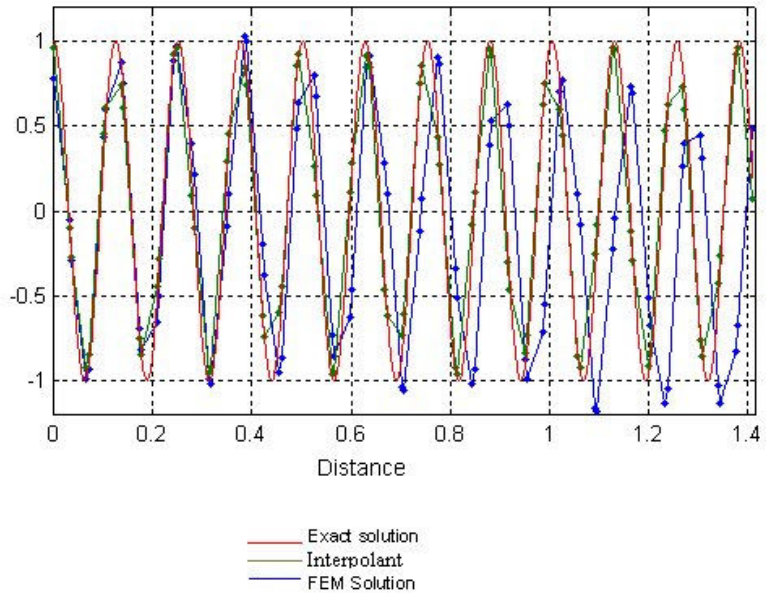

Figure 5.10: Exact, interpolant and Galerkin FEM solution for $k_0 = 50,\ N = 40$. Diagonal of the Ω_{ac} domain in (5.101). Model problem 2.

In Fig. 5.10 we have plotted the exact solution, the interpolant and the Galerkin-FEM solution for the diagonal of the computation domain $\partial\Omega_{ac}$ in (5.101) with $k_0 = 50,\ N = 40$. We can observe that while the interpolant and the exact solution have the same phase, the Galerkin-FEM solution suffers from the pollution effect and becomes out of phase due again to the fact that it propagates with a discrete, dispersive, wave number k_0^h. In Fig. 5.11 a comparison between the Galerkin-FEM solution and the interpolant solution for the cases $k_0 = \{10, 50, 50\}$ with $N = \{20, 20, 40\}$ is given. The first case corresponds to the preasymptotic range and the Galerkin-FEM solution resembles the interpolant one. The second case lays in the second interval of convergence and the Galerkin-FEM solution is clearly dominated by the pollution effect. As opposite, the interpolant solution still recovers the oscillatory character of the exact solution. The third case still lays in the second interval of convergence although it is closer to the preasymptotic range ($N_0 = 70$ for the present problem). Although both solutions resemble the exact solution, their relative errors are still high (see Figs. 5.9- 5.10).

From the above results, we can conclude that the FEM solution for the two dimensional model problem 2 will essentially behave like the one dimensional one. Similar conclusions can be derived for the two dimensional convected Helmholtz equation although a more intricate behaviour is encountered due to the directional effects of the mean flow [84].

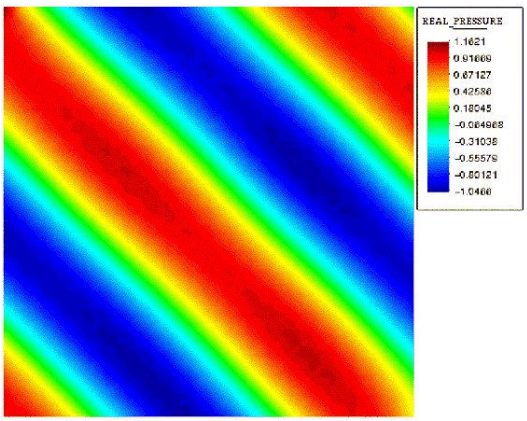

a) FEM solution $k_0 = 10,\ N = 20$

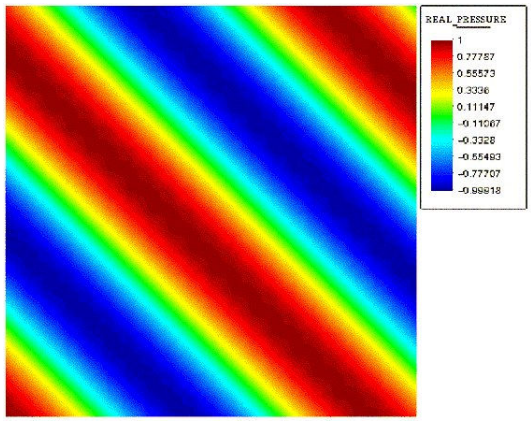

b) Int solution $k_0 = 10,\ N = 20$

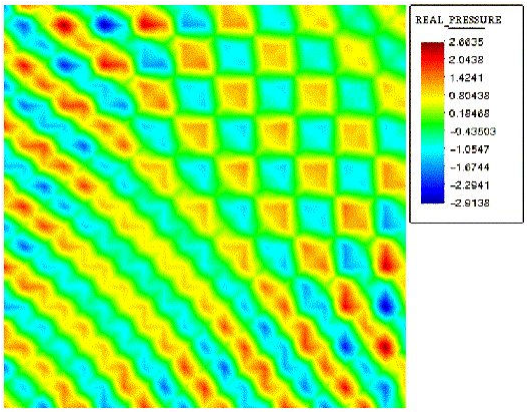

c) FEM solution $k_0 = 50,\ N = 20$

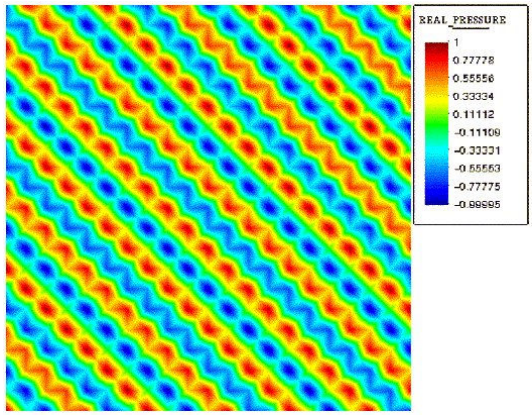

d) Int solution $k_0 = 50,\ N = 20$

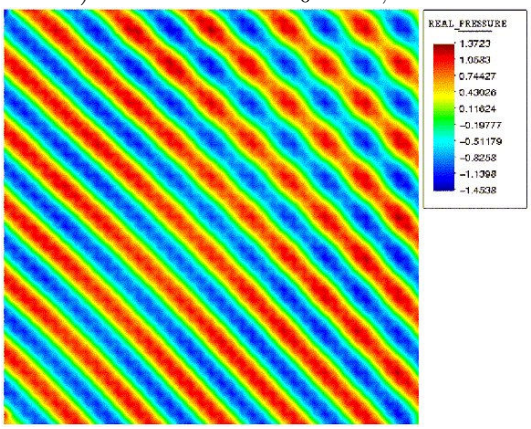

e) FEM solution $k_0 = 10,\ N = 40$

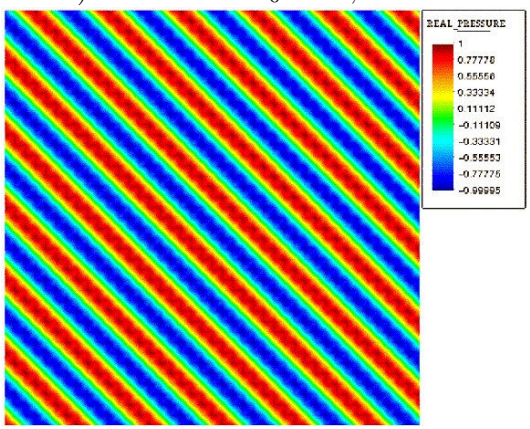

f) Int solution $k_0 = 10,\ N = 40$

Figure 5.11: Real part of Galerkin FEM and interpolant solutions for various combinations of k_0 and N. Model problem 2.

5.5 Numerical approximation using an ASGS stabilised FEM

5.5.1 Subgrid scale stabilisation

We have seen in the previous sections that the appearance of the pollution error in the Galerkin FEM solution of the Helmholtz and convected Helmholtz equations is related to the loss of stability of their associated weak forms. As mentioned in the introduction, several stabilisation strategies have been developed to avoid this problem. The basic idea of most stabilisation approaches is to modify the Galerkin discrete weak form with the addition of some extra terms that allow to "circumvent" the inf-sup condition, so that an unconditionally stable discretisation scheme is obtained. This is in fact the result of applying the subgrid scale approach followed through all this thesis [150,154]. As shown in Chapter 3 a modified equation is obtained for the large scales having better stabilisation proprieties.

In this section we will focus on the two dimensional convected Helmholtz equation. Results for the Helmholtz equation can be simply recovered by setting the Mach number equal to zero ($M = 0$) whereas results for one dimensional cases can be obtained suppressing one of the problem dimensions. The work developed below can be also found in [106].

We remind from section 3.4.4 that the key idea of the SGS finite element approach when applied to the convected Helmholtz equation (5.60) is to decompose the continuous spaces $\mathcal{W} = \mathcal{W}_h \oplus \tilde{\mathcal{W}}$, $\mathcal{W}_0 = \mathcal{W}_{h,0} \oplus \tilde{\mathcal{W}}_0$, being $\tilde{\mathcal{W}}$ and $\tilde{\mathcal{W}}_0$ any continuous spaces to respectively complete $\mathcal{W}_h$ and $\tilde{\mathcal{W}}_0$ in $\mathcal{W}$ and $\mathcal{W}_0$. Then, any function in $\mathcal{W}$ can be split as $\hat{p} = \hat{p}_h + \tilde{\hat{p}}$, $\hat{p}_h$ representing the part of $\hat{p}$ that can be captured with the finite element mesh and $\tilde{\hat{p}}$ the subscale or subgrid scale. Making the same decomposition for the test function and substituting into (5.60), we obtain the following two equations respectively governing the large scales and subscales behaviour

$$a\left(\hat{p}_h, w_h\right) + a\left(\tilde{\hat{p}}, w_h\right) = l\left(w_h\right) \quad \forall w_h \in \mathcal{W}_{h,0} \tag{5.112}$$

$$a\left(\hat{p}_h, \tilde{w}\right) + a\left(\tilde{\hat{p}}, \tilde{w}\right) = l\left(\tilde{w}\right) \quad \forall \tilde{w} \in \tilde{\mathcal{W}}_0 \tag{5.113}$$

where $a\left(\cdot,\cdot\right)$ stands for the sesquilinear form (now written in components)

$$\begin{aligned} a\left(u,w\right) := & -2ik_0 M_j\left(\partial_j u, w\right) + \left[\delta_{ij} - M_i M_j\right]\left(\partial_i u, \partial_j w\right) - k_0^2\left(u,w\right) \\ & - ik_0\alpha_S\left(u,w\right)_{\Gamma_\infty} + ik_0\alpha_N\left(u,w\right)_{\Gamma_N} \end{aligned} \tag{5.114}$$

and $l\left(w\right)$ is the antilinear functional

$$l\left(w\right) = \langle \hat{s}_h, w\rangle + \left(\hat{g}, w\right)_{\Gamma_N}. \tag{5.115}$$

The next goal consists in finding an approximate value for the subscales $\tilde{\hat{p}}$ (i.e. an approximate solution to (5.113)) and to substitute it into (5.112) to account for its effects

on the large scales, resolvable by the finite element mesh. As explained in Chapter 3, the various ways in how this can be done give place to different subgrid scale stabilising methods.

If the algebraic subgrid scale (ASGS) approach is followed, it can be shown that the large scale equation (5.112) is modified to (see e.g., [39])

$$a\left(\hat{p}_h, w_h\right) + \sum_{n_e} \left(-\mathcal{L}_{CH}^{\dagger}\left(w_h\right), \tau_{SGS}\left[\mathcal{L}_{CH}\left(\hat{p}_h\right) - \hat{s}_h\right] \right)_{\Omega_e} = l\left(w_h\right) \tag{5.116}$$

where $\mathcal{L}_{CH}$ is the differential convected Helmholtz operator defined in (5.8) and τ_{SGS} is a stabilisation parameter to be determined below. It is expected that the modified sesquilinear form (5.116) together with an appropriate choice for the stabilisation parameter τ_{SGS} will avoid some of the stability problems detected when solving the convected Helmholtz equation [83, 84].

If instead of the ASGS method the GLS one is used, it can be shown that (5.116) is modified to (see again [39])

$$a\left(\hat{p}_h, w_h\right) + \sum_{n_e} \left(-\mathcal{L}_{CH}\left(w_h\right), \tau_{GLS}\left[\mathcal{L}_{CH}\left(\hat{p}_h\right) - \hat{s}_h\right] \right)_{\Omega_e} = l\left(w_h\right). \tag{5.117}$$

Taking into account that the convected Helmholtz differential operator is selfadjoint (5.9), it follows that both methods will yield the same results provided that the SGS stabilisation parameter is identified with minus the GLS stabilisation parameter:

$$\tau_{SGS} \equiv -\tau_{GLS}. \tag{5.118}$$

5.5.2 Stabilisation parameter from a dispersion analysis

In what follows, we will obtain τ_{SGS} for the convected Helmholtz equation in two dimensions. A dispersion analysis will be performed considering a uniform mesh of element size $h \times h$ and the use of bilinear elements (see [119, 120, 163, 287]). Let us first explicitly write the stabilised SGS sesquilinear form (5.116) for the two dimensional case without considering the boundary terms, as we will be interested in results concerning interior mesh nodes. This form is given by

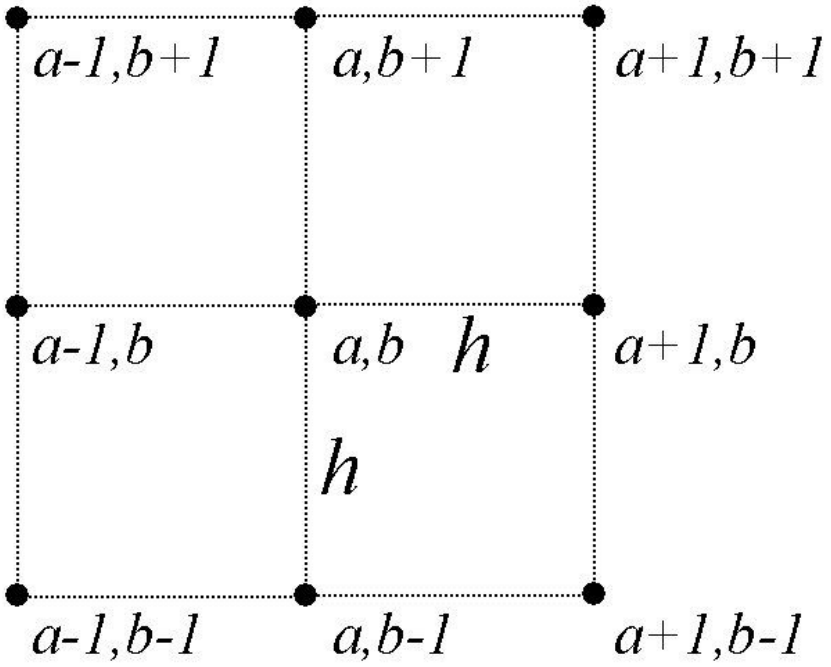

Figure 5.12: Patch in a two-dimensional uniform mesh.

$$
\begin{aligned}
a_{SGS}\left(\hat{p}_h, w_h\right) = & -2ik_0 M_x \underbrace{\left(\partial_x \hat{p}_h, w_h\right)}_{C_x} - 2ik_0 M_y \underbrace{\left(\partial_y \hat{p}_h, w_h\right)}_{C_y} \\
& + \left[1 - M_x^2\right] \underbrace{\left(\partial_x \hat{p}_h, \partial_x w_h\right)}_{D_{xx}} + \left[1 - M_y^2\right] \underbrace{\left(\partial_y \hat{p}_h, \partial_y w_h\right)}_{D_{yy}} \\
& - 2M_x M_y \underbrace{\left(\partial_x \hat{p}_h, \partial_y w_h\right)}_{D_{xy}} - k_0^2 \underbrace{\left(\hat{p}_h, w_h\right)}_{S} \\
& + \tau_{SGS} 4k_0^2 M_x^2 \sum_{n_{el}} \left(\partial_x \hat{p}_h, \partial_x w_h\right)_{\Omega_{el}} + \tau_{SGS} 4k_0^2 M_y^2 \sum_{n_{el}} \left(\partial_y \hat{p}_h, \partial_y w_h\right)_{\Omega_{el}} \\
& + \tau_{SGS} 8k_0^2 M_x M_y \sum_{n_{el}} \left(\partial_x \hat{p}_h, \partial_y w_h\right)_{\Omega_{el}} - \tau_{SGS} k_0^4 \sum_{n_{el}} \left(\hat{p}_h, w_h\right)_{\Omega_{el}}
\end{aligned} \tag{5.119}
$$

where we have used the fact that $\left(\nabla \hat{p}_h, w_h\right) = -\left(\nabla w_h, \hat{p}_h\right)$ for w_h with support in the interior of Ω_{ac}, and we have identified the terms C_x, C_y, D_{xx}, D_{yy}, D_{xy} and S to simplify subsequent notation. The nodal unknowns for interior nodes corresponding to the patch

in Fig. 5.12 can be represented by the 9-point difference star

$$\left[P_{ab}^{int}\right] := \begin{bmatrix} \hat{P}^{a-1,b+1} & \hat{P}^{a,b+1} & \hat{P}^{a+1,b+1} \\ \hat{P}^{a-1,b} & \hat{P}^{a,b} & \hat{P}^{a+1,b} \\ \hat{P}^{a-1,b-1} & \hat{P}^{a,b-1} & \hat{P}^{a+1,b-1} \end{bmatrix}. \tag{5.120}$$

Analogously, when considering bilinear shape functions, the coefficients arising from C_x, C_y, D_{xx}, D_{yy}, D_{xy} and S can be written in compact form for the 9-point difference star in Fig. 5.12 as:

$$\left[C_{x,ab}^{int}\right] := \frac{h}{12}\begin{bmatrix} -1 & 0 & 1 \\ -4 & 0 & 4 \\ -1 & 0 & 1 \end{bmatrix},\ \left[C_{y,ab}^{int}\right] := \left[C_{x,ab}^{int}\right]^{\top} \tag{5.121}$$

$$\left[D_{xx,ab}^{int}\right] := \frac{1}{6}\begin{bmatrix} -1 & 2 & -1 \\ -4 & 8 & -4 \\ -1 & 2 & -1 \end{bmatrix},\ \left[D_{yy,ab}^{int}\right] := \left[D_{xx,ab}^{int}\right]^{\top},\ \left[D_{xy,ab}^{int}\right] := \frac{1}{4}\begin{bmatrix} 1 & 0 & -1 \\ 0 & 0 & 0 \\ -1 & 0 & 1 \end{bmatrix} \tag{5.122}$$

$$\left[S_{ab}^{int}\right] := \frac{h^2}{36}\begin{bmatrix} 1 & 4 & 1 \\ 4 & 16 & 4 \\ 1 & 4 & 1 \end{bmatrix}. \tag{5.123}$$

Taking into account the notation (5.120)-(5.123), the equation for the interior node ab (with no force acting on it) of the algebraic linear system associated to the discrete SGS weak problem can be written as

$$\begin{aligned} &- 2ik_0M_x\left[C_{x,ab}^{int}\right] : \left[P_{ab}^{int}\right] - 2ik_0M_y\left[C_{y,ab}^{int}\right] : \left[P_{ab}^{int}\right] \\ &+ \left(1-M_x^2\right)\left[D_{xx,ab}^{int}\right] : \left[P_{ab}^{int}\right] + \left(1-M_y^2\right)\left[D_{yy,ab}^{int}\right] : \left[P_{ab}^{int}\right] \\ &- 2M_xM_y\left[D_{xy,ab}^{int}\right] : \left[P_{ab}^{int}\right] - k_0^2\left[S_{ab}^{int}\right] : \left[P_{ab}^{int}\right] \\ &+ \tau_{SGS}4k_0^2M_x^2\left[D_{xx,ab}^{int}\right] : \left[P_{ab}^{int}\right] + \tau_{SGS}4k_0^2M_y^2\left[D_{yy,ab}^{int}\right] : \left[P_{ab}^{int}\right] \\ &+ \tau_{SGS}8k_0^2M_xM_y\left[D_{xy,ab}^{int}\right] : \left[P_{ab}^{int}\right] - \tau_{SGS}k_0^4\left[S_{ab}^{int}\right] : \left[P_{ab}^{int}\right] = 0 \end{aligned} \tag{5.124}$$

where : stands for a double contraction. If we now assume a plane wave solution with an effective wavenumber vector $\boldsymbol{k}_0^{eff} = \left(k_{0x}^{eff}, k_{0y}^{eff}\right)$ (to be determined lately in this section) so that at node mn

$$\hat{p}^{mn} = \exp\left[i\left(k_{0x}^{eff}hm + k_{0y}^{eff}hn\right)\right] \tag{5.125}$$

and substitute this expression into (5.124), a dispersion relation is obtained from which the following value for the stabilisation parameter τ_{SGS} can be derived by imposing that the discrete equations are satisfied:

$$\tau_{SGS} = \frac{A_{num} + B_{num}M_x + C_{num}M_y + D_{num}M_x^2 + E_{num}M_y^2 + F_{num}M_xM_y}{A_{den} + B_{den}M_x + C_{den}M_y + D_{den}M_x^2 + E_{den}M_y^2 + F_{den}M_xM_y} \tag{5.126}$$

with

$$A_{num} = -\frac{2}{3}\left[4 - \cos\left(k_{0x}^{eff}h\right) - \cos\left(k_{0y}^{eff}h\right) - 2\cos\left(k_{0x}^{eff}h\right)\cos\left(k_{0y}^{eff}h\right)\right] + \frac{k_0^2h^2}{9}\left\{\left[2 + \cos\left(k_{0x}^{eff}h\right)\right]\left[2 + \cos\left(k_{0y}^{eff}h\right)\right]\right\} \tag{5.127}$$

$$B_{num} = -\frac{2}{3}k_0h\left[\sin\left(k_{0x}^{eff}h\right)\cos\left(k_{0y}^{eff}h\right) + 2\sin\left(k_{0x}^{eff}h\right)\right] \tag{5.128}$$

$$C_{num} = -\frac{2}{3}k_0h\left[\sin\left(k_{0y}^{eff}h\right)\cos\left(k_{0x}^{eff}h\right) + 2\sin\left(k_{0y}^{eff}h\right)\right] \tag{5.129}$$

$$D_{num} = \frac{2}{3}\left\{2 - \cos\left(k_{0x}^{eff}h\right)\left[2 + \cos\left(k_{0y}^{eff}h\right)\right] + \cos\left(k_{0y}^{eff}h\right)\right\} \tag{5.130}$$

$$E_{num} = \frac{2}{3}\left\{2 - \cos\left(k_{0y}^{eff}h\right)\left[2 + \cos\left(k_{0x}^{eff}h\right)\right] + \cos\left(k_{0y}^{eff}h\right)\right\} \tag{5.131}$$

$$F_{num} = 2\sin\left(k_{0x}^{eff}h\right)\sin\left(k_{0y}^{eff}h\right) \tag{5.132}$$

$$A_{den} = -\frac{k_0^4h^2}{3}\left[2 + \cos\left(k_{0x}^{eff}h\right)\right]\left[2 + \cos\left(k_{0y}^{eff}h\right)\right] \tag{5.133}$$

$$B_{den} = 0 \tag{5.134}$$

$$C_{den} = 0 \tag{5.135}$$

$$D_{den} = 4k_0^2D_{num} \tag{5.136}$$

$$E_{den} = 4k_0^2E_{num} \tag{5.137}$$

$$F_{den} = 4k_0^2F_{num}. \tag{5.138}$$

It remains now to find the appropriate value for the effective wavenumber vector in (5.127)-(5.138). This can be done in a quite straightforward manner by taking into account the results from section 5.2.2. Our objective is to find the effective wavenumber for a plane wave propagating at an arbitrary direction, say angle θ with the x-axis, in a uniform flow characterised by a Mach vector $\boldsymbol{M}$ being at an angle φ with the x-axis (see Fig. 5.13). All that we have to do is to revert the full Lorentz transformation (5.16) for a plane wave

$$\hat{p}''\left(\boldsymbol{x}'', \boldsymbol{k}_0''\right) = \exp\left(i\boldsymbol{k}_0'' \cdot \boldsymbol{x}''\right). \tag{5.139}$$

Hence, the plane wave propagating in the uniform medium will be given by

$$\hat{p}''\left(\boldsymbol{x}, \boldsymbol{k}_0\right) = \exp\left\{i\beta^{-1}\left[\boldsymbol{R}\boldsymbol{k}_0 - k_0\boldsymbol{R}\boldsymbol{M}\right] \cdot \left(\boldsymbol{D}\boldsymbol{R}\boldsymbol{x}\right)\right\} \equiv \exp\left(i\boldsymbol{k}_0^{eff} \cdot \boldsymbol{x}\right). \tag{5.140}$$

Inserting the rotation matrix

$$\boldsymbol{R} = \begin{bmatrix} \cos\varphi & -\sin\varphi \\ \sin\varphi & \cos\varphi \end{bmatrix} \tag{5.141}$$

in (5.140) we arrive to the following values for the components of the effective wavenumber vector defined in the last equality of (5.140)

$$k_{0x}^{eff} = k_0\beta^{-2}\left[\cos\left(\theta - \varphi\right)\cos\varphi - M_x\right] - k_0\beta^{-1}\sin\left(\theta - \varphi\right)\sin\varphi \tag{5.142}$$

$$k_{0y}^{eff} = k_0\beta^{-2}\left[\cos\left(\theta - \varphi\right)\sin\varphi + M_y\right] - k_0\beta^{-1}\sin\left(\theta - \varphi\right)\cos\varphi. \tag{5.143}$$

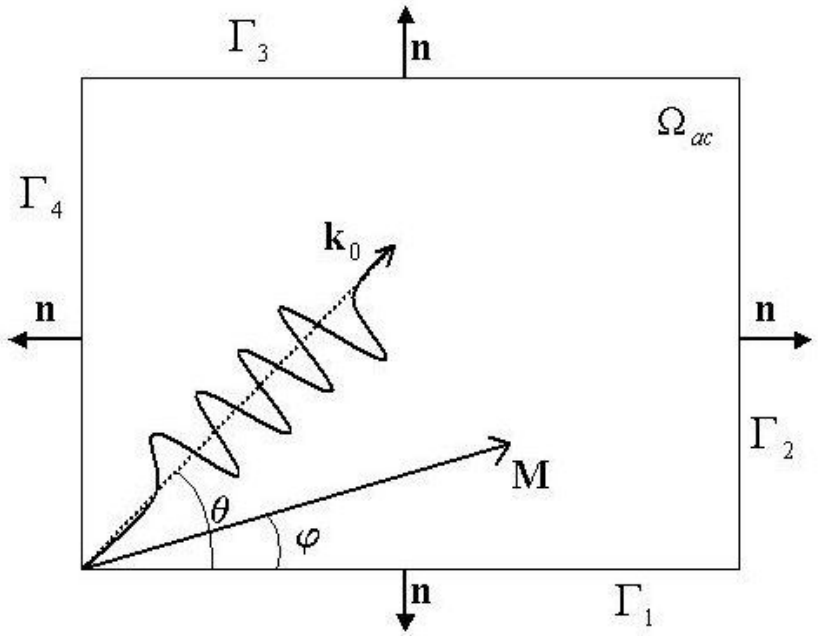

Figure 5.13: Scheme for a plane wave propagating with $\boldsymbol{k}_0$ in a uniform flow characterised by $\boldsymbol{M}$.

Note that $\boldsymbol{k}_0^{eff}$ is nothing but $\boldsymbol{k}_0''$ expressed in the original coordinates and variables. Expressions (5.142) and (5.143) are finally to be inserted in equations (5.127)-(5.138) to find the appropriate value for the parameter τ_{SGS}.

Remarks

- If there is no convection i.e., $\boldsymbol{M} = (0, 0)$, it follows from (5.142)-(5.143) that

$$k_{0x}^{eff} = k_{0x}, \qquad k_{0y}^{eff} = k_{0y}, \tag{5.144}$$

which inserted in (5.126) yields

$$\begin{aligned}\tau_{SGS} &= \frac{A_{num}}{A_{den}} \\ &= -\frac{1}{k_0^2} + \frac{6}{k_0^4 h^2} \frac{\left[4 - \cos\left(k_{0x}^{eff} h\right) - \cos\left(k_{0y}^{eff} h\right) - 2\cos\left(k_{0x}^{eff} h\right)\cos\left(k_{0y}^{eff}\right)\right]}{\left[2 + \cos\left(k_{0x}^{eff} h\right)\right]\left[2 + \cos\left(k_{0y}^{eff} h\right)\right]}.\end{aligned} \tag{5.145}$$

As expected, (5.145) is nothing but minus the stabilisation parameter found from the GLS stabilisation of the Helmholtz equation in [287].

- The one dimensional counterpart of (5.141) can be obtained e.g., by setting $M_y = 0$ ($\varphi = 0$) and $k_{0y} = 0$ ($\theta = 0°$) in it and by taking into account that the effective wavenumber components (5.142) and (5.143) will become

$$k_{0x}^{eff} = \frac{k_{0x}}{1+M} \equiv k^{eff}, \qquad k_{0y}^{eff} = 0. \tag{5.146}$$

  It then follows that τ_{SGS} is given by (we use $M \equiv M_x$)

$$\tau_{SGS} = \frac{A_{num} + B_{num}M + D_{num}M^2}{A_{den} + B_{den}M + D_{den}M^2}, \tag{5.147}$$

  with

$$A_{num} = 2\left[\cos\left(k_{0x}^{eff}h\right) - 1\right] + \frac{k_0^2h^2}{3}\left[2 + \cos\left(k_{0x}^{eff}h\right)\right], \tag{5.148}$$

$$B_{num} = -2k_0h\sin\left(k_{0x}^{eff}h\right), \tag{5.149}$$

$$D_{num} = 2\left[1 - \cos\left(k_{0x}^{eff}h\right)\right], \tag{5.150}$$

$$A_{den} = -\frac{k_0^4h^2}{3}\left[2 + \cos\left(k_{0x}^{eff}h\right)\right], \tag{5.151}$$

$$B_{den} = 0, \tag{5.152}$$

$$D_{den} = 4k_0^2D_{num}. \tag{5.153}$$

- The non-convective one-dimensional case follows from setting $M = 0$ in (5.147) and noting that now (5.146) yields $k_0^{eff} = k_0$. The stabilisation parameter then becomes

$$\tau_{SGS} = \frac{A_{num}}{A_{den}} = -\frac{1}{k_0^2} + \frac{6}{k_0^4h^2}\frac{[1 - \cos(k_0h)]}{[2 + \cos(k_0h)]}, \tag{5.154}$$

  which is nothing but minus the τ_{GLS} obtained for the one-dimensional Helmholtz equation in [119, 120].

- It should be noted from the above formulation that while the flow orientation φ is a given parameter, the plane wave orientation θ is an artifact of the analysis whose "optimum" value may be unknown even after the problem is solved (see section 5.5.3).

In Fig. 5.14a we have plotted the dependence of $-\tau_{SGS}$ with k_0h for various Mach numbers in the one dimensional case, see (5.147). We can observe the role played by the Doppler effect: for positive Mach numbers (downstream propagation) the effective wavenumber k_0^{eff} is smaller than k_0 (see (5.146)) so that less stabilisation is required and $|\tau_{SGS}|$ is smaller than for the Helmholtz case ($M = 0$, equation (5.154)). On the opposite, for negative Mach numbers (upstream propagation) the effective wavenumber is larger than k_0 and consequently more stabilisation is required than for the Helmholtz case.

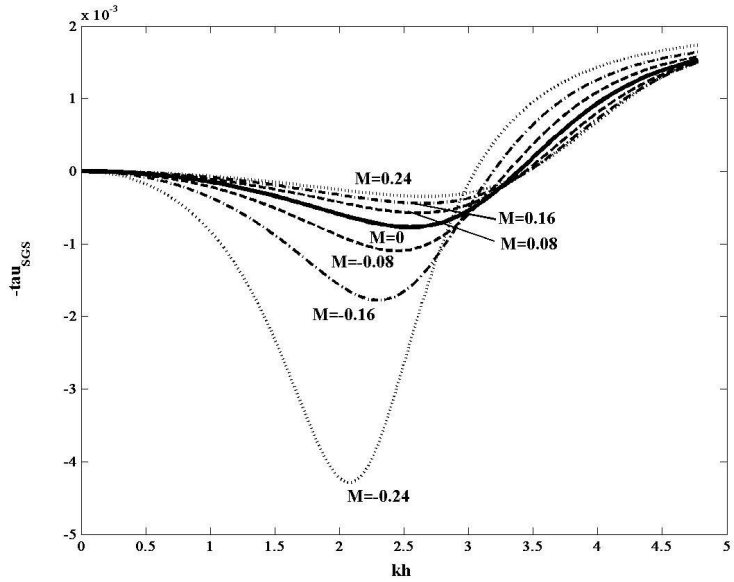

a) One dimensional $-\tau_{SGS}$ for various Mach numbers. Continuous line: $M = 0$, dashed line: $M = 0.08, -0.08$, dotted-dashed line: $M = 0.16, -0.16$, dotted line: $M = 0.24, -0.24$.

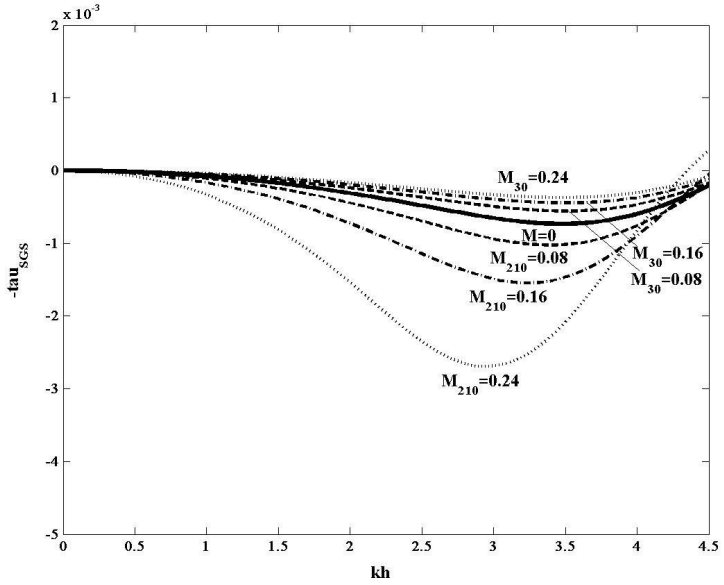

b) $-\tau_{SGS}$ for various Mach numbers. Continuous line: $M_{\rho\varphi} = (0, 0^\circ)$, dashed line: $M_{\rho\varphi} = (0.08, 30^\circ), (0.08, 210^\circ)$, dotted-dashed line: $M_{\rho\varphi} = (0.16, 30^\circ), (0.16, 210^\circ)$, dotted line: $M_{\rho\varphi} = (0.24, 30^\circ), (0.24, 210^\circ)$.

Figure 5.14: stabilisation parameter dependence with Mach number

In Fig. 5.14b we have plotted the dependence of $-\tau_{SGS}$ with $k_0 h$ for a plane wave having a wavenumber vector in polar coordinates $\boldsymbol{k}_0 = (k_0, \theta) = (24, 50^\circ)$ propagating in uniform flows characterised by Mach number vectors $\boldsymbol{M} = (M, \varphi)$, with $M = \{0.08, 0.16, 0.24\}$ and $\varphi = \{30^\circ, 210^\circ\}$. τ_{SGS} has been computed from (5.126) and compared with the non-convected stabilisation parameter given by (5.145). A very similar behaviour to the one in Fig. 5.14a can be appreciated, $|\tau_{SGS}|$ now being smaller because the projection of $\boldsymbol{k}_0$ onto $\boldsymbol{M}$ will be always smaller than for the one-dimensional case ($\theta - \varphi = 0^\circ$) yielding to a less significant influence of the convective term in (5.114).

5.5.3 Discussion

It is clear that due to the Doppler effect different mesh resolutions should be used to properly capture an acoustic field containing upstream and downstream propagating waves in a uniform mean flow. In [83] it was shown that even if we were able to built a mesh keeping the number of points per wavelength constant (hence avoiding the lack of resolution due to the Doppler effect), the pollution effects for the Galerkin finite element solution of the convected wave equation still differ for upstream and downstream propagation waves. It was also shown that a large degree of anisotropy is detected when analysing the dispersion and amplitude error dependences on wave and flow orientations [84]. As a conclusion, it was suggested that the use of mesh adaptative strategies based, for instance, on a posteriori error estimations, may be useful to deal with complex acoustic fields with waves propagating in many directions. Obviously, this can be a good procedure although it requires either the performance of several simulations (at least two) or a previous knowledge of the resulting acoustic field to build an adequate mesh. However, the former might turn rather unpractical for large problems while the latter rarely occurs.

An alternative (or complement) to the adaptative mesh strategy is the use of stabilisation techniques. If we were able to compute the right amount of stabilisation needed at each mesh zone to yield a good solution, it would not be necessary to modify the mesh. In the previous sections we have presented a finite element method to do so. Unfortunately, this stabilised formulation is not free of problems. Note that while the flow orientation φ is a given quantity, the wavenumber direction θ will be unknown prior to the solution of the problem. The resulting τ_{SGS} will consequently depend on the values chosen for θ and the stabilisation effect may be significant for waves propagating in this direction but much weaker or inexistent for other ones. As already mentioned in the introduction, this is probably the main drawback of obtaining the stabilisation parameter from a dispersion analysis in the GLS stabilisation for the Helmholtz equation [163, 287]. However, it has been checked in [121, 287, 288] that some particular values for θ are able to yield good results for a wide variety of problems with waves propagating in several directions (recommended values are $\theta = \{0^\circ, 22.5^\circ\}$). It is expected that this can also be the case for the stabilisation parameter found in the present analysis. The results of the examples in the next section seem to support this idea.

5.6 Numerical examples

5.6.1 Free waves in one and two dimensions

We present in this section the effects of stabilisation on the previously analized model problem 1 (equations (5.83)-(5.85)) and model problem 2 (equations (5.101)-(5.110)).

Concerning the former, the corresponding ASGS stabilised weak form is given by (5.116) with one dimension suppressed, $M_1 = 0$ and the stabilisation parameter τ_{SGS} in (5.154). In Fig. 5.15 the effects of stabilisation can be clearly observed. We have plotted the H^1-seminorm error of the Galerkin FEM, interpolant and ASGS stabilised solutions. It is apparent that once the resolution threshold of two points per wavelength (first interval of convergence) has been surpassed, the ASGS solution (red line in the figure) decreases with the same slope as the interpolant one and presents no pollution error.

The ASGS stabilised weak form for model problem 2 corresponds to weak form (5.116) with $M_1 = 0$ and τ_{SGS} given by (5.145). In Fig. 5.16 we present the values of $-\tau_{SGS}k_0^2$ for increasing normalised wavenumbers k_0h/π and for waves propagating in the directions $\theta = \{0°, 22.5°, 45°\}$. In Fig. 5.16a, the results are shown for the range $k_0h/\pi \in [0, 1]$ that corresponds to the second, preasymptotic and asymptotic convergence ranges ($k_0h \approx \pi$). On the contrary, Fig. 5.16b shows the results for k_0h/π up to 16 and we can observe that $-\tau_{SGS}k_0^2$ oscillates towards 1. In this case the ASGS method is not able to improve the Galerkin solution and can even worsen it. Hence in order for the method to work it is necessary that we are at least over the resolution threshold value. This point can be also appreciated in Fig. 5.17 where we have plotted the H^1-seminorm error of the Galerkin FEM, interpolant and ASGS stabilised solutions for model problem 2. Again, once surpassed the resolution threshold value, the ASGS solution presents no pollution error.

In Fig. 5.18 analogous results to those of Fig. 5.10 are given together with the corresponding result for the ASGS method. As seen the ASGS solution is in phase with the exact and interpolant ones, as expected from the results in Fig. 5.17. Finally, in Fig. 5.19, a comparison among the Galerkin-FEM, ASGS stabilised, Interpolant and Exact solutions for a wave propagating in the direction $\theta = 45°$ with $k_0 = 50$ is presented. A seen, the ASGS solution considerably improves the Galerkin-FEM solution as insinuated by the results in Fig. 5.17.

5.6.2 Two dimensional free wave propagating in a mean flow

As a second numerical example we consider the case of finding the acoustic pressure in a computational domain, $\Omega_{ac} = (0, 1) \times (0, 1)$, with inhomogeneous Dirichlet boundary conditions on $\partial\Omega_{ac}$ and normal surface vector $\boldsymbol{n}$ pointing outwards of the domain (see Fig. 5.13), such that

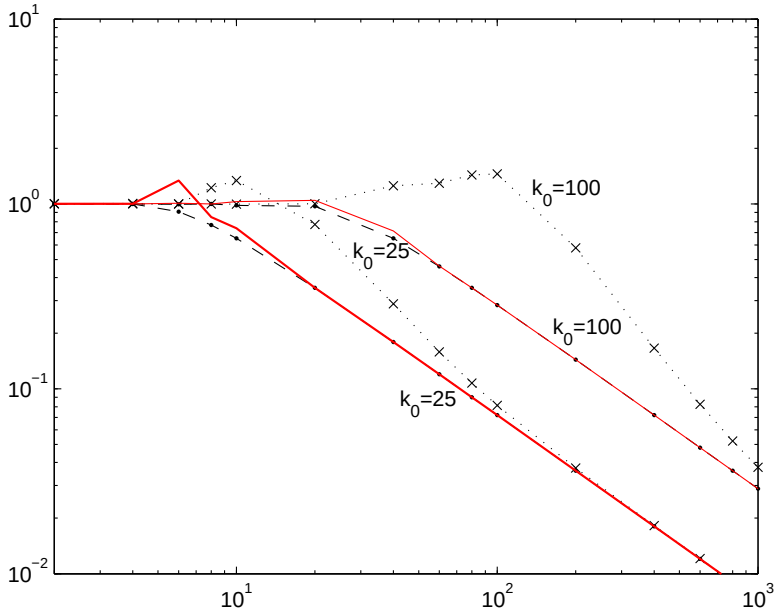

Figure 5.15: H^1-seminorm relative error for the Galerkin-FEM (cross-dotted), interpolant (dashed) and ASGS stabilised (red continuous) solutions. Model problem 1.

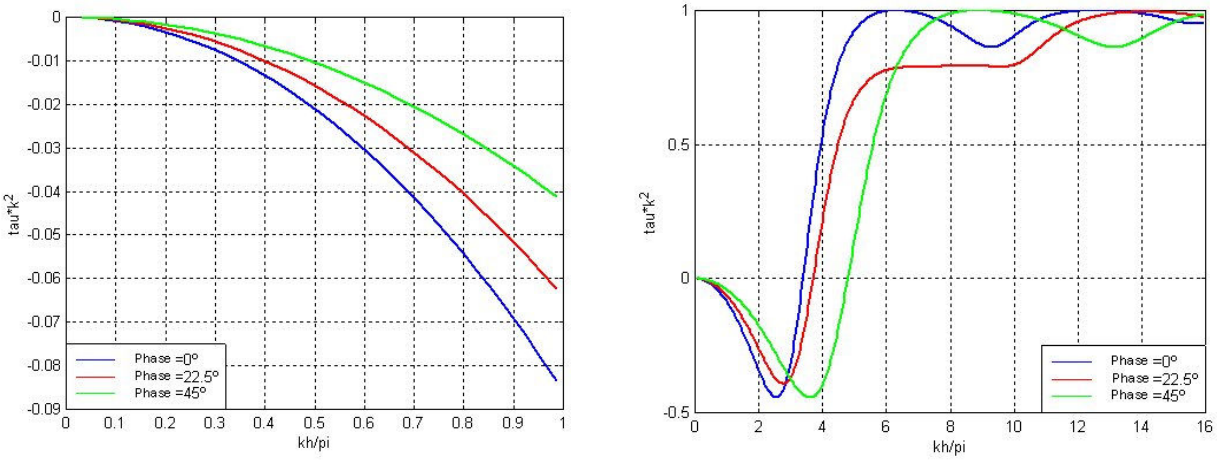

a) $0 < k_0 h/\pi < 1$ b) $0 < k_0 h/\pi < 16$

Figure 5.16: $-\tau_{SGS} k_0^2$ from SGS vs normalised wavenumber $k_0 h/\pi$, for waves propagating in the directions $\theta = \{0°, 22.5°, 45°\}$. Model problem 2.

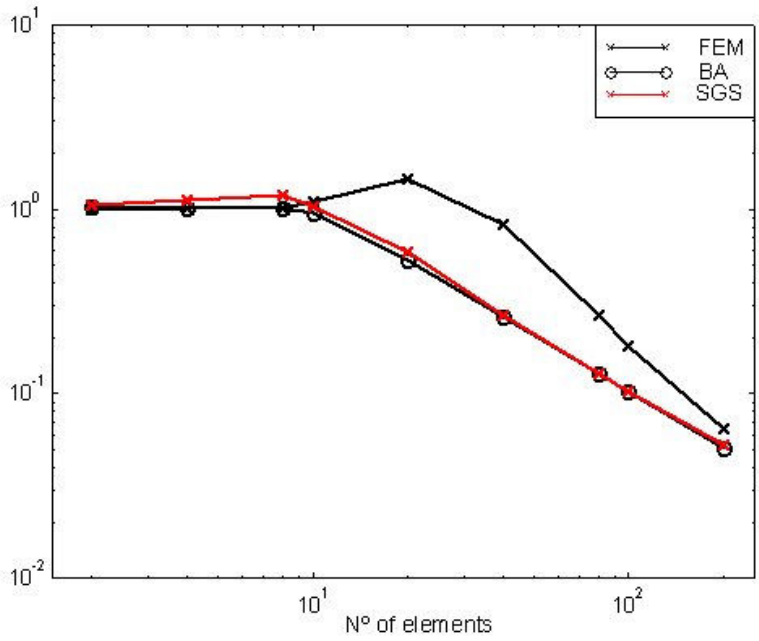

Figure 5.17: H^1-seminorm relative error for: Galerkin-FEM (cross-continuous), interpolant (circle-continuous) and ASGS stabilised (red continuous). Model problem 2.

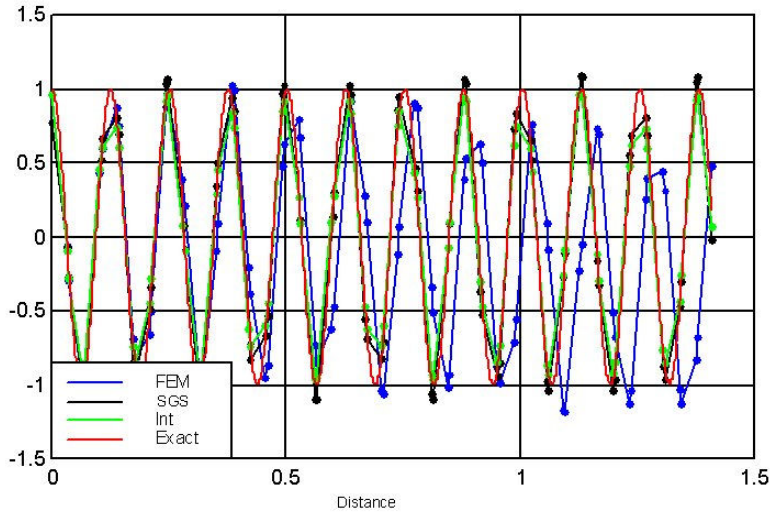

Figure 5.18: Exact, ASGS stabilised, Interpolant and Galerkin FEM solution for $k_0 = 50$, $N = 40$. Diagonal of the Ω_{ac} domain in (5.101). Model problem 2.

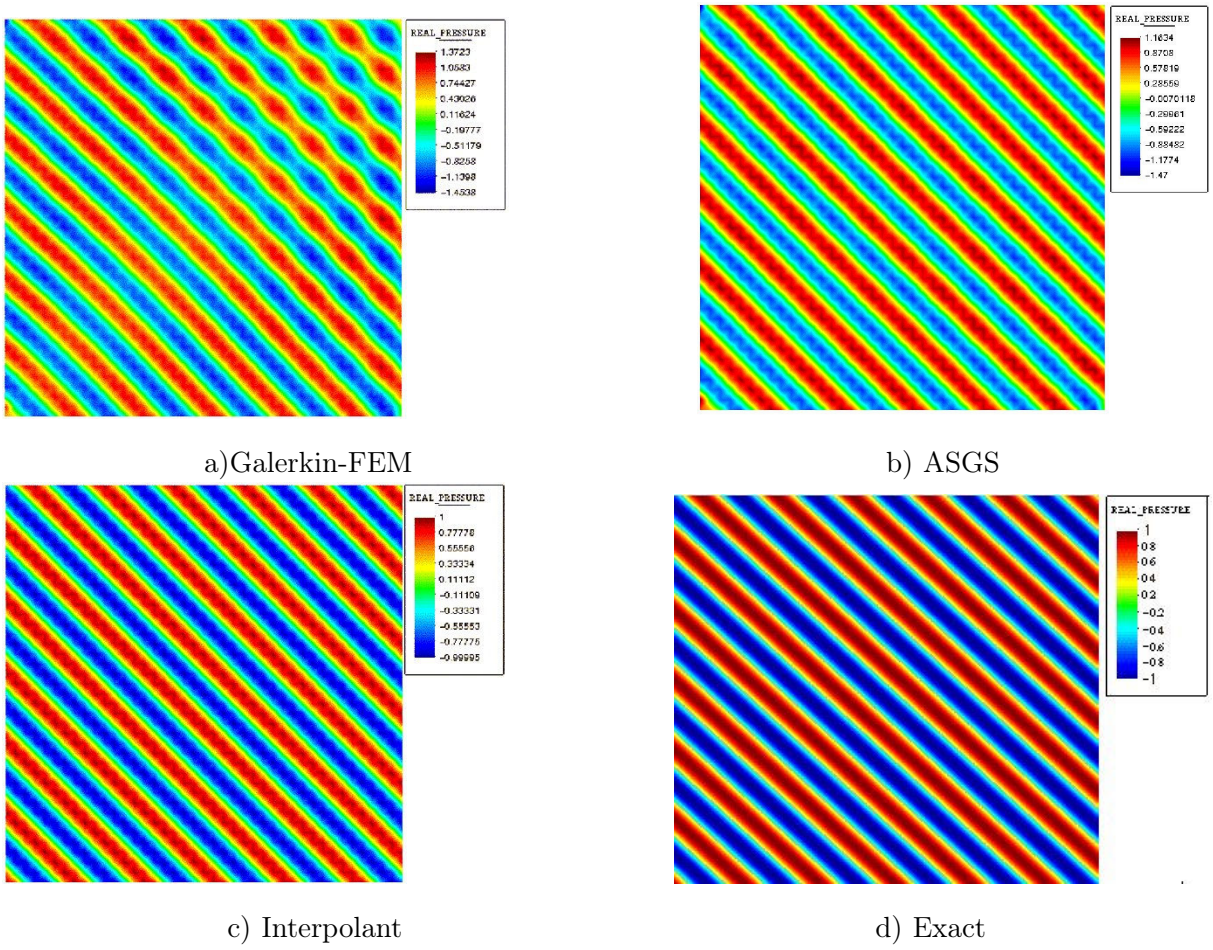

a)Galerkin-FEM b) ASGS

c) Interpolant d) Exact

Figure 5.19: Comparison of the Galerkin-FEM, ASGS, Interpolant and exact solutions for a wave propagating in the direction $\theta = 45°$ and $k_0 = 50$. Model problem 2.

$$\left[\nabla^2 + (k_0 + i\boldsymbol{M}\cdot\nabla)^2\right]\hat{p} = 0 \quad \text{in } \Omega_{ac} \tag{5.155}$$

$$\hat{p} = \exp\left[i\left(k_{0x}^{eff}x + k_{0y}^{eff}y\right)\right] \quad \text{on } \partial\Omega_{ac}. \tag{5.156}$$

The corresponding ASGS stabilised weak form for this problem is given by (5.116). For the Mach number vector characterising the mean flow we take the values in polar coordinates $\boldsymbol{M} = (M, \varphi) = (0.6, 30°)$ and for the wavenumber vector we use $\boldsymbol{k}_0 = (k_0, \theta) = (24, 50°)$ to be inserted in (5.155)-(5.156). The effective wavenumber $\boldsymbol{k}_0^{eff} = \left(k_{0x}^{eff}, k_{0y}^{eff}\right)$ in (5.156) is computed from (5.142)-(5.143).

The exact solution for the problem above is the plane wave

$$\hat{p} = \exp\left(i\boldsymbol{k}_0^{eff}\cdot\boldsymbol{x}\right) \tag{5.157}$$

propagating with an effective wavenumber in polar coordinates $\boldsymbol{k}_0^{eff} = \left(k_0^{eff}, \theta^{eff}\right) = (16.35, 68.8^\circ)$. Hence, the effect of the mean flow on the original wave, having wavenumber $\boldsymbol{k}_0$, is to reduce the modulus of the wavenumber and to change its direction upstream.

If we now proceed to solve (5.155)-(5.156) using the Galerkin finite element method (5.64) on a uniform grid with elements of size $h \times h$, with $h = 0.025$, we will observe that even though $k_0^{eff} h = 0.4$ (more than the recommended ten points per wavelength), the method is unable to yield an accurate solution for the problem. On the contrary, the stabilised SGS finite element approach using the modified weak form (5.116) and the stabilisation parameter (5.126) has been designed to yield exact nodal values for this case. This can be clearly appreciated in Fig. 5.20a and Fig. 5.20b where the imaginary part of the Galerkin and SGS solutions have been respectively plotted. It is apparent from Fig. 5.20a that the Galerkin solution distorts the shape of the wave and yields much higher amplitudes than the correct ones. This can also be observed in Fig. 5.21, where the imaginary part of the acoustic pressure in a one dimensional cut of the domain, $\Omega_{ac}|_{x=0.25} := \{(0.25, y) \,|\, 0 < y < 1\}$, is plotted for both cases, together with the exact solution.

On the other hand, to make the stabilised ASGS method useful in as many situations as possible, it should perform well for other meshes than the structured bilinear quadrilateral elements for which the stabilisation parameter τ_{SGS} has been optimised. To check this point we have constructed an unstructured mesh of quadrilateral elements (see Fig. 5.22) and studied the dependence of the numerical solution relative error in the L^2-norm, $\|\hat{p}_h - \hat{p}_{exact}\| \,/\, \|\hat{p}_{exact}\|$, when refining the mesh. $\hat{p}_{exact}$ is given by (5.157) and $\hat{p}_h$ denotes the numerical solution obtained by either the Galerkin method or by the stabilised ASGS one. Results are plotted in Fig. 5.23a together with the -2 slope of the *best approximation* solution. It can be clearly observed that the ASGS stabilised solution improves the results of the Galerkin method for all meshes. Moreover, we have plotted the results of using the ASGS formulation with the stabilisation parameter, τ_{SGS}, corresponding to $\theta = 0^\circ$ instead of $\theta = 50^\circ$. It can be seen that the solution is also better than the Galerkin one (and for some meshes even better than the $\theta = 50^\circ$ one). However, this cannot be taken as a general result stating that any value of θ in τ_{ASGS} would result in an improvement of the solution (see the discussion in section 5.5.3).

Further tests are presented in Figs. 5.23b and 5.23c. In Fig. 5.23b we have considered the same Mach number and meshes than for Fig. 5.23a, but for a plane wave with wavenumber $\boldsymbol{k}_0 = (24\, m^{-1}, 80^\circ)$. This results in a free plane wave with effective wavenumber $\boldsymbol{k}_0^{eff} = (23\, m^{-1}, 116^\circ)$, i.e. almost propagating in the normal direction to the mean flow. It can be observed in Fig. 5.23b that once the resolution threshold is surpassed ($h^{-1} \gtrsim 50$) the ASGS solution error is clearly lower than the Galerkin one. The ASGS solution taking $\theta = 0^\circ$ in the stabilisation parameter also yields better solutions. On the opposite, if using the ASGS stabilisation without taking into account convection (5.145), large errors are encountered depending on the mesh, either when setting $\theta = 0^\circ$ or $\theta = 80^\circ$ in the stabilisation parameter.

Next we have repeated the test but for a plane wave having wavenumber $\boldsymbol{k}_0 =$

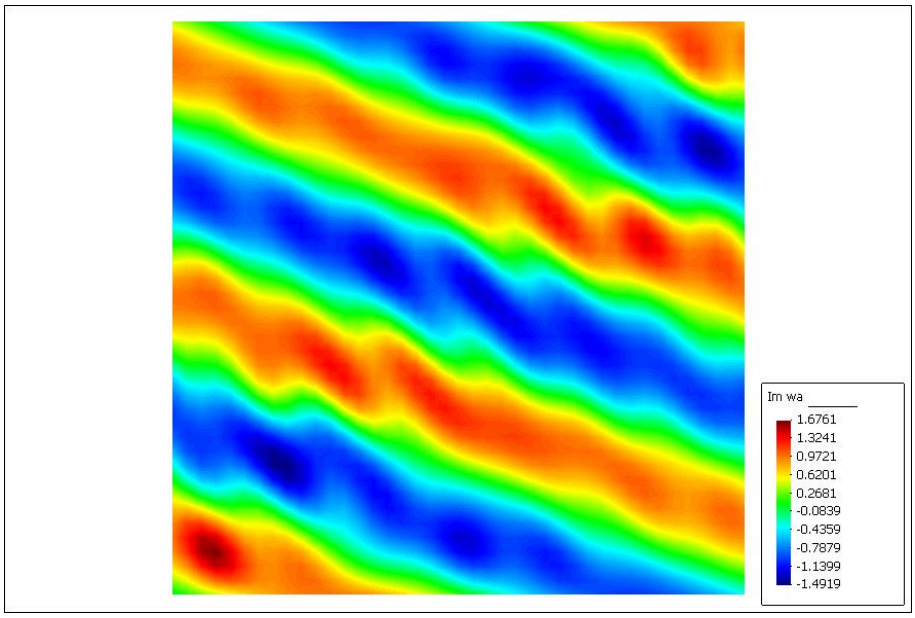

a) Galerkin FEM solution

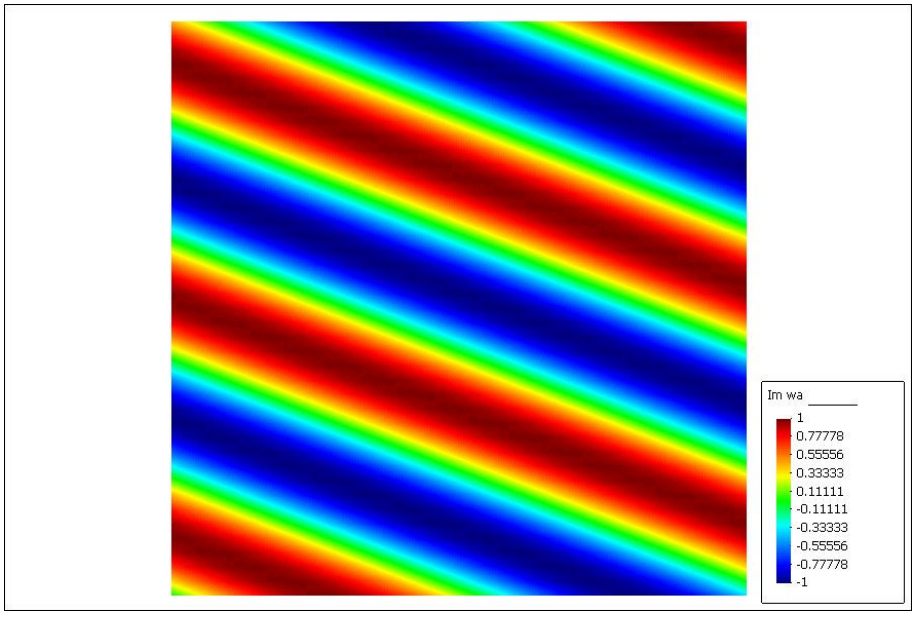

b) ASGS solution

Figure 5.20: Imaginary part of the Galerkin and ASGS finite element solutions to problem (5.155)-(5.156) in text.

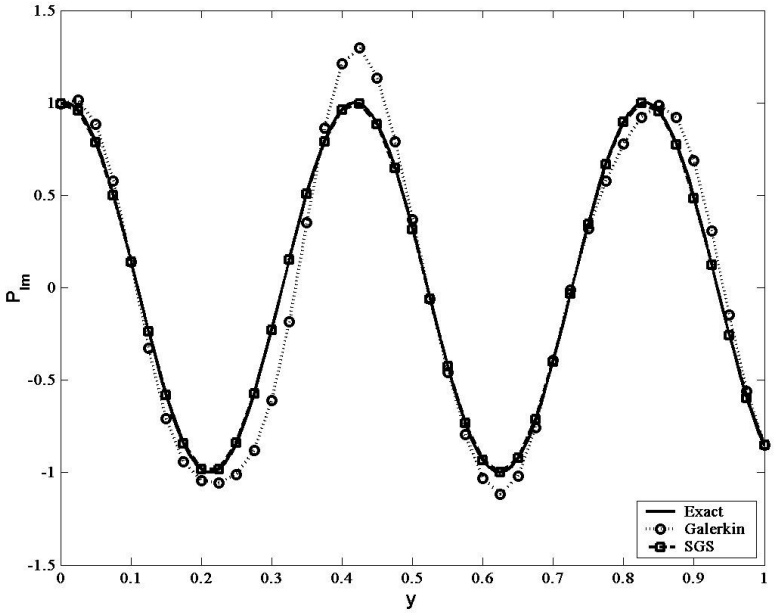

Figure 5.21: Imaginary part of the reference, Galerkin and SGS solutions for a one dimensional cut of the domain corresponding to the Dirichlet problem (5.155)-(5.156) in text.

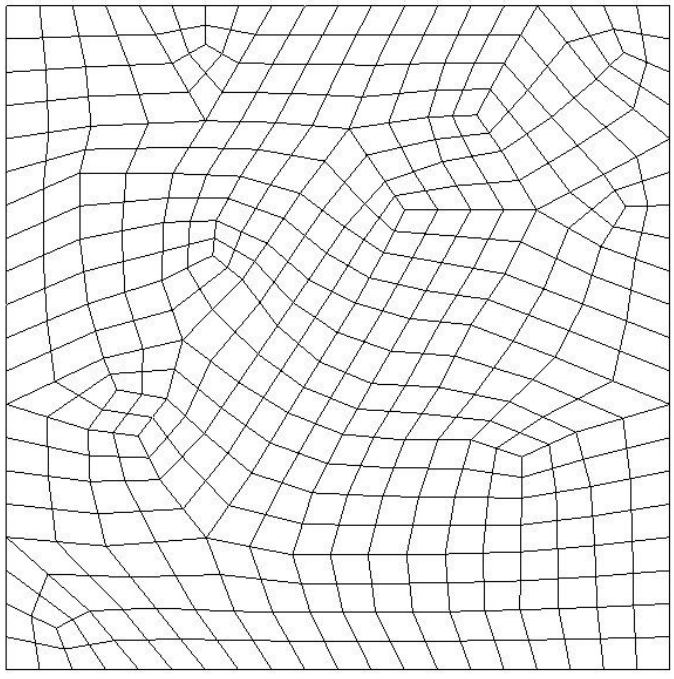

Figure 5.22: Unstructred mesh of quadrilateral elements.

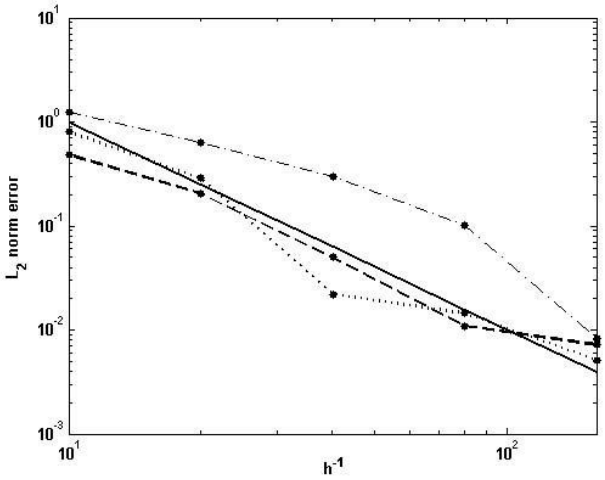

a) $\boldsymbol{M} = (0.6, 30°)$, $\boldsymbol{k}_0 = \left(24\, m^{-1}, 50°\right)$.

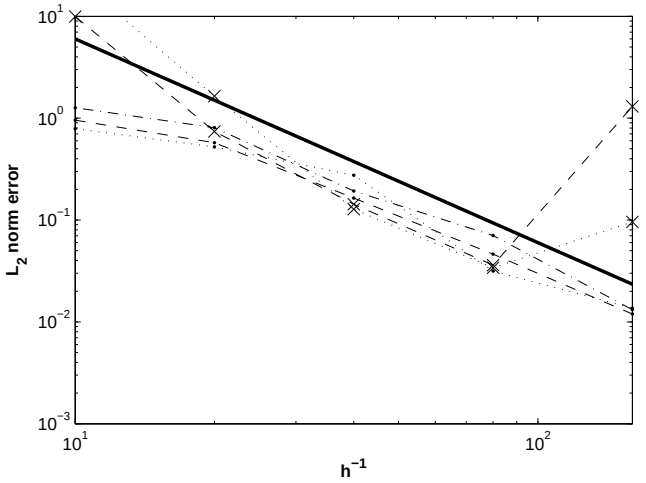

b) $\boldsymbol{M} = (0.6, 30°)$, $\boldsymbol{k}_0 = \left(24\, m^{-1}, 80°\right)$.

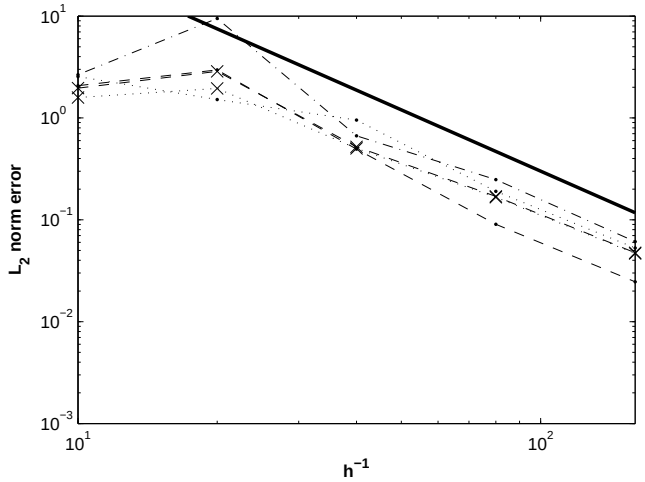

c) $\boldsymbol{M} = (0.2, 30°)$, $\boldsymbol{k}_0 = \left(24\, m^{-1}, 190°\right)$.

Figure 5.23: Numerical solution error for propagating plane wave. a) Dashed-dotted: Galerkin, Dashed: ASGS with $\theta = 50°$, Dotted: ASGS with $\theta = 0°$, Continuous line: -2 slope. b) Dashed-dotted: Galerkin, Dashed: ASGS with $\theta = 50°$, Dotted: ASGS with $\theta = 0°$, Cross-dashed: ASGS ($\boldsymbol{M} = 0$) and $\theta = 50°$, Cross-dotted: ASGS ($\boldsymbol{M} = 0$) and $\theta = 0°$, Continuous line: -2 slope. c) Dashed-dotted: Galerkin, Dashed: ASGS with $\theta = 50°$, Dotted: ASGS with $\theta = 0°$, Cross-dashed: ASGS ($\boldsymbol{M} = 0$) and $\theta = 50°$, Cross-dotted: ASGS ($\boldsymbol{M} = 0$) and $\theta = 0°$, Continuous line: -2 slope.

$(24\,m^{-1}, 190°)$. Given that this will result in a very large effective wavenumber modulus, we have reduced the speed of the uniform flow in order to achieve proper resolution using the same meshes of the previous examples. A flow with Mach number $\boldsymbol{M} = (0.2, 30°)$ has been considered. The resulting free wave has an effective wavenumber of $\boldsymbol{k}_0^{eff} = (29.7\,m^{-1}, 194°)$, and is travelling almost in the reverse direction of the mean flow, 210°. The numerical errors when using the various stabilisation and Galerkin methods are plotted in Fig. 5.23c. In this case it can be also clearly observed how the ASGS method gives a better solution than the Galerkin one, once the necessary resolution threshold has been surpassed. It can also be seen that the ASGS method taking $\theta = 0°$, and the ASGS without considering convection for $\theta = 0°, 190°$ improve now the Galerkin solution.

On the other hand, note the disparity of errors for fixed h in Figs. 5.23a, Figs. 5.23b and Figs. 5.23c ($M = 0.2$ for the latter) in accordance with the highly anisotropic error values found in [84], when analysing the error dependence on the flow and wave orientations. In this line, note that the improvement of the solution when using stabilisation in the analysed cases, strongly depend on the relative direction of the wave with respect to the mean flow. Better relative results have been obtained when comparing with the Galerkin solution for waves propagating close or reversal to the flow direction, than for waves propagating normal to it.

5.6.3 Aeolian tones for the convected Helmholtz equation

As a third numerical example, we will apply the methodology presented in the previous sections to compute the aeroacoustic field generated by flow past a two dimensional circular cylinder. The problem of aeolian tone generation by flow past a cylinder was already addressed in section 3.6.1, see also section 4.3.1. However, use will be made here of both, the Helmholtz and convected Helmholtz equations for comparison, and a higher Reynolds number than in 3.6.1 will be considered (Re = 1000). The main purpose of this example will be to check the performance of the stabilised formulation in a somehow more intricate problem than the usual benchmark tests. We will check if the stabilisation formulation derived in section 5.5 is able to yield good results for this case, which contains waves propagating in several directions that have been computed in an unstructured mesh of linear triangular elements (again a different mesh than the one used to optimise τ_{SGS} for a single propagation direction).

The physical problem: Aeolian tones

We remind that the physical problem is that of computing the noise generated by flow past a two-dimensional cylinder when a von Kármán vortex street of alternating vortices is established behind it (see section 3.6.1). The cylinder has a diameter D and the free stream velocity impinging on it is $\boldsymbol{U}_0 = (U_0, 0)$. The problem Mach number is given by $\boldsymbol{M} = (M, 0) = (U_0/c_0, 0)$ and the Reynolds number based on these variables is $\mathrm{Re} = \rho_0 \mathrm{U}_0 \mathrm{D}/\mu$.

As already explained, aeolian tones correspond to sound generated by the cylinder as

a reaction to lift fluctuations. The frequency of the emitted noise, f_{vsh}, is that of vortex shedding and it can be computed from (3.66) and (3.67). The radiated noise exhibits a clear dipole pattern.

In order to compute the aeroacoustic source term we have followed the three steps approach described in section 3.2 and plenty developed, from a computational point of view, throughout Chapter 3. Two cases have been considered: the first one corresponds to the straightforward application of Lighthill's acoustic analogy. This has given the acoustic field as seen by an observer that is at rest with the cylinder and feels the uniform inflow impinging on it at speed $(U_0, 0)$. Actually, we have been interested in knowing the acoustic field spatial distribution at the vortex shedding frequency, which is given by the time Fourier transform of Lighthill's equation (see Chapters 2, 3)

$$-\left(\nabla^2 + k_0^2\right)\hat{p} = \hat{s}_L \quad \text{in } \Omega_{ac} \tag{5.158}$$

$$\nabla\hat{p}\cdot\boldsymbol{n} = 0 \quad \text{on } \Gamma_{cyl} \tag{5.159}$$

$$\nabla\hat{p}\cdot\boldsymbol{n} = ik_0\hat{p} \quad \text{on } \Gamma_{\infty}, \tag{5.160}$$

with $\hat{s}_L$ standing for the Fourier transform of $s_L = \rho_0\left(\nabla\otimes\boldsymbol{u}\right):\left(\nabla\otimes\boldsymbol{u}\right)^{\top}$, $k_0 = \omega/c_0 = 2\pi f_{vsh}/c_0$, $\Omega_{ac}\subset\mathbb{R}^2$ being a bounded domain, Γ_{cyl} the cylinder boundary and Γ_{∞} the far field boundary of Ω_{ac}.

The second case has consisted in considering the acoustic field as seen by an observer at rest with the flow that sees the cylinder approaching at speed $(-U_0, 0)$. To obtain this result we can perform a full Lorentz transformation of Lighthill's equation (5.158) (note that the source term is Galilean invariant so it will be not affected by the uniform mean flow). This results in the convected Helmholtz equation:

$$\left[\nabla^2 + \left(k_0 + i\boldsymbol{M}\cdot\nabla\right)^2\right]\hat{p} = \hat{s}_L \quad \text{in } \Omega_{ac} \tag{5.161}$$

$$\nabla\hat{p}\cdot\boldsymbol{n} = -ik_0\alpha_N\hat{p} \quad \text{on } \Gamma_{cyl} \tag{5.162}$$

$$\nabla\hat{p}\cdot\boldsymbol{n} = ik_0\alpha_S\hat{p} \quad \text{on } \Gamma_{\infty}. \tag{5.163}$$

Notice that the low Mach number limitation for this example does not arise from the convected wave equation, which is valid up to transonic flows, but from the use of the Reynolds tensor as an approximation for Lighthill's tensor, which is only valid for incompressible flows ($M < 0.3$). Note also that the convected Helmholtz equation (5.161)-(5.163) only applies to uniform flows, which is not the case for the vortex street past the cylinder. However, Lighthill's acoustic analogy establishes a clear separation between the acoustic source zone, where acoustic waves are generated (in this case the boundary of the cylinder and the periodic vortices past it) and the propagation zone (acoustic media) where acoustic waves are radiated and propagate (in this case the remaining of the domain). Hence one can imagine the problem as that of a set of acoustic sources placed near the cylinder (with independence of the fact that they have been obtained from a CFD computation of a non-uniform flow) radiating into an acoustic media that may be at rest or moving e.g., at uniform speed. The convected Helmholtz equation can be applied to this acoustic media.

Numerical results

For the numerical example we have considered a circular cylinder of diameter $D = 0.3$ in a circular computational domain Ω_{CFD} of diameter $3 \times 10^3 D$. We have taken a dynamic viscosity coefficient of $\mu = 0.006$ and an impinging flow velocity in Cartesian coordinates of $\boldsymbol{U}_0 = (20, 0)$, leading to Reynolds and Mach numbers at the far field (away from the cylinder) of $\mathrm{Re} = 10^3$ and $\boldsymbol{M} = (5.83 \times 10^{-2}, 0)$, for a sound speed of $c_0 = 343$ (all units are in SI). The incompressible Navier-Stokes problem has been solved in an unstructured mesh of triangular elements ranging in size from $\sim 3 \times 10^{-3} D$ near the cylinder surface to $\sim 30D$ at the far field.

In what concerns the acoustic field, computations have been performed in the same domain used for the CFD computation, i.e., $\Omega_{ac} = \Omega_{CFD}$. As there is no analytical solution for this problem, the Galerkin finite element method has been first used to solve equations (5.158)-(5.160) and (5.161)-(5.163) in a very fine mesh that has a high resolution at the far field. It has been checked that the obtained results show no appreciable differences with the results obtained using the SGS stabilisation in the same mesh. The solution corresponding to this fine mesh will be termed hereafter as reference solution for the simplicity of notation and used to assess the performance of the method in the line of what is done in [121]. In order to verify the performance of the implemented ASGS stabilisation for the convected Helmholtz equation, problem (5.161)-(5.163) has been also solved in a rather coarse mesh that has a resolution of $7 - 8$ nodes per wavelength at the far field. The Galerkin finite element method and the ASGS stabilised finite element method have been used to solve (5.161)-(5.163) in the coarse mesh and their solutions have been compared with the reference solution to see which one performs better.

Let us first have a look at the results from the CFD computation. A periodic flow is established with vortex shedding at a frequency of $f_{vsh} = 15.3\ Hz$ ($S_t = 0.229$). This can be appreciated in Fig. 5.24a and Fig. 5.24b, where the temporal evolution and normalised spectrum of the lift coefficient are plotted. The lift coefficient has a mean amplitude of ~ 1.36. The computed frequency and Strouhal number are slightly higher than the ones obtained from (3.66)-(3.67), $f_{vsh} = 13\ Hz$ ($S_t = 0.194$). This is in part due to the fact that (3.66)-(3.67) are valid for three dimensional cylinders, while we are performing two dimensional simulations. The three dimensional effects begin to be significant for $\mathrm{Re} > 300$ and, as already mentioned in Chapter 3, two dimensional simulations tend to over predict the values for f_{vsh} and S_t (see [229] and references therein).

In Fig. 5.25a we have plotted a snapshot of the isovelocity contourlines at a given instant of time showing the von Kármán vortex street. In Fig. 5.25b we present the contourlines corresponding to the acoustic source term $\rho_0 (\nabla \otimes \boldsymbol{u}) : (\nabla \otimes \boldsymbol{u})^{\top}$ used as an approximation for Lighthill's tensor. It can be observed that the source term rapidly decreases to zero when moving away from the cylinder surroundings. As explained in section 3.6.1, the fast decay of the source term is of crucial importance and in fact justifies the acoustic analogy approaches. Otherwise, it would not be possible to distinguish between a source region and a propagating one (see e.g., [53, 55]).

In what concerns the acoustic results, the imaginary part of the reference acoustic

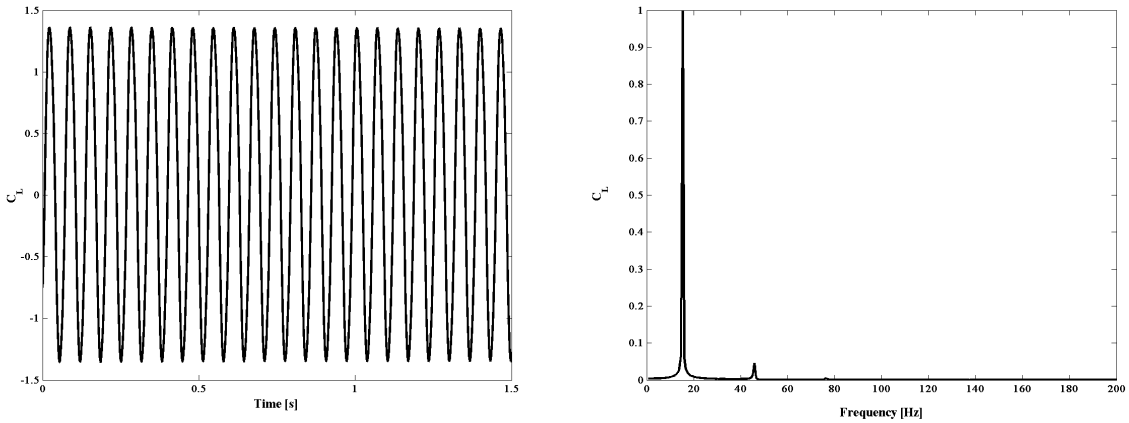

a) C_L time evolution. b) C_L normalised spectrum.

Figure 5.24: Temporal evolution and spectrum of the cylinder lift coefficient, C_L.

pressure for the convected Helmholtz equation (5.161)-(5.163) in the near field is shown in Fig. 5.26. It can be clearly observed that although there is sound generated at the wake of the cylinder, only sound having a dipole pattern and generated by lift fluctuations on the cylinder propagates outwards, to the far field. In Fig. 5.27a, where the reference far field solution is plotted, this becomes fully evident. In Fig. 5.27b we have presented the results corresponding to the reference solution of the Helmholtz equation (5.158)-(5.160). By comparison with Fig. 5.27a, we can observe as expected that the observer being at rest with the flow sees the wave fronts bended upstream. This effect is not very strong for this example because the Mach number is not very high, but it is clearly visible e.g., near the boundaries of the domain. While the solution in Fig. 5.27b is totally symmetric this is not the case for the solution in Fig. 5.27a.

In Fig. 5.28a and Fig. 5.28b we have respectively plotted the Galerkin solution and SGS solution corresponding to the coarse mesh case. It can be observed that the Galerkin solution presents pollution error, which manifests as a phase lag in the wave fronts of Fig. 5.28a when compared with those of the reference solution in Fig. 5.27a. This phase error is considerably reduced when using the SGS stabilisation, see Fig. 5.28b. The situation becomes more apparent in Fig. 5.29a where the results for a one dimensional cut of the domain $\Omega_{ac}|_{\theta=90^\circ} = \{(r, 90^\circ)\,|D/2 < r < 1.5 \times 10^3\}$ are given. It can be seen that the ASGS stabilised solution has almost the same phase as the reference one, while the Galerkin solution clearly presents a phase lag. In Fig. 5.29b, we give the results for another one dimensional cut, $\Omega_{ac}|_{\theta=135^\circ} = \{(r, 135^\circ)\,|D/2 < r < 1.5 \times 10^3\}$, which is near the limits of the silent cone in front of the cylinder. In this case the ASGS stabilisation is not able to fully match the reference solution although it improves the results from the Galerkin one. From Fig. 5.28 and Fig. 5.29 we can then conclude that the ASGS stabilisation yields a solution clearly better than the Galerkin one.

The results for the ASGS solution in this section have been obtained using an angle

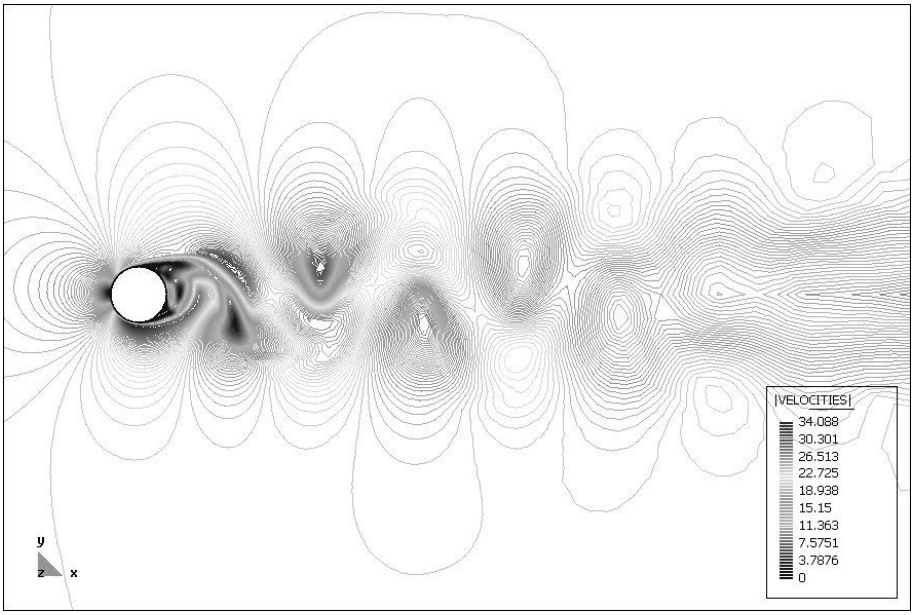

a) Isovelocity contourlines showing von Kármán vortex street.

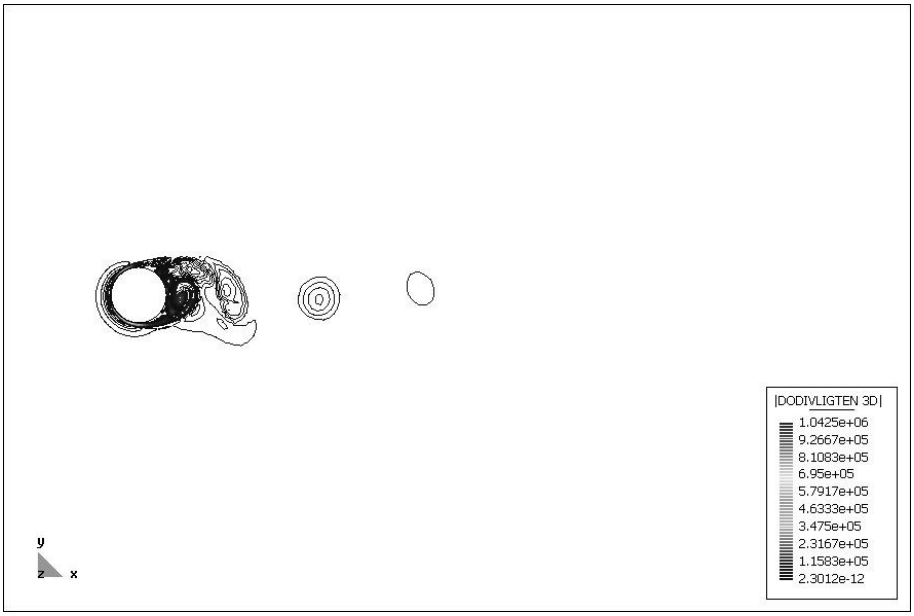

b) Snapshot of the acoustic source term (Lighthill's tensor double divergence).

Figure 5.25: CFD results.

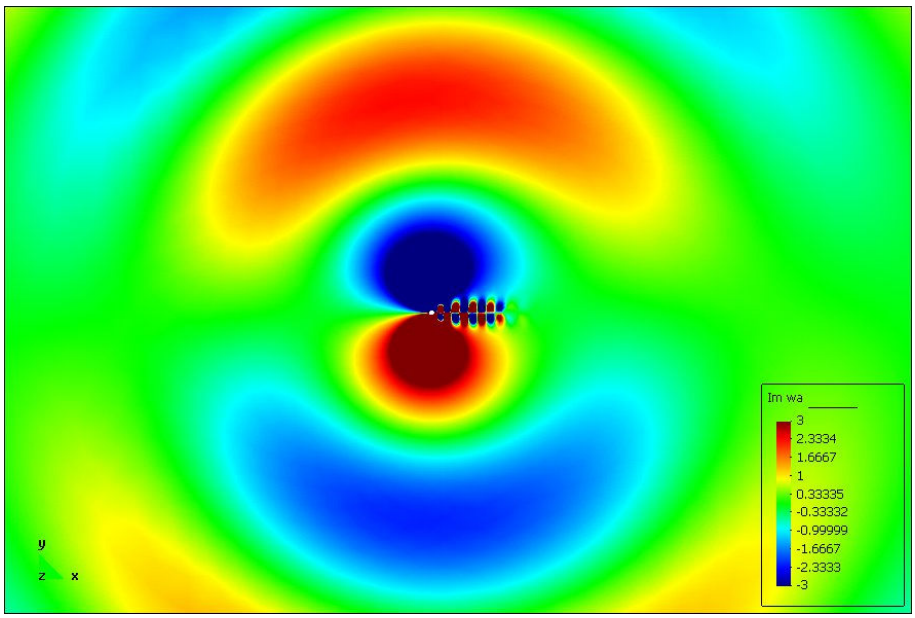

Figure 5.26: Near field results for the imaginary part of the convected reference acoustic pressure.

of $\theta = 0°$ in the effective wavenumber components (5.142)-(5.143), to be inserted in the expression (5.126) for the stabilisation parameter, τ_{SGS}.

5.7 Conclusions

In this chapter we have presented a general framework where to relate the wave and convected wave equations, as well as their Fourier transform counterparts. The latter correspond to specific cases of the more general CDR system of equations. Specific boundary conditions for the convected Helmholtz equation have been also derived. We have then introduced the Galerkin FEM approach to solve these equations and reviewed the information available from well-posedness theorems. The pattern of convergence of the Galerkin FEM solution has been analysed and the characteristic problem of the so called pollution error for Helmholtz equations has been presented.

To avoid the pollution error, an algebraic subgrid scale finite element method to solve the two dimensional convected Helmholtz equation has been proposed. The method does in fact correspond to the application of the Galerkin / Least Squares approach with appropriate redefinition of its stabilisation parameter, because the involved convected Helmholtz differential operator is selfadjoint. The stabilisation parameter has been derived from a dispersion analysis and it reduces to well known expressions for the one dimensional and two dimensional Helmholtz equations in the case of no convection.

As an application, we have considered the case of a plane wave propagating in a uniform flow. It has been shown that the proposed subgrid scale stabilised method

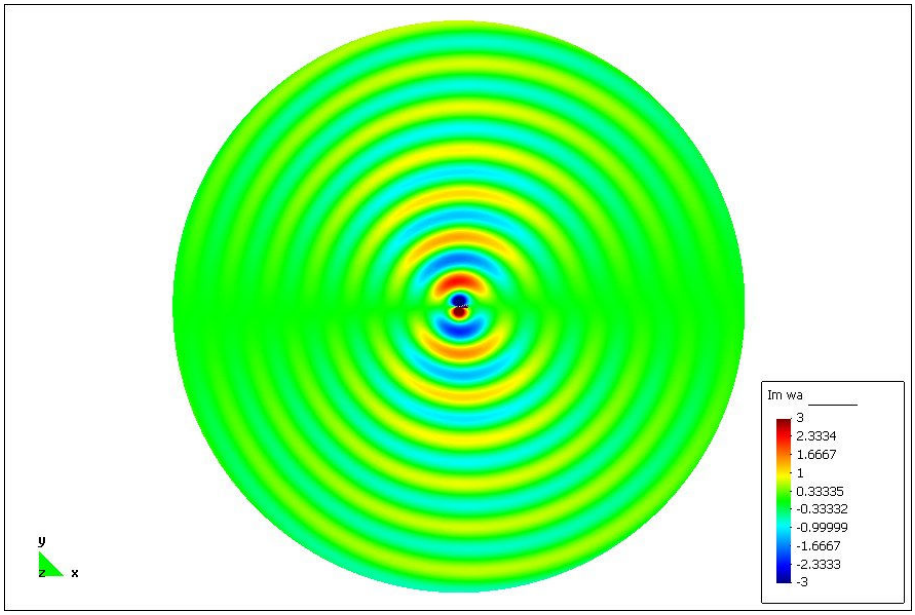

a) Reference convected Helmholtz

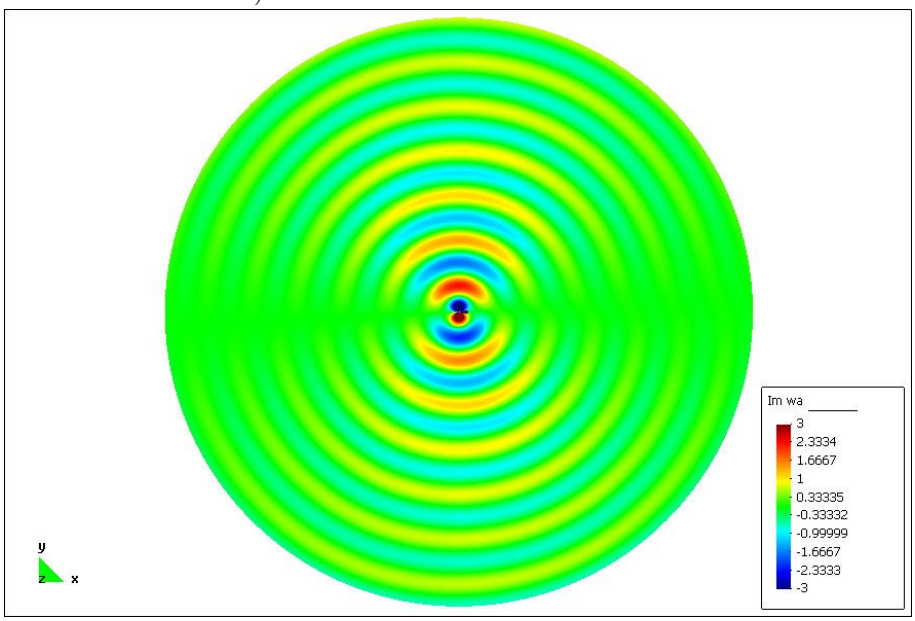

b) Reference Helmholtz

Figure 5.27: Far field results for the imaginary part of the acoustic pressure.

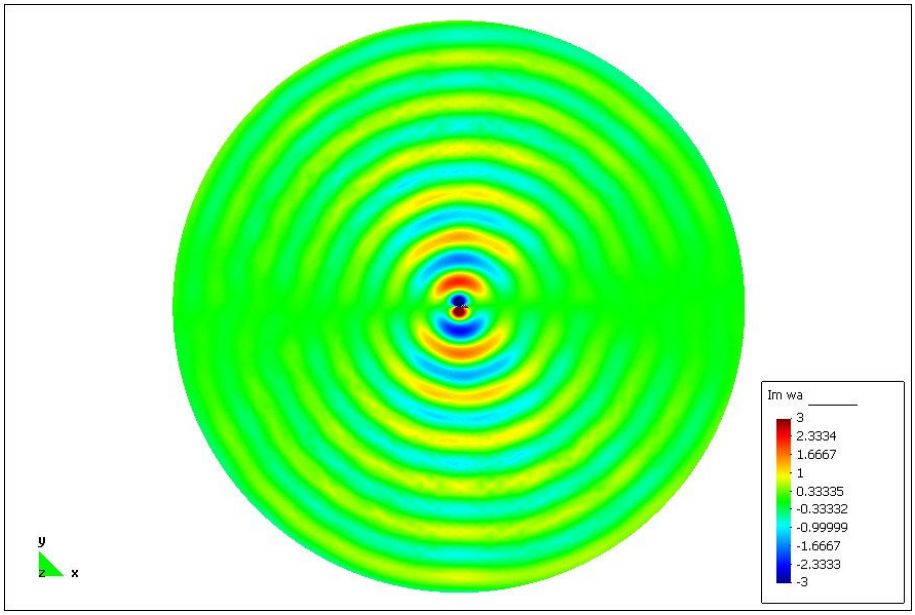

a) Galerkin convected Helmholtz

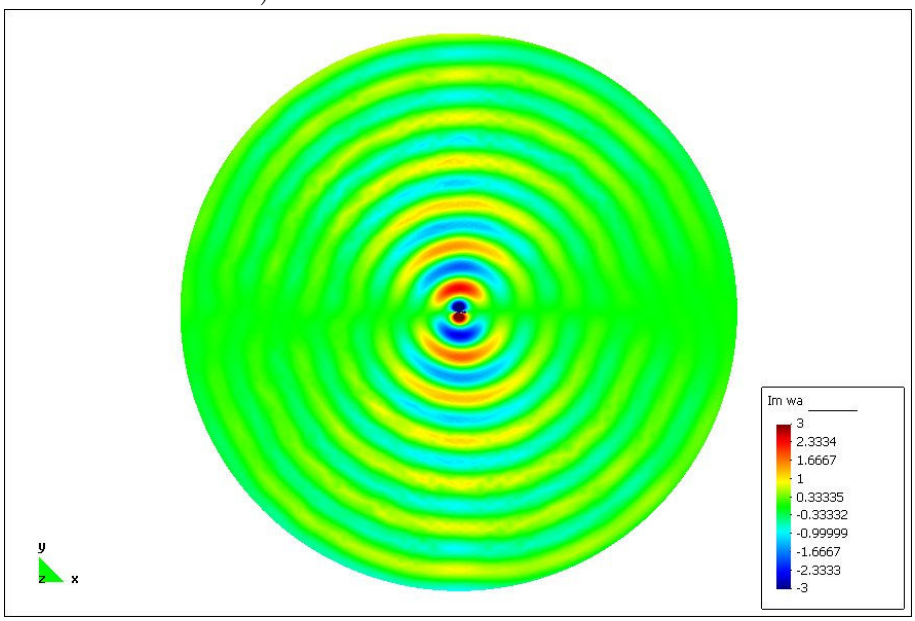

b) SGS convected Helmholtz

Figure 5.28: Far field results for the imaginary part of the acoustic pressure.

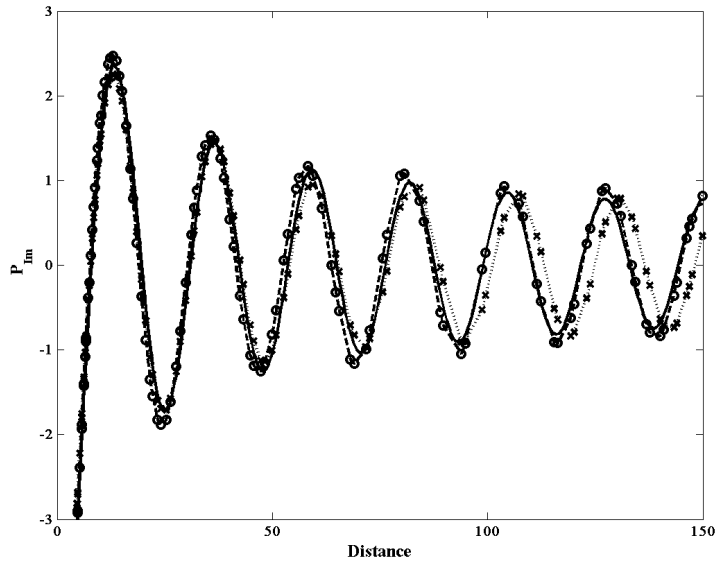

a) Imaginary part of the reference, Galerkin and SGS solutions
for a one dimensional cut of the domain at 90° with respect to the x-axis.
Continuous line: reference solution, Dashed with circles: ASGS, Dotted cross: Galerkin.

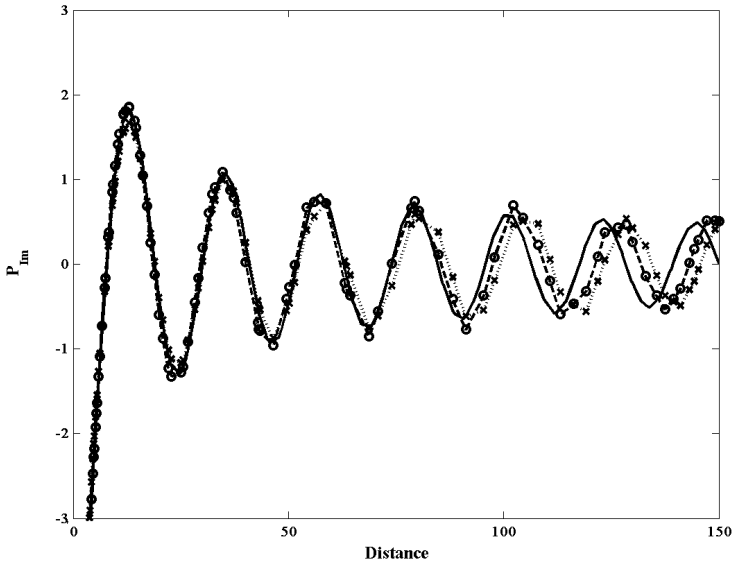

b) Imaginary part of the reference, Galerkin and SGS solutions
for a one dimensional cut of the domain at 135° with respect to the x-axis.
Continuous line: reference solution, Dashed with circles: ASGS, Dotted cross: Galerkin.

Figure 5.29: Imaginary part of the solutions for one dimensional cuts.

yields exact nodal solutions, while the Galerkin method is unable to give a valid solution. Improvements have been also obtained for nonstructured meshes different to the one used to derive the stabilisation parameter. A more involved case consisting of the aerodynamic sound generated by flow past a two dimensional cylinder has been also considered. We have limited to low speed cases and made use of Lighthill's acoustic analogy. Although a non structured mesh of triangular elements has been used for this problem, it has been shown that using the subgrid scale stabilisation to find the solution of the convected Helmholtz equation clearly improves the results that otherwise would have been obtained using the Galerkin finite element method.

As a general conclusion we may say, on one hand, that the herein presented ASGS stabilised method could prove very useful for problems where we have a certain degree of a priori information on the wave propagation directions. This would be the case, for instance, of duct acoustics (note that in this case two optimum stabilisation parameters respectively accounting for upstream and downstream waves could be easily implemented). On the other hand, we have also checked that the method could also be useful in much more intricate problems such as the generation of aeolian tones described above.

Chapter 6

Applied example

In this chapter we explore the possibility of applying some of the strategies and methods previously presented to problems of industrial interest. In particular, we concentrate on the simulation of the airflow over the leading coach of a high-speed train. CFD is usually employed in railway aerodynamics to derive mean values such as overall lift and drag coefficients, or the torque experienced by the train. It is also used to determine the influence of cross-winds or the wave front forming at a tunnel entrance. However, we will concentrate here on the very different subject of using CFD to make predictions of outward radiated aerodynamic noise. Similar strategies can be also applied to determine the train's interior noise due to surface pressure fluctuations. Computational limitations will restrict our results to very low frequencies, out of the whole range of acoustic industrial interest. However, the proposed methodology is still valid and suitable for implementation in supercomputing devices to reach the desired frequency range.

6.1 Introduction

Apart from aeronautics where it experienced its major development, the field of aeroacoustics and CAA has recently become of great importance in the railway industry. With the development of high-speed trains, the aerodynamic sound has become the origin of several problems (see e.g., [86, 182, 184, 269, 281]), which might be roughly divided into three categories. The first concerns an important, although quite specific, problem. This is the generation of a compression wave when a high-speed train enters a tunnel. The wave propagates into the tunnel and if it is long enough, non-linear steeping causes the generation of a micro-pressure wave at the tunnel exit. Its effects can be as noticeable as the sonic boom generated by supersonic airplanes. For obvious reasons, this problem has recently deserved great attention [139, 140, 143].

The second and widest problem concerns the train's radiated exterior noise (see e.g., [179–183]). For high-speed trains, the noise generated from the airflow impinging on the pantograph zone, the bogie zone or the inter-coaches zone (see [117, 132, 181, 184, 259]), can exceed by far classical noise sources such as wheel-rail interaction noise, engine noise, or auxiliary equipment noise. The understanding of the implied physical phenomena as

well as the localisation of the various source terms has allowed to design e.g., more silent pantographs [165,166]. Recently, some attempts have been performed in order to compute the aerodynamic noise generated by some of the above cited items [131,267]. On the other hand, for magnetic levitation trains (maglevs) that can circulate at speeds $U_0 \geq 500$ km/h further aerodynamic noise sources may be of importance, such as the noise generated by the turbulent boundary layer (TBL) [181, 237].

The third problem concerns the aerodynamic sound contribution to the train's overall interior noise level. Although some rough models have been proposed that take into account the TBL unsteady pressure loading, flow detachment and coherent structures in order to perform initial predictions [205], it is clear that further research involving airflow CFD simulations combined with the mechanical response of the train's structural response is necessary.

In Fig. 6.1a we show a simplified scheme of a train's general exterior noise prediction process. The first column concerns the modelling of the noise sources. For low-mid speed trains (say trains circulating with velocity $U_0 \leq 250$ km/h) the main noise sources correspond to the wheel-rail interaction (*rolling noise*), the engine noise and the auxiliary equipment noise. In what refers to pass by noise, rolling noise is generally predominant with the engine contribution depending on the train's speed and on the type of train (diesel or electrical). Exterior noise due to auxiliary equipment is usually of importance for the train stopped in a station. In the case of mid-high speed trains and as mentioned above, the interactions of the airflow with several appendices such as the pantograph or the bogie's area may be the cause of intense aerodynamic noise radiation. The speed at which the aerodynamic noise contribution increases the pass-by sound pressure level by 1 dB is known as the *acoustical impact speed*, U_i, whereas the velocity at which aerodynamic noise equals the contribution from all other sources (essentially rolling noise) is known as the *acoustical transition speed*, U_t. For a 12-coach ICE (German high-speed train) $U_i \approx 220$ km/h, while $U_t \approx 320$ km/h [182].

In order to be able to predict railway exterior noise, one has to model all noise sources in the first column of Fig. 6.1a, with the aim of finding acoustic power values for them. Given the large disparity of these sources, a very wide range of techniques and theories is needed to do so, involving several areas of vibroacoustics. Moreover, different theoretical and experimental approaches are required depending on the analysed frequency range. Even when focusing on aerodynamic noise sources, the physics of the underlying phenomena can strongly vary. For instance, the celebrated Lighthill acoustic analogy turns not to be valid for the simulation of cavity noise (e.g., generated at an airtake inlet), given that there is a feedback interaction between the aerodynamic and acoustic fields in this case. Consequently, it can be already intuited that a complete review of railway noise source mechanisms is certainly out of the scope of this work and we will limit ourselves to problems that can be addressed in the general framework depicted in Fig. 3.1, section 3.2 in Chapter 3.

On the other hand, the second step in the prediction of exterior noise involves the modelling of the noise radiation. Again several techniques and methods are combined to do so, depending on the type of source and desired frequency range. Wave as well

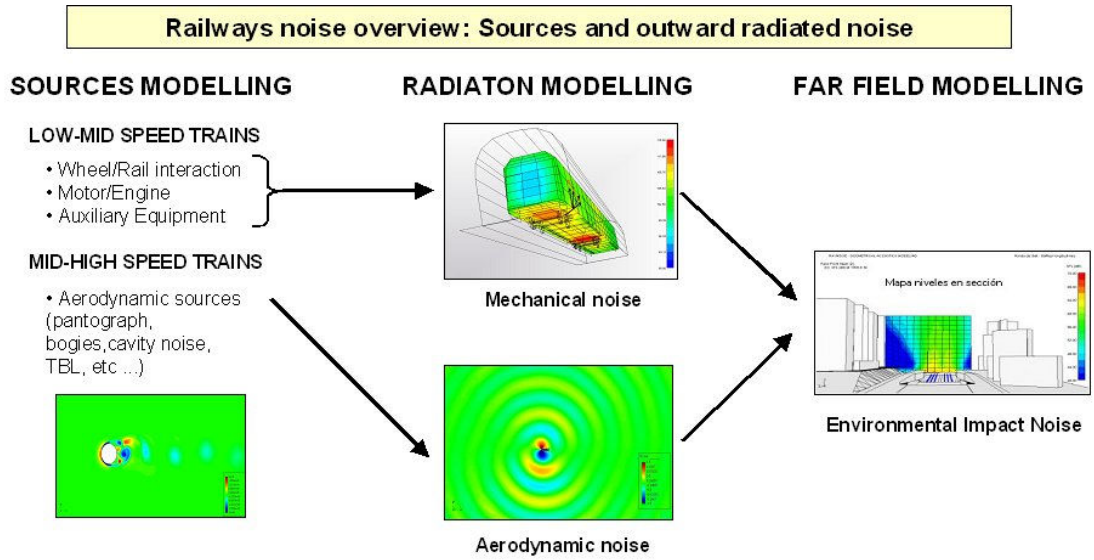

a) Outward radiated noise

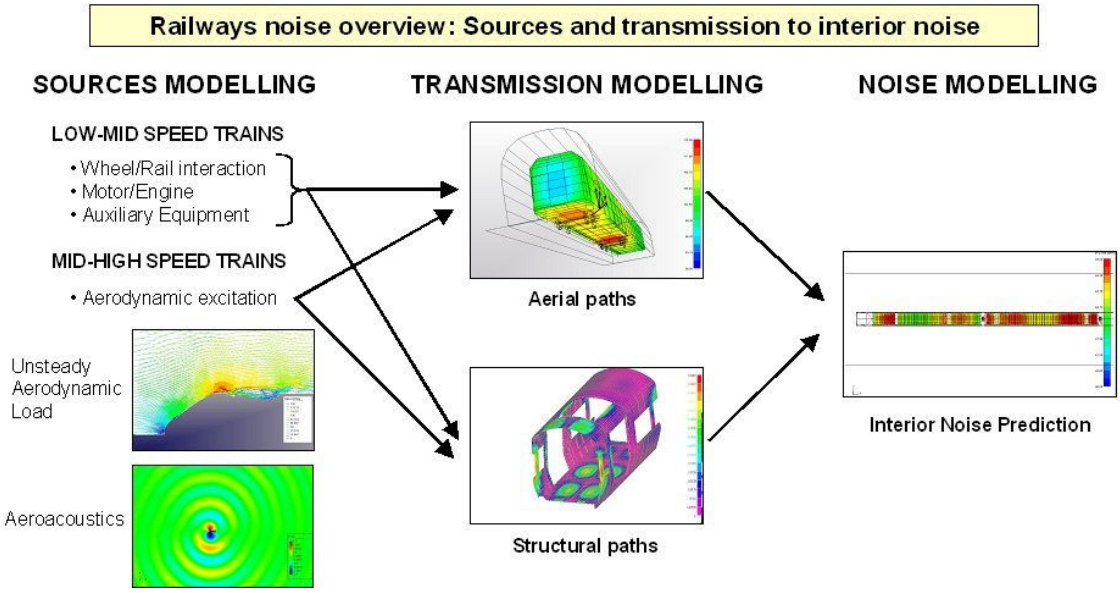

b) Interior noise

Figure 6.1: Railways noise overview

as ray methods are commonly used. When one is interested in how railway noise would affect inhabited areas, it becomes necessary to simulate the whole environment taking into account topography and building effects (third column in Fig. 6.1a).

In what concerns train's interior noise prediction, a scheme analogous to Fig. 6.1a is shown in Fig. 6.1b. In addition to the classical mechanical sources of low-mid speed trains that affect interior noise, we observe that aerodynamic sources have to be taken also into account. Concerning the latter, different aspects have to be considered. One one hand flow separation at the first coach leading end, and at the bogie's area, may cause strong unsteady pressure loading. This will induce mechanical vibrations on the train surface, which will be transmitted through the structure and finally result in the generation of interior noise. On the other hand, the intense pressure fluctuations developed beneath the turbulent boundary layer (TBL), known as *blocked pressure*, will be also a source of structural vibrations that will generate interior noise.

Flow separation strongly depends on the geometry of the body immersed in the airflow stream, so general models accounting for their effects on the train's surface cannot be built without very restrictive and simplifying hypothesis. Therefore, CFD turns to be a good option to face this type of problems. On the contrary and under certain considerations, TBLs share a universal character so that several semi-empirical models exist for them. These models give expressions for the *wall-presure wavenumber-frequency spectrum*, $P(\boldsymbol{k}, \omega)$, which is commonly used to characterize the blocked pressure. For an introduction to the subject one may consult [137, 145]. A comparison of the most outstanding models for $P(\boldsymbol{k}, \omega)$ can be found in [103], see also [24], and references therein. On the other hand, it is worthwhile to mention that the TBL will be also a source of aerodynamic noise. In what respects to exterior noise its contribution is of little importance (with the possible exception of maglevs). In what concerns the pressure loading, the TBL aerodynamic noise has again negligible influence, given that the TBL blocked pressure is mainly due to the turbulence interaction with the mean shear flow and to the turbulent eddies interaction. However, other aerodynamic noise sources may affect interior noise. For instance, the acoustic waves generated by the flow impinging on the pantograph may induce structural vibrations that will be a source of interior noise (note that pantographs are generally placed at the end of the leading coach in high-speed trains to avoid its direct exposition to the free stream velocity).

The second column in Fig. 6.1b concerns the simulation of the transmission paths from the sources to the train's interior. Transmission paths may be either aerial (e.g. engine noise radiate acoustic waves outwards, which impinge on the train walls and windows -*parietal noise*- causing them to vibrate and to radiate interior noise) or structural (e.g., engine vibrations are transmitted to the coach through the connection dampers and as a result the coach subsystems also vibrate and radiate interior noise). Again the number of experimental, numerical and analytical methods used to address the transmission process is very wide and out of our scope. Finally, in the third column we see how the information of the preceding columns can be combined to build an acoustic model of the train. The various interior noise contributions can be combined to determine the overall sound pressure value and to establish the ranking of influence of every noise source

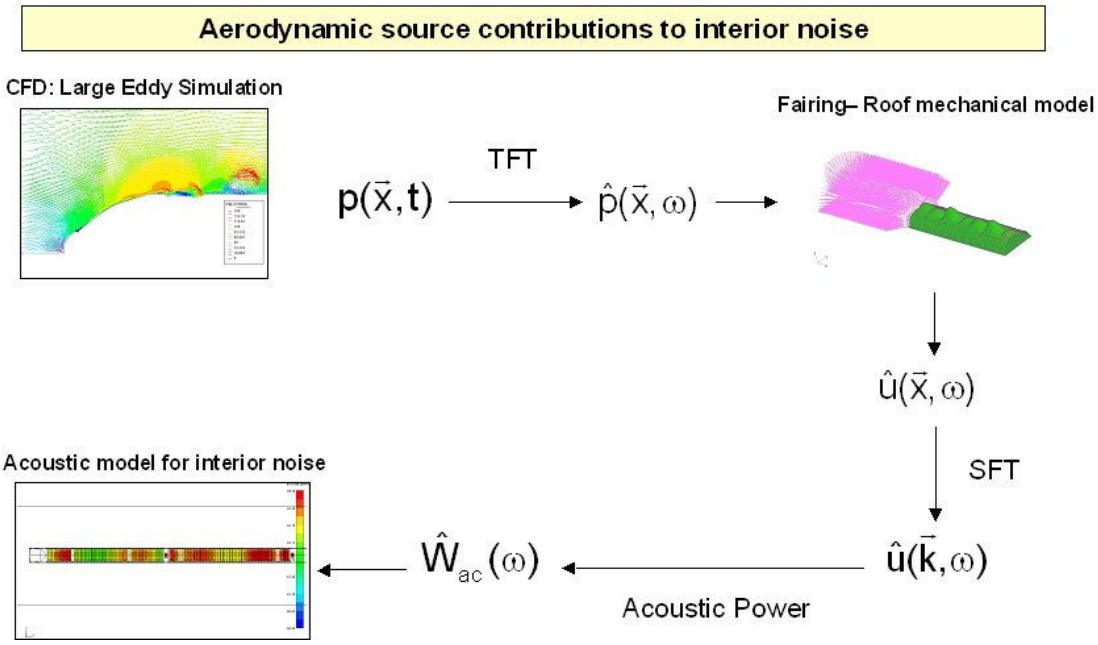

Figure 6.2: Scheme for the prediction of aerodynamic source contributions to train's interior noise

at each frequency.

As mentioned above, in this chapter we will focus on a case of Fig. 6.1a that can be embedded in the CAA framework proposed in this thesis (see Fig. 3.1). In particular we will address the problem of aerodynamic noise generation by flow separation at the leading end of the first coach of a high speed train. We note that this problem is of no practical importance when compared with exterior noise radiated by other sources, such as sound generated by the pantograph or the bogie area. However, it is of great importance for train manufacturers given that it may affect interior noise. In this sense, observe that a scheme analogous to the one in Fig. 3.1 can be used to predict the influence of aerodynamic sources on interior noise. This scheme is presented in Fig. 6.2. The first step of the procedure consists of a CFD simulation but now the unsteady pressure $p(\boldsymbol{x}, t)$ at the roof fairing is the desired result, instead of the double divergence of the velocity Reynolds tensor. $p(\boldsymbol{x}, t)$ can be next time Fourier transformed to $\hat{p}(\boldsymbol{x}, \omega)$ and inserted as an external input in a numerical model for the mechanical behaviour of the fairing (note that we are neglecting fluid-structure interaction). This model will allow to compute the inner roof vibration characterised by its velocity $\hat{u}(\boldsymbol{x}, \omega)$. The latter can be then spatial Fourier transformed to $\hat{u}(\boldsymbol{k}, \omega)$, from which an acoustic power for the roof can be derived. Finally, the inner roof acoustic power can be inserted in an acoustic model for the train to determine the contribution of flow separation to interior noise. It should be noted that alternatives to the scheme in Fig. 6.2 are also possible.

Although no inner noise predictions will be performed in this chapter, we have found worthwhile to observe the conceptual similarity needed for both, the prediction of interior

and exterior noise, in the herein treated problem. Moreover, note that the most difficult step of the schemes in Fig. 3.1 and Fig. 6.2, namely the CFD simulation, is shared in both cases.

The chapter is organized as follows. In section 6.2 we concentrate on the CFD simulation of the airflow past a high speed train. In section 6.3 we present the results that would be useful for interior noise prediction, namely the unsteady pressure loading at several surface points. On the other hand, in section 6.4 we present the results corresponding to the aerodynamic noise sources due to flow separation, i.e., the double divergence of the Reynolds tensor for the velocity field. In section 6.5 we compute the outward radiated noise at some chosen frequencies and finally, conclusions are drawn in section 6.6.

6.2 CFD simulation of airflow past a high-speed train

6.2.1 Computational features

Again, the mathematical problem to be dealt with is that of solving the incompressible Navier-Stokes equations (4.1)-(4.2) in a given computational domain Ω, with boundary $\partial\Omega$, once some initial and boundary conditions have been specified. We will consider the case of a train running at $U_0 = 69.5$ m/s (≈ 250 km/h). The incompressibility constrain will be assumed because the problem Mach number is of the order of $M = 0.2$.

Simulations have been performed using an ASGS strategy (see section 3.4 and details below) and making use of a nodal based-implementation for the spatial discretisation [40]. The nodal-based implementation has the advantage to save a considerable amount of computational time because all integrals involving combinations of shape function products and their corresponding derivatives are carried out at the beginning of the computation. This requires some approximations but avoids the necessity to recompute the volume and surface integrals anymore. Concerning the temporal discretisation, the second order accurate in time Crank-Nicholson scheme has been used (see section 3.3.1).

The main computational features of the simulation are listed below:

- The train has been embedded in a $14 \times 44 \times 20$ m^3 rectangular hexahedral domain that minimizes the influence of the far field boundaries (the free stream velocity is reached inside the computational domain).
- An unstructured mesh of 1.884.524 elements (1.661.752 tetrahedral elements + 222.952 surface triangular elements) corresponding to 322.784 nodes (1.291.136 d.o.f) has been used. The mesh has been refined near the train contours.
- Equal linear interpolation functions have been used for the velocity and the pressure as allowed by the ASGS stabilised finite element approach.
- 10 linearisation Picard iterations have been used for each time step.
- A GMRES solver has been used to solve all matrix systems.

- The time increment has been $\Delta t = 0.002$ s, once the initial transient period has been surpassed. The maximum frequency that can be captured (Nyquist frequency) is ~ 250 Hz. The resulting pressure spectra to be presented below have a resolution of 1.6 Hz as they have been calculated by means of the Fourier transform of a 300 steps interval (0.6 s) once the initial transients have finished. In order to exceed the initial transients, an initial simulation of 400 time steps with $\Delta\ t' = 10\Delta t$ has been carried out. In turn, this simulation has been started from a previous Stokes calculation.

- In order to surpass the initial transients some extra dissipation to that provided by the stabilisation terms has been needed. The Smagorinsky model with a constant $C_S^2 = 0.015$ has been used to do so. Once the initial transients have finished this value has proven to be too high to capture the flow fluctuations. Numerical experiments have been carried out in order to see the effects of decreasing the Smagorinsky constant value. It has been found that for C_S^2/n with $n \geq 5$, the magnitude of the fluctuations does not change substantially. That is, the dissipation provided by the ASGS stabilisation terms is the one governing the flow motion.

6.2.2 Computational domain and boundary conditions

The computational domain is shown in Fig. 6.3. Some general and detailed views are shown as well as all boundaries. The intermediate volumes between the external rectangular parallelepiped and the train surface are needed for an appropriate mesh transition size.

The Dirichlet boundary is built from $\Gamma_D = \overline{\Gamma_i^a \cup \Gamma^t}$ while the mixed boundary is given by $\Gamma_M = \overline{\Gamma_u^a \cup \Gamma_d^a \cup \Gamma_o^a \cup \Gamma_{lat1}^a \cup \Gamma_{lat2}^a}$. The corresponding boundary conditions are given by:

Dirichlet boundary Γ_D:

$$\boldsymbol{u}_D = (u_x, u_y, u_z)^\top = \left\{ \begin{array}{l} (69.5, 0, 0)^\top \text{ m/s on } \Gamma_{\mathrm{i}}^{\mathrm{a}} \\ (0, 0, 0)^\top \text{ m/s on } \Gamma^{\mathrm{t}} \end{array} \right. \tag{6.1}$$

Mixed boundary Γ_M:

$$\left. \begin{array}{l} t_x, t_y = 0 \\ u_z = 0 \end{array} \right\} \text{ on } \Gamma_{\mathrm{u}}^{\mathrm{a}}, \Gamma_{\mathrm{d}}^{\mathrm{a}} \qquad \left. \begin{array}{l} t_x, t_z = 0 \\ u_y = 0 \end{array} \right\} \text{ on } \Gamma_{\mathrm{lat1}}^{\mathrm{a}}, \Gamma_{\mathrm{lat2}}^{\mathrm{a}} \tag{6.2}$$

$$\boldsymbol{t}_M = (t_x, t_y, t_z)^\top = (0, 0, 0)^\top \text{ on } \Gamma_{\mathrm{o}}^{\mathrm{a}} \tag{6.3}$$

In Fig. 6.4 some mesh details are shown. As already mentioned, the mesh has been refined at the train surface where the flow is expected to present a more complex pattern.

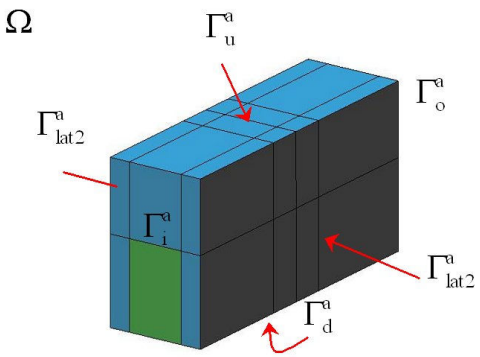

a) Exterior boundaries

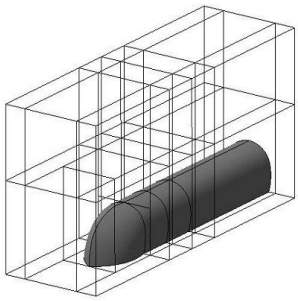

b) Inner domain

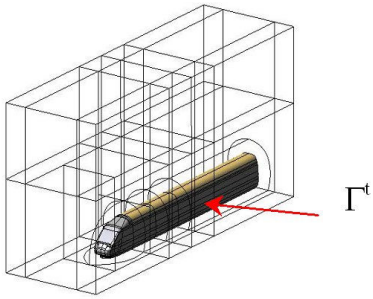

c) Train boundary

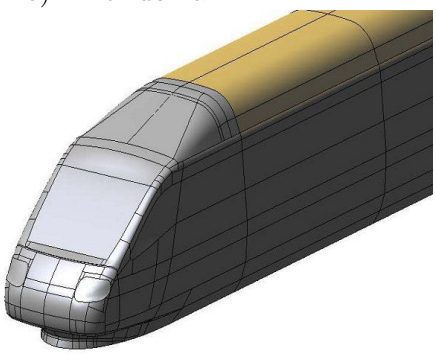

d) Leading coach profile

Figure 6.3: Train computational domain. General and detailed views.

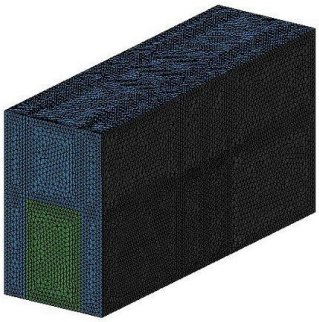

a) Exterior boundaries

b) Train surface

Figure 6.4: Train mesh: General and detailed views.

6.2.3 Pressure and velocity fields

In this section the pressure and velocity fields for the train running at maximum speed ($U_0 = 69.5$ m/s) will be presented. The results correspond to an arbitrary chosen snapshot at $t = 13$ s, once the initial transient period has been surpassed.

In Fig. 6.5 several isovelocities and pressure plots are shown. Figures Fig. 6.5a and b correspond to the vertical plane $y = -1$ m, while figures Fig. 6.5c, d and Fig. 6.5e, f respectively correspond to the vertical planes $y = 0, +1$ m. $y = 0$ corresponds to the train centreline. The pressure plots show, as expected, a maximum value at the train nose, see Fig. 6.5c, corresponding to a minimum velocity value, see Fig. 6.5d. From that point, the velocity increases following the train profile and reaches its highest value when the train's full section is achieved at the leading end. Then flow separation takes place due to the presence of an adverse pressure gradient. The isovelocity plots clearly show that the complex pattern of generated vortices, which are responsible of the intense unsteady pressure loading on the train's surface. This unsteady flow field may induce undesirable fairing and roof vibrations at low frequencies.

On the other hand, note that the pressure at the nose sides (Fig. 6.5a and Fig. 6.5e) is smaller than that of Fig. 6.5b because the flow can escape laterally increasing its speed (Fig. 6.5b and Fig. 6.5f).

It should be remarked that the herein presented simulation is not able to properly capture the velocity gradient inside the boundary layer (see Fig. 6.5 and [269] for standard values on the high-speed trains TBL thickness). Actually, a much finer mesh would be needed to do so. However, this is not a big problem given that our aim is to find the unsteady pressure distribution on the train surface, as well as the aerodynamic noise generated by the large vortices due to flow separation. We remind that there is no boundary layer for the pressure and that the wall equations clearly state that the pressure does not depend at all on the velocity distribution beneath the TBL (see e.g. [255]). In any case, what is guaranteed is that the energetic effects of the non-resolved scales on the resolved ones will be taken into account thanks to the SGS strategy used in the simulation. On the other hand, note that some standard approaches used in aeronautics in order to solve the boundary layer, such as the Euler-Boundary layer interaction, cannot be applied here because flow detachment takes place.

Fig. 6.6 presents the same results as Fig. 6.5 but for the case of three horizontal plane cuts. The heights of these cuts are $z = 2.6,\ 3,\ 3.3$ m, $z = 0$ corresponding to ground. It can be observed that lateral vortices are also formed and that its strength increases at the train fairing.

In Fig. 6.7 we present the pressure distribution at the leading coach for $t = 13$ s. As mentioned and expected, the maximum pressure is exerted at the nose of the train where the velocity is minimum. Then, the pressure decreases until the windshield is reached and a second pressure maximum appears due to a change in the train's slope profile. The pressure diminishes again and it does so very strongly at the upper part of the train leading end. However, in the next few meters of the fairing the pressure grows suddenly giving place to the strong adverse pressure gradient responsible for flow separation. The

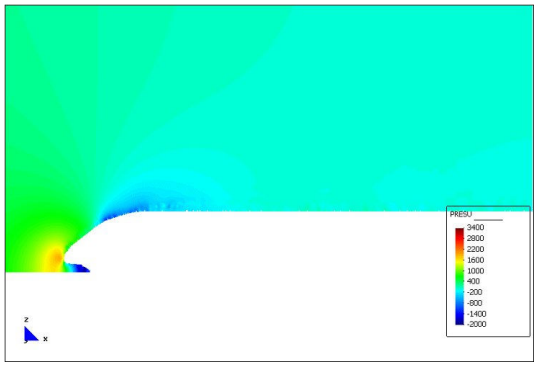

a) Pressure at $y = -1$ m, $t = 13$ s

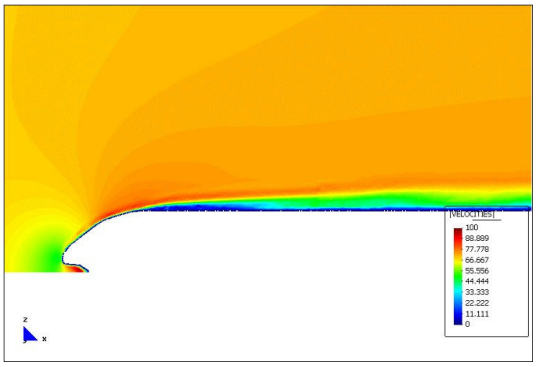

b) Isovelocity at $y = -1$ m, $t = 13$ s

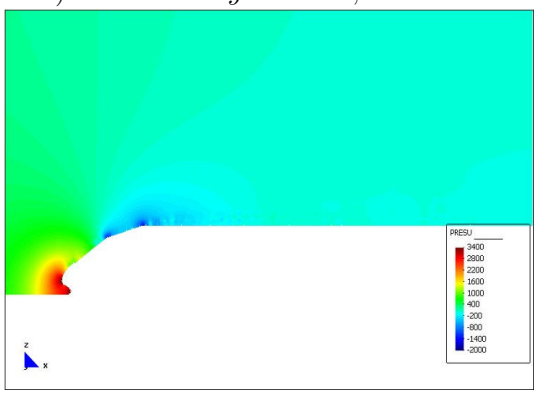

c) Pressure at $y = 0$ m, $t = 13$ s

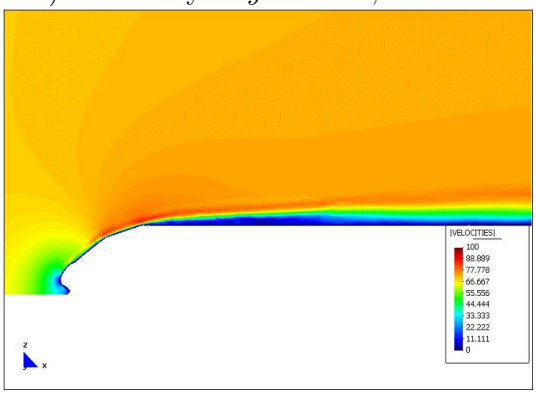

d) Isovelocity at $y = 0$ m, $t = 13$ s

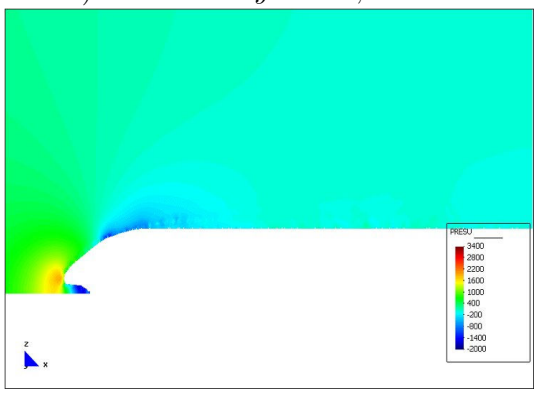

e) Pressure at $y = +1$ m, $t = 13$ s

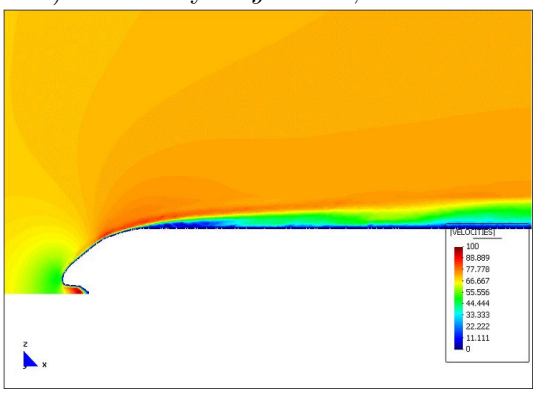

f) Isovelocity at $y = +1$ m, $t = 13$ s

Figure 6.5: Isovelocity and pressure field snapshots for $t = 13$ s. Vertical cuts.

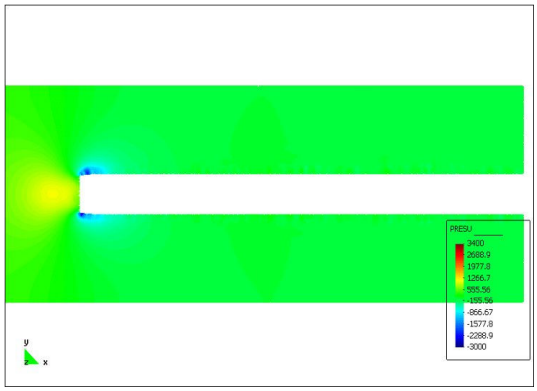

a) Pressure at $z = 2.6$ m, $t = 13$ s

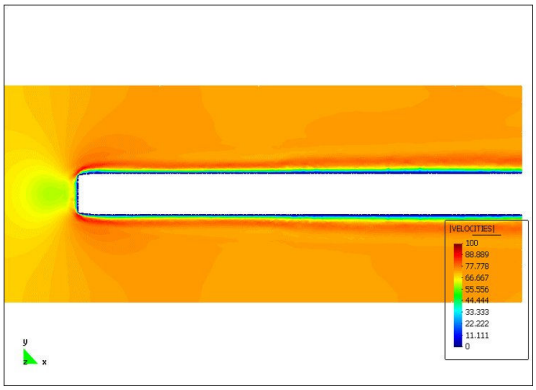

b) Isovelocity at $z = 2.6$ m, $t = 13$ s

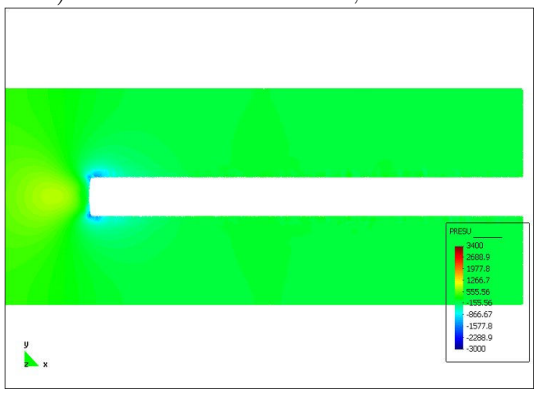

c) Pressure at $z = 3$ m, $t = 13$ s

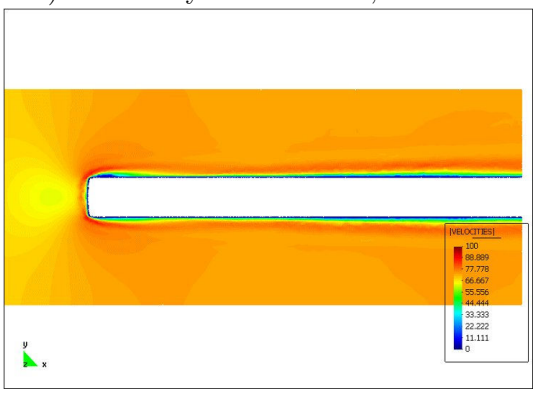

d) Isovelocity at $z = 3$ m, $t = 13$ s

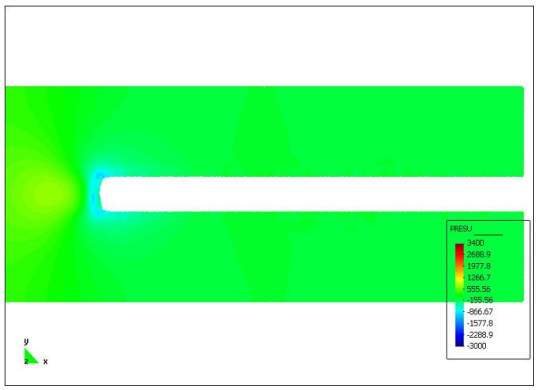

e) Pressure at $z = 3.3$ m, $t = 13$ s

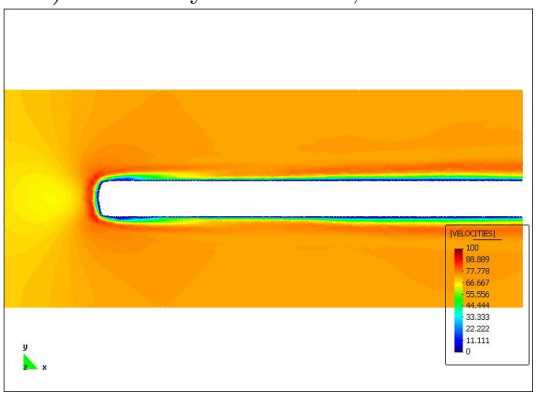

f) Isovelocity at $z = 3.3$ m, $t = 13$ s

Figure 6.6: Isovelocity and pressure field snapshots for $t = 13$ s. Horizontal cuts.

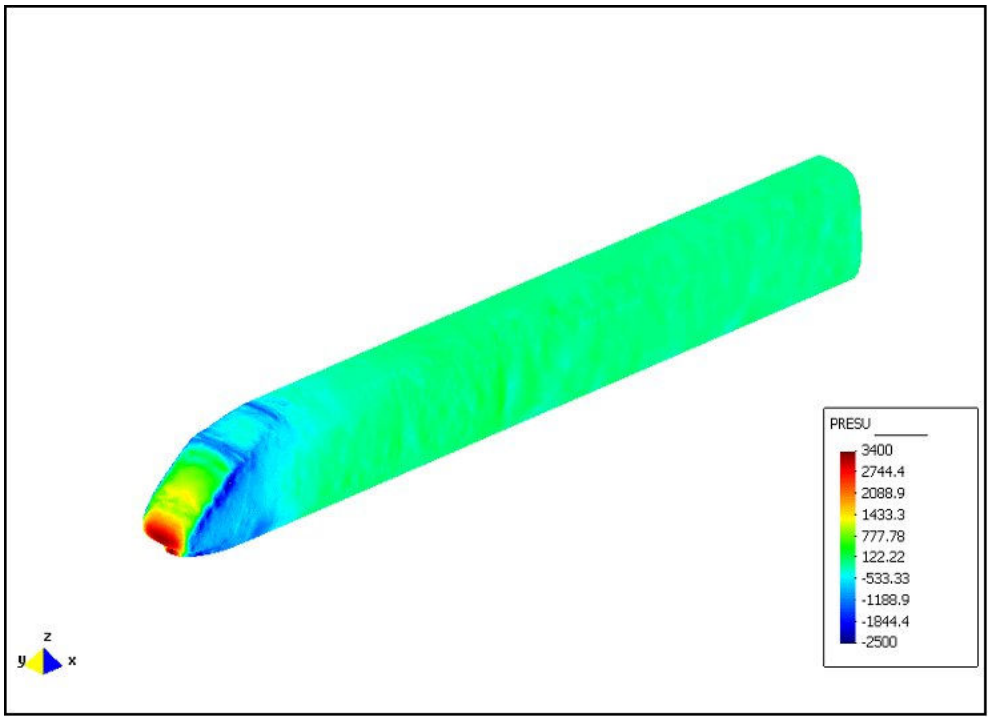

Figure 6.7: Surface pressure distribution for $t = 13$ s. Train at $U_0 = 69.2$ m/s.

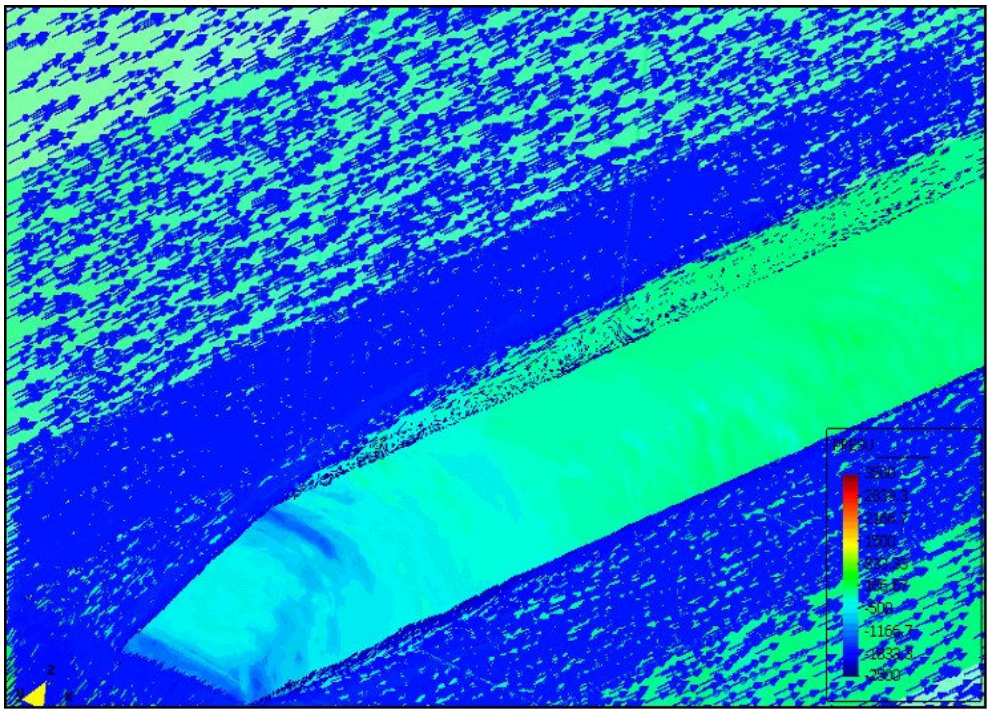

Figure 6.8: Surface pressure distribution and velocity vector field for $t = 13$ s. Train at $U_0 = 69.2$ m/s.

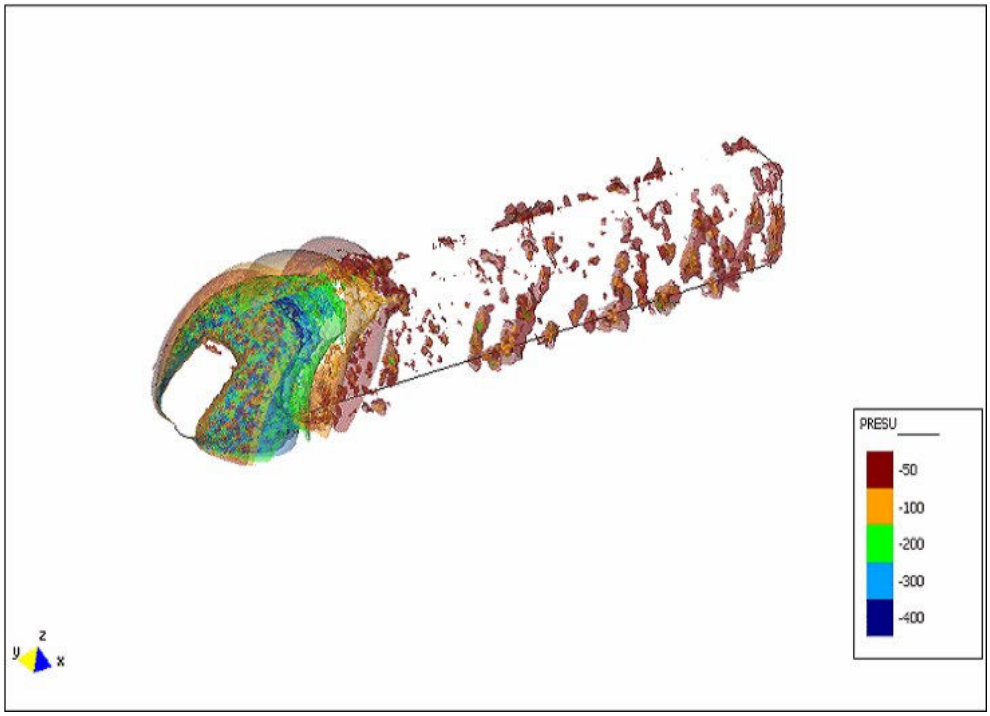

Figure 6.9: Isopressure surfaces for $t = 13$ s. Train at $U_0 = 69.2$ m/s.

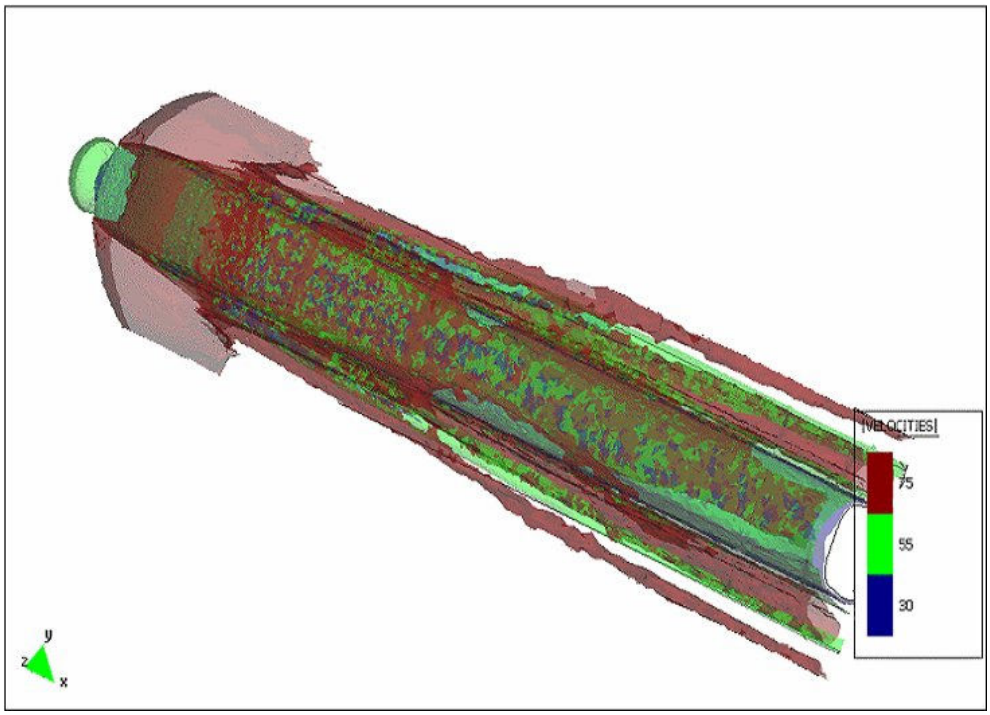

Figure 6.10: Isovelocity surfaces for $t = 13$ s. Train at $U_0 = 69.2$ m/s.

Point Code	x	y	**Point Code**	x	y
P1	2.8	0.0	P10	8.6	0.5
P2	3.5	0.0	P11	9.1	0.5
P3	8.1	−0.5	P12	11.2	0.7
P4	8.6	−0.5	P13	14.2	0.7
P5	9.1	−0.5	P14	11.2	−0.7
P6	8.1	0.0	P15	14.2	−0.7
P7	8.6	0.0	P16	8.2	1.2
P8	9.1	0.0	P17	8.6	1.2
P9	8.1	0.5	P18	9.0	1.2

Table 6.1: Location of surface control points. x: distance from train's nose, y: distance from centreline

zone where this separation occurs is rather apparent in Fig. 6.7. In Fig. 6.8 we have plotted the surface pressure distribution and a vertical cut containing the velocity vector field. The vortices generated at the flow separation zone can be appreciated.

Finally, in Fig. 6.9 we show some pressure isosurfaces for the inner computational domain in Fig. 6.3b. Although some spherical isosurfaces may be expected from Fig. 6.5a,c and e and from Fig. 6.6a,c and e, the complex pattern of the flow is made apparent. In Fig. 6.10 we have plotted the corresponding isovelocity surfaces, which show the formation of two lateral rolling vortices.

6.3 Unsteady pressure loading

In order to be able to carry out interior noise predictions, the pressure spectrum at the train's surface is needed according to the scheme in Fig. 6.2. Although interior noise prediction is not our objective in this work, it is worthwhile to have a look to the pressure spectra at several control points. This is so because we can easily compare the obtained pressure spectra using the ASGS approach with others in order to check their relative performances. Moreover we have had access to some experimental values for these spectra (although they cannot be reproduced here for confidentiality reasons) that will serve to check the reliance of the simulation.

In Fig. 6.11 we show the position of the analysed control points on the train surface, whereas their exact location is detailed in Table 6.1. In this table, the coordinate x stands for the distance from the nose of the train while y stands for the distance from the train's centreline.

The resulting pressure spectra for the control points in Fig. 6.11 are given in Fig. 6.12. The considered frequency range comprises [0, 200] Hz. All spectra show a similar shape, i.e. some high low frequency components and a quite constant value (slowly decreasing with frequency) for $f > 40$ Hz. The fluctuations vary from spectrum to spectrum. It can

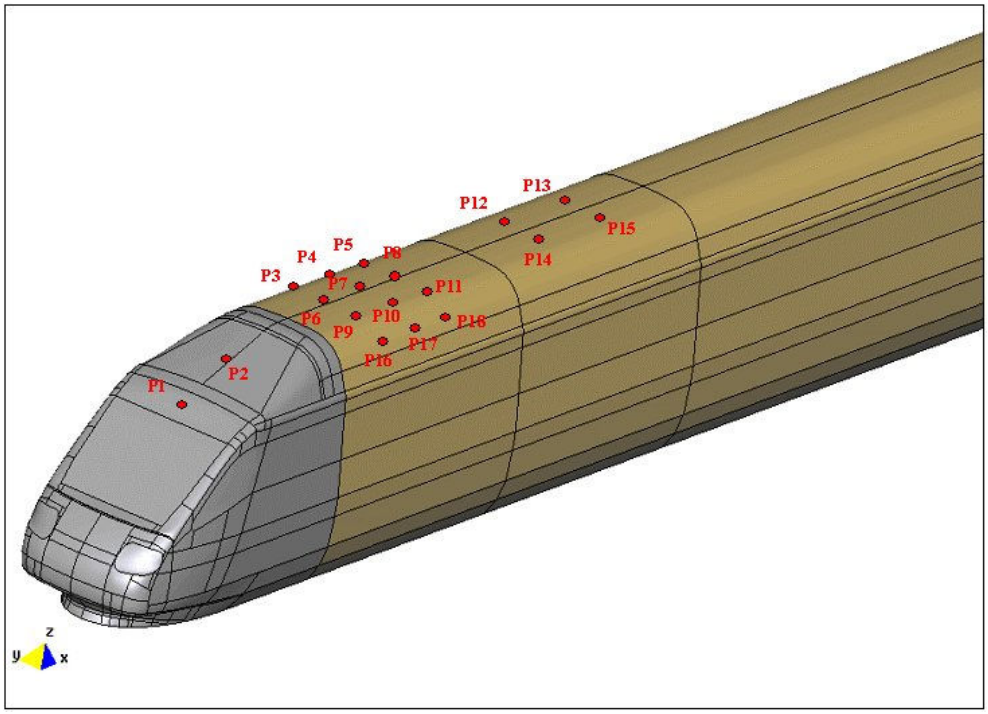

Figure 6.11: Location of surface control points.

be observed that the levels of the points placed at the leading end of the fairing tend to be inferior to the levels of those located behind, at the flow separation zone. In what concerns the low frequency components, they will be of no problem with regards to the dBA filtered interior noise level (see section 2.2.1). On the contrary, the remaining portions of the spectra combined with the fairing-roof mechanical response and its efficiency of radiation will determine the aerodynamic loading influence in the interior of the train.

In Fig. 6.13 we have plotted the results of performing a simulation using the ASGS stabilised finite element method and a LES simulation consisting of a Smagorinsky model plus ASGS stabilisation terms, in the line of what it is usually performed in commercial finite element codes. Remind that we have argued in the last paragraph of section 4.4.3 (see also the discussion in section 4.6.5) that the latter approach was redundant in our opinion. The results in Fig. 6.13 show that the solution provided by the Smagorinsky+ASGS is much more dissipative than the ASGS one (actually it is smaller by an order of magnitude).

When comparing the results in Fig. 6.12 and Fig. 6.13 with experimental data, it becomes apparent that the Smagorinsky+ASGS solution is clearly too dissipative so that the computed spectra are much weaker than the measured ones. Concerning the ASGS results in Fig. 6.12, it follows that they are only reliable at very low frequencies ($f < 20 - 30$ Hz). For higher frequencies, the measured data is also higher than the computed one. The only way to solve this problem is to use a much finer mesh, which implies the use of supercomputer facilities. That is, the problem we are facing nowadays

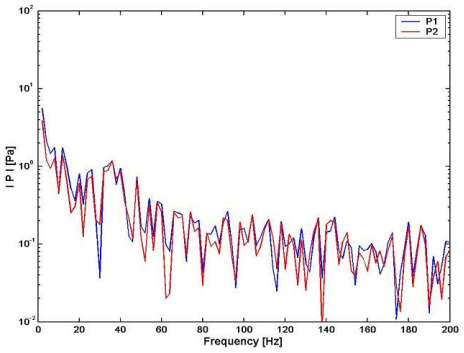

a) Pressure at P1, P2

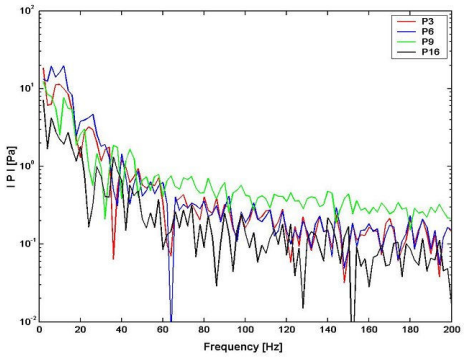

b) Pressure at P3, P6, P9, P16

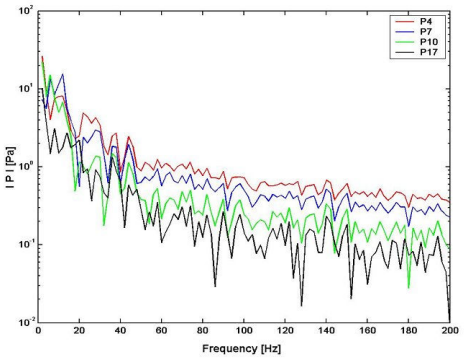

c) Pressure at P4, P7, P10, P17

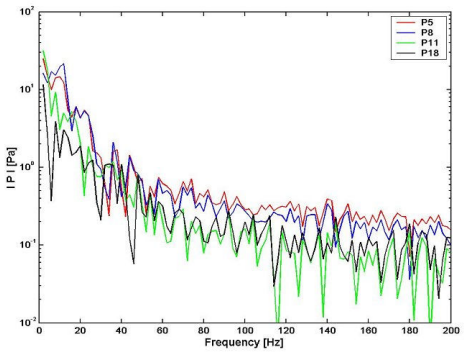

d) Pressure at P5, P8, P11, P18

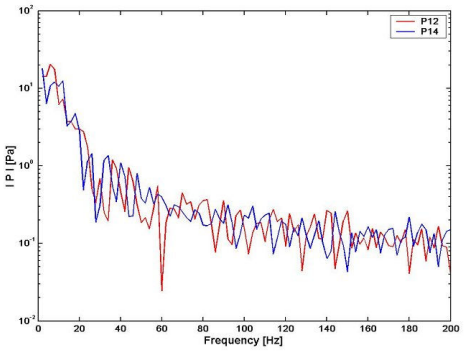

e) Pressure at P12, P14

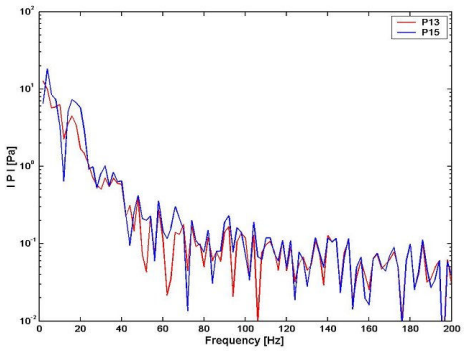

f) Pressure at P13, P15

Figure 6.12: Loading pressure spectra at some control points.

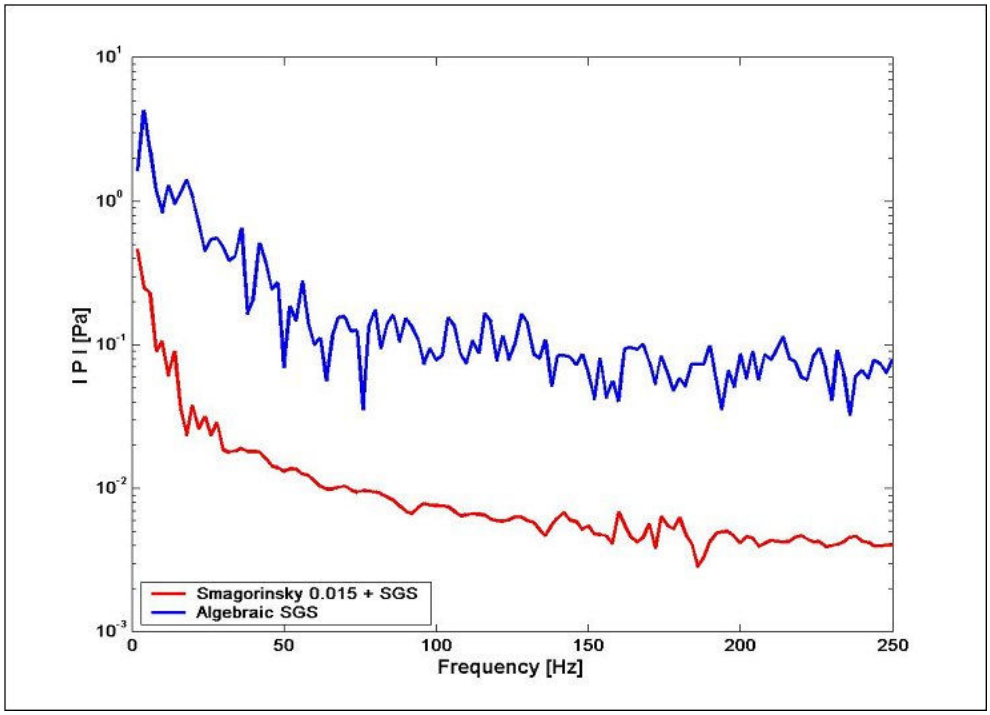

Figure 6.13: ASGS versus ASGS+LES (Smagorinsky).

can only be addressed with the use of powerful parallel supercomputers, if the audible acoustic frequency range is to be considered (remind from section 2.2.1 that it comprises from 20 Hz to 20.000 Hz).

Despite our simulation cannot cover the audible acoustic frequency range, the methodology applied to face the aerodynamic sound generation problem remains valid. In the next sections, we will give some results for the acoustic field generated by the vortices shed by flow separation at the leading end of the train for some very low frequencies.

6.4 Aerodynamic acoustic source

Prior to presenting the results for the acoustic field we will have a look at the acoustic source term, computed as the Reynolds tensor double divergence, $\rho_0 \left(\nabla \otimes \boldsymbol{u}\right) : \left(\nabla \otimes \boldsymbol{u}\right)^{\top}$. In Figs. 6.14a and b we respectively present a vertical and a horizontal cut showing the source term isocontours for $t = 13$ s (we note that the plot limiting values have been adapted to attain a better visualization). It can be observed that the source term localises at those zones where flow separation takes place and strongly decreases to zero when moving away from them. The situation is more more apparent in Fig. 6.15, where the source term isosurfaces have been plotted. We remind that the fast decay of the source term is at the core and actually justifies the acoustic analogy approach.

From Fig. 6.15 it can be seen that the acoustic source zone extends quite a long way

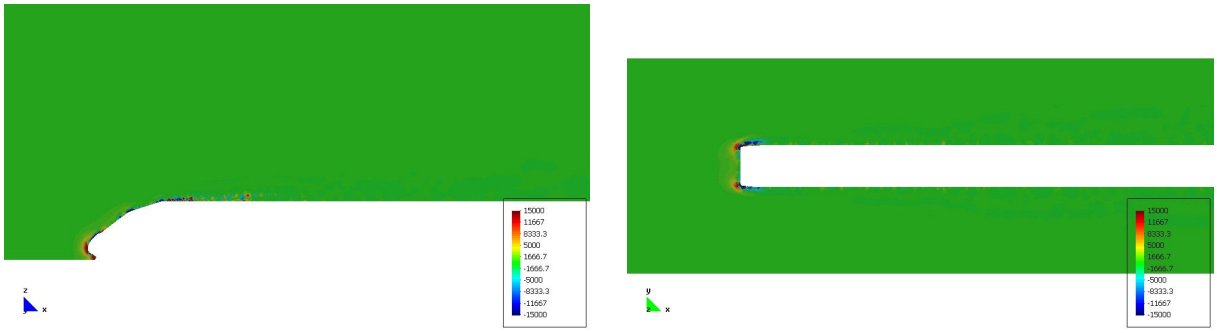

a) Acoustic source term at $y = 0$ m, $t = 13$ s

b) Acoustic source term at $z = 3$ m, $t = 13$ s

Figure 6.14: Isocontours for the acoustic source term (Reynolds tensor double divergence) for $t = 13$ s. Vertical and horizontal cuts.

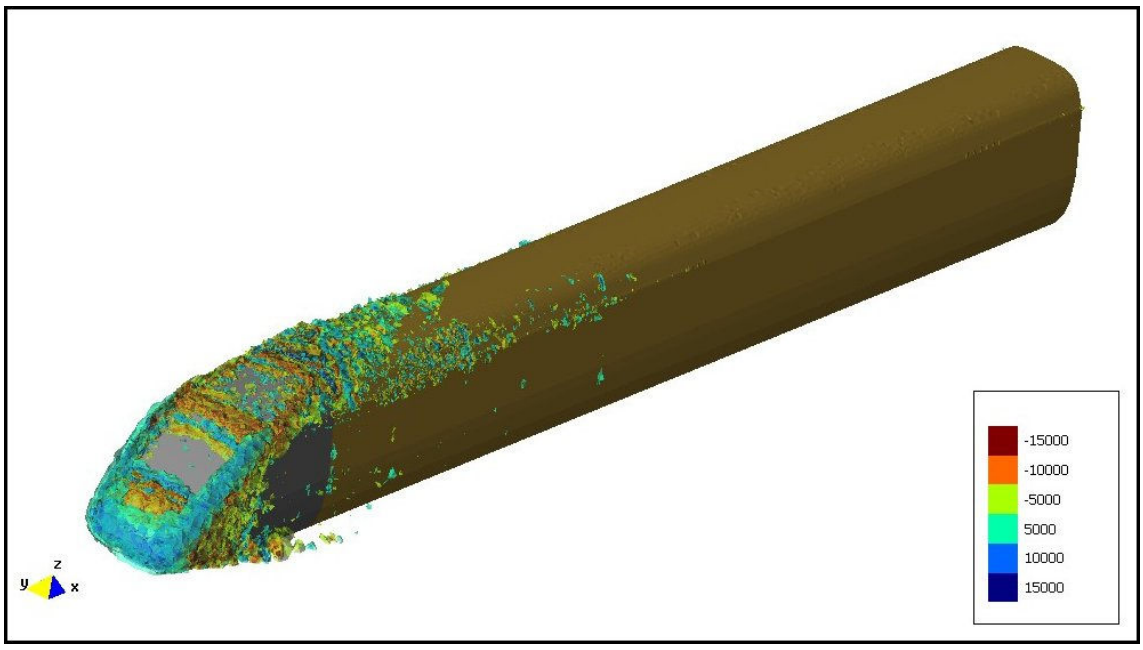

Figure 6.15: Isosurfaces for the acoustic source term (Reynolds tensor double divergenece) for $t = 13$ s. Train at $U_0 = 69.2$ m/s.

on the train's fairing surface, but remains quite concentrated at the laterals of the train's head. It will be seen in the next section that this will give place to a quite intricate acoustic field on the upper part of the computational domain (above the train), while clearly identifiable plane waves will propagate along the train laterals.

We would like to remark that the direct visualization of the acoustic source term, as that provided by the herein presented methodology, may be extremely useful when addressing control noise problems.

6.5 Outward radiated aerodynamic noise

6.5.1 Computational features and boundary conditions

Let us focus now on the computation of the outward radiated aerodynamic noise. Results will be presented for three frequencies on the lower part of the audible spectrum, namely $f = 20, 25, 30$ Hz. It is expected that for these low frequencies the computed velocity field becomes more or less reliable, at least in what concerns the vortex shedding due to flow separation.

In order to compute the acoustic field, use has been made of the same computational domain and mesh used and described in section 6.2.2. for the aerodynamic field. The mesh has turned to be fine enough so as not to require the use of stabilisation for the low frequencies being considered.

In what concerns the problem boundary conditions, no Dirichlet boundary exists. The Neumann boundary is built from $\Gamma_N = \overline{\Gamma^a_d \cup \Gamma^t}$, while the Sommerfeld boundary condition has been applied to $\Gamma_\infty = \overline{\Gamma^a_u \cup \Gamma^a_i \cup \Gamma^a_o \cup \Gamma^a_{lat1} \cup \Gamma^a_{lat2}}$ (see Fig. 6.3). The corresponding boundary conditions are given by:

Neumann boundary Γ_N:

$$\nabla \hat{p}' \cdot \boldsymbol{n} = 0 \quad \text{on } \Gamma_N \tag{6.4}$$

Sommerfeld radiation condition Γ_∞:

$$\nabla \hat{p}' \cdot \boldsymbol{n} = ik_0 \hat{p} \quad \text{on } \Gamma_\infty, \tag{6.5}$$

where we remind that $\omega = 2\pi f$, $k_0 = \omega / c_0$.

6.5.2 Acoustic field

The resulting acoustic field for the three analysed frequencies is first shown in Fig. 6.16. In Figs. 6.16a and b we have plotted the imaginary part of the acoustic pressure, $\mathrm{Im}\,(\hat{p}')$, corresponding to $f = 20$ Hz and for vertical and horizontal planes respectively located at $y = 0$ m (train centreline) and $z = 2.6$ m. The same results are plotted for the frequency $f = 25$ Hz in Figs. 6.16c and d, and for $f = 30$ Hz in Figs. 6.16e and f.

In Fig. 6.16b we observe a clear plane wave pattern generated by sources located at the laterals of the train nose. The waves propagate up and downstream with the wavelength

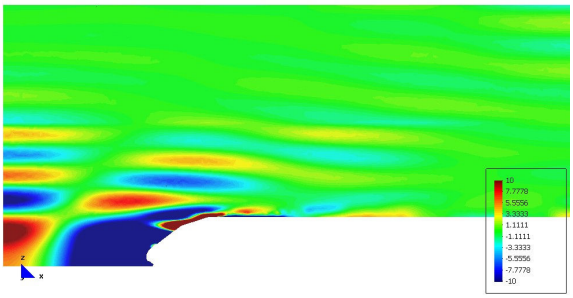

a) $\mathrm{Im}\,(\hat{p}')$ at $y = 0$ m for $f = 20$ Hz

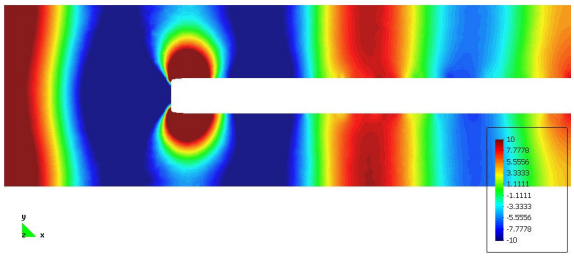

b) $\mathrm{Im}\,(\hat{p}')$ at $z = 2.6$ m for $f = 20$ Hz

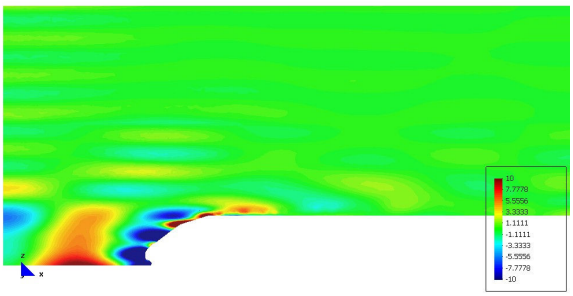

c) $\mathrm{Im}\,(\hat{p}')$ at $y = 0$ m for $f = 25$ Hz

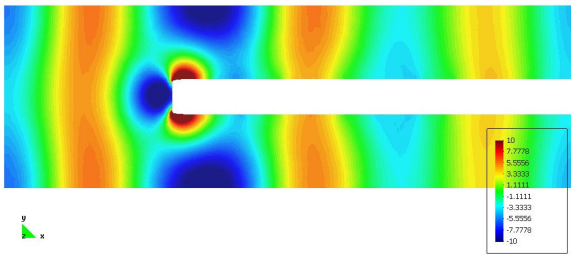

d) $\mathrm{Im}\,(\hat{p}')$ at $z = 2.6$ m for $f = 25$ Hz

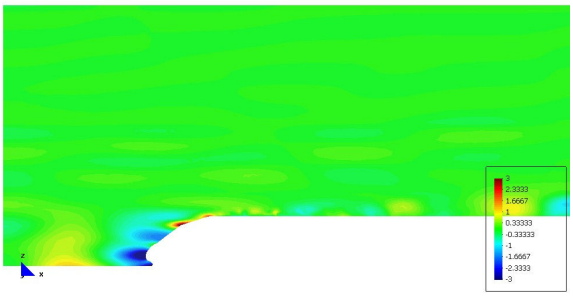

e) $\mathrm{Im}\,(\hat{p}')$ at $y = 0$ m for $f = 30$ Hz

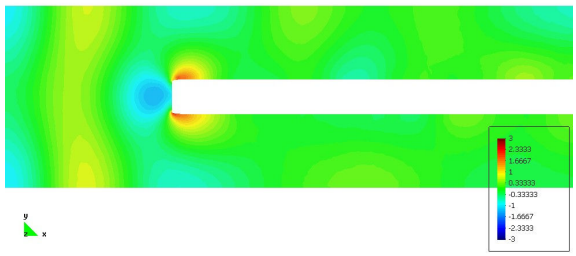

f) $\mathrm{Im}\,(\hat{p}')$ at $z = 2.6$ m for $f = 30$ Hz

Figure 6.16: Isocontours of the imaginary part of the acoustic pressure $\mathrm{Im}\,(\hat{p}')$ for various frequencies. Vertical and horizontal cuts.

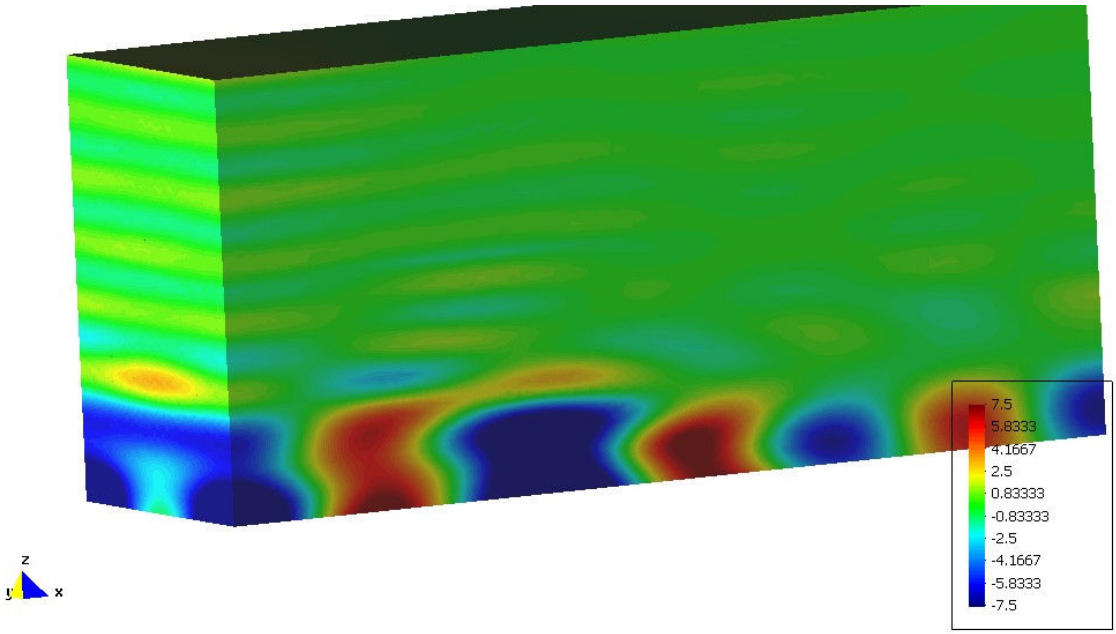

Figure 6.17: Isocontours of the imaginary part of the acoustic pressure on the outer computational domain for $f = 25$ Hz

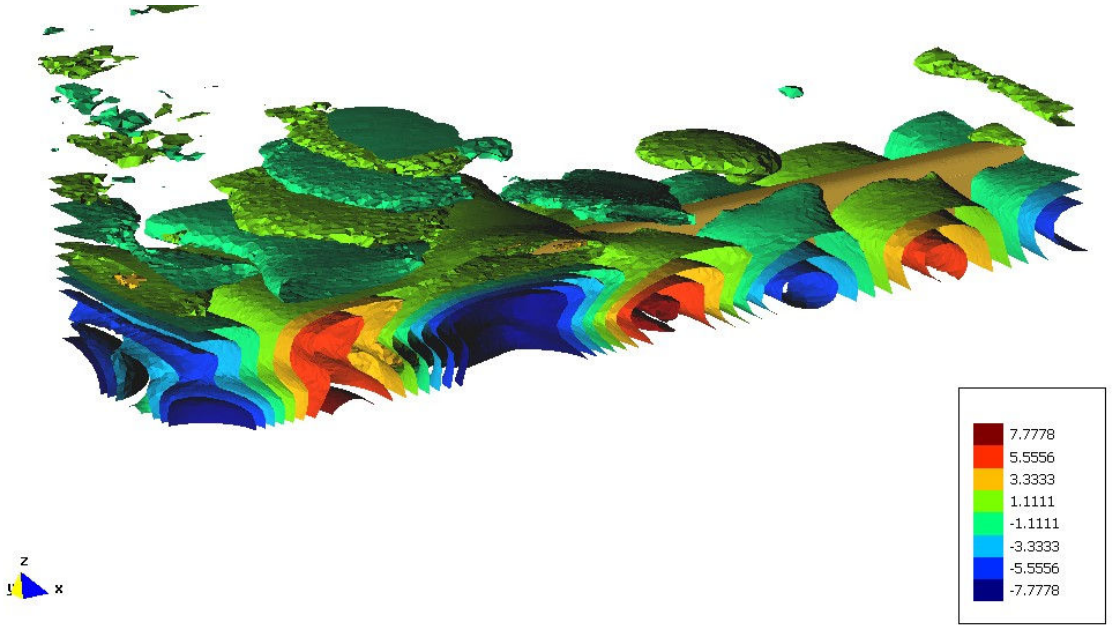

Figure 6.18: Isosurfaces of the imaginary part of the acoustic pressure $f = 25$ Hz.

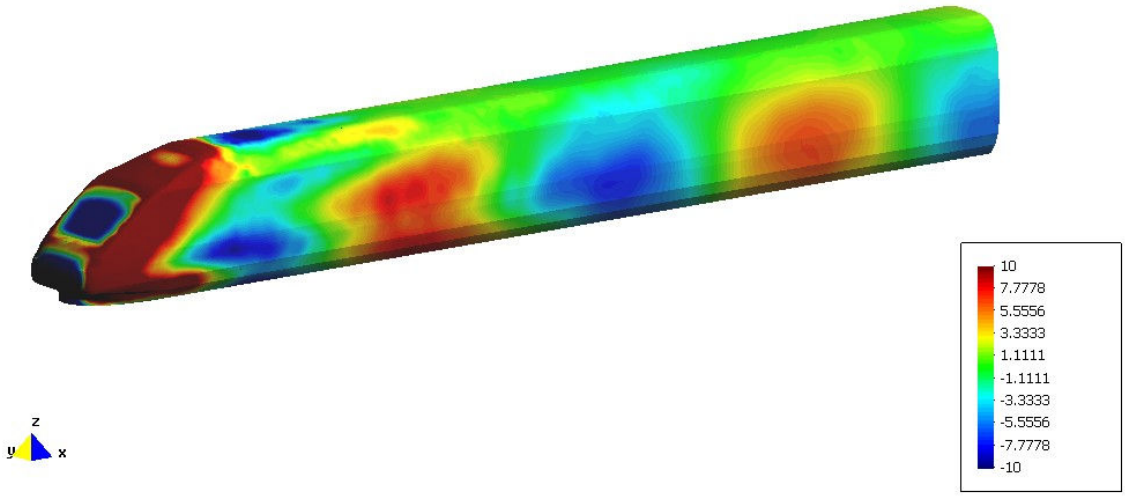

Figure 6.19: Imaginary part of the acoustic pressure on the train's surface for $f = 25$ Hz.

corresponding to the $f = 20$ Hz frequency ($\lambda = c_0/f \sim 17$ m). Unfortunately, the outward radiated waves propagating to the upper part of the domain, Fig. 6.16a, do not show the correct wavelength, a fact attributed to the limited size of the computational domain in the vertical direction. Similar considerations apply to the $f = 25$ Hz case presented in Fig. 6.16a and b. The acoustic field is now weaker than for the $f = 20$ Hz case but a clear pattern of plane waves propagating up and downstream can be identified having the correct wavenumber ($\lambda = c_0/f \sim 13.7$ m). Again problems arise due to the finite extension of the computational domain in the vertical direction. This fact is more clearly appreciated in Figs. 6.17 and 6.18, where we have respectively plotted $\mathrm{Im}\,(\hat{p}')$ on the outer boundary of the computational domain and its isosurfaces. On the other hand, we have plotted the train's parietal noise in Figs. 6.19 for $f = 25$ Hz. Note that the maxima and minima due to the lateral waves propagating downstream can be clearly appreciated.

In what concerns the sound field for $f = 30$ Hz (Figs. 6.16e and f) it is worthwhile to mention that it is much weaker than for the $f = 20, 25$ Hz cases. Actually, the pressure range in Figs. 6.16a,b,c and d was limited to $[-10\ 10]$ Pa to distinguish the generated sound waves. In Figs. 6.16e and f it has been limited to $[-3\ 3]$ Pa for the same purposes. We note that upstream propagating plane waves can be still distinguished, but that the plane waves propagating downstream become distorted, probably due to noise generated by shed vortices also travelling downstream.

As a result of the acoustic simulation we may conclude that although we have been able to capture some main features of the acoustic field (upstream and downstream

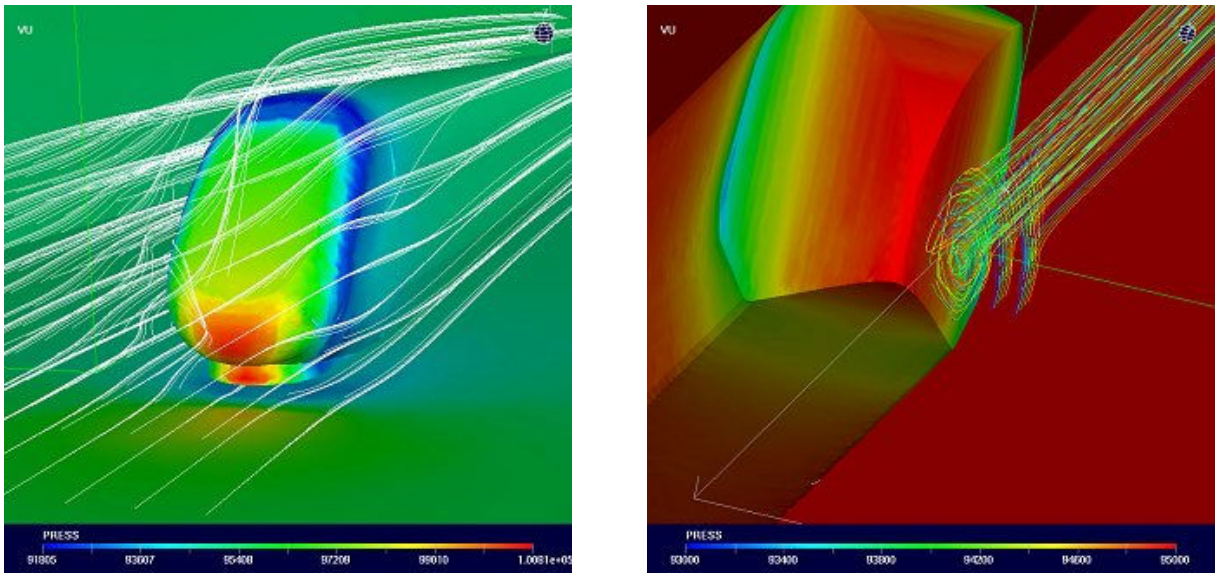

a) Streamlines b) Lateral vortex formation

Figure 6.20: Flow past high-speed train using supercomputing facilities. Courtesy of Dr. G. Houzeaux from BSC (Barcelona Supercomputing Center).

propagating waves), we face again computational limitations that can seriously distort the expected results. In fact, the present simulation has clearly made apparent one of the main difficulties of computational aeroacoustics, namely the need to combine very fine meshes to properly capture the flow aerodynamics with large computational domains needed to correctly compute the generated acoustic field.

6.6 Conclusions

In this chapter we have considered the possibility to apply the methodology proposed for computational aeroacoustics of low speed flows to an example of industrial interest. We have focused on aeroacoustics of high-speed trains. After reviewing some general schemes on how to face the general problem of acoustic noise prediction in railways, we have concentrated on exterior noise radiation due to flow separation at the nose of the leading coach. Although this is not the main source of externally radiated aerodynamic noise, flow separation may be of importance concerning interior noise at low frequencies. The latter question is of great interest for high-speed train manufacturers and shares the CFD step needed for exterior aerodynamic noise prediction. Hence, we have addressed a case yielding some results of direct industrial interest, which also serves as a test to see the type of results to be obtained and difficulties to be faced, in the prediction of external aerodynamic noise.

In what concerns the CFD step, the ASGS approach has provided much better results

than the Smagorinsky model, which has turned to be too dissipative. However, when comparing with experimental data we have seen that the computed pressure spectra at the train's fairing only becomes reliable for very low frequencies. A much finer mesh is then needed to cover the whole acoustic frequency range of interest.

Concerning the acoustic source term computation, we have seen that its direct visualization can provide very useful information for noise control. As expected, the source term is strongly localised in the vicinities of flow separation zones, this localization justifying the acoustic analogy approach.

The computation of the aerodynamically generated acoustic field has outcome some interesting features. On one hand, waves propagating up and downstream the laterals of the train have been well-captured. On the other hand, the computational domain has revealed too small to properly capture waves propagating in the vertical direction.

In summary, we may conclude that the proposed methodology in the framework of stabilised finite element methods seems to be valid to reproduce the main physical characteristics of the analysed aerodynamic noise generation problem. However, the herein presented simulation suffers from one of the main difficulties of CAA, namely the need to use extremely fine meshes to capture the aerodynamic velocity field, in combination with large computational domains to properly capture the acoustic field. Alternative CAA approaches exist aiming at the solution of this question. However, if one wants to cover the whole acoustic frequency range for an industrial problem such as the herein proposed for high-speed trains, the only way to proceed with some guarantee of success is to resort to supercomputer facilities (see Figs. 6.20a and b). This is the future line of work we have began to face.

Chapter 7

Conclusions and future work

Given that detailed conclusions have been given at the end of each chapter, in this section we will limit to briefly review and summarise the main outcomes of this thesis. Future lines of research to pursue the herein developed work will be also outlined.

The main contributions and conclusions of this thesis are:

- As a first outcome, a methodology for Computational Aeroacoustics (CAA) has been proposed in the framework of stabilised finite element methods. The method is based on a three step approach consisting of a first unsteady Computational Fluid Dynamics (CFD) simulation for incompressible flow in the spatial domain. This simulation serves to obtain the acoustic source term (double divergence of the velocity field Reynolds tensor) responsible for the generation of aerodynamic noise. In the second step of the method, the latter source term is Fourier transformed to the frequency domain (in practice, this Fourier transform is performed during the CFD computation for initially selected frequencies, to save the storage of a large amount of time data). Finally, in the third step of the method a Helmholtz equation is solved using the acoustic source obtained in the second step as the inhomogeneous term (Lighthill's acoustic analogy in the frequency domain).

  The proposed approach makes use of stabilised finite element methods to solve both, the incompressible Navier-Stokes equations in the first step of the method and the inhomogeneous Helmholtz equation in the third step. The method has some advantages when compared to more standard approaches such as allowing a direct visualization of the acoustic source term, making use of C^0-class finite elements, maintaining the multipolar character of the acoustic field (given that noise generated by flow motion is considered naturally in a addition to noise generated by the flow/boundary interaction) and avoids the typical retarded time integration problem of the classical time integral approach to CAA. These points have been supported by presented simulations on aerodynamic noise generated by flow past rigid bodies, showing very good performance when compared to other methods.

- The second main contribution of this work concerns some issues of the first step of the method, namely the CFD simulation of turbulent incompressible flows.

After reviewing some aspects of the mathematical theory of the Navier-Stokes equations, and after showing its close relation with very recent approaches to Large Eddy Simulation (LES), we have addressed the question if standard physical LES modelling is in fact necessary. That is to say, we have aimed at giving support to the idea that the simulation of turbulence should probably rely on appropriate numerical simulation schemes rather than on physical modelling. A heuristic argument has been developed to do so and some numerical examples have been also presented.

The heuristic argument states that the rate of transfer of subgrid kinetic energy provided by the stabilisation terms in the Orthogonal Subgrid Scale (OSS) finite element method is already proportional to the molecular physical dissipation rate. Hence, the inclusion of an extra LES physical model in the equations to achieve this behaviour seems at least redundant. To prove this result we have combined some results of statistical fluid mechanics with some results of numerical methods. In particular, we have assumed that the flow statistics, which are valid for the exact velocity field, remain also valid for its finite element approximation. Concerning the flow statistics, use has been made of Kolmogorov's first and second similarity hypotheses and of the quasi-normal approximation for two point fourth-order velocity correlations. The argumentation is valid for a fine enough computational mesh so that its characteristic length lies in the inertial subrange of a turbulent flow.

On the other hand, two numerical examples, the decay of two-dimensional isotropic turbulence and a three-dimensional turbulent flow impinging on a plate have shown how the use of appropriate finite element stabilisation scheme (the herein ones including the time tracking of subscales) may properly capture the behaviour of turbulence.

- The third basic result of this thesis is the development of an algebraic subgrid scale (ASGS) finite element method for the two dimensional convected Helmholtz equation that improves the standard Galerkin solution to it. The method is formally equivalent to the Galerkin / Least Squares (GLS) approach reverting the sign of its stabilisation parameter. The latter has been obtained from a dispersion analysis and it reduces to well-known GLS values for the Helmholtz equation in the case of no convection.

  Although the stabilisation parameter has been specifically derived for a structured mesh of quadrilateral elements and it includes a preferred direction for which yields exact nodal values, numerical examples have shown that it improves the Galerkin solution in a large amount of cases. On one hand, it has been shown that improvements can be obtained for plane waves propagating in different directions with respect to the mean flow and using non-structured meshes of quadrilateral elements. On the second hand, even for more intricate problems involving meshes of triangular elements, the stabilised solution has shown superior behaviour than the Galerkin solution. This has been the case of aerodynamic noise generated by

flow past a cylinder.

It is also worthwhile to mention that the developed ASGS method can prove very useful for problems where a certain degree of information on the wave propagation directions is known a priori. This would be the case, for instance, of duct acoustics where two stabilisation parameters accounting for upstream and downstream propagating waves could be implemented. Finally, it should be noticed from the formulation that a remarkable advantage of the method is that it can be implemented at almost no computational cost.

Let us focus now on possible future lines of work and research that could be followed in order to complement and improve the herein presented developments.

Concerning the CAA strategy, the following points should be considered.

- Some type of analysis should be performed in order to know the degree of precision of the computed acoustic field. Although the validity of Lighthill's acoustic analogy has been extensively analysed for the continuous case by some authors, further work is needed to asses similar results for the herein presented and similar numerical CAA approaches.

- In the line of the previous point, it would be worthwhile to implement Ristorcelli's closure and compare its degree of accuracy with Lighthill's acoustic analogy for some benchmark problems.

- When applying the proposed CAA approach to problems of industrial interest (high-speed train example in chapter 6) we have found that large computational facilities are required in order to cover the whole acoustic frequency range. Hence, implementation of the CAA approach in supercomputing facilities turns to be mandatory to solve this kind of problems, a subject that is being currently performed.

- In order to cover a wider class of problems, Lighthill's acoustic analogy could be extended to include thermo-acoustic sources to be also implemented in the stabilised finite element framework we have used. A very similar approach to the one exposed in his work could be followed.

In what refers to the work developed for the computation of the aerodynamic field, the following would be useful:

- The heuristic argument developed for the OSS method could be extended to other subgrid scale stabilised (SGS) finite element methods.

- It would be worthwhile to check if the various SGS methods constitute suitable approximations to the Navier-Stokes equations. Since now it has only been proved that the Galerkin finite element method for problems with periodic or Dirichlet boundary conditions satisfy this assumption.

- Further numerical experiments should be carried out to check the performance of the SGS methods as alternatives to classical LES approaches for the simulation of turbulent flows. We have seen that the inclusion of the time tracking for the subscales has allowed to properly capture the energy spectrum for the decay of two-dimensional isotropic turbulence and the pressure spectrum for a three-dimensional turbulent flow impinging on a plate. However, more tests are required to assess the validity of this approach. In particular, we should be able to reproduce Kolmogorov's energy spectrum for decaying three-dimensional turbulence as well as the appropriate decay in time of energy, enstrophy and other related statistical variables. Another standard test that should be carried out is the channel flow, which will allow to see if the log behaviour after the laminar sublayer (Prandtl theory) in the flow turbulent boundary layer is correctly captured. Other questions such as if the SGS methods allow for backscatter or if the dimension of the global attractor is properly reproduced should be also addressed.

Finally, related to the third step of the method, i.e., the computation of the acoustic field, the following should be noted:

- The numerical study of the convected wave and Helmholtz equations is very recent. Hence, the use of stabilisation techniques and other related approaches is still at its first beginnings. We have proposed a simple extension of the ASGS approach for the stabilisation of the two-dimensional convected Helmholtz equation, which could be extended to the three-dimensional case. On the other hand, probably many other stabilisation methods already developed for the more general convection-diffusion-reaction systems or for the non-convected Helmholtz equation could be applied and/or extended for the convected Helmholtz case. In this sense, a large amount of work is still to be done and the possibilities are extremely vast.

- We have concentrated on the development of the ASGS method for the convected Helmholtz equation and on testing its behaviour by means of some examples. A numerical analysis of its performance including stability and convergence analysis should be also carried out.

Bibliography

[1] S. Abarbanel and D. Gottlieb. A mathematical analysis of the PML method. *J. Comput. Phys.*, 134 (2):357–363, 1997.

[2] R. Astley. Infinite elements for wave problems: a review of current formulations and an assessment of accuracy. *Int. J. Numer. Meth. Engrg.*, 49 (7):951–976, 2000.

[3] I. M. Babuška, F. Ihlenburg, E. Paik, and S. A. Sauter. A generalized finite element method for solving the Helmholtz equation in two dimensions with minimal pollution. *Comput. Methods Appl. Mech. Engrg.*, 128:325–359, 1995.

[4] I. M. Babuška and J. E. Osborn. Generalized Finite Element Methods: Their performance and their relation to mixed methods. *SIAM J. Numer. Anal.*, 20 (3):510–536, 1983.

[5] I. M. Babuška and S. A. Sauter. Is the pollution effect of the FEM avoidable for the Helmholtz equation considering high wave numbers. *SIAM J. Numer. Anal.*, 34 (6):2392–2423, 1997.

[6] C. Bailly and D. Juvé. A stochastic approach to compute subsonic noise using linearized Euler equations. *AIAA Paper*, 99:1872–, 1999.

[7] J. Bardina, J. Ferziger, and W. Reynolds. Improved subgrid models for large eddy simulation. Technical Report AIAA Paper 80-1357.

[8] F. Bastin, P. Lafon, and S. Candel. Computation of jet mixing noise due to coherent structures: the plane jet case. *J. Fluid Mech.*, 335:261–304, 1997.

[9] G. Batchelor. Pressure fluctuations in isotropic turbulence. *Proc. Camb. Phil. Soc.*, 47:359–374, 1951.

[10] G. Batchelor. *An Introduction to Fluid Dynamics*. Cambridge University Press, 1967.

[11] G. Batchelor. Computation of the energy spectrum in homogeneous two-dimensional turbulence. *Phys. Fluids*, 12 (Suppl. II):233–239, 1969.

[12] Y. Bazilevs, V. Calo, J. Cottrell, T. Hughes, A. Reali, and G. Scovazzi. Variational multiscale residual-based turbulence modeling for large eddy simulation. *Comput. Methods Appl. Mech. Engrg.*, to appear, 2007.

[13] E. Bécache, S. Fauqueux, and P. Joly. Stability of perfectly matched layer. *J. Comput. Phys.*, 188 (2):399–433, 2003.

[14] L. Beranek and I. Vér. *Noise and Vibration Control Engineering: Principles and Applications*. John Wiley and Sons, 1992.

[15] J. Berenger. A perfectly matched layer for the absorption of electromagnetic waves. *J. Comput. Phys.*, 114:185–200, 1994.

[16] L. Berselli, G. Galdi, T. Iliescu, and W. Layton. Mathematical analysis of the rational large eddy simulation model. *Math. Models Meth. Appl. Sci.*, 12:1131–1152, 2002.

[17] L. Berselli, T. Iliescu, and W. Layton. *Mathematics of Large Eddy Simulation of Turbulent Flows*. Springer-Verlag, 2006.

[18] P. Bettess. *Infinite Elements*. Penshaw Press, 1992.

[19] W. Blake. *Mechanics of flow-induced sound and vibration*. Academic Press, New York, 1986.

[20] J. Boris, F. Grinstein, E. Oran, and R. Kolbe. New insights into large eddy simulation. *Fluid Dyn. Res.*, 10:199–228, 1992.

[21] V. Borue. Inverse energy cascade in stationary two-dimensional homogeneous turbulence. *Phys. Rev. Lett.*, 72 (10):1475–1479, 1994.

[22] S. Brenner and L. Scott. *The mathematical theory of finite element methods*. Springer–Verlag, 1994.

[23] A. Brooks and T. Hughes. Streamline upwind / Petrov-Galerkin formulations for convection dominated flows with particular emphasis on the incompressible Navier-Stokes equation. *Comput. Methods Appl. Mech. Engrg.*, 32:199–259, 1982.

[24] M. Bull. Wall-pressure fluctuations beneath turbulent boundary layers: some reflections on forty years of research. *J. Sound Vibr.*, 190 (3):299–315, 1996.

[25] L. Caffarelli, R. Kohn, and L. Nirenberg. Partial regularity of suitable weak solutions of the Navier-Stokes equations. *Comm. Pure Appl. Math.*, 35:771–831, 1982.

[26] V. Calo. *Residual based multiscale turbulence modeling: finite volume simulations of bypass transition*. PhD thesis, Department of Civil and Environmental Engineering, Stanford University, 2004.

[27] V. Canuto. Large Eddy Simulation of turbulence: a subgrid scale model including shear, vortivity, rotation and buoyancy. *Astrophysical J.*, 428:729–752, 1994.

[28] D. Carati, S. Ghosal, and P. Moin. On the representation of backscatter in dynamic localization models. *Phys. Fluids*, 7 (3):606–616, 1995.

[29] D. Carati, G. Winckelmans, and H. Jeanmart. On the modelling of the subgrid-scale and filtered-scale stress tensors in large-eddy simulation. *J. Fluid Mech.*, 441:119–138, 2000.

[30] S. Ceruti and C. Meneveau. Statistics of filtered velocity in grid and wake turbulence. *Phys. Fluids*, 12 (5):1143–1165, 2000.

[31] S. Chang, X. Wang, and C. Chow. The space-time Conservation-Element and Solution-Element method. a new high resolution and genuinely multidimensional paradigm for solving conservation laws. *J. Comput. Phys.*, 159:89–136, 1999.

[32] D. Chapman. Computational aerodynamics, development and outlook. *AIAA J.*, 17:1293–1313, 1979.

[33] J. Chasnov. Simulation of the Kolmogorov inertial subrange using an improved subgrid model. *Phys. Fluids A*, 3:188–200, 1991.

[34] C. Cheong and S. Lee. Grid-optimized dispersion-relation-preserving schemes on general geometries for computational aeroacoustics. *J. Comput. Phys.*, 174:248–276, 2001.

[35] F. Chow and P. Moin. A further study of numerical errors in large-eddy simulations. *J. Comput. Phys.*, 184, 2003.

[36] J. Cipolla. Subgrid modeling in a Galerkin method for the helmholtz equation. *Comput. Methods Appl. Mech. Engrg.*, 177:35–49, 1998.

[37] R. Clark, J. Ferziger, and W. Reynolds. Energy spectra for decaying 2D turbulence in a bounded domain. *J. Fluid Mech.*, 91:1–16, 1979.

[38] H. Clercx and G. van Heijst. Energy spectra for decaying 2D turbulence in a bounded domain. *Phys. Rev. Lett.*, 85 (2):306–309, 2000.

[39] R. Codina. Comparison of some finite element methods for solving the diffusion-convection-reaction equation. *Comput. Methods Appl. Mech. Engrg.*, 156:185–210, 1998.

[40] R. Codina. A nodal-based implementation of a stabilized finite element method for incompressible flow problems. *Int. J. Numer. Meth. Fluids*, 33:737–766, 2000.

[41] R. Codina. On stabilized finite element methods for linear systems of convection-diffusion-reaction equations. *Comput. Methods Appl. Mech. Engrg.*, 188:61–82, 2000.

[42] R. Codina. Stabilization of incompressibility and convection through orthogonal sub-scales in finite element methods. *Comput. Methods Appl. Mech. Engrg.*, 190:1579–1599, 2000.

[43] R. Codina. A stabilized finite element method for generalized stationary incompressible flows. *Comput. Methods Appl. Mech. Engrg.*, 190:2681–2706, 2001.

[44] R. Codina. Stabilized finite element approximation of transient incompressible flows using orthogonal subscales. *Comput. Methods Appl. Mech. Engrg.*, 191:4295–4321, 2002.

[45] R. Codina. Analysis of a stabilized finite element approximation of the Oseen equations using orthogonal subscales. *Appl. Numer. Math.*, To appear.

[46] R. Codina and J. Principe. Dynamic subscales in the finite element approximation of thermally coupled incompressible flows. *Int. J. Numer. Meth. Fluids*, 54 (6-8):707–730, 2007.

[47] R. Codina, J. Principe, O. Guasch, and S. Badia. Time dependent subscales in the stabilized finite element approximation of incompressible flow problems. *Comput. Methods Appl. Mech. Engrg.*, 196 (21-24):2413–2430, 2007.

[48] F. Collino and P. Monk. Optimizing the perfect matched layer. *Comput. Methods Appl. Mech. Engrg.*, 164 (1-2):157–171, 1998.

[49] C. Colosqui and A. Oberai. Generalized Smagorinsky model in physical space. *Submitted*, 2007.

[50] P. Constantin, C. Foias, and R. Temam. Attractors representing turbulent flows. *Memoirs of AMS*, 53:314, 1985.

[51] D. Crighton. Basic principles of aerodynamic noise generation. *Progr. Aerospace Sci.*, 16:31–96, 1975.

[52] D. Crighton. Acoustics as a branch of fluid mechanics. *J. Fluid Mech.*, 106:261–298, 1981.

[53] D. Crighton. Computational aeroacoustics for low Mach number flows. In J. Hardin and M. Hussaini, editors, *Computational Aeroacoustics*. Springer–Verlag, 1993.

[54] D. Crighton, P. Dowling, J. F. Williams, M. Heckl, and F. Leppington. *Modern methods in analytical acoustics*. Springer–Verlag, 1992.

[55] S. Crow. Aerodynamic sound emission as a singular perturbation problem. *Stud. Appl. Math.*, 49 (1):21–44, 1970.

[56] N. Curle. The influence of solid boundaries on aerodynamic sound. *Proc. R. Soc. Lond.*, 231 A 1187:505–514, 1955.

[57] A. Deraemaeker, I. Babuška, and P. Bouillard. Dispersion and pollution of the FEM solution for the Helmholtz equation in one, two and three dimensions. *Int. J. Numer. Meth. Engrg.*, 46:471–499, 1999.

[58] J. Djambazov, C. Lai, and K. Pericleous. Development of numerical techniques for near-field aeroacoustic computations. *Int. J. Numer. Meth. Fluids*, 29:719–731, 1999.

[59] C. Doering and J. Gibbon. *Applied analysis of the Navier-Stokes equations*. Cambridge Texts in Applied Mathematics. Cambridge University Press, 1995.

[60] J. Donea. A Taylor-Galerkin method for convection transport problems. *Int. J. Numer. Meth. Engrg.*, 20:101–119, 1984.

[61] J. Douglas and T. Russel. Numerical methods for convection dominated problems based on combining the method of characteristics with finite elements or finite difference procedures. *SIAM J. Numer. Anal.*, 19:871–885, 1982.

[62] P. Drazin. *Introduction to Hydrodynamic Stability*. Cambridge Texts in Applied Mathematics. Cambridge University Press, 2002.

[63] J. Duchon and R. Robert. Inertial energy dissipation for weak solutions of incompressible euler and Navier-Stokes equations. *Nonlinearity*, 13:249–255, 2000.

[64] A. Dunca, V. John, and W. Layton. *The commutation error of the space averaged Navier-Stokes equations on a bounded domain in Contributions to Current Challenges in Mathematical Fluid Mechanics, Advances in Mathematical Fluid Mechanics, G.P. Galdi and J.G. Heywood and R. Rannacher (Eds.)*, pages 53–78. Birkhauser Verlag Basel, 2004.

[65] J. Eckmann. Roads to turbulence in dissipative systems. *Rev. Mod. Phys.*, 53(4):643–654, 1981.

[66] F. Farassat. The acoustic analogy as a tool of computational aeroacoustics. In J. Hardin and M. Hussaini, editors, *Computational Aeroacoustics*. Springer–Verlag, 1993.

[67] C. Farhat, I. Harari, and L. Franca. The discontinuous enrichment method. *Comput. Methods Appl. Mech. Engrg.*, 190:6455–6479, 2001.

[68] F. Farrassat. The acoustic analogy as a tool of computational acoustics. In J. Hardin and M. Hussaini, editors, *Computational Aeroacoustics*. Springer–Verlag, 1993.

[69] F. Farrassat and M. Meyers. Extension of Kirchoff's formula to radiation from moving surfaces. *J. Sound Vibr.*, 123:451–460, 1988.

[70] M. Feigenbaum. The transition to aperiodic behaviour in turbulent systems. *Comm. Math. Phys.*, 77:65–86, 1980.

[71] J. Ffowcs-Williams. Hydrodynamic noise. *Annu. Rev. Fluid Mech.*, 1:197–222, 1969.

[72] J. Ffowcs-Williams and D. Hawkings. Sound generated by turbulence and surfaces in arbitrary motion. *Phil. Trans. Roy. Soc. A*, 264:321–342, 1969.

[73] P. Filippi, A. Bergassoli, D. Habault, and J. Lefebvre. *Acoustics: Basic Physics Theory and Methods*. Academic Press, New York, 1999.

[74] C. Foias, O. Manley, R. Rosa, and R. Temam. Estimates for the energy cascade in three-dimensional turbulent flows. *C. R. Acad. Sci. Paris Ser. I*, 333 (5):499–504, 2001.

[75] C. Foias, O. Manley, R. Rosa, and R. Temam. *Navier-Stokes equations and turbulence*. Encyclopedia of Mathematics and its Applications. Cambridge University Press, 2001.

[76] L. Franca and C. Farhat. Bubble functions prompt unusual stabilized finite element methods. *Comput. Methods Appl. Mech. Engrg.*, 123:299–308, 1994.

[77] L. Franca and A. Macedo. A two-level finite element method and its application to the Helmholtz equation. *Int. J. Numer. Meth. Engrg.*, 43:23–32, 1998.

[78] L. Franca and R. Stenberg. Error analysis of some Galerkin least-squares methods for the elasticity equations. *SIAM J. Numer. Anal.*, 28:1680–1697, 1991.

[79] H. Frid and M. Perepelitsa. Partial regularity of solutions of the 3-d incompressible navier-stokes equations. In *23th Brazilian Colloquium of Mathematics*, 2001.

[80] U. Frisch. *Turbulence, the legacy of A.N. Kolmogorov*. Cambridge University Press, 1995.

[81] C. Fureby and G. Tabor. Mathematical and physical constraints on large eddy simulations. *Theoret. Comput. Fluid Dynamics*, 9:85–102, 1997.

[82] C. Fureby, G. Tabor, H. Weller, and A. Gosman. A comparative study of subgrid scale models in homogeneous isotropic turbulence. *Phys. Fluids*, 9 (5):1416–1429, 1997.

[83] G. Gabard, R. Astley, and M. Tahar. Stability and accuracy of finite element methods for flow acoustics I: general theory and application to one-dimensional propagation. *Int. J. Numer. Meth. Engrg.*, 63 (7):947–973, 2005.

[84] G. Gabard, R. Astley, and M. Tahar. Stability and accuracy of finite element methods for flow acoustics II: two-dimensional effects. *Int. J. Numer. Meth. Engrg.*, 63 (7):974–987, 2005.

[85] G. Galdi and W. Layton. Approximation of the larger eddies in fluid motion II: a model for space-filtered flow. *Math. Models Meth. Appl. Sci.*, 10 (3):343–350, 2000.

[86] P. Gautier. A review of railway noise research and results since the 5^{th} IWRN in Voss (Norway). *J. Sound Vibr.*, 231 (3):477–489, 2000.

[87] M. Gennaretti, L. Lucer, and L. Morino. A unified integral methodology for aerodynamics and aeroacoustics of rotors. *J. Sound Vibr.*, 200:467–489, 1997.

[88] K. Gerdes. A review of infinite element methods for exterior Helmholtz problems. *J. Comput. Acoust.*, 8 (1):43–62, 2000.

[89] K. Gerdes and F. Ihlenburg. On the pollution effect in FE solutions of the 3D-Helmholtz equation. *Comput. Methods Appl. Mech. Engrg.*, 170:155–172, 1999.

[90] M. Germano. Differential filters for the large eddy simulation of turbulent flows. *Phys. Fluids*, 29(6):1755–1757, 1986.

[91] M. Germano. Differential filters of elliptic type. *Phys. Fluids*, 29(6):1757–1758, 1986.

[92] M. Germano, U. Piomelli, P. Moin, and W. Cabot. A dynamic subgrid-scale eddy viscosity model. *Phys. Fluids A*, 3 (7):1760–1765, 1991.

[93] S. Ghosal. An analysis of numerical errors in large-eddy simulations of turbulence. *J. Comput. Phys.*, 125:187–206, 1996.

[94] S. Ghosal. Mathematical and physical constraints on large eddy simulation of turbulence. *AIAA J.*, 37 (4):425–433, 1999.

[95] S. Ghosal, T. Lund, P. Moin, and K. Akselvoll. A dynamic localization model for large-eddy simulation of turbulent flows. *J. Fluid Mech.*, 286:229–255, 1995.

[96] S. Ghosal and P. Moin. The basic equations of the large eddy simulation of turbulent flows in complex geometry. *J. Comput. Phys.*, 118:24–37, 1995.

[97] J. Gibbon and E. Titi. Attractor dimension and small length scale estimates for the three dimensional Navier-Stokes equations. *Nonlinearity*, 10:109–119, 1997.

[98] D. Givoli and J. Keller. A finite element method for large domains. *Comput. Methods Appl. Mech. Engrg.*, 76 (1):41–66, 1989.

[99] M. Goldstein. Unified approach to aerodynamic sound generation in the presence of solid boundaries. *J. Acoust. Soc. Am.*, 56:497–509, 1974.

[100] M. Goldstein. A generalized acoustic analogy. *J. Fluid Mech.*, 488 (3):315–333, 2003.

[101] M. E. Goldstein. *Aeroacoustics*. Mc Graw-Hill, 1976.

[102] S. Goldstein. *Modern developments in fluid mechanics (Vol. 2)*. New York: Dover, 1965.

[103] W. Graham. A comparison of models for the wavenumber-frequency spectrum of turbulent boundary later pressures. *J. Sound Vibr.*, 206 (4):541–565, 1997.

[104] V. Gravemeier. The variational mulstiscale method for laminar and turbulent flow. *Arch. Comput. Mech.*, 13:249–324, 2006.

[105] O. Guasch and R. Codina. Cálculo del ruido aerodinámico generado por el flujo de aire alrededor de un cuerpo. Simulación mediante métodos estabilizados de elementos finitos. In C. M. Soares and et. al, editors, *Proc. Métodos Computacionais em Engenharia, APMTAC-SEMNI*. Laboratório Nacional de Engenharia Civil de Lisboa, ISBN 972-49-2008-9, 2004.

[106] O. Guasch and R. Codina. An algebraic subgrid scale finite element method for the convected Helmholtz equation in two dimensions with applications in aeroacoustics. *Comput. Methods Appl. Mech. Engrg.*, 196 (45-48):4672–4689, 2007.

[107] O. Guasch and R. Codina. Computational aeroacoustics of viscous low speed flows using subgrid scale stabilized finite element methods. *In preparation*, 2007.

[108] O. Guasch and R. Codina. A heuristic argument for the sole use of numerical stabilization with no physical LES modeling in the simulation of incompressible turbulent flows. *Submitted*, 2007.

[109] J. Guermond. Finite-element-based Faedo-Galerkin weak solutions to the Navier-Stokes equations in the three-dimensional torus are suitable. *J. Math. Pures Appl.*, 85 (3):451–464, 2006.

[110] J. Guermond. Faedo-Galerkin weak solutions of the Navier-Stokes with dirichlet boundary conditions are suitable. *J. Math. Pures Appl.*, 88 (1):87–106, 2007.

[111] J. Guermond, J. Oden, and S. Prudhomme. An interpretation of the navier-stokes-alpha model as a frame-indifferent leray regularization. *Phys. D*, 177:23–30, 2003.

[112] J. Guermond, J. Oden, and S. Prudhomme. Mathematical perspectives on large eddy simulation models for turbulent flows. *J. Math. Fluid Mech.*, 6 (2):194–248, 2004.

[113] J. Guermond and S. Prudhomme. Mathematical analysis of a spectral hyperviscosity LES model for the simulation of turbulent flows. *Mathematical Modelling and Numerical Analysis*, 37 (6):893–908, 2003.

[114] J. Guermond and S. Prudhomme. On the construction of suitable solutions to the Navier-Stokes equations and questions regarding the definition of large eddy simulation. *Phys. D*, 207:64–78, 2005.

[115] Y. Guo. Application of the Ffowcs-Williams/Hawkings equation to two-dimesnional problems. *J. Fluid Mech.*, 403:201–221, 2000.

[116] L. Gutin. On the sound field of a rotating airscrew. *Phys. Z. Sowjetunion*, 9:57–71, 1936.

[117] J. Hamet, M. Pallas, and K. Scmitz. Deufrako-1: microphone array techniques used to locate acoustic sources on ICE, TGV-A and Transrapid 07. In *Proc. Inter-noise 94*, volume Vol I, page 187, 1994.

[118] I. Harari. A survey of finite element methods for time harmonic acoustics. *Comput. Methods Appl. Mech. Engrg.*, 195:1594–1607, 2006.

[119] I. Harari and T. Hughes. Finite element methods for the Helmholtz equation in an exterior domain: model problems. *Comput. Methods Appl. Mech. Engrg.*, 87:57–96, 1991.

[120] I. Harari and T. Hughes. Galerkin/least-squares finite element methods for the reduced wave equation with non-reflecting boundary conditions in unbounded domains. *Comput. Methods Appl. Mech. Engrg.*, 98 (3):411–454, 1992.

[121] I. Harari and F. Magoulès. Numerical investigations of stabilized finite element computations for acoustics. *Wave Motion*, 39:339–349, 2004.

[122] I. Harari and C. Nogueira. Reducing dispersion of linear triangular elements for the Helmholtz equation. *ASCE J. Eng. Mech.*, 128 (3):351–358, 2002.

[123] I. Harari, M. Slavutin, and E. Turkel. Analytical and numerical studies of a finite element PML for the Helmholtz equation. *J. Comput. Acoust.*, 8 (1):121–137, 2000.

[124] J. Hardin and M. Hussaini. *Computational Aeroacoustics*. Springer-Verlag, 1993.

[125] G. Hauke. A simple subgrid scale stabilized method for the advection-diffusion-reaction equation. *Comput. Methods Appl. Mech. Engrg.*, 191:2925–2947, 2002.

[126] D. Haworth and K. Jansen. Large-eddy simulation on unstructured deforming meshes: towards reciprocating IC engines. *Computers & Fluids*, 29:493–524, 2000.

[127] C. He. On partial regularity for weak solutions to the Navier-Stokes equations. *J. Funct. Anal.*, 211 (1):153–162, 2004.

[128] E. Heikkola, T. Rossi, and J. Toivanen. Fast direct solution of the helmholtz equation with a perfectly matched layer or an absorbing boundary condition. *Int. J. Numer. Meth. Engrg.*, 57 (14):2007–2025, 2003.

[129] R. Hill and J. Wilczak. Pressure structure functions and spectra for locally isotropic turbulence. *J. Fluid Mech.*, 296:247–269, 1995.

[130] J. Hoffman and C. Johnson. A new approach to computational turbulence modeling. *Comput. Methods Appl. Mech. Engrg.*, 195:2865–2880, 2006.

[131] B. Holmes, J. Dias, B. Jaroux, T. Sassa, and Y. Ban. Predicting the wind noise from the pantograph cover of a train. *Int. J. Numer. Meth. Fluids*, 24:1307–1319, 1997.

[132] G. Hölzl, P. Fodiman, K. Schmitz, M. Pallas, and B. Barsikow. Deufrako-2: localized sound sources on the high-speed vehicles ICE, TGV-A and TR07. In *Proc. Internoise 94*, volume Vol I, page 193, 1994.

[133] E. Hopf. über die aufanswertaufgabe für die hydrodynamischen grundgleichungen. *Mathematische Nachrichten*, 4:213–231, 1951.

[134] M. Howe. Contributions to the theory of aerodynamic sound, with application to excess jet noise and the theory of the flute. *J. Fluid Mech.*, 71 (4):625–673, 1975.

[135] M. Howe. The generation of sound by aerodynamic sources in an inhomogeneous steady flow. *J. Fluid Mech.*, 67 (3):597–610, 1975.

[136] M. Howe. A review of the theory of trailing edge noise. *J. Sound Vibr.*, 61 (3):437–465, 1978.

[137] M. Howe. Surface pressures and sound produced by turbulent flow over smooth and rough walls. *J. Acoust. Soc. Am.*, 90 (2):1041–1047ž, 1991.

[138] M. Howe. Emendation of the Brown & Michael equation with application to sound generation by vortex motion near a half plane. *J. Fluid Mech.*, 329:89–101, 1996.

[139] M. Howe. The compression wave generated by a high-speed train at a vented tunnel entrance. *J. Acoust. Soc. Am.*, 104 (2):1158–1164, 1998.

[140] M. Howe. Mach number dependence of the compression wave generated by a high-speed train entering a tunnel. *J. Sound Vibr.*, 212 (1):23–36, 1998.

[141] M. Howe. Trailing edge noise at low Mach numbers. *J. Sound Vibr.*, 225 (2):211–238, 1999.

[142] M. Howe. Trailing edge noise at low Mach numbers, part 2: attached and separated edge flows. *J. Sound Vibr.*, 234 (5):761–775, 2000.

[143] M. Howe. Aeroacoustics of a tunnel-entrance hood with rectangular window. *J. Fluid Mech.*, 487:211–243, 2003.

[144] M. Howe. Edge-source acoustic Green's function for an airfoil of arbitrary chord, with application to trailing-edge noise. *Quart. J. Mech. Appl. Math.*, 54 (1):139–155, 2003.

[145] M. S. Howe. *Acoustics of Fluid-Structure Interactions*. Cambridge University Press, 1998.

[146] M. S. Howe. *Theory of vortex sound*. Cambridge Texts in Applied Mathematics, 2003.

[147] H. Hubbard. *Aeroacoustics of flight vehicles. Theory and practice. Volume I: Noise Sources*. Acoustical Society of America, 1995.

[148] H. Hubbard. *Aeroacoustics of flight vehicles. Theory and practice. Volume II: Noise Control*. Acoustical Society of America, 1995.

[149] T. Hughes. Multiscale phenomena: Green's function, subgrid scale models, bubbles, and the origins of stabilized formulations. In M. M. Cecchi, K. Morgan, J. Periaux, B. Schrefler, and O. Zienkiewicz, editors, *Proc. 9th International Conference on Finite Elements in Fluids, Venice, Italy*. Dip. di Matematica Pura ed Applicata, Università di Padova, 1995.

[150] T. Hughes. Multiscale phenomena: Green's function, the Dirichlet-to-Neumann formulation, subgrid scale models, bubbles and the origins of stabilized formulations. *Comput. Methods Appl. Mech. Engrg.*, 127:387–401, 1995.

[151] T. Hughes and A. Brooks. *A multi-dimensional upwind scheme with no crosswind diffussion, in FEM for convection dominated flows*. ASME, 1979.

[152] T. Hughes, V. Calo, and G. Scovazzi. Variational and multiscale methods in turbulence. In *Proc. of the XXI International Congress of Theoretical and Applied Mechanics (IUTAM)*. Kluwer, 2004.

[153] T. Hughes, G. Feijóo, L. Mazzei, and J. Quincy. The variational multiscale method–a paradigm for computational mechanics. *Comput. Methods Appl. Mech. Engrg.*, 166:3–24, 1998.

[154] T. Hughes, L. Franca, and M. Balestra. A new finite element formulation for computational fluid dynamics: V. Circumventing the Babuška-Brezzi condition: a stable Petrov-Galerkin formulation for the Stokes problem accommodating equal-order interpolations. *Comput. Methods Appl. Mech. Engrg.*, 59:85–99, 1986.

[155] T. Hughes, L. Franca, and G. Hulbert. A new finite element formulation for computational fluid dynamics: VII. The Stokes problem with various well-posed boundary conditions: symmetric formulations that converge for all velocity/pressure spaces. *Comput. Methods Appl. Mech. Engrg.*, 65:85–96, 1987.

[156] T. Hughes, L. Franca, and G. Hulbert. A new finite element formulation for computational fluid dynamics: VIII. The Galerkin / least-squares method for advective-diffusive equations. *Comput. Methods Appl. Mech. Engrg.*, 73:173–189, 1989.

[157] T. Hughes, L. Mazzei, and K. Jansen. Large eddy simulation and the variational multiscale method. *Comput. Visual. Sci.*, 3:47–59, 2000.

[158] T. Hughes, L. Mazzei, and A. Oberai. Large eddy simulation of turbulent channel flow by the variational multiscale method. *Phys. Fluids*, 13(6):1784–1798, 2001.

[159] T. Hughes, L. Mazzei, and A. Oberai. The multiscale formulation of large eddy simulation: Decay of homogeneous isotropic turbulence. *Phys. Fluids*, 13(2):505–512, 2001.

[160] T. Hughes and G. Sangalli. Variational multiscale analysis: the fine-scale Green's function, projection, optimization, localization and stabilized methods. *SIAM J. Numer. Anal.*, 45(2):539–557, 2007.

[161] T. Hughes and G. Wells. Conservation properties for the Galerkin and stabilised forms of the advection-diffusion and incompressible Navier-Stokes equations. *Comput. Methods Appl. Mech. Engrg.*, 194:1141–1159, 2005.

[162] T. Hughes, G. Wells, and A. Wray. Energy transfers and spectral eddy viscosity in large-eddy simulations of homogeneous isotropic turbulence: Comparison of dynamic Smagorinsky and multiscale models over a range of discretizations. *Phys. Fluids*, 16 (11):4044–4052, 2004.

[163] F. Ihlenburg. *Finite Element Analysis of Acoustic Scattering*. Applied Mathematical Sciences 132, Springer Verlag, 1998.

[164] F. Ihlenburg and I. M. Babuska. Finite element solution to the Helmholtz equation with high wave number. part I: The h-version of the FEM. *Comput. Math. Appl.*, 39:9–37, 1995.

[165] A. Iida, Y. Takano, T. Makino, K. Kobayashi, and M. Hattori. Development of a low-noise electric-current collector for high-speed trains. In *Proc. Inter-noise 94*, volume Vol I, page 163, 1994.

[166] M. Ikeda, T. Morikawa, and K. Manabe. Development of low aerodynamic noise pantograph for high speed train. In *Proc. Inter-noise 94*, volume Vol I, page 169, 1994.

[167] T. Iliescu and P. Fischer. Large eddy simulation of turbulent channel flows by the rational large eddy simulation model. *Phys. Fluids*, 15 (10):3036–3047, 2003.

[168] T. Iliescu, V. John, W. Layton, G. Matthies, and L. Tobiska. A numerical study of a class of LES models. *Int. J. Comput. Fluid Dyn.*, 17 (1):75–85, 2003.

[169] O. Inoue and N. Hatakeyama. Sound generation by a two-dimensional circular cylinder in a uniform flow,. *J. Fluid Mech.*, 471:285–314, 2002.

[170] K. Jansen. A stabilized finite element method for computing turbulence. *Comput. Methods Appl. Mech. Engrg.*, 174:299–317, 1999.

[171] V. John. *Large Eddy Simulation of Turbulent Incompressible Flows*. Springer-Verlag, 2004.

[172] C. Johnson. *Numerical Solution of Partial Differential Equations by the Finite Element Method*. Cambridge University Press, 1987.

[173] T. Kambe, T. Minota, and Y. Ikushima. Acoustic wave emitted by vortex ring passing near the edge of a half plane. *J. Fluid Mech.*, 155:77–103, 1985.

[174] T. Kambe, T. Minota, and Y. Ikushima. Acoustics emissions by vortex motions. *J. Fluid Mech.*, 173:643–666, 1986.

[175] S. Kaniel. On the initial value problem for an incompressible fluid with nonlinear viscosity. *J. Math. Mech.*, 19:681–706, 1970.

[176] R. Kechroud, A. Soulaimani, Y. Saad, and S. Gowda. Preconditioning techniques for the solution of the Helmholtz equation by the finite element method. *Math. Comput. Simul.*, 65 (4-5):303–321, 2004.

[177] J. Keller and D. Givoli. Exact nonreflecting boundar conditions. *J. Comput. Phys.*, 82 (1):172–192, 1989.

[178] D. Kelly, S. Nakazawa, O. Zienkiewicz, and J. Heinrich. A note on upwinding and anisotropic balancing dissipation in finite element approximations to convective diffusion problems. *Int. J. Numer. Meth. Engrg.*, 15:1705–1711, 1980.

[179] W. King III. On the role of aerodynamically generated sound in determining wayside noise levels from high speed trains. *J. Sound Vibr.*, 54 (3):361, 1977.

[180] W. King III. The components of wayside noise generated by high-speed tracked vehicles. In *Proc. Inter-noise 90*, volume Vol I, page 375, 1990.

[181] W. King III. On the boundary layer contribution to wayside noise generated by high-speed tracked vehicles. In *Proc. Inter-noise 94*, volume Vol I, page 175, 1994.

[182] W. King III. A précis of developments in the aeroacoustics of fast trains. *J. Sound Vibr.*, 193 (1):349–358, 1996.

[183] W. King III and D. Bechert. On the sources of wayside noise generated by high-speed trains. *J. Sound Vibr.*, 66 (3):311, 1979.

[184] T. Kitagawa and K. Nagakura. Aerodynamic sound generated by Shinkansen cars. *J. Sound Vibr.*, 231 (3):913–924, 2000.

[185] B. Knaepen, O. Debliquy, and D. Carati. Large-eddy simulation without filter. *J. Comput. Phys.*, 205:98–107, 2005.

[186] A. Kolmogorov. The local structure of turbulence in incompresible viscous fluids for very large reynolds number. *Dokl. Akad. Sci. Nauk. SSSR*, 30:299–330, 1941.

[187] A. Kolmogorov. A refinement of previous hypothesis concerning the local structure of turbulence in a viscous incompressible fluid at high reynols number. *J. Fluid Mech.*, 13:82–85, 1962.

[188] R. Kraichnan. Inertial ranges transfer in two-dimensional turbulence. *Phys. Fluids*, 10:1417–1423, 1967.

[189] A. Krothapalli and C. Smith. *Recent advances in aeroacoustics*. Springer-Verlag, New York, 1986.

[190] O. Ladyzhenskaya. New equations for the description of motion of viscous incompressible fluids and solvability in the large of boundary value problems for them. *Proc. Steklov. Inst. Math.*, 102:95–118, 1967.

[191] O. Ladyzhenskaya. *The Mathematical Theory of Viscous Incompressible Flow*. Gordon and Breach, 2nd edition, 1969.

[192] O. Laghrouche and P. Bettess. Short wave modelling using special finite element method. *J. Comput. Acoust.*, 8 (1):189–210, 2000.

[193] M. Landahl and E. Mollo-Christensen. *Turbulence and random processes in fluid mechanics*. Cambridge University Press, 1986.

[194] J. Langford and R. Moser. Optimal LES formulations for isotropic turbulence. *J. Fluid Mech.*, 398:321–346, 1999.

[195] J. Laval, B. Dubrulle, and S. Nazarenko. Nonlocality of interaction of scales in the dynamics of 2D incompressible fluids. *Phys. Rev. Lett.*, 83 (20):4061–4064, 1999.

[196] W. Layton. Advanced models for large eddy simulation. In *Computational Fluid Dynamics-Multiscale Methods*, Rhode-Saint-Genèse, Belgium, September 2002. Von Karman Institute for Fluid Dynamics, Ed. H. Decononck.

[197] W. Layton. A mathematical introduction to Large Eddy Simulation. In *Computational Fluid Dynamics-Multiscale Methods*, Rhode-Saint-Genèse, Belgium, September 2002. Von Karman Institute for Fluid Dynamics, Ed. H. Decononck.

[198] W. Layton. Variational Multiscale Methods and Subgrid Scale Viscosity. In *Computational Fluid Dynamics-Multiscale Methods*, Rhode-Saint-Genèse, Belgium, September 2002. Von Karman Institute for Fluid Dynamics, Ed. H. Decononck.

[199] R. Legendre. Bruits émis par la turbulence. ONERA Publ. 1981-3, 1981.

[200] L. Lencina, P. Mueller, E. Dari, and G. Buscaglia. Stabilized finite elements in the simulation of homogeneous isotropic turbulence. In *Proc. VIII Congreso Argentino de Mecánica Computacional. Mecánica Computacional*, volume 24, page 142, Buenos Aires, Argentina, November 2005. Ed. A. Larreteguy.

[201] A. Leonard. Energy cascade in large eddy simulation of turbulent fluid flows. *Adv. Geophys.*, 618:237–248, 1974.

[202] J. Leray. Essai sur le mouvement d'un fluide visqueux emplissant l'espace. *Acta Math.*, 63:193–248, 1934.

[203] M. Lesieur. *Turbulence in fluids*. 3d Edition. Kluwer Academic Publishers, 1997.

[204] M. Lesieur and O. Métais. New trends in large-eddy simulation of turbulence. *Annu. Rev. Fluid Mech.*, 28:45–82, 1996.

[205] F. Létourneaux and S. Guerrand. Low-frequency acoustic transmission of high-speed trains: simplified vibroacoustic models. *J. Sound Vibr.*, 231 (3):847–851, 2000.

[206] M. Lighthill. On sound generated aerodinamically I. General theory. *Proc. R. Soc. Lond.*, 211 A 1107:564–587, 1952.

[207] M. Lighthill. On sound generated aerodinamically II. Turbulence as a source of sound. *Proc. R. Soc. Lond.*, 222 A 1148:1–32, 1954.

[208] M. Lighthill. *Waves in fluids*. Cambridge University Press, 1978.

[209] M. Lighthill. *The final panel discussion, in Computational Aeroacoustics, J.C. Hardin and M.Y. Hussaini (Eds.)*, pages 499–513. Springer Verlag, 1993.

[210] G. Lilley. On noise from air jets. *Proc. R. Soc. Lond.*, 211 A 1107:564–587, 1952.

[211] D. Lilly. The representation of small-scale turbulence theory in numerical simulation experiments. In H. Goldstine, editor, *Proc. IBM Scientific Computing Symp. on Environmental Sciences*, 1967.

[212] D. Lilly. A proposed modification of the Germano subgrid-scale closure method. *Phys. Fluids A*, 4 (3):633–635, 1992.

[213] F. Lin. A new proof of the Caffarelli-Kohn-Nirenberg theorem. *Comm. Pure Appl. Math.*, 51:241–257, 1998.

[214] J. Lions. Sur certaines équations paraboliques non linéaires. *Bulletin de la Société Mathématique de France*, 93:155–175, 1965.

[215] J. Lions. *Quelques Méthodes de Résolution Des Problèmes Aux Limites Non Linéaires*, volume 1. Ed. Dunod, 1969.

[216] S. Liu, C. Meneveau, and J. Katz. On the propierties of similarity subgrid-scale models as deduced from easurements in a turbulent jet. *J. Fluid Mech.*, 275:83–119, 1994.

[217] P. Lockard. An efficient, two-dimensional implementation of the Ffwocs-Williams and Hawkings equation. *J. Sound Vibr.*, 229:897–911, 2000.

[218] R. Löhner, K. Morgan, and O. Zienkiewicz. The solution of non-linear hyperbolic equations system by the finite element method. *Int. J. Numer. Meth. Fluids*, 4:1043–1063, 1984.

[219] E. Manoha, B. Trof, and P. Sagaut. Trailing-edge noise prediction using large-eddy simulation and acoustic analogy. *AIAA J.*, 38 (4):575–583, 2000.

[220] W. Matthaeus, W. Stribling, D. M. ans S. Oughton, and D. Montgomery. Selective decay and coherent vortices in two-dimensional incompressible turbulence. *Phys. Rev. Lett.*, 66 (21):2731–2734, 1991.

[221] E. Mcllwain and A. Pollard. Large eddy simulation of the effects of mild swirl on the near field of a round free jet. *Phys. Fluids*, 14 (2):653–661, 2002.

[222] J. McWilliams. The vortices of two-dimensional turbulence. *J. Fluid Mech.*, 195:303–340, 1988.

[223] J. Melenk and I. Babuska. The partition of unity method: basic theory and applications. *Comput. Methods Appl. Mech. Engrg.*, 139 (1-4):289–314, 1996.

[224] C. Meneveau. Statistics of turbulence subgrid-scale stresses: necessary conditions and experimental tests. *Phys. Fluids*, 6 (2):815–833, 1994.

[225] C. Meneveau and J. Katz. Scale-invariance and turbulence models for large-eddy simulation. *Annu. Rev. Fluid Mech.*, 32:1–32, 2000.

[226] C. Meneveau, T. Lund, and W. Cabot. A Lagrangian dynamic subgrid-scale model of turbulence. *J. Fluid Mech.*, 319:353–385, 1996.

[227] B. Mitchell, S. Lele, and P. Moin. Direct computation of the sound from compressible co-rotating vortex pair. *J. Fluid Mech.*, 285:181–202, 1995.

[228] B. Mitchell, S. Lele, and P. Moin. Direct computation of the sound generated by vortex pairing in an axisymmetric jet. *J. Fluid Mech.*, 383:113–142, 1999.

[229] S. Mittal and V. Kumar. Flow-induced vibrations of a light circular cylinder at Reynolds numbers 10^3 to 10^4. *J. Sound Vibr.*, 245(5):923–946, 2001.

[230] W. Möhring. On vortex sound at low Mach number. *J. Fluid Mech.*, 85:685–691, 1978.

[231] R. R. . P. Moin. Numerical simulation of turbulent flows. *Annu. Rev. Fluid Mech.*, 16:99–137, 1984.

[232] A. Monin and A. Yaglom. *Statistical Fluid Mechanics: Mechanics of Turbulence. Volume II.* Cambridge, MA: MIT Press., 1975.

[233] P. Morse and K. Ingard. *Theoretical acoustics.* Princeton University Press, 1968.

[234] R. Moser, J. Kim, and N. Mansour. Direct numerical simulation of turbulent flow up to $Re_\tau = 590$. *Phys. Fluids*, 11 (4):943–945, 1999.

[235] MP. Millennium Problems. Clay Mathematics Institute. www.claymath.org/millennium/. 2000.

[236] D. Muller and L. Davidson. Comparison of different subgrid turbulence models and boundary conditions for large-eddy simulations of room air flows. In M. M. Cecchi, K. Morgan, J. Periaux, B. Schrefler, and O. Zienkiewicz, editors, *7th International Conference on air distribution in rooms, roomvent 2000*, pages 301–306, 2000.

[237] K. Nagakura, Y. Moritoh, Y. Zenda, and Y. Shimizu. Aerodynamic noise of maglev cars. In *Proc. Inter-noise 94*, volume Vol I, page 157, 1994.

[238] P. Nelson and S. Elliot. *Active Control of Sound.* Academic Press, 1992.

[239] S. Newhouse, D. Ruelle, and F. Takens. Ocurrence of strange axiom A attractors near quasi-periodic flows on Tm, m bigger than 3. *Comm. Math. Phys.*, 64:35–40, 1978.

[240] A. Oberai and P. Pinsky. A multiscale finite element method for the Helmholtz equation. *Comput. Methods Appl. Mech. Engrg.*, 154:3281–297, 1998.

[241] A. Oberai and P. Pinsky. A numerical comparison of finite element methods for the Helmholtz equation. *J. Comput. Acoust.*, 8(1):211–221, 2000.

[242] A. Oberai and P. Pinsky. A residual-based finite element method for the Helmholtz equation. *Int. J. Numer. Meth. Engrg.*, 49:399–419, 2000.

[243] A. Oberai, F. Roknaldin, and T. Hughes. Computational procedures for determining structural-response due to hydrodynamic sources. *Comput. Methods Appl. Mech. Engrg.*, 190:345–361, 2000.

[244] A. Oberai, F. Roknaldin, and T. Hughes. Computation of trailing-edge noise due to turbulent flow over an airfoil. *AIAA J.*, 40(11):2206–2216, 2002.

[245] A. Obukhov. On the distribution of energy in the spectrum of trubulent flow. *Dokl. Akad. Sci. Nauk. SSSR*, 32 A:22–24, 1949.

[246] A. Obukhov. Some specific features of atmospheric turbulence. *J. Fluid Mech.*, 13:77–81, 1962.

[247] J. O'Neil and C. Meneveau. Subgrid-scale stresses and their modelling in a tubulent plane wake. *J. Fluid Mech.*, 349:253–293, 1997.

[248] O. Phillips. The intensity of aeolian tones. *J. Fluid Mech.*, 1:607–624, 1956.

[249] A. Pierce. *Acoustics: An introduction to its physical principles and applications.* Mc Graw-Hill, 1981.

[250] U. Piomelli. High Reynolds number calculations using the dynamic subgrid-scale stress model. *Phys. Fluids A*, 5 (6):1484–1490, 1993.

[251] U. Piomelli and J. Liu. Large-eddy simulation of rotating channel flows using a localized dynamic model. *Phys. Fluids*, 7 (4):839–848, 1995.

[252] U. Piomelli, P. Moin, and J. Ferziger. Model consistency in large eddy simulation of turbulent channel flows. *Phys. Fluids*, 31 (7):1884–1891, 1988.

[253] O. Pironneau. On the transport-diffusion algorithm and its application to the Navier–Stokes equations. *Numer. Math.*, 38:309–332, 1982.

[254] Y. Pomeau and P. Manneville. Intermitent transition to turbulence in dissipative dynamical systems. *Comm. Math. Phys.*, 74:189–197, 1980.

[255] S. Pope. *Turbulent Flows.* Cambridge University Press, 2000.

[256] A. Powell. On flow fields driving a contiguous acoustic field. *J. Acoust. Soc. Am.*, 36, 1964.

[257] A. Powell. Theory of vortex sound. *J. Acoust. Soc. Am.*, 36, 1964.

[258] A. Powell. Vortex sound: An alternative derivation of Møhring's formulation. *J. Acoust. Soc. Am.*, 97 (1), 1994.

[259] S. Putcrabey, P. Bertrand, and A. Jaques. Localization of flow noise sources on high speed train models in anechoic wind tunnel. In *Proc. Inter-noise 94*, volume Vol I, page 181, 1994.

[260] J. Rayleigh. *The theory of sound.* Reprinted by Dover, New York, 1945, 1896.

[261] H. Ribner. The generation of sound by turbulent jets. *Adv. Appl. Mech.*, 8, 1964.

[262] L. Richardson. Weather prediction by numerical process. *Cambridge: Cambridge University Press*, 1922.

[263] J. Ristorcelli. A closure for the compressibility of the source terms in Lighthill's acoustic analogy. Technical Report ICASE Report 97-44, NASA/CR-1997-201738, 1997.

[264] D. Ruelle and F. Takens. On the nature of turbulence. *Comm. Math. Phys.*, 20:167–192, 1971.

[265] P. Sagaut. *Large Eddy Simulation for Incompressible Flows.* Scientific Computing, Springer, 2001.

[266] P. Sampaio, P. Hallak, A. Coutinho, and M. Pfeil. A stabilized finite element procedure for turbulent fluid-structure interaction using adaptive time-space refinement. *Int. J. Numer. Meth. Fluids*, 44:673–693, 2004.

[267] T. Sassa, T. Sato, and S. Yatsui. Numerical analysis of aerodynamic noise radiation from a high-speed train surface. *J. Sound Vibr.*, 247 (3):407–416, 2001.

[268] V. Scheffer. Hausdorff measure and the Navier-Stokes equations. *Comm. Math. Phys.*, 55:97–112, 1977.

[269] J. Schetz. Aerodynamics of high-speed trains. *Annu. Rev. Fluid Mech.*, 33:371–414, 2001.

[270] C. Seror, P. sagaut, C. Bailly, and D. Juvé. On the radiated noise computed by large-eddy simulation. *Phys. Fluids*, 13 (2):4876–4878, 2001.

[271] S. Slimon, M. Soteriou, and D. Davis. Development of computational aeroacoustics equations for subsonic flows using a Mach number expansion approach. *J. Comput. Phys.*, 159:377–406, 2000.

[272] J. Smagorinsky. General circulation experiments with the primitive equations. I: The basic experiment. *Mon. Wea. Rev.*, 91(3):99–164, 1963.

[273] P. Spalart. Trends in turbulence treatment. Technical Report AIAA Paper 2000-2306, 2000.

[274] P. Spalart, W. Jou, M. Strelets, and S. Allmaras. *Comments on the feasibility of LES for wings and on a hybrid RANS/LES approach, in Advances in DNS/LES, C. Liu and Z. Liu (Eds.)*, pages 137–148. Columbus, OH: Greyden, 1997.

[275] C. Speziale. Galilean invariance of subgrid-scale stress models in large-eddy simulation of turbulence. *J. Fluid Mech.*, 156:55–62, 1985.

[276] J. Stewart and T. Hughes. *h*-adaptative finite element computation of time-harmonic exterior acoustics problems in two dimensions. *Comput. Methods Appl. Mech. Engrg.*, 146 (1-2):65–89, 1997.

[277] S. Stolz and N. Adams. An approximate deconvolution procedure for large eddy simulation. *Phys. Fluids*, 11 (7):1699–1701, 1999.

[278] S. Stolz, N. Adams, and L. Kleiser. An approximate deconvolution model for large eddy simulation with application to incompressible wall-bounded flows. *Phys. Fluids*, 13 (4):997–1015, 2001.

[279] V. Strouhal. On a special type of tone excitation. *Ann. Phys.*, 5 (7):216–251, 1878.

[280] P. Tabeling. Two-dimensional turbulence: a physicist approach. *Phys. Reports*, 362:1–62, 2002.

[281] C. Talote. Aerodynamic noise: a critical survey. *J. Sound Vibr.*, 231 (3):549–562, 2000.

[282] C. Tam and J. Webb. Dispersion-relation-preserving schemes for computational acoustics. *J. Comput. Phys.*, 107:262–281, 1993.

[283] A. Tejada-Martínez and K. Jansen. Spatial test filters for dynamic model large-eddy simulation with finite elements. *Commun. Numer. Meth. Engrg.*, 19 (3):205–213, 2003.

[284] A. Tejada-Martínez and K. Jansen. On the interaction between dynamic model dissipation and numerical dissipation due to streamline upwind/Petrov-Galerkin stabilization. *Comput. Methods Appl. Mech. Engrg.*, 194:1225–1248, 2005.

[285] R. Temam. *Navier-Stokes equations*. North-Holland, 1984.

[286] R. Temam. Some developments on Navier-Stokes equations in the second half of the 20th century. *In "Dévelopment des Mathématiques au cours de la seconde moitié du XXème siècle". J.P. Pier Managing Editor, Birkhauser Verlag*, 2000.

[287] L. Thompson and P. Pinsky. A Galerkin least-squares finite element method for the two-dimensional Helmholtz equation. *Int. J. Numer. Meth. Engrg.*, 38:371–397, 1995.

[288] L. Thompson and P. Pinsky. *Acoustics, in Encyclopedia of Computational Mechanics, E. Stein and R. de Borst and T.J.R Hughes (Eds.)*. Wiley, 2004.

[289] O. Vasilyev, T. Lund, and P. Moin. A general class of commutative filters for LES in complex geometries. *J. Comput. Phys.*, 146:82–104, 1998.

[290] J. von Neumann and R. Richtmyer. A method for the numerical calculation of hydrodynamical shocks. *J. Appl. Phys.*, 21:232, 1950.

[291] B. Vreman, B. Geurts, and H. Kuerten. Large-eddy simulation of the turbulent mixing layer. *J. Fluid Mech.*, 339:357–390, 1997.

[292] M. Wang and P. Moin. Computation of trailing-edge flow and noise using large-eddy simulation. *AIAA J.*, 38 (12):2201–2209, 2000.

[293] V. Wells and R. Renaut. Computing aerodynamically generated noise. *Annu. Rev. Fluid Mech.*, 29:161–199, 1997.

[294] J. Whitmire and S. Sarkar. Validation of acoustic-analogy predictions for sound radiated by turbulence. *Phys. Fluids*, 12 (2):381–391, 2000.

[295] G. Winckelmans, A. Wray, O. Vasilyev, and H. Jeanmart. Explicit-filtering large-eddy simulation using the tensor-diffusivity model supplemented by a dynamic Smagorinsky term. *Phys. Fluids*, 13 (5):1385–1403, 2001.

[296] O. Zienkiewicz and R. Codina. A general algorithm for compressible and incompressible flow—Part I. The split, characteristic-based scheme. *Int. J. Numer. Meth. Fluids*, 20:869–885, 1995.

[297] W. Zorumski. Classical theoretical approaches to computational aeroacoustics. In J. Hardin and M. Hussaini, editors, *Computational Aeroacoustics*. Springer Verlag, 1993.